Influence of crack opening, aggregates size and volume fraction on hydro-mechanical properties of concrete in a Brazilian splitting test : 3D meso-macro scale modeling and experimental work

Hayder Al-Khazraji

UNIVERSITE BRETAGNE LOIRE

UNIVERSITÉ DE NANTES

Thèse de Doctorat

Hayder AL-KHAZRAJI

Mémoire présenté en vue de l'obtention du
grade de Docteur de l'Université de Nantes
sous le sceau de l'Université Bretagne Loire

École doctorale : Sciences pour L'ingénieur, Géosciences, Architecture

Discipline : Sciences pour l'ingénieur
Spécialité : Génie Civil
Unité de recherche : Génie Civil et Mécanique UMR CNRS 6183

Soutenue le 30 Novembre 2017

Influence of crack opening, aggregates size and volume fraction on hydro-mechanical properties of concrete in a Brazilian splitting test: 3D meso-macro scale modeling and experimental work

JURY

Président du jury	**Nadia SAIYOURI**	Professeur, Université de Bordeaux
Rapporteurs :	**Farid BENBOUDJEMA**	Professeur, l'ENS Cachan
	Abdelkarim AÏT-MOKHTAR	Professeur, Université de La Rochelle
Invité(s) :	**Frédéric GRONDIN**	Professeur, Ecole Centrale Nantes
Directeur de Thèse :	**Abdelhafid KHELIDJ**	Professeur, Université de Nantes
Co-encadrant de Thèse :	**Nathan BENKEMOUN**	Maitre de Conférences, Université de Nantes
Co-encadrant de Thèse :	**Marta CHOINSKA**	Maitre de Conférences, Université de Nantes

Contents

List of Figures

List of Tables

Acknowledgements

I would like to express my deep gratitude to **Prof. Abdelhafid KHELIDJ**, my supervisor, for his patient guidance, enthusiastic encouragement and useful critiques of this research. I would like to thank **Dr. Nathan BENKEMOUN**, my co-supervisor, for his advice and assistance in keeping my progress on schedule for this work. My grateful thanks are also extended to **Dr. Marta CHOINSKA**, my co-supervisor. I wish to thank my officemates and friends especially **Mohammed Naji** for thier support and encouragement throughout my study.

Last but not least, I would like to thank my mother and father and my wife for their encouragement, unequivocal support and great patience at all times.

Abstract

Permeability is a parameter that may indirectly influence the durability of concrete structures by governing the rate of penetration of aggressive substances responsible for degradation under a pressure gradient.

The aim of this thesis is to study the interaction between the crack opening and the transfer of fluids in concrete of the Brazilian splitting tensile test (BSTT). Herein, the influence of aggregates size and volume fraction on hydro-mechanical properties of concrete is investigated. This study consists of two parts: the numerical and the experimental one. The first one focuses on the meso-scale modeling of a heterogeneous material like a concrete, which may be characterized by two features: multi-phase behavior and 3D crack propagation. The numerical study deals therefore with the coupling between crack opening and gas permeability according to a developed hydro-mechanical model at a meso-scale. The objective of the second, experimental part, is to provide data for numerical models and to validate the latter. This work is carried out on mortar specimens with 3 different aggregate sizes, submitted to gas transfer during a BSTT.

The numerical meso-scale model is based upon a 3D lattice approach to represent the heterogeneity of the material and the failure mechanism of concrete. This model considers concrete as a two-phases material in which aggregates melt within a cement paste. Because a non-adapted meshing process was used to mesh the microstructure, a weak discontinuity was introduced in the first enhancement of the kinematics.

The second enhancement of kinematics introduced here is the displacement discontinuity (strong) to represent crack opening (discontinuous displacement-field). The hydro-mechanical model represents the transport of fluids (gases) through

the concrete, depending on Darcy's law for a uncracked section (porosity) and Poiseuille's law for a cracked section (laminar flow). In this model, the interaction between the crack opening, obtained from the mechanical model (meso-scale), and the gas permeability is investigated.

The experimental work is presented for the validation of the hydro-mechanical model. The numerical results show good agreement with some previous experimental and theoretical studies.

Résumé

La perméabilité influe indirectement sur la durabilité des structures en béton. Elle gouverne le taux de pénétration des agents agressifs, responsables de dégradations, sous un gradient de pression.

Ce travail a pour but l'étude des interactions entre l'ouverture des fissures et le transport des fluides dans le béton, soumis à un essai Brésilien de traction indirect par fendage. Ici, l'influence de la taille des granulats et de la fraction volumique sur les propriétés hydro-mécaniques du béton est étudiée. Cette étude est composée de deux parties : une numérique et une expérimentale. La première concerne la modélisation des matériaux hétérogènes, tels que le béton, et met en évidence ses deux particularités : l'aspect multiphasique du matériau et la propagation 3D de fissures. Ainsi, nous proposons un couplage entre l'ouverture de fissure et la perméabilité au gaz selon un modèle hydro-mécanique à l'échelle mésoscopique. L'objectif de la deuxième partie expérimentale est de fournir des données pour des modèles numériques et de les valider ainsi. Ce travail est réalisé sur des éprouvettes de mortier avec 3 différents tailles de granulat, soumises au transfert de gaz au cours du chargement par l'essai Brésilien.

Le modèle numérique mésoscopique, employé dans cette étude, est basé sur une approche tridimensionnelle pour représenter l'hétérogénéité du matériau et les mécanismes de rupture du béton. Ce modèle considère le béton comme un matériau bi-phasique où les granulats sont fondre dans la pâte du ciment. Afin de pallier aux hétérogénéités du matériau et l'emploi du maillage non-adaptatif, une faible discontinuité a été introduite dans le premier enrichissement de la cinématique.

Le deuxième enrichissement de la cinématique introduite ici est la discontinuité du déplacement (forte) afin de représenter l'ouverture de la fissure (champ du déplacement discontinu). Le modèle hydromécanique représente le transport du fluide (gaz) dans le béton par l'intermédiaire de la loi de Darcy pour la section non fissurée (porosité) et par la loi de Poiseuille pour la section fissurée (flux laminaire). Dans ce modèle, une interaction entre l'ouverture de fissure, obtenue par le modèle mécanique (mésoscopique), et la perméabilité du gaz est considérée.

Le travail expérimental effectué est présenté pour la validation du modèle hydro-mécanique numérique proposé. Les résultats de simulations numériques sont en accord avec des travaux expérimentaux et théoriques précédents.

0.1 Introduction

Le béton est un matériau poreux, hétérogène composé de granulats et de pate de ciment. L'objectif de ce travail de thèse est de fournir une meilleure compréhension du comportement du béton sous un chargement et des interactions entre l'ouverture de fissures et la perméabilité. En effet, deux modèles numériques sont présentés : un modèle mécanique pour expliquer le comportement du matériau hétérogène tel que le béton sous un chargement dans le contexte de l'essai Brésilien. Aussi, un modèle hydromécanique est employé pour l'investigation du couplage entre la perméabilité et l'ouverture de fissure. Plusieurs paramètre influencent le comportement mécanique du béton sous un chargement tels que : le type de ciment, les propriétés des granulats, les conditions environnementales et le type du chargement, etc. Dans cette étude, l'influence de la taille de granulats et du volume granulaire sur le comportement mécanique et hydromécanique du béton sous un chargement est étudié. Deux modèles 3D basés sur la méthode des éléments finis sont présentés. Le premier, mécanique et prend en compte différente tailles de granulats et volume de fraction utilisés. Ces deux paramètres conduisent à des différents comportements du béton sous un chargement basé sur des modèles mécanique à l'échelle mésoscopique. Le deuxième modèle (hydromécanique) explique les interactions entre les propriétés physiques (perméabilité) et la fissuration dues à un chargement mécanique.

Grâce à ce couplage entre les propriétés hydromécaniques, effectué par un modèle numérique (basé sur la méthode des éléments finis) capable de représenter le comportement complexe du béton mentionné ci-dessus. Ce modèle est utilisé pour étudier l'importance de la contrainte du béton sous un chargement et l'évolution de la perméabilité des fluides dans ces conditions. L'objectif derrière est la caractérisation des interactions entre les paramètres influençant la perméabilité du béton dont la perméabilité au gaz est le paramètre primordial qui désigne la capacité du béton à transporter un fluide (liquide ou gaz). La perméabilité du béton peut être affectée, d'une manière significative, par le réseau poreux, la connectivité et la teneur en eau du matériau.

La durabilité du béton est influencée par le flux de fluides, de gaz et de polluants dans la porosité. La présence de fissures dans les structures en béton armé affaiblit la résistance du milieu poreux (béton) vis-à-vis la pénétration de ces fluides et fournit des chemins

d'écoulement pour des agents agressifs tels que: l'oxygène (désaération), l'hydrogène sulfuré, les chlorures…etc.

0.2 Motivation et objectif de la recherche effectuée

L'hétérogénéité du béton est l'un des points les plus caractéristiques pour laquelle ce travail a donc été réalisé. Peu de travaux numériques dans la littérature ont considéré que le béton est un matériau multiphasique. En outre, il existe des paramètres qui ont une grande importance sur la durabilité et les performances structurelles des matériaux cimentaires tels que la taille, le contenu et le type des agrégats.

Enfin, la fraction volumique des agrégats occupe environ 75% du volume total de béton. L'étude de ces caractéristiques est le premier objectif de ce travail.

Le second objectif est le phénomène de perméabilité. Cette dernière est définie comme la capacité d'un matériau poreux tel que du béton à transporter des fluides (eau ou gaz) sous un gradient de pression. L'écoulement se produit dans un réseau poreux, y compris des vides ou des fissures de pores initiaux et spécifiques. Ceux-ci sont induits par différentes contraintes, connectant les chemins de percolation, qui réduisent la résistance au flux du milieu poreux et provoquent une augmentation de la perméabilité. La perméabilité peut influencer sur la durabilité des structures en béton en régissant le taux de pénétration des agents agressifs. Cet effet est direct lorsque la structure a une partie scellée tels que les réservoirs et les centres de bâtiment réacteurs nucléaires. Le matériau poreux comprend de nombreuses caractéristiques qui influent sur la durabilité des structures et offrent une protection optimale aux armatures.

De nombreux phénomènes provoquent la corrosion des armatures et, par conséquent, la détérioration du béton armé. Généralement, le dioxyde de carbone (CO_2) contenu dans l'air et les chlorures, venant de sels de mer ou de déverglaçage sont les deux principaux agents qui cause de la corrosion des armatures. La principale complication est ainsi constituée par la nature hétérogène du béton (mortier et granulés), ce qui conduit à la présence de fissures micro / macro inévitables même avec une faible contrainte à un âge précoce. Ces fissures nécessitent une étude approfondie, car elles peuvent former des voies préférentielles pour le transport des fluides (eau ou gaz). Par conséquent, nous nous sommes intéressés à la prédiction du flux dans le béton, ainsi que l'évaluation des performances structurelles associées à la dégradation des propriétés du matériau

(corrosion des armatures, carbonatation du béton, etc), ainsi que la prédiction des fissures et de leur impact sur les propriétés de transfert du matériau tels que la perméabilité et le coefficient de diffusion…etc.

Cette recherche a pour objectif le développement d'une méthode numérique permettant d'étudier l'influence de la taille de granulats et la fraction volumique sur le comportement mécanique du béton sous un chargement et d'évaluer la perméabilité dans ce matériau hétérogène. Ainsi, ce travail étudie les interactions entre la fissuration et la perméabilité du fluide dans le test brésilien et étudie l'importance de la taille des granulats et de la fraction volumique sur les propriétés hydromécaniques et la perméabilité des matériaux poreux. Pour obtenir ces conditions, trois catégories doivent être assurées :

1. Les principaux aspects du béton fissuré (hétérogénéité, effet d'échelle…) et les informations locales fournies lors de la fissuration (emplacement, direction et l'ouverture des fissures) doivent être pris en compte dans le modèle.
2. Un modèle de couplage hydromécanique doit être conçu afin de décrire les interactions entre les propriétés de transfert du milieu poreux et l'ouverture de la fissure dans le contexte du test brisé brésilien.
3. Enfin, les lois constitutives pour le travail expérimental doivent être expliquées pour décrire l'influence de la taille de granulats et de la fraction de volume sur les propriétés mécaniques et hydromécaniques du matériau.

Plusieurs modèles dans la littérature décrivent la fissuration dans les milieux poreux. Colliat *et al.* [**Colliat et al., 2007**], Bruggi *et al.* [**Bruggi et al., 2008**], Yang et Frank Xu [**Yang et Xu, 2008**], Ibrahimbegovic *et al.* [**Ibrahimbegovic et al., 2011**], et Syroka-Korol *et al.* [**Syroka-Korol et al., 2013**] décrivent certains des modèles tenant compte de l'hétérogénéité du matériau par l'introduction des champs aléatoire des propriétés mécaniques. Pour cette raison, ces méthodes et leurs hypothèses ont été présentées. Dans cette étude, nous nous basons sur ces modèles. En outre, ces modèles sont en mesure de fournir des informations pertinentes sur les propriétés géométriques des fissures telles que l'ouverture de fissures, l'orientation des fissures…etc. Ceci est primordial lorsque nous considérons le transfert de fluide dans un milieu poreux.

Le contexte de l'approche de modélisation conduit à décrire les propriétés des fissures et la relation entre la perméabilité et l'ouverture des fissures et leurs géométries (tortuosité, rugosité…etc) [**Réthoré et al., 2007**], [**Khoei et al., 2011**], [**Barani et al., 2011**], [**Meschke et al., 2011**]. Il existe dans la littérature une loi permettant de décrire l'impact local de l'ouverture des fissures sur l'augmentation de la conductivité hydraulique à travers les éléments structurels. Le modèle le plus utilisé pour décrire le flux d'un fluide incompressible dans le flux laminaire à travers l'ouverture de fissure est nommé modèle de plaques parallèles (PPC) [**Poiseuille, 1844**], [**Snow, 1969**].

De nombreux travaux théoriques et expérimentaux ont été présentés à cet effet dans le contexte de la mécanique des roches [**Lomize, 1951**], [**Romm, 1966**], [**Louis, 1974**], [**Brush et Thomson, 2003**] et [**Crandall et al., 2010**]. En revanche, très peu d'études ont été réalisées sur des structures en béton. Wang *et al.* [**Wang et al., 1997**], Aldea *et al.* [**Aldea et al., 1999**], Choinska *et al.* [**Choinska et al., 2007**], Picandet *et al.* [**Picandet et al., 2009**], Akhavan *et al.* [**Akhavan et al., 2012**] ont présenté des études expérimentales concernant l'évolution des propriétés de transport dans les structures en béton. Un modèle mécanique numérique 3D pour représenter l'ouverture de fissures dans un matériau hétérogène et un comportement hydromécanique ne permet pas d'obtenir suffisamment d'informations. Par conséquent, un travail expérimental pour la validation et la fourniture de ce contexte seront nécessaires et démontrés dans ce travail.

0.3 Plan de la thèse

L'objectif de cette thèse est de développer un modèle numérique basé sur la méthode des éléments fini enrichis (E-FEM). Cette dernière est réalisée à l'échelle mésoscopique pour représenter l'ouverture de la fissure dans un matériau 3D hétérogène pour simuler l'essai brésilien. Ce modéle est connu sous le nom du modèle mécanique. Le deuxième hydromécanique est utilisé pour le couplage entre l'ouverture de fissures et le transfert de fluide (perméabilité de l'eau ou du gaz). Ce modèle est basé sur l'équation de Poiseuille pour les fluides laminaires dans les tuyaux et la loi de Darcy pour les pores. Un travail expérimental est également présenté pour la validation des modèles numériques.

Afin d'expliquer les méthodes, les caractéristiques choisies et les résultats obtenus, rapport est divisée en six chapitres :

- Le premier chapitre se focalise sur une introduction générale du sujet et explique le comportement mécanique du béton sous un chargement et de la perméabilité du fluide (eau ou gaz) dans les structures en béton sous un gradient de pression. Aussi, nous présentons les modèles hydromécaniques utilisés dans la littérature pour simuler la perméabilité du fluide dans les milieux poreux tenant compte de l'influence de l'ouverture de fissures.
- Le second chapitre expose les travaux expérimentaux présentant le comportement du béton en cours de chargement et les paramètres influençant le comportement mécanique, tels que la taille des agrégats et la fraction de volume. Ensuite, la partie physique explique le transfert de fluide dans les structures en béton (La perméabilité). Dans ce document, certains paramètres influençant la perméabilité est sont présentés. Enfin, nous présentons le couplage entre la fissuration et la perméabilité dans les structures en béton.
- Le troisième chapitre présente le modèle mécanique (à l'échelle mésoscopique) proposé par Benkemoun *et al.* [**Benkemoun et al., 2010**]. Le modèle est basé sur une approche en treillis 3D représentant l'hétérogénéité et le mécanisme de défaillance du béton pour la mise en œuvre de l'ouverture des fissures. Ce modèle considère le béton comme un matériau bi-phasique dans lequel les granulats fondent dans une pâte de ciment. La méthode des éléments finis (E-FEM) et le programme d'analyse des éléments finis (FEAP) sont utilisés dans cette étude pour la simulation 3D de la rupture par le test brésilien. Le modèle mécanique peut représenter un matériau hétérogène 3D et fournit trois types d'éléments de barre (agrégats, mortiers et auréole de transition entre eux). Aussi, nous étudie l'influence de la taille des granulats et de la fraction de volume sur le comportement mécanique d'un matériau hétérogène.

  En plus, se concentre sur le modèle hydromécanique dans cet chapitre, qui repose sur la loi de Darcy pour représenter la perméabilité dans la porosité et la loi de Poiseuille pour la perméabilité de la section fissurée (écoulement laminaire). Nous présentons le modèle hydromécanique (couplage) qui explique lien entre la fissuration et la perméabilité à l'échelle mésoscopique. Ensuite, nous étudions l'effet de l'ouverture de fissures, calculée à partir du modèle exposé

dans le chapitre trois, et le lien avec la perméabilité basé sur la loi de Poiseuille. Aussi, la perméabilité dans les milieux poreux est basée sur la loi de Darcy. En fin, l'influence de la taille des granulats et de la fraction volumique sur la perméabilité du béton est présentée.

- Le chapitre quatre se focalise sur le travail expérimental élaboré pour la validation du modèle mécanique et hydromécanique à l'échelle mésoscopique. En effet, quatre types d'échantillons cylindriques ont été réalisés en utilisant des billes de verre comme granulats. Un type est considéré comme référence : ces échantillons sont sans granulats grossiers, mortier seulement. Pour les deux autres types, trois diamètres de granulat sont examinés : 2, 6 et 10 mm, le volume de fraction étant de 20%. Une compagne expérimentale est présentée, à savoir l'essai brésilien de rupture par traction pour le comportement mécanique sous charge diamétrale et l'essai de perméabilité au gaz pour le comportement hydromécanique. Les effets de la taille des granulats, de l'ouverture de la fissure, de la position de la fissure et de son trajet sont étudiés.
  Enfin, les résultats expérimentaux sont comparés à ceux numériques en utilisant un modèle mécanique et hydromécanique à l'échelle mésoscopique.

- Les conclusions et les perspectives sont présentées dans le chapitre cinq.

Chapter 1

INTRODUCTION

1.1 Introduction

Concrete is considered as a heterogeneous material in which composite aggregate particles melt into a cement paste. It is also a porous medium. Therefore, concrete durability is strongly influenced by the flow of fluids, gas and pollutants in the porous matrix.The presence of cracks in concrete structures weakens the strength of the porous medium (concrete) and provides paths of flow for aggressive agents such as: sulphates, chlorides, carbon dioxide, etc. This work aims to provide a better understanding of the mechanical behavior of concrete under loading and to demonstrate the interactions between crack opening and the flow of fluid or permeability. This parameter is the main one that defines the ability of concrete to carry a fluid (liquid or gas). The porous network and its connectivity and the water content of the material significantly affect on the permeability of concrete. In order to develop predictive concrete durability today, two numerical models are investigated in this thesis: a **mechanical one** to represent the behavior of a heterogeneous material such as concrete under diametral loading in the context of the Brazilian splitting tensile test, and a **hydro-mechanical model** to inves-

tigate the gas of permeability coupling with the crack opening. There are many parameters that need to be studied which influence the mechanical behavior of concrete under service loading, such as: the type of cement, the aggregate properties, its size and content, the weather conditions, the type of loading, the quality of manufacturing, etc. In this study, the influence of aggregates size and of volume fraction on the mechanical and hydro-mechanical behavior of concrete under loading is investigated. The presented two numerical are based on 3D Embedded Finite Element Method (E-FEM) formulation to describe meso-scale behavior (see [Benkemoun, 2010]). The first model (mechanical one) provides the effects of aggregates size and of volume fraction on concrete tensile behavior. The second model (hydro-mechanical one) is carring out with the interactions between the physical properties (permeability) and crack opening, aggregates size and volume fraction when concrete is under loading.

Through this hydro-mechanical coupling the proposed numerical model is able to represent the complex behavior mentioned above, and especially to investigate the significance of the stress effects under loading and the development of the permeability under these conditions.

To validate and provide the numerical models, mechanical model and hydro-mechanical model, an experimental work is presented. Three aggregate sizes (galss beads) are investigated varying from 2 to 10mm. The numerical results show good agreement with the experimental results and some previous experimental and theoretical studies in literature review.

1.2 Motivations and objectives of the research

The heterogeneity of concrete is one of its most characteristic points, thus this work was carried out. Furthermore, few numerical studies have pointed out that

concrete is a multi-phase material in three dimensions. In addition, there are some parameters that greatly affect on the durability and structural performance of concrete material such as aggregates size, content and type. Lastly, the volume fraction of aggregates occupies approximately 75 % of the total volume of concrete. Investigating these features is the first goal of this study.

The second goal is the phenomenon of permeability, which is defined as the ability of a porous material such as concrete to transport fluids (water or gas) under a pressure gradient. The flow occurs in a porous network, including initial and specific pore voids or cracks. These are induced by various stresses, usually interconnecting the percolation paths, which reduce the flow resistance of the porous medium and cause an increase in permeability. Permeability is a parameter that can indirectly influence the durability of concrete structures by governing the rate of penetration of aggressive agents, but this effect is direct when the structure has a sealed part, such as confining structures (reservoir tanks or nuclear power reactors buildings). The porous material includes many characteristics that influence on the durability of structures and provides optimum protection for the steel reinforcement.

There are many problems causing the deterioration of reinforced concrete, which consists of the corrosion of the reinforcement. The pores in the concrete enable the penetration of fluid over time, which leads to the gradual degradation of the material's characteristics. Generally, carbon dioxide (CO_2) contained in the air and the chlorides in marine environmental or de-icing salt are the two main agents that cause corrosion of the reinforcement. The major complication is thus constituted by the heterogeneous nature of concrete (paste and aggregate), which leads to the presence of micro/macro cracks that are inevitable even with weak stress at an early age. These cracks and those that will be introduced are very important to study because they may form preferential pathways for fluid flow (water

or gas). Therefore, we are interested in estimating the flow rate in concrete, as well as the evaluation of structural performance associated with the degradation of the material's properties (reinforcement corrosion, carbonation of concrete, etc.) and the prediction of cracks and their effect on the transfer properties of the material such as permeability coefficient, diffusion coefficient, etc.

The aim of this research is the development of a numerical method to study the influence of aggregates size and volume fraction on the mechanical behavior under diametral loading, and to evaluate the permeability in a heterogeneous material such as concrete. Thus, this work investigates the interactions between cracking and the permeability of fluid in the tensile splitting test (Brazilian test) and studies the effect of aggregates size and volume fraction on the hydro-mechanical properties and the permeability of porous materials. To obtain these conditions, three categories must be ensured:

1. For the modeling process, the main aspects of the cracked concrete must be taken into account (such as heterogeneity, scale effects, etc.) and local information provided on cracking (such as location, direction and crack opening).

2. A coupling model (hydro-mechanical) must be devised to describe the interaction between the transfer properties of the porous medium and crack opening in the context of the Brazilian splitting test.

3. Finally, the constitutive laws for the experimental work must be explained to describe the influence of the aggregates size and volume fraction on the mechanical properties and the development of the hydro-mechanical properties of the material.

There are many models in the literature that describe the cracks in a porous medium but few describe the flow in these cracks. Colliat et al. [Colliat et al.,

2007], Bruggi et al. [Bruggi et al., 2008], Yang and Frank Xu [Yang and Xu, 2008], Ibrahimbegovic et al. [Ibrahimbegovic et al., 2011], and Syroka-Korol et al. [Syroka-Korol et al., 2013] describe some of the models that take into account the heterogeneity of the material through the introduction of the random distribution of mechanical properties. For this reason, this formulation (the numerical method of finite element) and assumptions were presented. We depended on these models in this study. At the same time, these models are able to provide relevant information about the geometrical properties of cracks such as (crack openings, cracks orientation, etc.). This issue appears to be an essential point when considering the transfer of fluid in a porous medium.

The context of the modeling approach leads to describing the properties of cracks: in fact, the relationship between the permeability and the crack opening and its geometry (tortuosity, roughness, etc.), Réthoré et al. [Réthoré et al., 2007], Khoei et al. [Khoei et al., 2011], Barani et al. [Barani et al., 2011], and Meschke et al. [Meschke et al., 2011]. There is a law which is constitutive of this relationship to estimate the local effect of crack opening on the increase in hydraulic conductivity through the structural elements. The model most commonly used to describe the flow of an incompressible fluid in laminar flow through the crack opening is named the parallel plates model (PPM) (cubic law), Poiseuille [Poiseuille, 1844], Snow in [Snow, 1969].

Many theoretical and experimental works have been presented for this purpose in the context of rock mechanics, Lomize [Lomize, 1951], Romm [Romm, 1966], Louis [Louis, 1974], Brush and Thomson [Brush and Thomson, 2003], Crandall et al. [Crandall et al., 2010], while few studies have been carried out on concrete structures. Wang et al. [Wang et al., 1997], Aldea et al. [Aldea et al., 1999], Choinska et al. [Choinska et al., 2007] Picandet et al. [Picandet et al., 2009], Akhavan et al. [Akhavan et al., 2012] presented experimental studies concerning

the evolution of the transport properties in concrete structures. A 3D numerical mechanical model to represent crack opening in a heterogeneous material and hydro-mechanical behavior is not possible to obtain enough information. Therefore, experimental work for validation and providing this context will be needed and demonstrated in this work.

1.3 Plan of the thesis

The objective of this thesis is to develop numerical models using the finite element method (E-FEM); this method is carried out at the meso-scale to represent crack opening in a 3D heterogeneous material for simulating the Brazilian splitting tensile test. This model is known as the mechanical model. The second model is known as the hydro-mechanical model for the coupling between crack opening and the transfer of fluid (permeability of water or gas). This model is based on Poiseuille's equation for laminar fluid in pipes and Darcy's law for the pores.

Experimental work is also presented for the validation of numerical models. To explain the methods and characteristics chosen and the results obtained, this thesis is divided into five chapters:

⇒ Chapter one focuses on a general introduction of the subject including the mechanical behavior of concrete under service load and the permeability of fluid (water or gas) for concrete structures under a fluid pressure gradient. It also consists of some previous studies of researchers who presented a hydro-mechanical model to represent the permeability of fluid in porous media with the influence of crack opening. In addition, this chapter describes the plan of the thesis.

⇒ Chapter two consists of a literature review of the many experimental and theoretical research works to explain the behavior of concrete under loading and provided some parameters that affect on the mechanical behavior, such as aggre-

gates size and volume fraction, and investigated the types of cracks. Then, the physical part is explained about the transfer of fluid (water or gas) in concrete structures thereby defining permeability in porous media. Herein, some of the parameters that affect on the permeability are pointed out. Finally in this chapter, a literature review is presented about coupling cracking and permeability in concrete structures and the influence of cracking on the permeability of porous media such as concrete.

⇒ Chapter three presents the numerical-mechanical model (meso-scale) and hydro-mechanical model which are proposed by Benkemoun et al. [Benkemoun et al., 2010]. The meso-scale model is based on a 3D lattice approach to represent the heterogeneity and failure mechanism of concrete for implementing crack opening. This model considers concrete as a two-phase material in which aggregates melt into a cement paste. The finite element method (E-FEM) and the FEAP (Finite Element Analysis Program) are used in this study for 3D simulation of the Brazilian splitting tensile test. The mechanical model can represent a 3D heterogeneous material and provides three types of bar elements (aggregate, mortar and the interaction zone between them). Herein, the influence of aggregates size and volume fraction on the mechanical behavior of a heterogeneous material is investigated.

The hydro-mechanical (coupling) model is presented, which used to make the link between cracking and permeability at the meso-scale. Herein, is studied the effect of crack openings, which were computed from the meso-scale model and the link with permeability is presented, based on Poiseuille's law, and the permeability in porous media is computed based on Darcy's law. In addition, the influence of aggregates size and volume fraction on the permeability of concrete is presented.

⇒ Chapter four contains the experimental work to validate the meso-scale mechanical and hydro-mechanical models. Four groups of cylinderical specimens

have been realised, using glass beads particles as the coarse aggregate. One group is considered as reference: these specimens without coarse aggregates , mortar only. Three aggregate diameters are examined: 2, 6 and 10 mm, with the volume of fraction is 20 %. Two types of tests are presented, firstly is the Brazilian splitting tensile test for mechanical behavior under diametral loading and secondly the gas permeability test for the hydro-mechanical behavior. Effects of aggregates size, crack opening, crack position and its path are investigated. Finally, the experimental results are compared with the mechanical meso-scale and hydro-mechanical models.

$\Rightarrow$ Conclusions and perspectives are presented in chapter five.

Chapter 2

THE MECHANICAL BEHAVIOR OF POROUS STRUCTURES AND THE PERMEABILITY OF CONCRETE

This chapter consists of two parts: the first is the mechanical part, which describes the behavior of porous media under service loading, i.e. the indications of concrete structures under different applied loads. The second part explains the physical part, which is the transfer of fluids, such as water or gas, in porous media. This part also presents the most widely used theories for the coupling between damaged concrete (cracked section) and uncracked section / permeability. Finally, this chapter provides a literature review of experimental and theoretical studies.

2.1 Introduction

Concrete durability is related to its permeability. There are many authors pointed out that a well designed and manufactured of concrete structure according to transport fluids (gas and water), this behavior due to the porosity of material and microcracks.Concrete structures are deteriorating and cracking caused by the service loads or weathering should be taken into account during durability design. Cracks in concrete consider pathway of fluids, therefore the permeability increases in cracked concrete.

There are many parameters play a critical role in controlling a durability of concrete such as: aggregates size, type, volume fraction and surface area. Tasdemir et al. [Tasdemir et al., 1996]investigated the influence of aggregates size and its type on the mechanical properties. Tasdemir et al. [Tasdemir et al., 1996] investigated the effecting of maximum aggregate size and its length on the number of cracks and its width. While there is a little informations in the previous studies about the effect of volume fraction of aggregate on the fracture properties of concrete, therefore this study is presented. Petersson [Petersson, 1980] and Zhang et al. [Zhang et al., 2005] explained the influence of maximum aggregate size on the mechanical properties of concrete and fracture energy. Hillerborg [Hillerborg, 1985] reported that the fracture energy values for the concretes larger than corresponding mortars. Bisschop and van Mier [Bisschop and Van Mier, 2002] showed increasing aggregates size from 2 to 6 mm leads to an increase in total crack length but also in the maximum crack depth. Chen and Lui [Chen and Liu, 2004] found that the increasing volume of aggregate from 40 % to 80 % both fracture energy and critical stress intensity increase, this indication for low-strength concrete, while for high-strength concrete this percent was achieved 60 %. Saouma et al. [Saouma et al., 1991] showed the fracture energy increases when the volume fraction is increasing,

while the tensile strength shows a reserve tendency with the volume fraction for high-strength concrete. Burcu Akcay et al. [Akcay et al., 2012] carried out the increasing of splitting tensile strength, compressive strength, modulus of elasticity and bending strength of concrete with the increasing volume fraction of aggregate.

Some of the authors found a reverse result that corresponds the volume fraction. On the other word, Grassl et al. [Grassl et al., 2010] carried out the increasing of volume fraction in concrete caused to decrease of tensile strength, fracture energy, crack width and modulus of elasticity. The experimental study was presented by Amparano et al. [Amparano et al., 2000], it explained the decreasing of fracture energy caused by the increasing of volume fraction of aggregate before its minimum value at 65 % volume of aggregate, and when the minimum percent is more than 65 % leads to increase the fracture energy. Also, the coarsenes of random grain structure of concrete effects on the fracture transition zone and , based on a morphological model: mosaic pattern.

Grassl et al. [Grassl et al., 2010] found out that permeability increases with the increasing of aggregates diameter and decreasing of the volume fraction. Picandet et al. [Picandet et al., 2009] pointed out the permeability of gas and water increase with the increasing of crack opening . Care et al. [Care and Derkx, 2011] presented the correlation between the aggregate size and volume fraction with the permeability of gas, i.e. gas permeability depends upon aggregate size and its content.

2.2 Mechanical part

This part presents the type of fractures (cracks) in concrete and shows the characteristics that affect on the properties of transferring fluids in concrete structures, such as: type of load, cracks, crack width, orientation of cracks, aggregates size,

volume fraction, etc.

2.2.1 Type of fractures (cracks)

There are three types of fracture in concrete structures. However, to understand the fracture mechanics, which depend on many characteristics such as the properties of materials, the geometry of the body, loads, etc., the type of crack must be known. The aggregate particles melt into a cement paste in three dimensions and to evaluate the numerical results, a good model for the engineering work will be necessary when applying a load (tensile stress) until the ultimate tensile stress is reached (tensile strength) in the context of splitting tensile strength. As shown in Figure (2.1), the three modes of cracking in bodies are:

1. **Mode I**: the crack opens when the loading is normal (tensile load).
2. **Mode II**: the in-plane shear when the loading is perpendicular to the surface of the body.
3. **Mode III**: the out of plane shear when the rupture or crack is parallel to the loading.

2.2.2 Effects of mechanical stress on the initial porous structure

This section presents the types of cracks corresponding to the kinds of loading for different works. When applying load on the concrete structure causing damage of the material (cracks), this damage will decrease the module of elasticity and bond strength between the cement and the aggregate, i.e. the presence of cracks in concrete structures weakens the strength of the concrete under loading. Figure

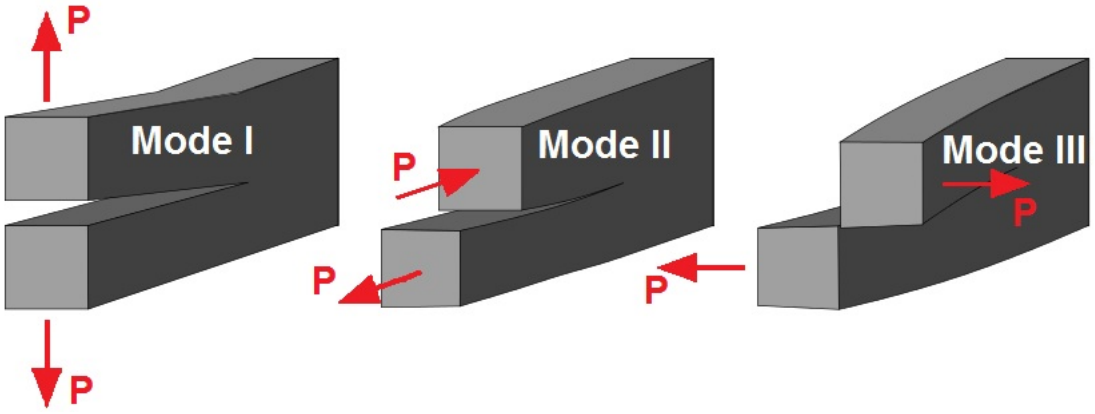

Figure 2.1: Three types of fractures by Bao-Chan Do in [Bao-Chan, 2014].

(2.2) shows the stress-strain relations for the cement paste, aggregate and concrete. There are many methods in experimental work for locating and showing the position of cracks (optical microscopy, X-ray, ultrasonic wave propagation, acoustic emission and strain gauge). Mehta in [Mehta, 1986] investigated the type of cracks when applying a compression load on a concrete structure. The cracks are divided into two types that correspond to their position: the first one is the interaction zone between the aggregates and cement paste, i.e. the crack surrounds the aggregate particles; the second one is through the mortar or cement paste, see Figure (2.3).

The properties of concrete under a compression load are used more in concrete structures, therefore there are many studies regarding the behavior of concrete with cracks under a compression force [Mehta, 1986], [Neville, 1997]. Although the tensile strength of concrete is 10 % of the compression strength, it is an important factor that affects on the durability of concrete through the penetration of aggressive agents. Thus, some experimental studies will be reported that explain the tensile stress with cracks, this relation depending on the applied loads and the crack opening. Through this relationship, the behavior of concrete under tensile loading can be understood.

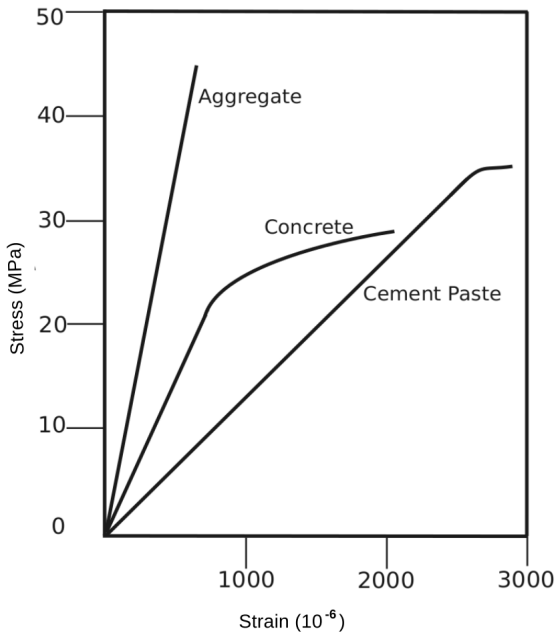

Figure 2.2: Typical stress-strain relations for cement paste, aggregate and concrete by Neville [Neville, 1997].

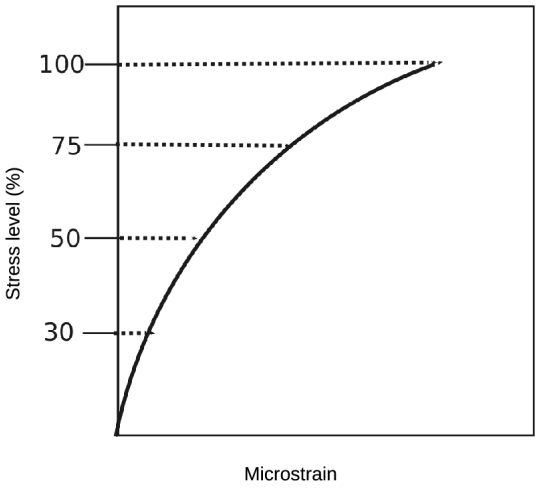

Figure 2.3: Schematic illustration of the cracking of concrete under a compression load (a) stress level with microstrain; (b) form of cracks under compression load by Mehta [Mehta, 1986].

2.2.3 Compression cracks

This type of crack occurs when the concrete specimen is under a compression load. Ramtani et al. [Ramtani et al., 1992] presented an experimental study, in which they showed the behavior of concrete under a compression load whose level was varied by loading-unloading cycles. Figure (2.4) shows the stress-strain relations for these cycles.

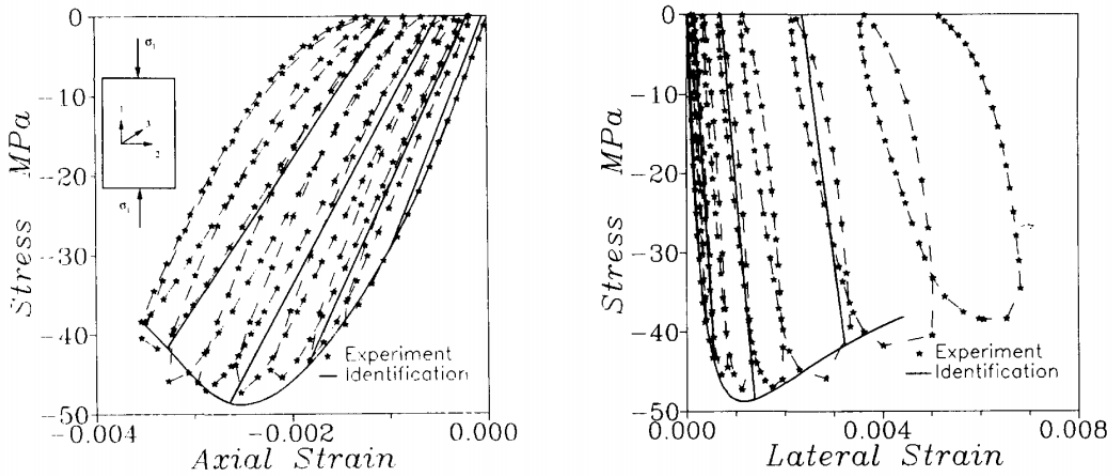

Figure 2.4: Behavior of concrete under a compression load by Ramtani et al. [Ramtani et al., 1992].

Mehta [Mehta, 1986] described the cracks resulting from a compression load with different levels of loading and this study was in agreement with the results obtained by Ramtani et al. [Ramtani et al., 1992].

The behavior of concrete under compression stress can be explained by four stages as follows:

1. Mehta [Mehta, 1986] explained the first microcracks occoured in the interaction field (interaction zone) between the aggregate particles and the mortar (cement paste) when the compression load was applied until 30 % of the

maximum loading, while the behavior was almost linear up to 40-60 % of the maximum loading, see Figure (2.3).

2. When the load was increased to 75-85 % of the maximum loading, the behavior of concrete became non-linear. According to Mehta [Mehta, 1986] when the load was increased to 75 % of the maximum loading, the network of microcracks was propagated at the interaction zone between the aggregates and cement paste, then it transferred to the mortar. However, Shah et al. [Shah and Sankar, 1987] demonstrated that increasing the applied load to 85 % of the maximum loading led to a decrease in the microcracking at the interaction zone. Mazars in [Mazars, 1984] reported microcracking due to extension at the microscopic scale, which developed into the crack opening (I) and in-plane shear (II) mode; also the microcracking was combined with the interaction zone. Picandet in [Picandet, 2001] reported that the increasing load after the maximum loading caused an increase in the overall volume of concrete, i.e. the extension of the material.

3. After the loading until the peak point of the maximum stress, the behavior of concrete became more softening and led to microcracks and a spread of damage in the material.

2.2.4 Tension cracks

This type of crack results from tensile loading. There are two types of tensile loading: direct and indirect. The direct tensile test is used when applying tensile loading directly and is very sensitive for concrete specimens during loading time. Figure (2.5) shows the behavior of concrete in a direct tensile test. The indirect tensile test is used when applying a compression load that leads to indirect tensile loading such as the splitting tensile test, which explains the behavior of concrete

under a diametral load. In addition, the behavior of concrete in tensile loading shows sensitive and strong instability according to Mazars's study in [Mazars, 1984].

Another type of test has been developed to obtain the tensile crack. Ramtani [Ramtani, 1990] and Gérard [Gerard, 1996] developed this test for controlling and obtaining one or more microcracks.

According to these studies, there are three stages of direct tensile test:

1. When loading was applied up to 50 % of the maximum loading, the behavior of concrete remained quasi-linear. The microcracks occoured in the interaction zone between the aggregates and cement paste (mortar) and were negligible.

2. The behavior of concrete became non-linear when the loading was increased until the peak point of stress. The concrete was damaged, due to lose of the stiffness and debonding in the interaction zone, then the increase in the microcracks in the cement paste was in agreement with the results presented by Mazars in [Mazars, 1984]. When the loading increases until the peak point of the maximum stress, microcracks will be localized; Mazars in [Mazars, 1984].

3. The behavior of concrete became more softening when the macrocracks were developed, which caused the failure of concrete.

2.2.5 Interaction between microcracks and pores in concrete

The mechanical behavior of concrete depends on voids in the aggregates and cement paste, therefore an increase in voids in concrete will result in cracks.

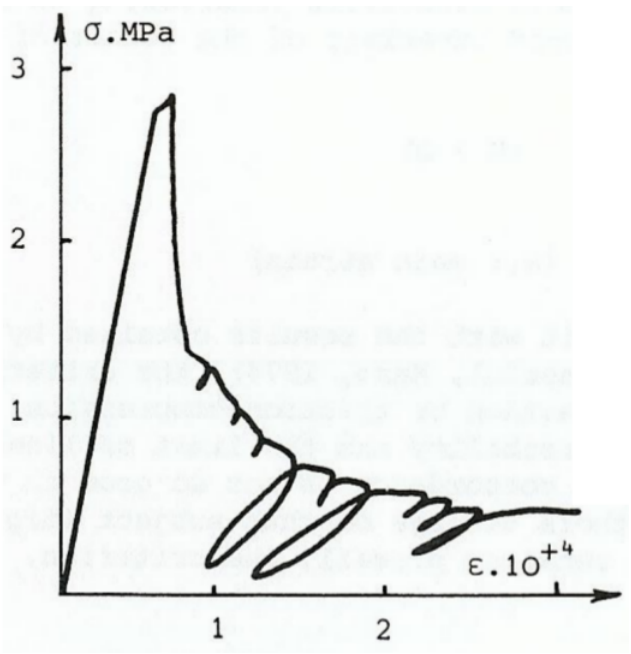

Figure 2.5: Behavior of concrete in direct tension by Terrien in [Terrien, 1980].

Baroghel-Bouny [Baroghel-Bouny, 1994] found that increasing cracks led to increasing the total porosity in concrete and caused the distribution of pores to vary. The size of the crack varied between 1 μm and a few millimeters and this size increased with the initial pores in the material. When the microcrack was connected with the initial pores, a macrocrack was formed. In addition, the connectivity between the network of the microcracks and the network of the initial pores caused macrocracks.

2.2.6 Influence of aggregates size and volume fraction

The aggregates size and volume fraction play an important role in controlling the properties of concrete and the performance of concrete structures. Wang in [Wang, 1994] observed the influence of the aggregate on the propagation of cracks, with the macrocracks having more tortuosity with a larger aggregate diameter in the

concrete. Concrete consists of aggregates melted into cement paste or mortar, therefore the mechanical behavior is influenced by the bonding force between them. The aggregates size and volume fraction influence on the bonding force, which is known as the interfacial transition zone (ITZ). The different parameters for concrete, such as Young's modulus, absorption, diffusivity, permeability, etc., between the aggregates and the cement paste lead microcracks to appear in the interaction zone when the concrete structure is under loading or unloading.

Bažant et al. [Bažnt and Raftshol, 1982] and Hwang et al. [Hwang and Young, 1984] showed that non-uniform drying caused a moisture gradient and non-uniform shrinkage of the concrete specimen. The surface area shrinks faster than the inner bulk material, therefore cracks will appear on the surface. Hobbs [Hobbs, 1974] focused on the aggregates within the composite material, reporting that restraint between them led to shrinkage cracking. Jensen et al. [Damgaard Jensen and Chatterji, 1996], Bisschop et al. [Bisschop and Van Mier, 2002] and Wang et al. [Wong et al., 2009] showed that the shrinkage of restrained aggregate led to microcracks, which influenced strongly on the transport properties of the material. However, the influence of the aggregates size and volume fraction on the evolution of microcracks is not fully understood yet. Wong et al. [Wong et al., 2009] observed that the increase in aggregates size at a constant volume fraction led to an increase in permeability as well as a decrease in the volume of interfacial transition zones ITZs, which are known to be more porous than the cement paste, Struble [Struble, 1987] and Scrivener et al. [Scrivener et al., 2004]. Witherspoon et al. [Witherspoon et al., 1980] observed that the increase in aggregate diameter at a constant aggregate fraction led to an increase in macrocrack width, which had relation with permeability. [Lagier et al., 2011] presented the drying shrinkage incompatibilities effects between cement paste and aggregate on mechanical behaviour of cementitious materials, using experimental and numerical studies.

2.2.6.1 Ultimate crack opening

The aggregates size plays a critical role in the behavior of concrete structures under loading. Some authors have investigated the influence of aggregates size and volume fraction on crack opening. This work focuses on the influence of these two parameters on the mechanical and hydro-mechanical behavior of concrete structures under diametral loading. In this section, some studies are presented that explain the significant affect of aggregates size on the critical crack opening ($\boldsymbol{w_c}$), i.e. an increase in the critical crack opening (w_c) due to an increase in aggregates size, Li et al. [Li et al., 2004a] and Mihashi et al. [Mihashi et al., 1989a] and [Mihashi et al., 1991]. Table (2.1) summarizes the effect of aggregates size on the critical crack opening. Grassl et al. [Grassl et al., 2010] presented a nonlinear finite element analyses to represent the concrete and mortar matrix based on a 2D lattice approach. They reported an increase in the critical crack width of concrete specimens with aggregates size; furthermore, increasing the volume fraction led to a decrease in the crack width, see Figure (2.6) for this relation.

Table 2.1: The effect of aggregates size on the critical crack opening ($\mathbf{w_c}$).

Authors	**W/C**	**Aggregates size (mm)**	$\mathbf{w_c}(\mu\mathbf{m})$
[Li et al., 2004a]	0.5	5-40	721
	0.5	5-150	1142
[Mihashi et al., 1989a] [Mihashi et al., 1991]	-	Mortar	260
	0.4	5-10	200
	0.4	10-15	400
	0.4	15-20	450
	0.4	20-30	500

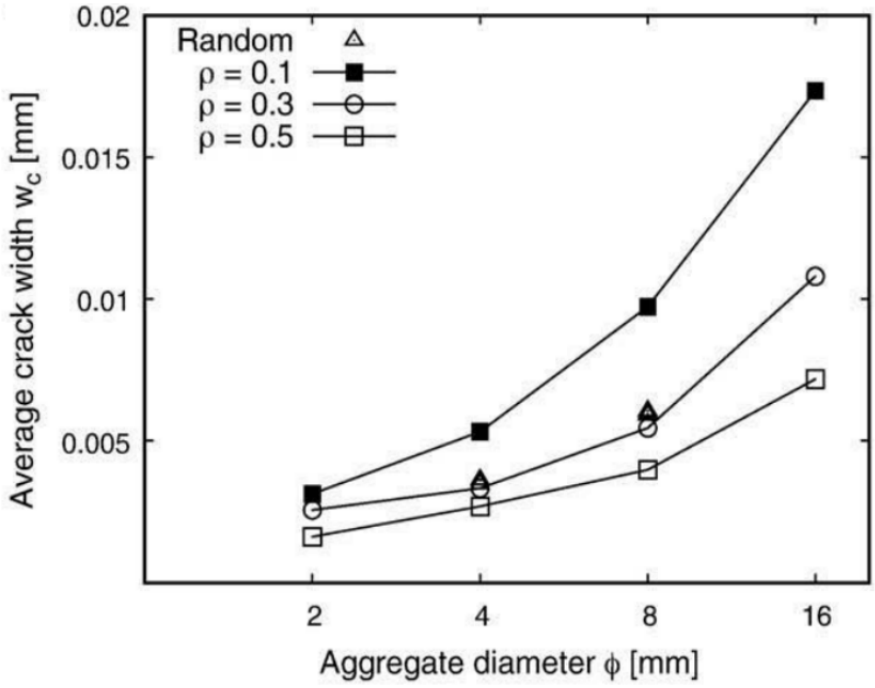

Figure 2.6: The average crack width ($\mathbf{w_c}$) versus the aggregate diameter for volume fractions of $\boldsymbol{\rho}$ =0.1, 0.3 and 0.5, Grassl et al. [Grassl et al., 2010].

2.2.6.2 Ultimate tensile stress

The published literature contains many experimental studies explaining the effect of the aggregates size and volume fraction on the tensile strength of concrete and, on the other hand, the increase in tensile strength in concrete influenced by the aggregates size. Rao et al. [Rao and Prasad, 2002] presented an explanation of the increase in tensile strength for high-strength concretes (HSC) according to the increase in aggregates size. However, Elices et al. [Elices and Rocco, 2008] found that the tensile strength of the matrix (cement paste) was higher than the concrete mixture, meaning that the tensile strength decreases as the aggregates size increases, while Chen and Liu [Chen and Liu, 2004] showed that the tensile strength of high-strength concrete (HSC) increased with the aggregates size, see Table (2.2). Johnston [Johnston, 1970] and Ward [Ward, 1969] reported the influence of the tensile strength of concrete by the aggregate volume fraction, as seems clear in Figure (2.7).

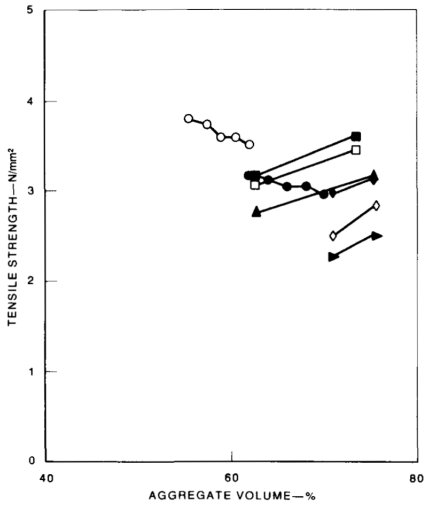

Figure 2.7: Relationship between the tensile strength and the aggregates volume fraction, Johnston [Johnston, 1970] and Ward [Ward, 1969].

Table 2.2: The effect of aggregates size on the tensile stress ($\boldsymbol{\sigma_t}$).

Authors	**W/C**	**Aggregates size (mm)**	$\boldsymbol{\sigma_t}$ **(MPa)**
[Rao and Prasad, 2002]	0.32	4.75 (max)	2.39
	0.32	6.3 (max)	2.7
	0.32	12.5 (max)	2.9
	0.32	20.0 (max)	3.06
[Chen and Liu, 2004]	-	Mortar	2.04
	0.37	5-10	2.61
	0.37	10-16	2.67
	0.37	16-20	2.58
[Elices and Rocco, 2008]	-	Mortar	3.26
	0.42**	3 (max)	3.25
	0.42**	9 (max)	3.0
	0.42**	14 (max)	3.05
	0.70*	3 (max)	2.62
	0.70*	9 (max)	2.19
	0.70*	14 (max)	1.91
	-	Mortar	2.18
	0.42**	3 (max)	1.78
	0.42**	9 (max)	1.4
	0.42**	14 (max)	1.7

*** treated.**; **** untreated.**

2.2.6.3 Young's modulus

Experimental study has shown that the modulus of elasticity of concrete varies with compressive strength. Furthermore, the ACI Code proposes emperical relation between the compressive strength and the density of concrete, see equations (2.1) and (2.2). Some authors have shown the influence of the modulus of elasticity for concrete as a function of the aggregates size while a few studies have referred to the effect of the aggregates volume fraction on this modulus. Table (2.3) shows the influence of aggregates size on the modulus of elasticity ($\mathbf{E_c}$) for some researchers. Saouma et al. [Saouma et al., 1991] and Petersson [Petersson, 1980] found that the modulus of elasticity ($\mathbf{E_c}$) decreased when the maximum aggregates size increased, this result was in agreement with Elices and Rocco [Elices and Rocco, 2008]. On the other hand, Rao et al. [Rao and Prasad, 2002] and Chen and Liu [Chen and Liu, 2004] observed the opposite result; the modulus of elasticity increased when the aggregates size increased. However, Amparano et al. [Amparano et al., 2000] conducted an experimental study and tested concrete specimens with varying volume fractions of aggregate. They showed that the modulus of elasticity increased when the volume fractions increased, see Figure (2.8).

$$\boldsymbol{E_c = W_c^{1.5} 33 \sqrt{f'_c}} \tag{2.1}$$

$$\boldsymbol{E_c = 57000 \sqrt{f'_c}} \tag{2.2}$$

where $\mathbf{E_c}$ is the modulus of elasticity of concrete in (psi), $\mathbf{W_c}$ is the unit weight of concrete in (lb/ft^3) and $\boldsymbol{f'_c}$ is the specified compressive stress of concrete in (psi).

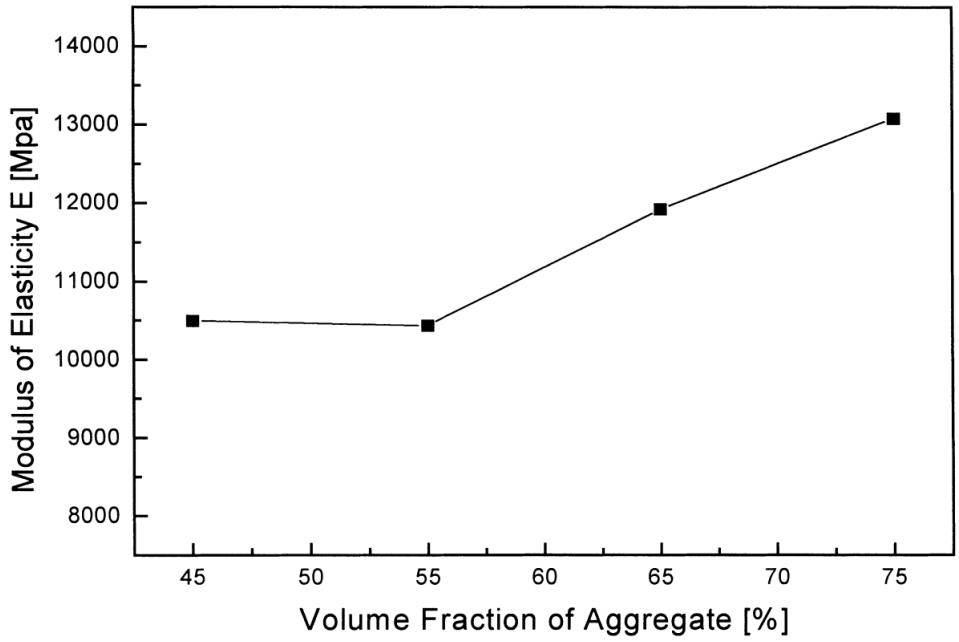

Figure 2.8: Relationship between the modulus of elasticity and the aggregate volume fraction by Amparano et al. [Amparano et al., 2000].

Table 2.3: The effect of aggregates size on the modulus of elasticity ($\mathbf{E_c}$).

Authors	**W/C**	**Aggregates size (mm)**	**E_c (GPa)**
[Petersson, 1980]	0.5	8 (max)	43.2
	0.5	12 (max)	42
	0.5	16 (max)	41.9
[Saouma et al., 1991]	0.55	19 (max)	18.0
	0.55	38 (max)	16.9
	0.55	76 (max)	16.5
[Elices and Rocco, 2008]	-	Mortar	27.0
	0.42**	3 (max)	24.5
	0.42**	9 (max)	23.4
	0.42**	14 (max)	22.9
	0.70*	3 (max)	20.9
	0.70*	9 (max)	20.3
	0.70*	14 (max)	20.9
	-	Mortar	24.0
	0.42**	3 (max)	20.0
	0.42**	9 (max)	16.7
	0.42**	14 (max)	17.9
[Rao and Prasad, 2002]	0.32	4.75 (max)	37
	0.32	6.3 (max)	39
	0.32	12.5 (max)	40
	0.32	20.0 (max)	42

*** treated.**; **** untreated.**

2.2.6.4 Fracture energy

As the aggregates size and volume influence on the fracture energy, the previous studies investigated the influence of compressive strength on the fracture energy ($\mathbf{G_F}$), Guinea et al. [Guinea et al., 2002] while other researchers presented the fracture energy ($\mathbf{G_F}$) in terms of the aggregates size. Elices et al. [Elices and Rocco, 2008] found the fracture energy as a function of aggregates size, the fracture energy for concrete higher than the corresponding matrix, and that the increase in aggregates size led to an increase in the fracture energy. Table (2.4) shows the effect of aggregates size on the fracture energy for some researchers, who concluded that the increase in fracture energy resulted from the varying aggregates size. Amparano et al. [Amparano et al., 2000] investigated the effect of the aggregate volume fraction on the fracture energy and concluded that increasing the volume fraction from 45 to 55 % led to a decrease in the fracture energy, whereas the fracture energy was increased by increasing the volume fraction from 55 to 75 %; this relation can be seen in Figure (2.9).

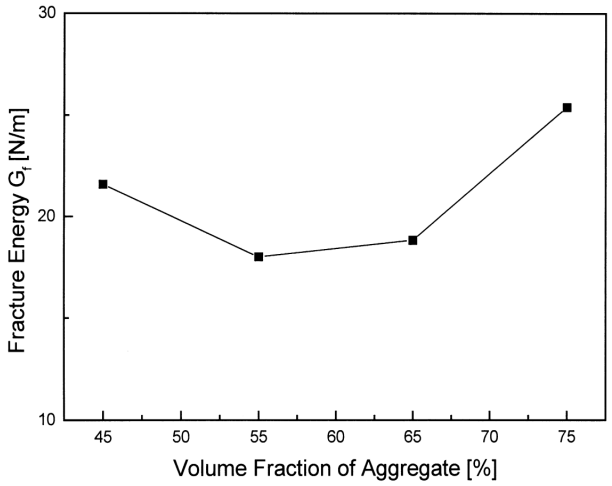

Figure 2.9: Relationship between fracture energy and volume fraction of aggregate by Amparano et al. [Amparano et al., 2000].

Table 2.4: The effect of aggregates size on the fracture energy ($\mathbf{G_F}$).

Authors	**W/C**	**Aggregates size (mm)**	**$\mathbf{G_F(J/m^2)}$**
[Petersson, 1980]	0.5	8 (max)	85
	0.5	12 (max)	88
	0.5	16 (max)	96
[Mihashi et al., 1989a] [Mihashi et al., 1991]	-	Mortar	105
	0.4	5-10	129
	0.4	10-15	158
	0.4	15-20	160
	0.4	20-30	188
[Tasdemir et al., 1996]	0.36	5-10	106
	0.36	10-20	142
[Rao and Prasad, 2002]	0.32	4.75 (max)	77
	0.32	6.3 (max)	98
	0.32	12.5 (max)	103
	0.32	20.0 (max)	142
[Chen and Liu, 2004]	-	Mortar	110
	0.37	5-10	175
	0.37	10-16	195
	0.37	16-20	240

2.2.7 Evaluating and modeling cracked concrete based on the finite element method

According to the previous review, the concrete material is considered an heterogeneous material and its behavior is elastic or quasi-brittle under loading. Therefore, there are three main methods to evaluate and describe the cracking and fracture process zones according to the finite element framework:

1. **Continuum method:** which describes the development of fractures as zones of inelastic strains based on higher-order constitutive models such as the integral-type nonlocal models, according to Bažant and Jirásek [Bazant and Jirásek, 2002].

2. **Hybrid method:** which describes fractures by modeling them as displacement discontinuities, according to Moës et al. [Moës and Belytschko, 2002], Jirásek [Jirásek, 2000] and Camacho et al. [Camacho and Ortiz, 1996].

3. **Discrete method:** which describes fractures by representing the non-linear fracture process as depending upon the failure of discrete elements, such as trusses and beams, according to Schlangen et al. [Schlangen and van Mier, 1992] and Herrmann et al. [Herrmann et al., 1989].

Bolander et al. [Bolander and Saito, 1998] presented the discrete lattice approach which was based on the Voronoi tessellation that had been shown to be very suitable for fracture simulation. Grassl et al. [Grassl et al., 2010] focused on the influence of aggregates size and volume fraction on the shrinkage induced microcracking in the concrete and cement paste, which were analyzed using the non-linear finite element method based on the lattice approach and used in combination with a damage-plasticity constitutive model.

2.2.8 Properties and testing of hardened concrete

For engineering design, the behavior of concrete must be studied under service loads. There are many tests for hardened concrete that estimate or determine the material parameters essential for engineering design, such as the compressive strength, tensile or shear strength, bending strength, bond strength and modulus of elasticity. These tests are based on experimental works or numerical models.

The parameters of concrete for studying tensile stress, modulus of elasticity and fracture energy are $\boldsymbol{f_{st}}$, $\mathbf{E_c}$ and $\mathbf{G_F}$, respectively. There are four main methods for testing concrete or rock materials:

1. **Uniaxial compression test:** this method most used for determining the mechanical properties of concrete. Cubic or cylinderical specimens are used. The description of the behavior of concrete at rupture faces is acceptable or not under loading, which is understood by two points:

   $\Rightarrow$ the parallel position of the two faces of loading.

   $\Rightarrow$ the weakness of the friction force at the supporting plates.

   Neville in [Neville, 2011] observed that the elastic behavior for normal concrete ended at approximately 30 % of the maximum compression stress. At this stage, the modulus of elasticity can be measured by using the instrument with three sensors placed around the circumference of the cylinder specimen. From this test, the result can be controlled without bending. From the different measurements at the three sensors, the deformation can be drawn and the behavior of the material at the peak point of loading characterized.

2. **Uniaxial direct tensile test:** the direct tensile test of concrete is the better method to characterize the parameters ($\boldsymbol{f_{st}}$, $\mathbf{E}$ and $\mathbf{G_F}$), splitting tensile strength, Young's modulus and fracture energy, respectively, because

the behavior of the concrete structure is presented when the tensile load is applied directly. However, this method is very difficult to represent the material up to the rupture loads according to van Mier and van Vliet in [Van Mier and Van Vliet, 2002]. In France, two standards are used to provide the direct tensile test: (CEN) (EN 13286-40) and (ASTM D 2936), the National European Commission and the United States of America standard, respectively.

3. **Three-point bend test:** this type of test has two advantages; it is simple and cheap when applying it to experimental work and implementing the test. Hillerborg in [Hillerborg, 1983] pointed out that the surface area of rupture in square meter depended on the RILEM, but there were difficulties in obtaining this criterion in experimental work. The size of specimens also depended on the maximum aggregates size ($\mathbf{D_{max}}$), therefore some specimen sizes were proposed for this testing. The dimensions of the beam are shown in Table (2.5) and Figure (2.10) with the cross-sectional area, which were used to compute the fracture energy ($\mathbf{G_F}$) and presented in this study according to the RILEM definition, based on Hillerborg's fictitious crack model in [Hillerborg, 1983], [Hillerborg, 1984] and [Hillerborg, 1985].

Table 2.5: Dimensions of the tested beam for computing the fracture energy ($\mathbf{G_F}$) based on the three-point bend test [TCS, 1985].

$\mathbf{D_{max}}$	Depth (mm) d	Width (mm) b	Length (mm) L	Span (mm) l
1-16	100 ± 5	100 ± 5	840 ± 10	800 ± 5
16.1-32	200 ± 5	100 ± 5	1190 ± 10	1130 ± 5
32.1-48	300 ± 5	150 ± 5	1450 ± 10	1385 ± 5
48.1-64	400 ± 5	200 ± 5	1640 ± 10	1600 ± 5

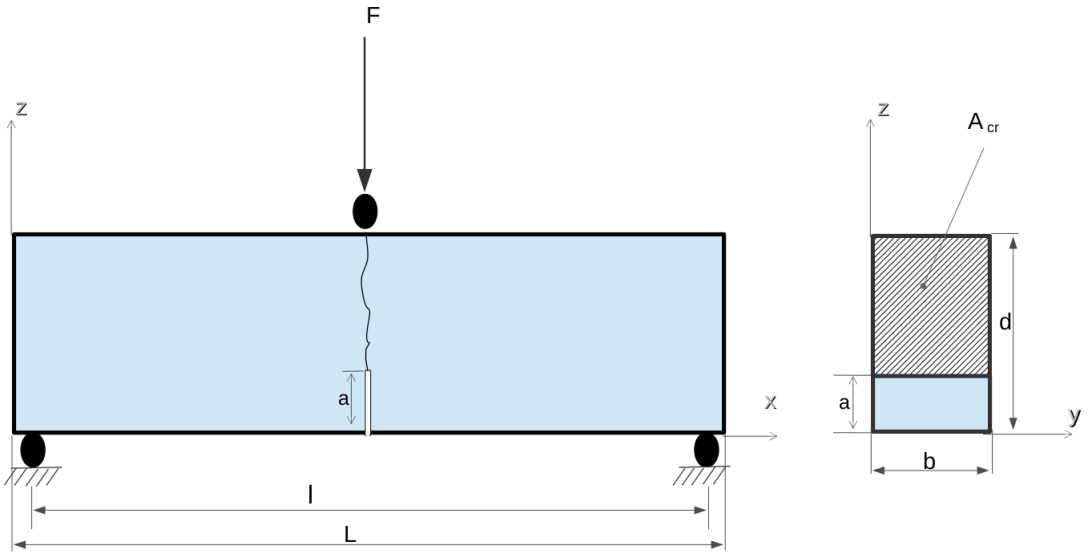

Figure 2.10: Dimensions of the tested beam with the cross-sectional area and fictitious crack to compute the fracture energy $\boldsymbol{G_F}$ [TCS, 1985].

The fracture energy ($\mathbf{G_F}$) can be computed from equation (2.3) according to the RILEM recommendations in [TCS, 1985], where $\boldsymbol{W_0}$ is the area under the load-deflection curve in (N.m), $\boldsymbol{m_1}$ is the mass of the beam between two supports in (kg), $\boldsymbol{m_2}$ is the mass of the loading device until the rupture of the beam in (kg), $\boldsymbol{g}$ is the gravity acceleration in (m.s^{-2}), $\boldsymbol{\delta_0}$ is the total deflection of the beam until the rupture in (m), and $\boldsymbol{A_{cr}}$ is the cross-sectional area of the cracked beam in (m^2).

$$\boldsymbol{G_F = \frac{W_0 + (m_1 + 2m_2)g\delta_0}{A_{cr}}} \tag{2.3}$$

4. **Splitting tensile test (Brazilian test):** this test refers to the indirect tensile test for concrete. From the previous studies in the literature review, many researchers have used the indirect tensile test, i.e. flexural testing and the splitting test (Brazilian test). These are easier to carry out than other

test procedures. The splitting test has been standardized in many codes, the ASTM C496 and the Euro Code among others. Fernando Carneiro in (1953) proposed the Brazilian splitting test in Brazil in [Fairbairn and Ulm, 2002]. In the strategy of the classic splitting test, as shown in Figure (2.11), the concrete specimen (cylinder or cube) is placed horizontally and loaded in compression (diametral load) by the loading platens of the compression testing machine along the length of the specimen.

The tensile strength of concrete ($\boldsymbol{f_{st}}$) according to ASTM C496 is computed by equation (2.4), where $\boldsymbol{P_u}$ is the peak (ultimate) diametral loading in (N), $\boldsymbol{D}$ is the diameter of the cylinder in (mm), and $\boldsymbol{B}$ is the specimen thickness or height in (mm).

$$\boldsymbol{f_{st} = \frac{2P_u}{\pi BD}} \tag{2.4}$$

There are some advantages of the Brazilian splitting tensile test:

1. One crack and displacement under a diametral load (indirect tensile load) can be demonstrated.
2. The crack width and its position and direction can be determined.
3. The parameters that are affected on the geometrical properties of the cylinder specimen of concrete can be evaluated.
4. The displacement and the crack opening during loading and after loading can be measured.
5. The post peak loading can be controlled in order to obtain cracks in cylinder specimens without a complete damage or splitting test.
6. The cracked specimens can be used for coupling with a permeability test.

While the disadvantages of this test are difficult of management, multiaxial stress and state of stress is non-homogeneous.

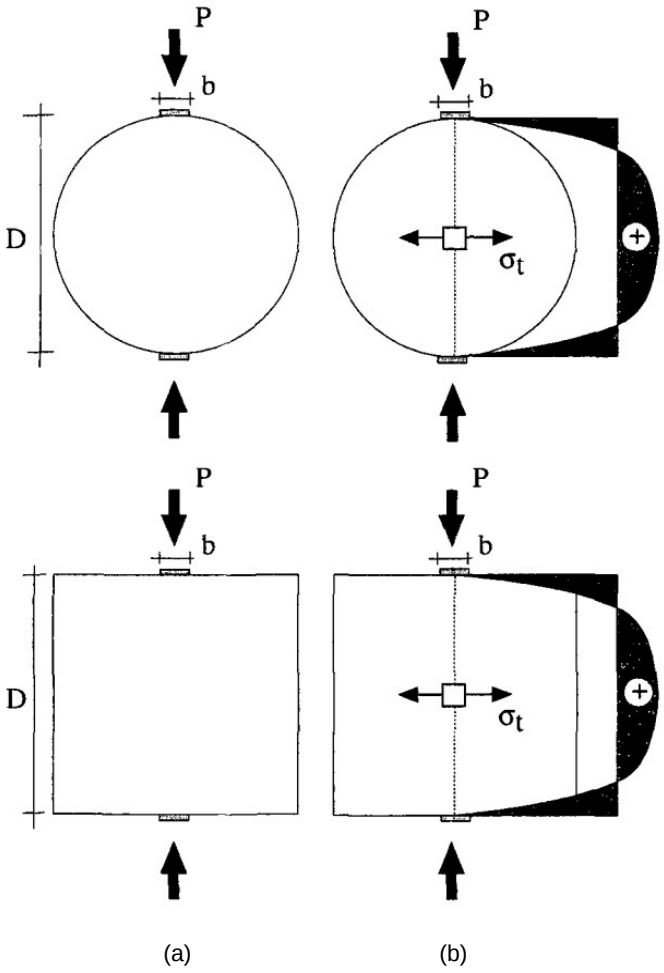

Figure 2.11: Description of the behavior of a specimen under splitting test; load configuration (a) and stress distribution (b) [Rocco et al., 1999].

2.3 Permeability part

This part presents the determination of the permeability of fluids in a porous medium such as concrete. In addition, reports are included of previous studies in the literature about the evolution of permeability with physical properties such as: porosity, connectivity, tortuosity, etc. Then, the context of coupling the crack width (crack opening) with the permeability of fluids, which has been studied by some authors, is presented.

2.3.1 Characteristics of the pore structure (concrete)

The cement paste is formed when the cement grains contact water, which causes the hydration of cement to different degrees. This phenomenon (hydration) refers to the chemical reactions due to the cement grains mixing with water, which results in the cement paste, and these reactions produce heat. Then cement paste is transformed into the solid state. The insoluble compounds and new material are gradually formed due to the hydration of cement. The main components of the hydrated products are calcium silicate hydrate (**C-S-H**), which occupies about 50 % of cement paste, and it is known a gel which consists Portlandite $\mathbf{Ca(OH)_2}$ and calcium aluminates ($\mathbf{C_3A}$) and sulfo-hydrated calcium aluminates. Therefore, when the excess water evaporates with time, capillary pores appear that allow the transport of fluids. However, the hydrate internal pores (**C-S-H** cement gel) are not affected by the water-cement ratio, see [Baroghel-Bouny, 1994].

However, the concrete produces an interface zone between the cement paste and aggregate particles according to the study of Maso in [Maso, 1982]. Previous experimental studies have reported that the thickness of the interaction zone depends on the radius of cement grains, Escadeillas et al. [Escadeillas and Maso, 1990]. This thickness varies between 20 and 50 $\boldsymbol{\mu}$m and the zone contains a high

quantity of water for hydration, which causes high porosity. However, Elsharief et al. [Elsharief et al., 2003] found that the thickness of the interaction zone depended on the aggregates size.

Some factors influenced on the durability of hardened concrete structures through the transfer properties such as the porosity, the pore size distribution, connectivity or pore tortuosity, etc.

2.3.1.1 Porosity

Porosity is a measure of the spaces in a material such as cement paste or aggregate particles or the interface zone between them. The structure of porosity significantly influences on the concrete performance. Equation (2.5) refers to the total porosity ($\mathbf{P}$) which is measured from the ratio of the pore volume of the material ($\mathbf{V_p}$) to the total volume ($\mathbf{V_t}$):

$$\boldsymbol{P} = \frac{\boldsymbol{V_p}}{\boldsymbol{V_t}} \tag{2.5}$$

The total porosity of a hardened concrete is usually 10 %, which results from the cement paste, the aggregates and the interface zone while this porosity is 2 % for the limestone aggregates, Baroghel-Bouny [Baroghel-Bouny, 1994]. However, concrete material has different sizes of pores, which are classified by their level of connectivity such as interconnected or isolated, see Figure (2.12). The isolated pores prevent the transport of fluids through the material, while the interconnected pores allow it.

2.3.1.2 Pores size distribution and microstructure of concrete

Some authors have classified the type of pores according to their size, for example Setzer [Setzer, 1975] and Meschke et al. [Meschke et al., 2011]. There are four types of pores in concrete, which are the result hydration of cement. The first is

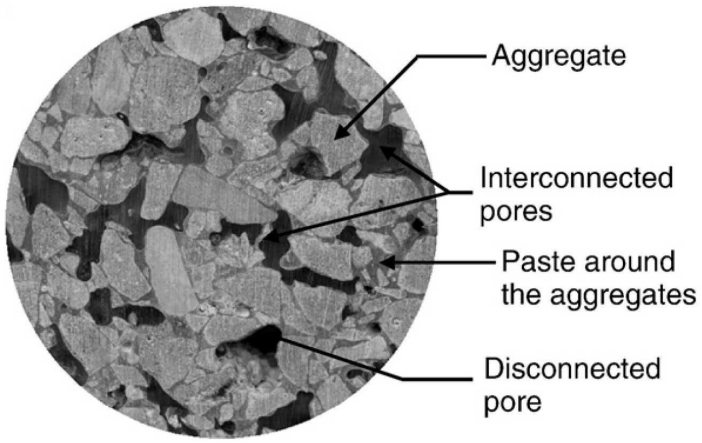

Figure 2.12: Classification of pores according to their level of connectivity by Neithalath et al. [Neithalath et al., 2006]

capillary pores, which are measured by mercury porosimetry, and the other three types are the internal pores in the hydrated products (gel pores, air pores and compaction pores). The capillary pores are found into the aggregate particles (intergranular spaces) and result from the mixing of water and cement. To obtain high workability, a high water-cement ratio is used, i.e. the volume of water applied for the production of concrete is greater than that is needed for hydration, which leads to more pores in the concrete structure. Therefore, when the excess water evaporates with time, capillary pores appear that allow the transport of fluids. However, the hydrate internal pores (**C-S-H** cement gel) are not affected by the water-cement ratio. Baroghel-Bouny [Baroghel-Bouny, 1994] pointed out that the intrinsic porosity of hydrates can be noted by using gas adsorption. As shown in Figure (2.13), the types of pores correspond to their dimensions.

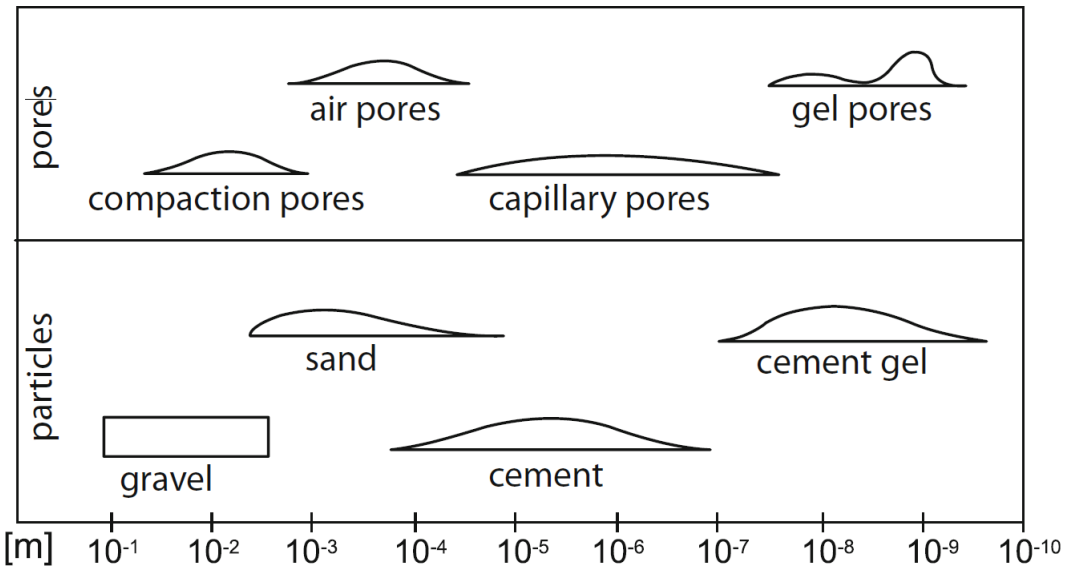

Figure 2.13: Classification of pores according to their dimensions as in the study of Setzer [Setzer, 1975] and Meschke et al. [Meschke et al., 2011]

2.3.1.3 Connectivity

Cairns [Cairns, 1961] and Fischmeister [Fischmeister, 1974] demonstrated that connectivity ($\boldsymbol{C}$) is one parameter of the topology of the pores structure. In addition, it characterizes the degree of connecting of the pores structure, which was presented by Dullien [Dullien, 2012]. It corresponds to the largest number of branches of the porous network that can be cut without disconnecting it. Dullien [Dullien, 2012] explained the relationship between the number of branches ($\boldsymbol{b}$) and the number of nodes ($\boldsymbol{n}$), see equation (2.6). As shown in Figure (2.15), the type of pores can be classified according to the connectivity such as: interconnected pores and disconnected pores.

$$\boldsymbol{C = b - n + 1} \tag{2.6}$$

2.3.1.4 Tortuosity

Carman [Carman, 1956] pointed out that the tortuosity ($\boldsymbol{\tau}$) was one of the important parameters that was introduced by the geometry of the material for transferring fluid. It characterizes the flow of fluid through the network of pores; equation (2.7) shows the relationship between the effective length of the fluid ($\boldsymbol{L_e}$) and the length of the sample in the direction of flow ($\boldsymbol{L}$), see Figure (2.14). It was determined by Quenard et al. [Quenard and Sallee, 1991].

$$\boldsymbol{\tau} = (\frac{\boldsymbol{L_e}}{\boldsymbol{L}})^{\boldsymbol{2}} \tag{2.7}$$

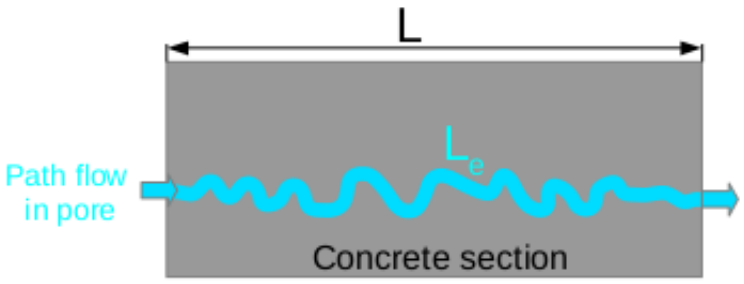

Figure 2.14: Sketch shows fluid path in pore according to the tortuosity.

2.3.1.5 Water content

There are three types of water in concrete and cement paste that influence on the mechanical properties, Bažant et al. [Bažant and Raftshol, 1982], Rossi et al. [Rossi and Boulay, 1990] and [Rossi et al., 1992], and the hydraulic properties, Dal Pont et al. [Dal Pont et al., 2005], of concrete significantly. The water in concrete is free or compounded with cement as follows:

1. **Chemically bound water:** this type of water is produced during the hydration reactions and combines with other components in hydrates.

2. **Adsorbed water:** this type is attached to the surface of the solid matrix due to the action of intermolecular forces known as Van der Waals and electrostatic forces.

3. **Capillary water:** the capillary water fills the pore spaces after the adsorbed layer and is separated from the gaseous phase by a meniscus. Figure (2.15) describes the content of water in concrete.

2.3.2 Permeability of concrete

There are some parameters that influence on the permeability of fluids (gas or water) in concrete structures such as: porosity, pores size, connectivity, crack width, aggregates size and volume fraction, type of load, water-cement ratio, degree of saturation, etc. Permeability influences on the durability of the concrete structure, indirectly, as it governs the rate of penetration of aggressive substances responsible for degradation under the pressure gradient. The pores in concrete enable the rapid permeation of fluid (permeability), which is considered a key parameter of durability. Park et al. [Park et al., 2001] and Samaha et al. [Samaha and Hover, 1992] reported that the permeability of water is more sensitive and affected by crack width than chloride diffusion . Applied stress on the concrete is considered another parameter that influences on water permeability, Hoseini et al. [Hoseini et al., 2009] and Hearn [Hearn, 1999] and Picandet [Picandet, 2001]. Neithalath et al. [Neithalath et al., 2006] found that the concrete structure under a compression load decreased in permeability, while under a tension load permeability increased even in a small crack.

Figure (2.16) shows the influence of parameters on permeability in a porous medium, such as: porosity, network of pores, connectivity, tortuosity and the porous network constrictivity related to the pores size, Scrivener in [Scrivener,

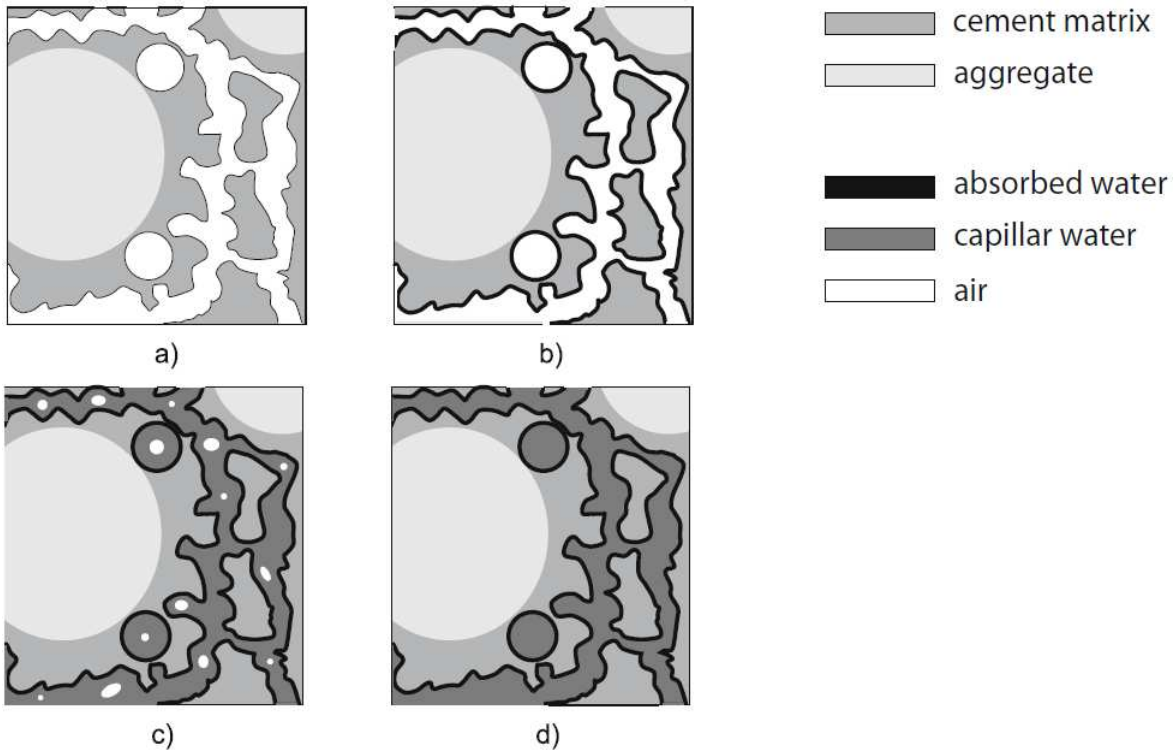

Figure 2.15: Diagram of the distribution of water in concrete with the different levels of saturation by Meschke et al. [Meschke et al., 2011].: a) dry material, b) generation a continuous liquid phase of water absorbed in the pores of **C-S-H** gel, c) the capillary porosity is filled with water when the degree of saturation increases, d) completely saturated.

2001]. Hearn et al. [Hearn and Lok, 1998] reported that the water cement ratio (**W/C**) of concrete affected on the permeability of concrete. In addition, the permeability is influenced by the additives in concrete such as: silica fume, slag or fly ash, as well as type and quantity of aggregate, which can create the halo of transition and change tortuosity, respectively.

The moisture content in concrete is also important. Villain et al. [Villain et al., 2001] reported that permeability is influenced by the moisture content of the material according to its saturation rate. They found that the gas permeability of concrete increases when the degree of saturation decreases. Abbas et al. [Abbas et al., 2000] observed that the increasing degree of saturation leads to a decrease in gas permeability, as shown in Figure (2.17). The difference in pore sizes is also affected, Baroghel-Bouny in [Baroghel-Bouny, 1994].

Yssorche-Cubaynes et al. [Yssorche-Cubaynes and Ollivier, 1999] presented an experimental study demonstrating the relationship between the permeability and strength of a material, as shown in Figure (2.18). Actually, the compression strength of a material is considered a function of its porosity, while the permeability depends on the connectivity of pores. In addition, the presence of cracks in concrete significantly influences on permeability. Picandet et al. [Picandet et al., 2009] explained the influence of crack width on gas and water permeability in high and normal strength concrete (see section **2.3.7**). There are many reasons that cause the initial cracks in a concrete structure such as: shrinkage at an early age, drying, the effects of mechanical stress, thermal stress, environmental factors, etc. Therefore, there are two kinds of fluid penetration: the first is through the cracks and the second is the flow of fluid through the network of pores. This means that an increase in interconnected cracks leads to a decrease in the strength of concrete and an increase in the permeability of fluid [Choinska et al., 2007].

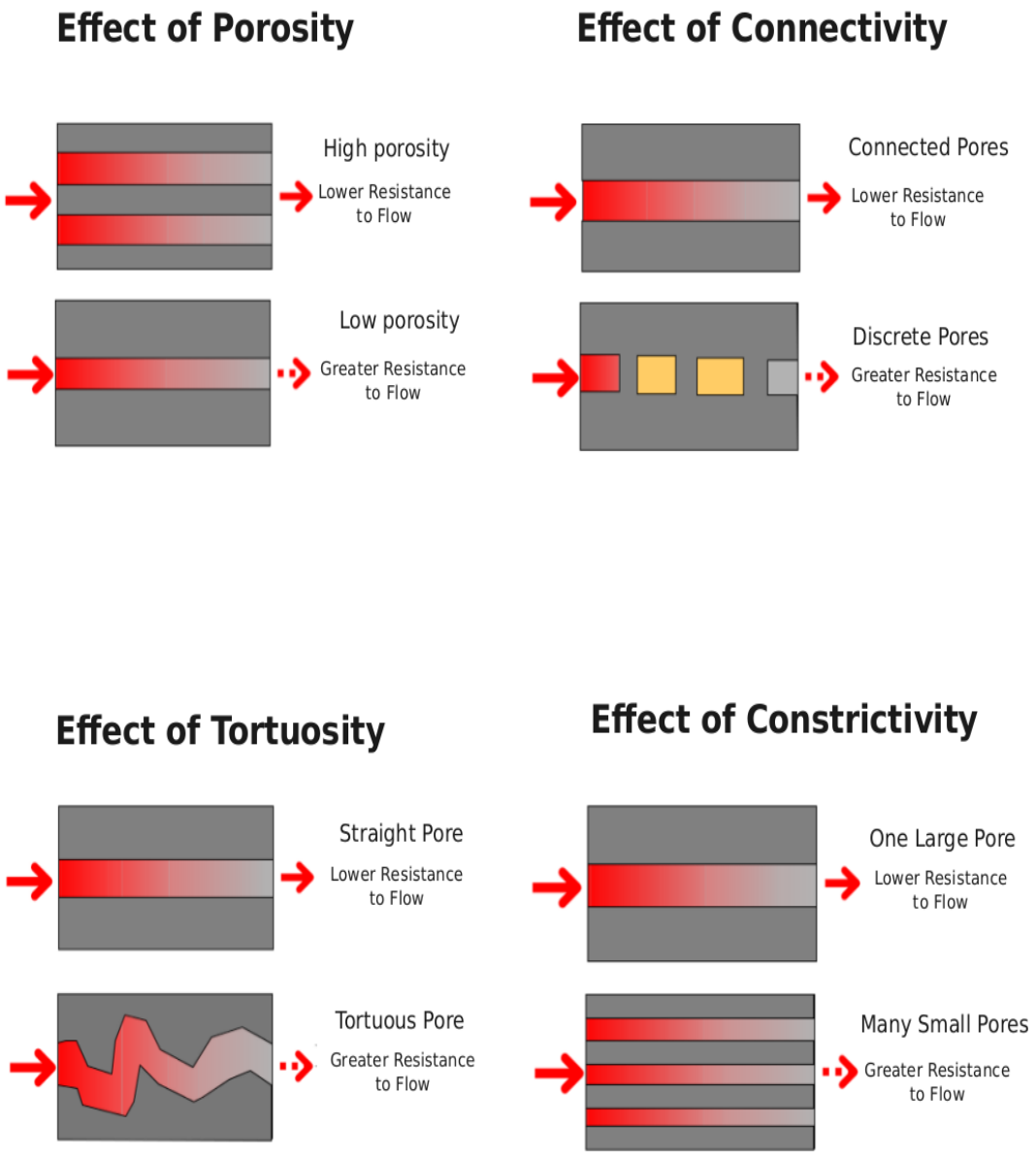

Figure 2.16: The type of parameters that influence on the permeability by Scrivener in [Scrivener, 2001].

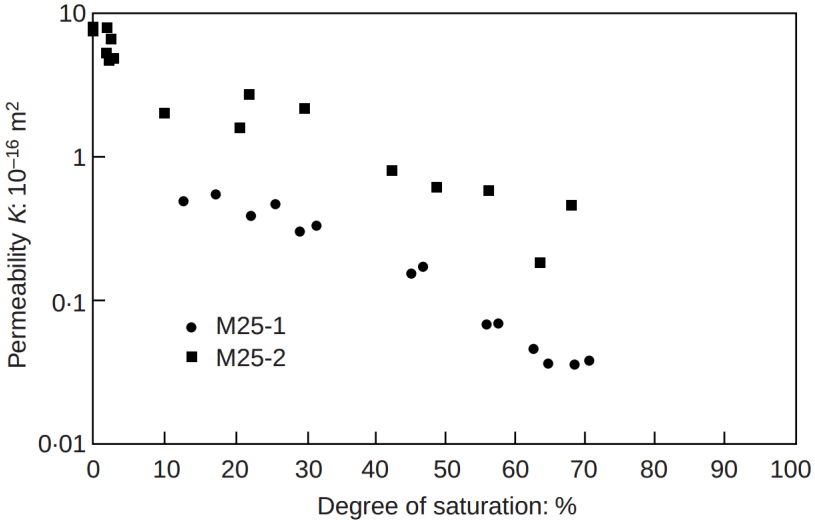

Figure 2.17: The effect of the degree of saturation on air permeability by Abbas et al. [Abbas et al., 2000].

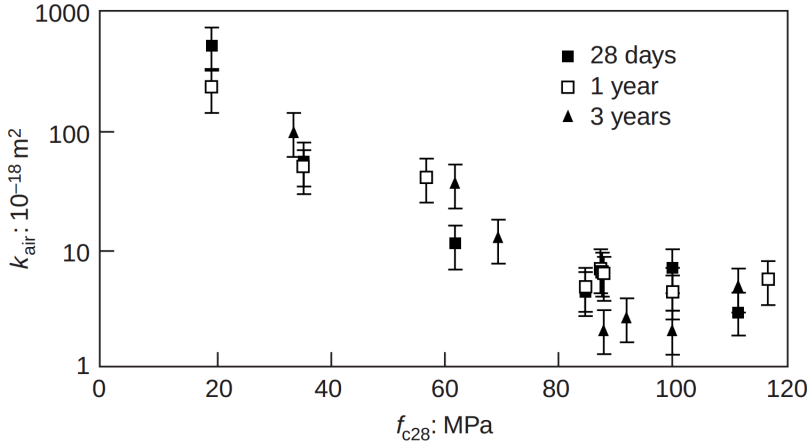

Figure 2.18: Relationship between air permeability and compressive strength, Yssorche-Cubaynes et al. [Yssorche-Cubaynes and Ollivier, 1999].

2.3.3 Darcy's law

The permeability in a porous medium can be calculated by Darcy's law, which is formulated by Henry Darcy (1803-1858). He used experimental results to explain the flow of water through beds of sand; Figure (2.19) shows the apparatus [Darcy, 1856]. Then he used Hagen-Poiseuille's law to represent the flow of fluid in a porous medium. From equation (2.8), which formulates the flow through a porous medium in one direction with a laminar system, two scales are available:

1. **Microscopic scale:** at this scale, the actual velocity of fluid in each pore in the material is calculated.

2. **Macroscopic scale:** when the porosity of the material is known, the macroscopic flow of fluid is known and the average velocity through the specimen deduced.

$$\boldsymbol{Q = -\frac{kS}{\mu}(\frac{h_2 - h_1}{e}) = -\frac{kS}{\mu}\frac{\Delta P}{L}} \tag{2.8}$$

where

•: **Q**: is the volume of fluid flow in (m^3/s).

•: **k**: is the intrinsic permeability of the porous medium in (m^2).

•: **S**: is the normal surface area to the direction of flow in (m^2).

•: **L**: is the length of material in the flow direction in (m).

•: $\boldsymbol{\mu}$: is the dynamic viscosity of the fluid in (Pa.s).

•: $\boldsymbol{\Delta P}$: is the gradient of the piezometric pressure in (Pa), and this relationship is written in equation (2.9):

$$\boldsymbol{P = p + \rho g z} \tag{2.9}$$

where

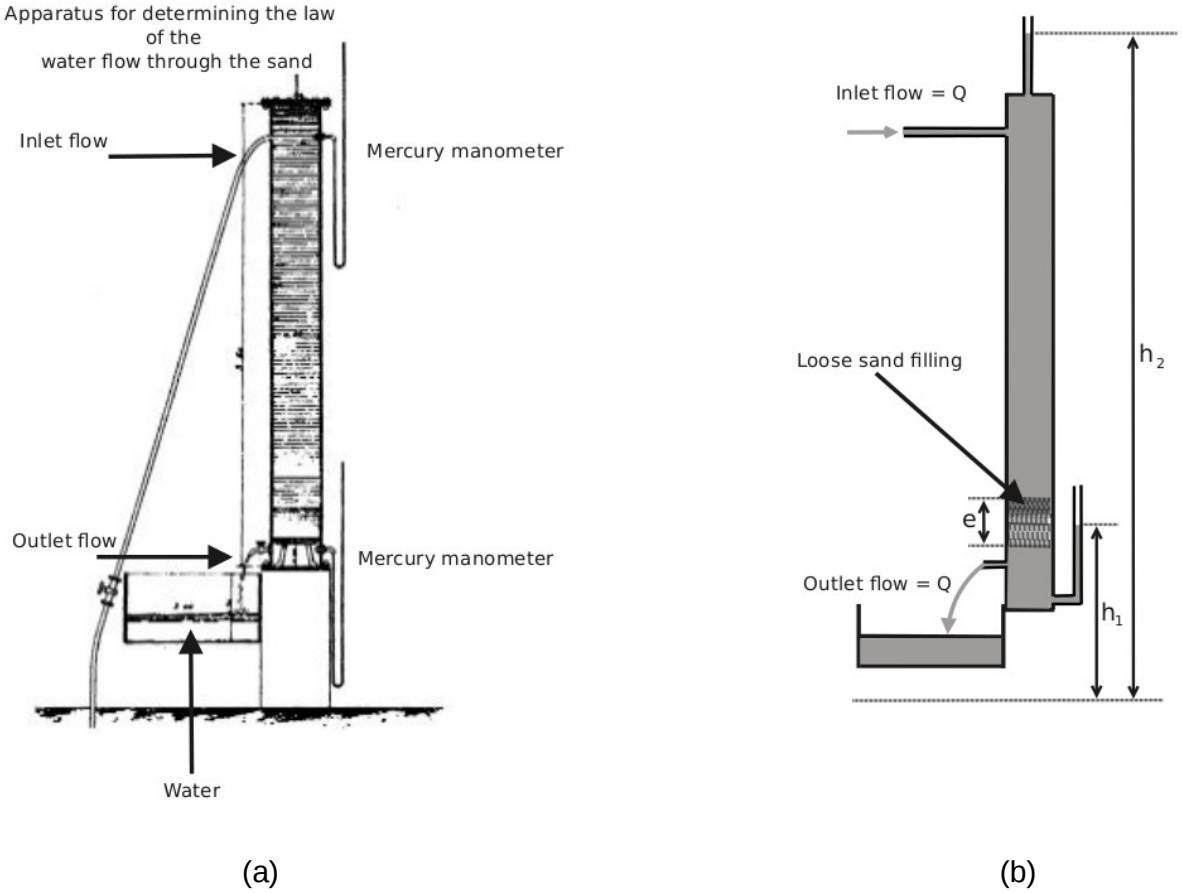

Figure 2.19: Apparatus for determining the flow of water through the sample of sand; drawing of the experiment [Darcy, 1856] (a) and sketch for the sample of thickness $\boldsymbol{e}$ (b).

•: **p**: is the fluid pressure in (Pa).

•: $\boldsymbol{\rho}$: is the fluid density in (kg/m$^{\mathbf{3}}$).

•: **g**: is the gravitational acceleration in (m/s$^{\mathbf{2}}$).

•: **z**: is the altitude relative to a reference level in (m).

When $\boldsymbol{\rho g z}$ equals zero, the density of fluid in the porous medium is low and the injection pressure is high.

After this step, Darcy's law has been simplified, see equation (2.10):

$$\boldsymbol{Q = -\frac{kS}{\mu}\frac{dP}{dx} = -\frac{kS}{\mu}\frac{\Delta P}{L}} \tag{2.10}$$

where $\frac{\boldsymbol{dP}}{\boldsymbol{dx}}$ is the pressure gradient in (Pa).

Equation (2.11) shows the velocity of flow in one direction in (m/s):

$$\boldsymbol{v = \frac{Q}{S}} \tag{2.11}$$

2.3.4 Types of fluids

The passing of fluid (gas or liquid) through a porous medium under a pressure gradient is known as the permeability, thus fluids can be classified according to their properties as follows:

1. **Incompressible fluid:** in this type of fluid, the density is considered constant when pressure is applied on the fluid such as water and therefore results in incompressible fluid flow in pores through the material. On the other hand, the liquid density is essentially constant at a particular temperature and thus the incompressible flow of liquid is produced. The flow velocity of an incompressible fluid through the porous medium ($\boldsymbol{V}$) is commonly represented by referring to Darcy's law. A description of the water flow in sand filters (unidirectional) was developed in France by Darcy's law from experimental work and this law corresponded to the theoretical work. Muskat

and Meres in [Muskat and Meres, 1936] carried out multiphase flows, Biot in [Biot, 1955] presented the flow in an anisotropic medium, Biot in [Biot, 1962] demonstrated the flow in three dimensions due to the deformation of the porous medium, while Slattery in [Slattery, 1967] explained the non-linear flow for a viscoelastic fluid . The other researchers found the solution of the Navier-Stokes equations, for example Whitaker in [Whitaker, 1986a] and [Whitaker, 1986b].

2. **Compressible fluid:** a compressible fluid has variable density when it is under a pressure gradient such as gas. Darcy's law can also be applied for this type of fluid. Therefore, the application of principles of the conservation of mass law and Darcy's law can be used for the isothermal flow of gas. In addition, the relationship shown below can be obtained. Figure (2.20) shows the principle inlet and outlet pressure of gas through a specimen of concrete that has a thickness of 50 mm and a diameter of 110 mm for the permeability test presented by Picandet et al. in [Picandet et al., 2009].

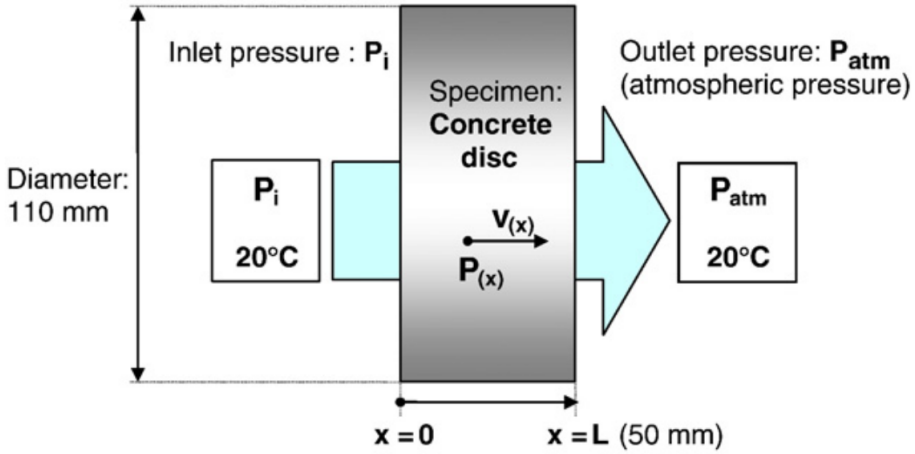

Figure 2.20: The conditions and flow geometry in a longitudinal concrete specimen by Picandet in [Picandet et al., 2009].

From the law of mass flow of gas, which corresponds to the isothermal flow, can be obtained:

$$\boldsymbol{F = \rho V} \tag{2.12}$$

Also, the inlet mass flow of gas ($\mathbf{Q_1}$) in the porous material under pressure of fluid is equal to the outlet flow ($\mathbf{Q_2}$) and using Darcy's law and equations (2.10) and (2.11), equations (2.13), (2.14) and (2.15) are obtained:

$$\boldsymbol{Q_1 = Q_2} \tag{2.13}$$

$$\boldsymbol{\rho_1 V_1 = \rho_2 V_2} \tag{2.14}$$

$$\boldsymbol{\rho V = -\rho \frac{k}{\mu} \frac{dP}{dx}} \tag{2.15}$$

where $\boldsymbol{\rho}$ is the density of gas in (kg/m$^{\mathbf{3}}$) under isothermal conditions, which is proportional to its pressure **P**, and the gas is considered under the minimum pressure (1 MPa), as shown below:

$$\boldsymbol{\rho = \frac{M}{RT} P} \tag{2.16}$$

where

•: **M**: is the molar mass of the gas in (g/mol).

•: **R**: is the universal gas constant in (J/mol.K).

•: **T**: is the temperature of the gas in (Kelvin).

From equations (2.15) and (2.16) can be written:

$$\boldsymbol{PV = -\frac{1}{2} \frac{k}{\mu} \frac{d(P)^2}{dx}} \tag{2.17}$$

By substituting equation (2.11) in equation (2.17) and integrating over the length of pass of the flow, the gas permeability will be introduced, when $\boldsymbol{S = \frac{\pi}{4} D^2}$, see equation below:

$$\boldsymbol{k = \frac{8 Q_1 \mu P_1 L}{(P_1^2 - P_2^2)}} \tag{2.18}$$

where

•: $\mathbf{P_1}$: is the input pressure of fluid in the specimen in (Pa).

•: $\mathbf{P_2}$: is the output pressure of fluid in the specimen in (Pa).

•: **D**: is the diameter of cylinder specimen in (mm).

•: **L**: is the length or thickness of the cylinder specimen in (mm).

2.3.5 Influence of slipping properties on the flow of fluid in a porous medium

The permeability of fluids in pores of concrete has two kinds of flow: the first one is viscous flow and the second one is slip flow or Knudsen flow. To interpret the flow of fluid due to slip, there is a governing equation to represent this phenomenon. The Navier-Stokes equation explains the motion of fluid in a pipe with a small diameter or between two plates. On the other hand, this equation shows the flow of fluid due to slipping through a capillary tube.

The Navier-Stokes equation is based on three principle conditions as follows:

1. First approximation, if the pipe is cylindrical in shape, the flow of fluid is parallel to the walls.

2. The adhesion at the walls, which means the fluid velocity is zero at two points.

3. The pressure does not vary through the thickness of the flow or it isperpendicular on the direction of flow.

From the previous conditions, Poiseuille's flow results, i.e. the flow is organized so that the velocity forms a parabolic field with zero velocity at the walls of the pipe and maximum velocity at the center of the pipe. Two phenomena can be represented by two profiles as follows: the first one shows the velocity of the fluid (gas) in the capillary tube due to the fluid viscosity and the second profile shows the velocity of the fluid in the capillary tube due to the viscous and slipping flow of the fluid, see Figure (2.21).

From these two profiles, the relationship between fluid velocity and the radius of a circular tube is found, assuming the pressure gradient is oriented along the x-axis and the radius is constant ($\mathbf{r_0}$). Therefore, the velocity parallel to the x-axis of the circular tube as a function of $\mathbf{r}$ varies at any point along the r-axis, see Figure (2.21). Equations (2.19) and (2.20) show this relationship, which are simplified to obtain equation (2.21):

$$\boldsymbol{V(r,x) = V(r) = V_{max}(1 - \frac{r^2}{r_0^2})} \tag{2.19}$$

$$\boldsymbol{V_{max} = \frac{r_0^2}{4\mu}\frac{dP}{dx}} \tag{2.20}$$

$$\boldsymbol{V = -\frac{1}{4\mu}\frac{dP}{dx}(r_0^2 - r^2)} \tag{2.21}$$

According to the Navier-Stokes equation and the Kundt and Warburg theory, the gas velocity can be calculated as a function of pressure and the distance from the wall of the capillary tube, which was depended by Picandet in [Picandet, 2001] . See equation (2.22), where $\boldsymbol{\lambda}$ is the mean free path of gas molecules in (mm),

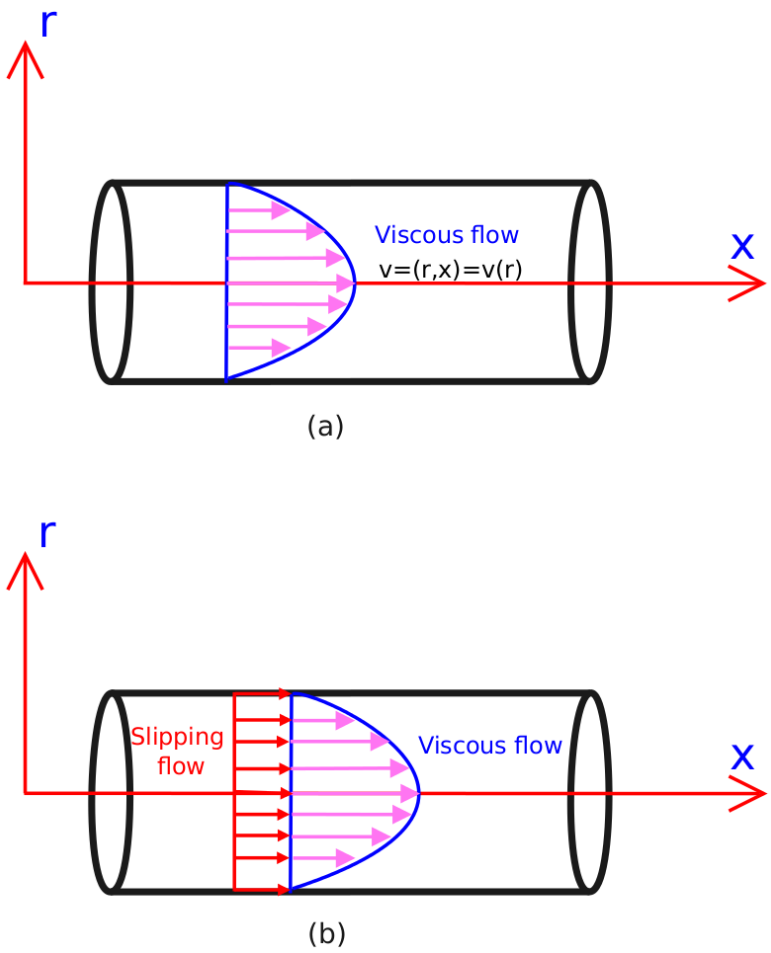

Figure 2.21: Velocity profiles of gas in the capillary tube viscous flow (a) viscous and slipping flow (b).

$\boldsymbol{c}$ is a constant which is nearly $\mathbf{1}$. This equation expresses the decrease in fluid pressure caused by increasing the mean free path of gas molecules ($\boldsymbol{\lambda}$).

$$\boldsymbol{V = -\frac{1}{4\mu}\frac{dP}{dx}(r_0^2 - r^2 + 2c\lambda r_0)} \tag{2.22}$$

2.3.6 Intrinsic permeability of concrete and it's determination

From previous studies, two methods have been shown for determining the intrinsic permeability of fluid in porous medium. The first is the laminar flow method, which present two types of flow in a porous medium, viscous and slipping flow. The second is the turbulent flow method, which may occur when the flow velocity is high.

Equation (2.18) shows the determinations under conditions of laminar viscous flow, which does not directly determine the intrinsic permeability, therefore this type of permeability is called apparent permeability ($\boldsymbol{k_a}$). This section shows the application of the Klinkenberg approach in [Klinkenberg et al., 1941] for a relative permeability to viscous flow only, i.e. there is no slipping flow. The apparent permeability ($\boldsymbol{k_a}$) is measured at different pressure gradients ($\boldsymbol{\Delta P}$) in order to find the intrinsic permeability ($\boldsymbol{k_v}$). On the other hand, Fochheimer's equation of flow determines the intrinsic permeability ($\boldsymbol{k_v}$) which is based on measurements of the apparent permeability ($\boldsymbol{k_a}$) at different pressure gradients ($\boldsymbol{\Delta P}$).

2.3.6.1 Permeability in the case of laminar flow

Klinkenberg in [Klinkenberg et al., 1941] demonstrated the measurement of permeability through sand, and this method was also used by Carman in [Carman, 1956]. The theoretical context was based on Klinkenberg's approach, and applied

to determine the intrinsic permeability of a porous medium.

To measure the flow of gas in a capillary tube according to equation (2.18) for an impermeable matrix, see equation (2.23):

$$\boldsymbol{Q = -\frac{\pi r_0^2}{8\mu}(P_2 - P_1)P_m(1 + \frac{4c\lambda}{r_0})} \tag{2.23}$$

where $\boldsymbol{P_1}$ is the inlet pressure in (Pa), $\boldsymbol{P_2}$ is the outlet pressure (atmospheric pressure) in (Pa), $\boldsymbol{P_m}$ is the mean pressure, $\boldsymbol{P_m = \frac{(P_1+P_2)}{2}}$ in (Pa).

The permeability of fluid according to Darcy's law for a capillary tube is given by equation (2.24):

$$\boldsymbol{k = \frac{\pi r_0^2}{8}} \tag{2.24}$$

From equation (2.23) and (2.24) will be obtained:

$$\boldsymbol{Q = -\frac{k}{\mu}(P_2 - P_1)P_m(1 + \frac{4c\lambda}{r_0})} \tag{2.25}$$

By applying Darcy's law, the following equations are obtained:

$$\boldsymbol{Q = -\frac{k_a}{\mu}(P_2 - P_1)P_m} \tag{2.26}$$

$$\boldsymbol{k_a = k(1 + \frac{4c\lambda}{r_0})} \tag{2.27}$$

According to the Klinkenberg approach, the gas pressure is inversely proportional to the mean free path of gas molecules, see equation (2.28):

$$\boldsymbol{\frac{4c\lambda}{r_0} = \frac{\beta}{P_m}} \tag{2.28}$$

where $\boldsymbol{\beta}$ is a constant called the Klinkenberg coefficient in (Pa). By substituting equation (2.28) in equation (2.27), we obtain:

$$k_a = k(1 + \frac{\beta}{P_m}) \tag{2.29}$$

The previous equation (2.29) shows the intrinsic permeability (k_v or k), relative to the viscous flow only.

Figure (2.22) shows that the intrinsic permeability (k_v) of ordinary concrete according to the Klinkenberg method, which means the intrinsic permeability of the gas presented in laminar flow, can be determined by extrapolation (linear regression) of the apparent permeability (k_a) by applying Darcy's law. Chatzigeorgiou [Chatzigeorgiou, 2004] applied this method for ordinary concrete and obtained a series of results shown in Figure (2.22).

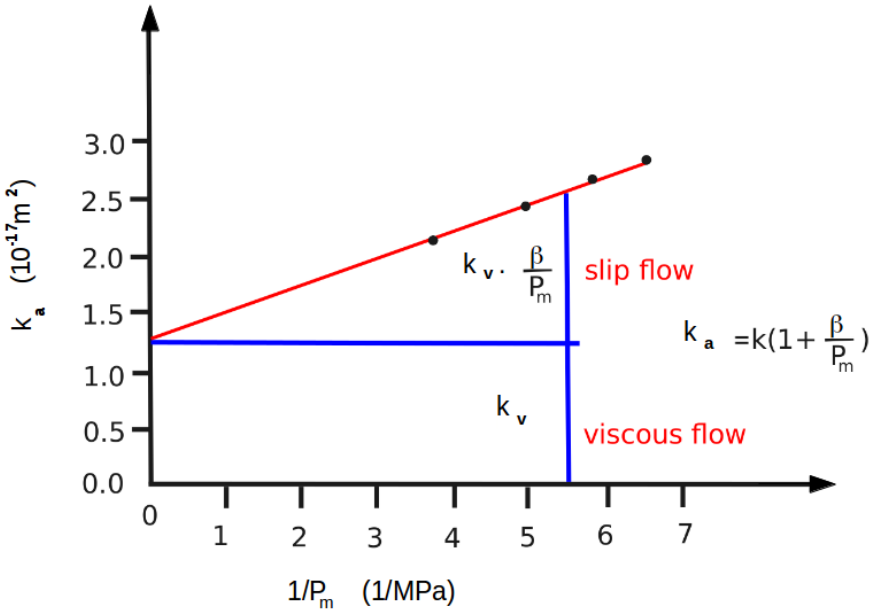

Figure 2.22: Behavior of gas permeability in a porous medium according to Klinkenberg in [Klinkenberg et al., 1941] and Chatzigeorgiou in [Chatzigeorgiou, 2004].

2.3.6.2 Permeability in the case of turbulent flow

When the fluid has a higher velocity, this causes turbulent flow. Picandet et al. [Picandet et al., 2009] investigated through the measurement of this type of flow, and the slipping flow was neglected in this study. Therefore, to calculate the intrinsic permeability using Darcy's law was not correct, so the determination of intrinsic permeability was based upon the equation of a monodirection flow (one direction) given by Dupit-Forchheimer's law, which was depended by the study of Dullien [FaL, 1992], as shown in equation (2.30):

$$-\frac{\boldsymbol{dP}}{\boldsymbol{dx}} = \boldsymbol{\alpha_t \mu V + \beta_t \rho V^2} \tag{2.30}$$

where $\boldsymbol{\alpha_t}$ is the constant that is found in Darcy's law and is equal to $\boldsymbol{\alpha_t = \frac{1}{k_v}}$, $\boldsymbol{\beta_t}$ is the constant equal to zero when the flow velocity is low.

Picandet [Picandet, 2001] presented a relationship from the previous equation (2.30) for measuring the fluid velocity at the upstream site, which depends on the principle of conservation of mass, see equation (2.31):

$$-\frac{\boldsymbol{\rho}}{\boldsymbol{\rho_1 V_1}}\frac{\boldsymbol{dP}}{\boldsymbol{dx}} = \frac{\boldsymbol{\mu}}{\boldsymbol{k_v}} + \boldsymbol{\beta_t \rho V} \tag{2.31}$$

The assumption is that behavior of gas according to the ideal gas law, see equation (2.32):

$$-\frac{\boldsymbol{P}}{\boldsymbol{P_1 V_1}}\frac{\boldsymbol{dP}}{\boldsymbol{dx}} = \frac{\boldsymbol{\mu}}{\boldsymbol{k_v}} + (\boldsymbol{\beta_t}\frac{\boldsymbol{M}}{\boldsymbol{RT}}\boldsymbol{PV}) \tag{2.32}$$

To calculate the permeability of gas in the disc specimen as shown in Figure (2.20), equation (2.32) is integrated in the direction of the length of the specimen and the start of flow at the injection flow ($\boldsymbol{Q_1}$), with upstream pressure ($\boldsymbol{P_1}$).

$$\frac{\boldsymbol{(P_1^2 - P_2^2)}}{\boldsymbol{8 Q_1 \mu P_1 L}} = \frac{\boldsymbol{1}}{\boldsymbol{k_v}} + (\boldsymbol{\beta_t}\frac{\boldsymbol{M}}{\boldsymbol{RT}}\frac{\boldsymbol{4P_1}}{\boldsymbol{\pi D^2 \mu}})\boldsymbol{Q_1} \tag{2.33}$$

From equations (2.20) and (2.29) can be obtained:

$$\frac{\mathbf{1}}{\boldsymbol{k_a}} = \frac{\mathbf{1}}{\boldsymbol{k_v}} + (\boldsymbol{\beta_t}\frac{\boldsymbol{M}}{\boldsymbol{RT}}\frac{\mathbf{4}\boldsymbol{P_1}}{\boldsymbol{\pi D^2 \mu}})\boldsymbol{Q_1} \tag{2.34}$$

As shown in equation (2.34), the apparent permeability ($\boldsymbol{k_a}$) is a function of the intrinsic permeability ($\boldsymbol{k_v}$) and flow ($\boldsymbol{Q_1}$). In this case, a similar Klinkenberg approach has been used.

2.3.7 Effect of crack dimensions on permeability in concrete

The crack dimensions are an important parameter that influences on the transport properties of a porous material like concrete. Breysse et al. [Breysse and Gérard, 1997] and Gérard et al. [Gérard et al., 1996] reported that the geometrical properties of cracks, such as crack width and tortuosity, influence on the permeability of concrete; they found an increase in water permeability with the maximum strain, as shown in Figure (2.23). Gérard [Gerard et al., 1997] pointed out that the permeability of concrete was proportional to the cube of the crack opening when the crack was wider than **1** mm. Rapoport et al. [Rapoport et al., 2002] and Lawler et al. [Lawler et al., 2002] reported that the permeability in a specimen with one crack was larger than in a specimen with several smaller cracks. Wang et al. [Wang et al., 1997] found that using the cylinder specimens depended on the splitting tensile strength; they reported that the crack opening displacement (COD) changed from 50 $\boldsymbol{\mu}$m to 550 $\boldsymbol{\mu}$m. In addition, the results referred to the similar behavior for water permeability with loading or unloading, as shown in Figure (2.24). Aldea et

al. [Aldea et al., 1999] loaded concrete and mortar specimens in the context of the splitting test and found increasing water permeability when the crack opening displacement was larger than 100 $\boldsymbol{\mu}$m, which was higher for concrete specimens than for mortar. They explained that the reason for this behavior was the difference in properties between the aggregate particles and cement paste at the interface zone. Aldea et al. [Aldea et al., 2000] demonstrated the influence of crack width on permeability, but there was no clear relationship between the crack length and water permeability, i.e. increasing water permeability with increasing crack opening. Samaha et al. [Samaha and Hover, 1992] loaded cylinder specimens of concrete and investigated the influence of microcracking on its transport properties. The results showed that chloride permeability and moisture movement increased with crack opening. Picandet et al. [Picandet et al., 2009] pointed out the influence of crack width on the gas and water permeability for cylindrical concrete specimens under a splitting tensile load. Figure (2.25) shows the relationship between the gas permeability and the residual lateral displacement ($\boldsymbol{\delta_{res}}$) for different mixtures.

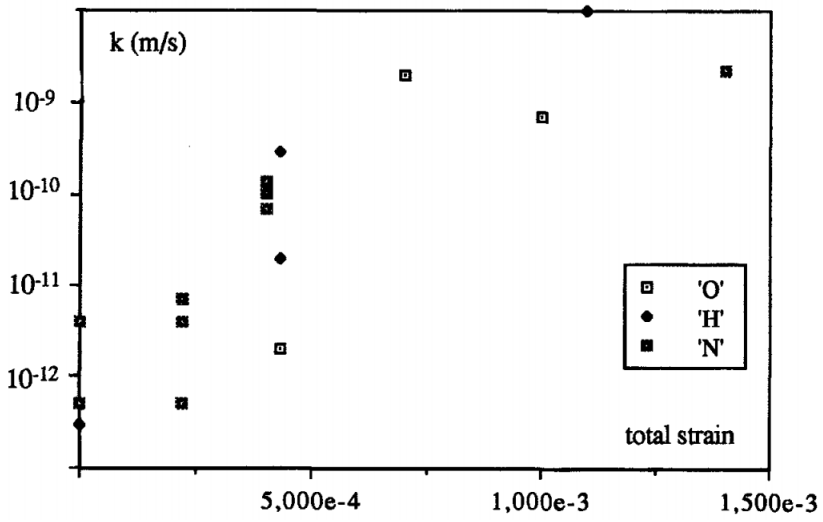

Figure 2.23: Relationship between water permeability with the maximum strain by Gérard et al. [Gérard et al., 1996], O: f'_c=32 MPa, H: f'_c=50 MPa, N: f'_c=60 MPa.

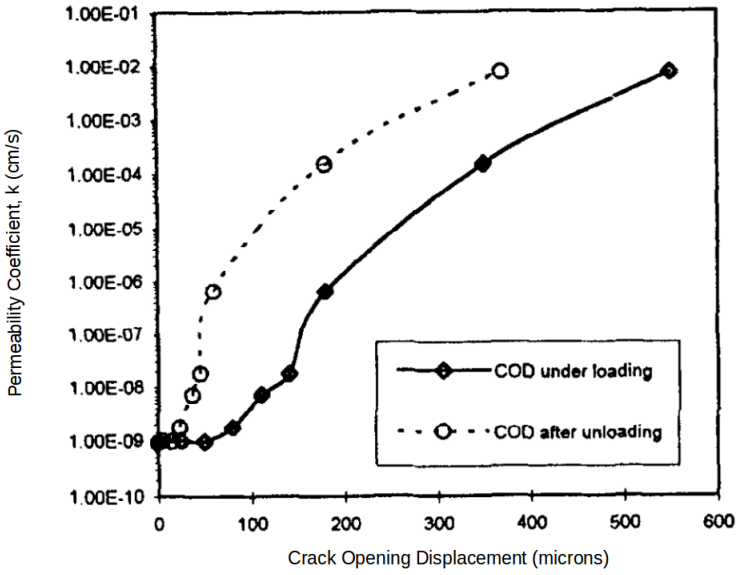

Figure 2.24: Relationship between water permeability and the crack opening displacement by Wang et al. [Wang et al., 1997].

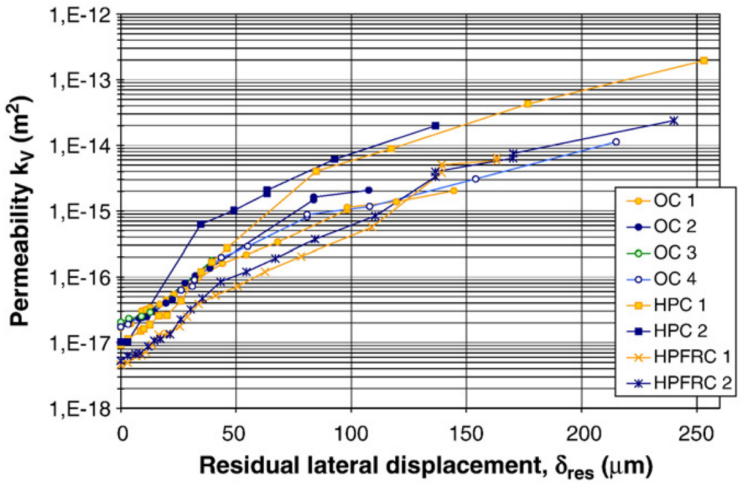

Figure 2.25: Relationship between gas permeability and the residual lateral displacement ($\boldsymbol{\delta_{res}}$) by Picandet et al. [Picandet et al., 2009].

2.3.8 Effect of the aggregate volume fraction on permeability in concrete

There is little research on the effect of the aggregate volume fraction on the transfer properties of concrete material. However, Grassl et al. [Grassl et al., 2010] carried out increases in permeability with increasing aggregate diameter and decreasing volume fraction and they found increasing the aggregate diameter led to an increase in permeability, as shown in Figure (2.26). In addition, Wong et al. [Wong et al., 2009] reported that increasing the sand content in mortar from 0 to 70 % caused oxygen permeability to decrease by a factor of 30-70, see Figure (2.27). Care et al. [Care and Derkx, 2011] presented the correlation between the aggregates size and volume fraction with gas permeability, i.e. gas permeability depends upon aggregates size and its content.

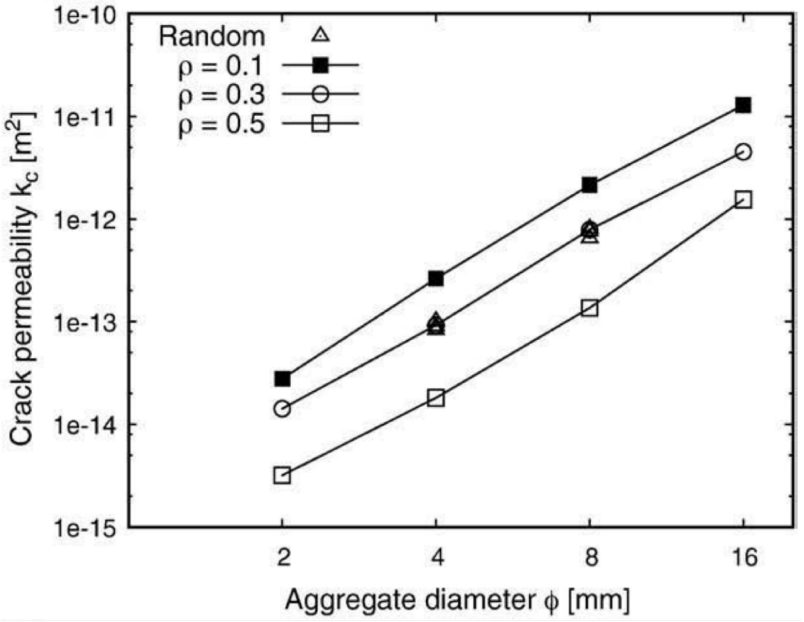

Figure 2.26: The effect of aggregate diameter on the permeability of concrete with three volume fractions $\boldsymbol{\rho} = 0.1$, 0.3 and 0.5 by Grassl et al. [Grassl et al., 2010].

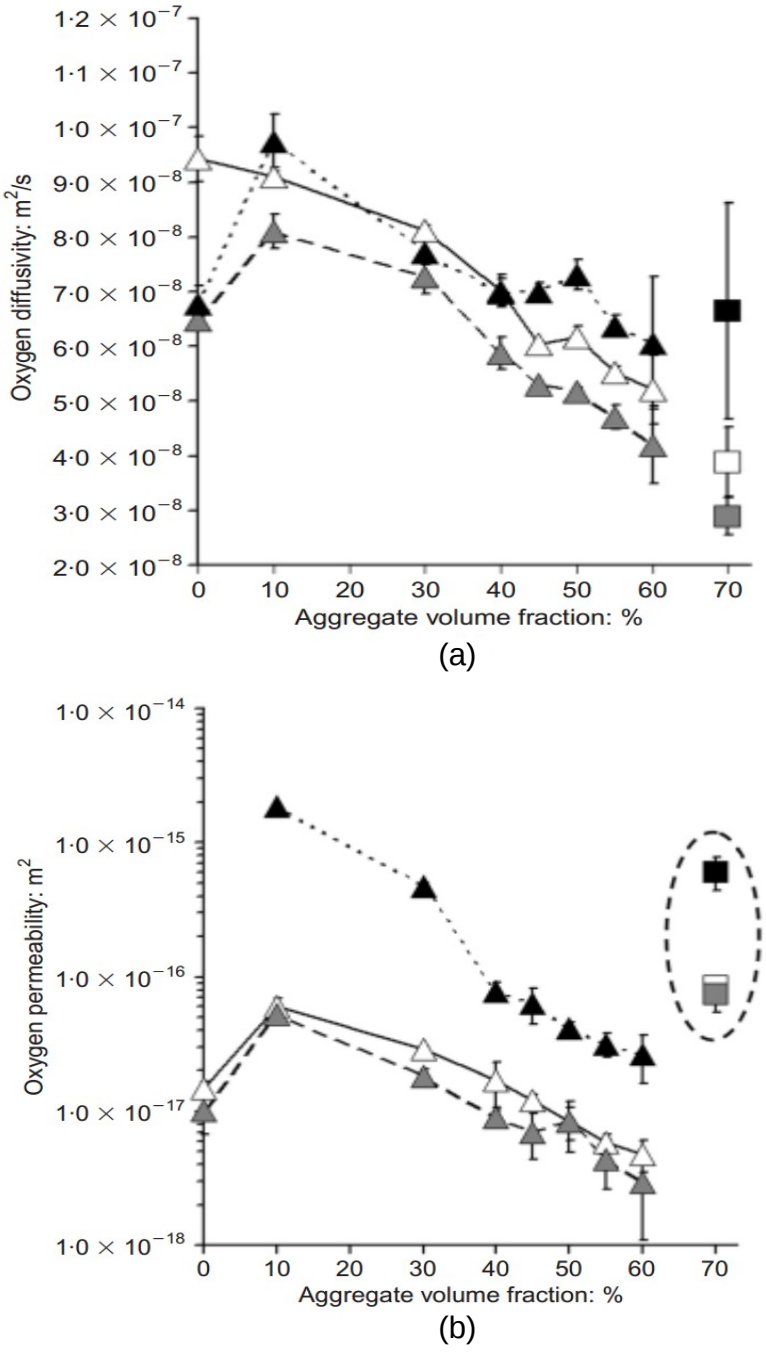

Figure 2.27: The effect of the aggregate volume fraction on the diffusivity (a) and permeability (b) of oxygen in mortar = M, concrete = C and containing 8 % silica fume = SF , Wong et al. [Wong et al., 2009].

2.4 Conclusions

This chapter reviews the previous studies and consists of two parts: the first part is the mechanical behavior of concrete under loading and describes the influence of some parameters on this behavior. The second part presents the transport properties of porous media such as concrete material and demonstrates the effect of some parameters on the hydro-mechanical behavior of cracked and uncracked concrete material. The following conclusions can be noted from this literature:

1. There are many factors which affect on the mechanical behavior and as well as hydro-mechanical behavior of concrete such as: type of applied loads, mix proportions, type of aggregates, aggregates content, aggregates size, type of cement, etc.

2. The hydro-mechanical properties of concrete are also influenced by a number of parameters such as: pores size, pores connectivity, load levels, mix design, aggregates content and shape and roughness, aggregates size, crack dimensions, tortuosity of crack, etc. However, these numbers parameters want be investigated in this thesis.

This study focuses on the influence of aggregates size and volume fraction on the mechanical behavior of concrete. In addition, the relationship between crack opening and permeability is explained and the effect of aggregates size and volume fraction on gas permeability is demonstrated. This work includes two numerical models and an experimental work to investigate and validate these model is designed.

Chapter 3

3D MESO-SCALE SIMULATION OF CRACK-PERMEABILITY COUPLING

This chapter presents two numerical models: the first one is meso-scale model for the implementation of the mechanical behavior of concrete under loading using the Brazilian splitting test. The second one is hydro-mechanical model for coupling crack opening and gas permeability for the specimens used in meso-scale model. This test is focused on the effect of aggregates size on the mechanical properties of the hardened concrete under loading. Finite element simulations for five cylinders have been carried out in this work to study the behavior of concrete under diametric compression load. Cylinder specimens of concrete with 50 mm of thickness and 110 mm of diameters have been regarded. Five different diameters sizes of aggregate have been employed in the analyses, ranging from 4 to 16 mm. Herein taking into account the volume fraction of aggregate is constant 20 %. In addition, nine cylindrical

specimens were simulated with three volume fractions of aggregate 10, 20 and 30 % with three aggregate diameters 10, 14 and 16 mm.

This study has employed a meso-scale model (mechanical model) based upon a 3D lattice approach, representing with explicitly heterogeneity and failure mechanism of the concrete. This model considered the concrete to be a two-phase material in which aggregates are melted within the cement paste. Three sets of bar elements were thus presented: one being completely located into the aggregate (no weak discontinuity). The second set of element was located within the cement paste (no weak discontinuity) and the last set of elements was splitted into two parts by a physical interface (weak discontinuity activated); each part having different elastic properties. The second enhancement of kinematics introduced here is a strong discontinuity representing crack opening (discontinuous displacement field) $[|\boldsymbol{u}|]$*. In addition, to compute the transfer of fluid (gas or water) two kinds of flow are presented in the crack opening and pores of material. Furthermore permeability evolution is also compared with experimental results from the literature.*

The results of the numerical simulations showed the ability of the meso-scale and hydro- mechanical simulations to evaluate the hydro-mechanical properties in the context of the Brazilian splitting test. Also, the results showed that (1) the ultimate tensile stress, (2) the ultimate crack opening, (3) the fracture energy were all had increased when the aggregate diameter and the volume fraction were increased, (4) the increasing of aggregates size leads to an increase in gas permeability and (5) decreases as the volume fraction increases.

3.1 Introduction

The heterogeneous nature of concrete (porous structure and presence of micro/macro cracks) is known to play a significant role in the penetration of fluids (gas or liquid). When it comes to cracking, connected micro cracks and macro cracks act as preferential flow paths for mass transport processes and consequently contribute to deteriorate the long-term durability of concrete, especially when considering exposure to deleterious agents. An understanding of such coupled transport between cracking and permeability is therefore necessary for improving the durability of concrete materials. On one hand, physical testing is an effective means for studying numerous aspects of durability. In the literature, experimental results attempting to understand the mutual interactions and relationship between cracking and permeability within concrete can be found (see for instance [Choinska et al., 2007]). In particular, experimental setups involving the Brazilian splitting test are often regarded. Indeed this test presents several advantages for studying the aforementioned coupling :

1. Generally one main macro-crack (see [Rocco et al., 1999] for details regarding the failure modes) induced by tensile stress and whose position is known a priori, is created during the test

2. Regarding 1., the crack opening displacement (COD) can be recorded during loading and after unloading on the font and rear faces (see [Rastiello et al., 2014], [El Dandachy et al., 2016], [Picandet et al., 2009] and [Wang et al., 1997] for instance)

3. Regarding 1., a permeability measurement apparatus can be a priori positionned so the fluid flux flows through the main macro-crack and be accurately measured (see [Rastiello et al., 2014] and [El Dandachy et al., 2016])

Combining 1., 2. and 3., the evolution of the mass flow - measured under a pressure gradient - versus the COD is obtained. Having the mass flow in hand, the corresponding permeability value, whose definition varies if gas or water permeability is regarded (see [Picandet et al., 2009]), is computed in a second time. In [Picandet et al., 2009], the authors test ordinary concrete (OC) and high-performance concrete (HPC). After unloading, gas and water permeability tests are both performed. In [Wang et al., 1997], water permeability tests are conducted after unloading. In [Rastiello et al., 2014], the authors propose to relate real time water permeability and COD in order to alleviate parasite effects such as crack healing or external ambient conditions changes. The water permeability is a function of crack width square (see [Akhavan et al., 2012]). In addition, water permeability of cracked section significantly increased with increasing crack width (see [Aldea et al., 1999]). Park et al. [Park et al., 2012] pointed out that increasing in water permeability with crack opening increases. The geometrical properties of fracture opening influence on the rate of water flow (see [Li et al., 2011]). The water permeability in concrete depends on the crack opening [Gérard et al., 1996]. Breysse et al. [Breysse and Gérard, 1997] investigated that the geometrical properties of cracks, such as crack width and tortuosity, influence on the permeability of concrete.

On the other hand, numerical modeling can serve as a complementary means of investigation. Unfortunately, regarding the literature dealing with the numerical modeling of the Brazilian splitting test and its coupling with permeability, few papers exist. Most of them are written in the context of macroscopic Finite Element models ([Pijaudier-Cabot et al., 2009], [Matallah and La Borderie, 2016], [Rastiello et al., 2015]), well suited for engineering oriented applications. Nevertheless these models in which a true discontinuity cannot be properly represented, need for a post-treatment of the damage variable ([Matallah et al., 2010]

and [El Dandachy et al., 2016]) to correctly capture crack opening values and the orientations of the cracks, in particular when it comes to localized crack. This is a serious drawback for the coupling with permeability and for the computation of the corresponding mass flow. We propose in this chapter to investigate the coupling between cracking and permeability within the Brazilian splitting test with a discrete meso-scale model ([Jourdain et al., 2013], [Benkemoun et al., 2013]). In this sense the discrete nature of cracks (micro and macro) and the corresponding mass flows are taken into account leading to an hydro-mechanical coupling set up on a physical basis. More precisely, the model is based upon a two-phase material with stiff aggregates embedded into a cement paste. Consequently, the influence of the shape, the size, the distribution and the hydro-mechanical properties of aggregates – playing a significant role on the hydro-mechanical behavior of concrete (see Yaman et al. [Yaman et al., 2002]) – is also taken into account. The simulations are made with a 3D Finite Element model relying on the work of Benkemoun et al. [Benkemoun et al., 2010]. The cracking is taken into account explicitly by means of the Strong Discontinuity Approach [Simo et al., 1993]. This approach consists in incorporing displacement discontinuities in the Finite Element interpolation of the displacement field, leading to an efficient way to compute crack opening values $[|\boldsymbol{u}|]$. The key point of the hydro-mechanical coupling is based upon the fact that the crack opening values $[|\boldsymbol{u}|]$ are computed when solving the mechanical problem at the meso-scale. This data leads to a straightforward way to compute mass flows within meso-scale cracks according to a double porosity method ([Maleki and Pouya, 2010] and [Jourdain et al., 2013]). This method takes into account crack openings through the Poiseuille law but also the initial permeability of the sound concrete. As this meso-scale cracks distribution is dependent of the crack openings, their orientations, the level of loading and the aggregates size, an induced anisotropy is taken into account into the mass flow field. Consequently the com-

putation of the apparent permeability by an homogenization method (see [Pouya and Courtois, 2002a]) accounts for : (1) the evolution from diffuse cracks in the bulk to localized macro-crack(s), (2) the influence of the aggregates size, (3) the influence of volume fraction and (4) the induced-anisotropy which is usually, except for low stress levels, a difficult task (see [Pijaudier-Cabot et al., 2009]). In addition, in the spirit of a sequential multi-scale approach [Feyel and Chaboche, 2001], macro-scale permeability equations are identified from hydro-mechanical results coming from the meso-scale computations. Once macro-scale permeability equations are identified, they can further be used in commercial Finite Element code based upon standard phenomenological models [Reynouard et al., 2009] and usual computational procedures [Simo and Hughes, 1997].

This chapter is as follows : in Section 3.2, we give a brief description of the concrete meso-scale model developed [Benkemoun et al., 2010] which is used to model the Brazilian splitting test. Then we present two examples to mechanical simulations to relate the effect of aggregates diameters and volume fraction on fracture features such as the ultimate crack opening, the macroscopic ulimate tensile stress and the total dissipated energy. In Section 3.3, we provide a short review of the hydro-mechanical coupling model developed in [Jourdain et al., 2013], making the link between cracking and permeability. First, we stress the key points of the hydro-mechanical coupling model then we present numerical simulations of gas permeability tests. Some comparisons with experimental data from [Choinska et al., 2008b] are provided. Besides, we investigate the influence of the aggregates size and volume fraction on the macroscopic permeability.

3.2 Meso-scale simulations of the Brazilian splitting test mechanical features

In this section, we give, in a first time, a brief description of the mechanical model. For the readers interested in more details, a complete description of the model, its numerical implementation and a number of illustrative examples of the model predictive capabilities can be found in the paper of Benkemoun et al. [Benkemoun et al., 2010]. In addition a enhanced version of this mechanical model based upon Timoshenko beam elements can be found [Roubin, 2013]. In a second time, we present numerical simulations concerning the Brazilian splitting test. We relate the effect of the aggregates diameter and volume fraction on mechanical features such as the ultimate crack opening, the ulimate tensile stress and the fracture energy.

As shown in Figure (3.1), set-up of the Brazilian splitting test, in this test a cylindrical specimen of concrete is loaded in diametral loading along the longitudinal axis of the cylinder between two platens of a testing machine.

The tensile stress is computed according to ASTM C496 [ASTM C496, 1996] such as:

$$\boldsymbol{\sigma_u} = \frac{\boldsymbol{2P_u}}{\boldsymbol{\pi BD}} \tag{3.1}$$

where a $\boldsymbol{\sigma_u}$ is the splitting tensile strength in (MPa) at the failure due to the ultimate diametral loading $\boldsymbol{P_u}$ in (N), $\boldsymbol{D}$ is the diameter of the cylinder specimen in (mm), and $\boldsymbol{B}$ is the specimen thickness in (mm).

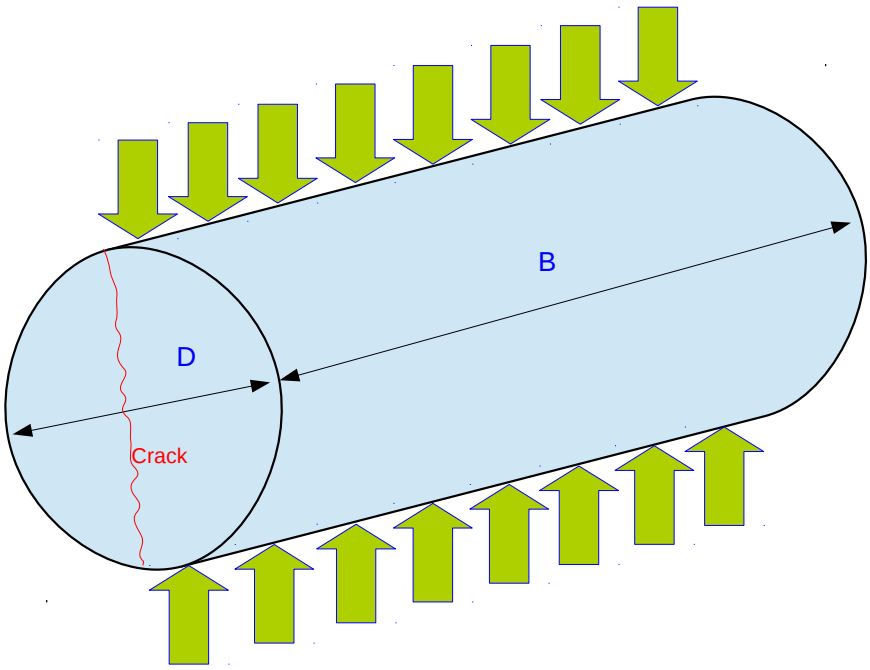

Figure 3.1: Schematic showing the Brazilian splitting tensile test set-up.

3.2.1 Meso-scale mechanical model

The numerical model for the mechanical simulations is based upon a two-phase (stiff aggregates embedded into a cement paste) quasi-brittle model capable of representing the behavior of concrete-like materials under complex loading paths. In order to take into account the influence of the shape, the size, the distribution and the mechanical properties of aggregates on the mechanical behavior of concrete, the mesoscale (see Roubin et al. [Roubin et al., 2015] and Nilenius et al. [Nilenius et al., 2015] for instance) is chosen to be the scale of computation.

In addition, in this work the kinematics of each 1D finite element is enhanced by two discontinuities embedded in the elements. For details concerning the numerical implementation, see **Appendix A**.

The first discontinuity is a weak discontinuity – continuous displacement field and discontinuous strain field (Ortiz et al. [Ortiz et al., 1987]) – introduced because of the non-adaptated meshing process (Moës et al. [Moës et al., 2003]). This process consists in a unique homogeneous mesh whose nodes are placed independently from the morphology of the aggregates. A significant amount of computation time is saved at this stage. However, some truss elements are cut into two parts, each having different elastic properties (see Figure 3.3 for a two-phase material). That's why in order to take into account this special kinematics in the truss elements, this weak discontinuity is introduced.

The weak discontinuity is present only for the truss elements split into two parts, each having a different Young modulus. The strong discontinuity is introduced by means of a yield function $\boldsymbol{g}$ which is triggered only in traction. Thus two constitutive models appear for a truss element: a continuum one (outside the discontinuity) which is elastic, see Figure (3.2(a)), and a discrete one (over the discontinuity) which is quasi-brittle, see Figure (3.2(b)). We denote by $\boldsymbol{t_\Gamma}$ the

traction vector over the discontinuity and $[|\boldsymbol{u}|]$ the crack width which belongs to the set of unknowns.

The yield function is such as:

$$\boldsymbol{g} = \boldsymbol{t_\Gamma} - (\boldsymbol{\sigma_u} - \boldsymbol{q}), \tag{3.2}$$

where $\boldsymbol{q}$ is the stress-like variable

$$\boldsymbol{q} = \mathbf{k}([|\boldsymbol{u}|]); \;\; \mathbf{k}([|\boldsymbol{u}|]) = \boldsymbol{\sigma_u}\left(1 - \exp\left(-[|\boldsymbol{u}|]\frac{\boldsymbol{\sigma_u}}{\boldsymbol{G_f}}\right)\right). \tag{3.3}$$

In summary, there are altogether eight model parameters: the Young modulus $\boldsymbol{E_1}$ for the mortar matrix and $\boldsymbol{E_2}$ for aggregates, for the continuum model and the ultimate tensile strength before softening, $\boldsymbol{\sigma_{u_i}}$ and the fracture energy, $\boldsymbol{G_{f_i}}$ ($\boldsymbol{i} = 1$, 2, 3 for respectively the mortar matrix, aggregates and interfaces) for the discrete model. We note $\boldsymbol{G_{f_i}}$ the area under the curve $\boldsymbol{t_\Gamma} - [|\boldsymbol{u}|]$, see **Appendix A**.

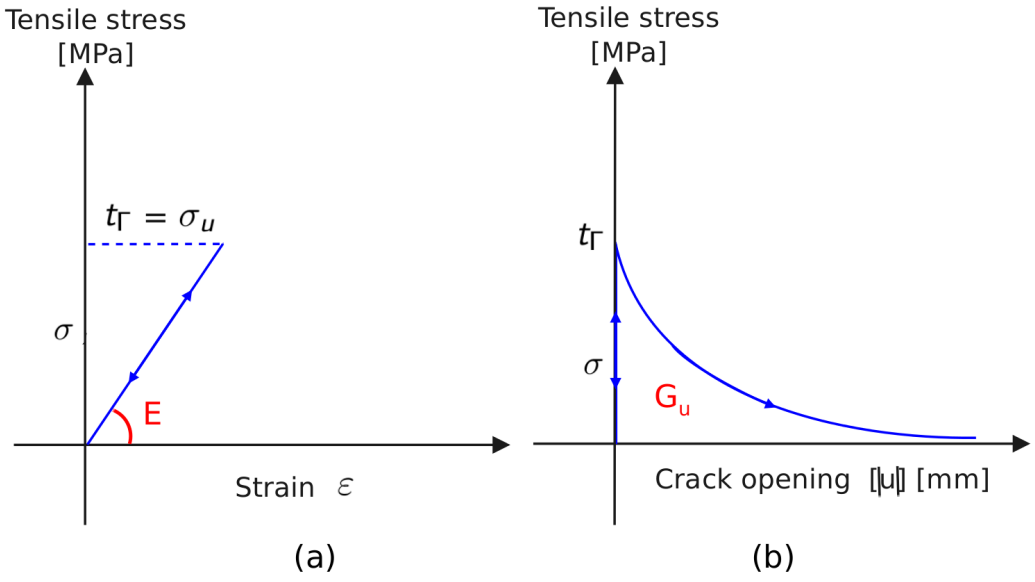

Figure 3.2: Elastic-quasi-brittle-behavior: outside the discontinuity (a) at the discontinuity (b) [Benkemoun, 2010].

3.2.2 Numerical simulations of the tensile splitting test: investigation of the aggregates size

This section presents five finite element simulations to investigate the behavior of concrete under diametral compression load in the context of the Brazilian splitting test. Five cylinder specimens of concrete have been simulated with dimensions 50 x 110 mm of thickness and diameter, respectively. Five diameters of aggregate have been employed in the analyses, ranging from 4 to 16 mm.

Table (3.1), shows sums up the mechanical properties for each phase. 3D numerical simulation for cylinder specimen has dimensions 50 mm of thickness and 110 mm of diameter presents in Figure (3.3). The relationship between the tensile stress and crack opening is shown in Figure (3.4). Herein, the numerical results for five simulations are explained the behavior of concrete under tensile stress with the influence of aggregates diameter. Also these numerical computations have been run for different mesh generations. The results are presented for mean values with statistical discrepancy. We can see more ductile behavior with increasing aggregates size after peak load. While the specimen with 16 mm aggregates size has difference tendency cause to the heterogeneity is more than other specimens. We used 0.3 mm imposed displacement at one point on the top specimen.

Usual value of Youngs modulus of aggregate for concrete is between 60 and 80 GPa. For a cement paste it is about 20 GPa and for mortar it lies between 30 and 40 GPa.

In our model, the values of Youngs modulus for cement paste and for aggregate are higher than the mentioned real values. In fact, these artefacts are needed in order to get a satisfying global mechanical behavior (stress-strain relationship, see Figure (3.4)).

Table 3.1: Mechanical properties of materials, $(\boldsymbol{E}, \boldsymbol{\sigma_u}, \boldsymbol{G_u})$ modulus of elasticity, tensile stress and fracture energy.

Cement paste	Aggregate	Interface	Volume of fraction
$\boldsymbol{E_{cem}} = 35$ GPa	$\boldsymbol{E_{agg}} = 100$ GPa	-	20 %
$\boldsymbol{\sigma_u} = 3$ MPa	-	$\boldsymbol{\sigma_u} = 3$ MPa	
$\boldsymbol{G_u} = 80$ J/m^2	-	$\boldsymbol{G_u} = 80$ J/m^2	

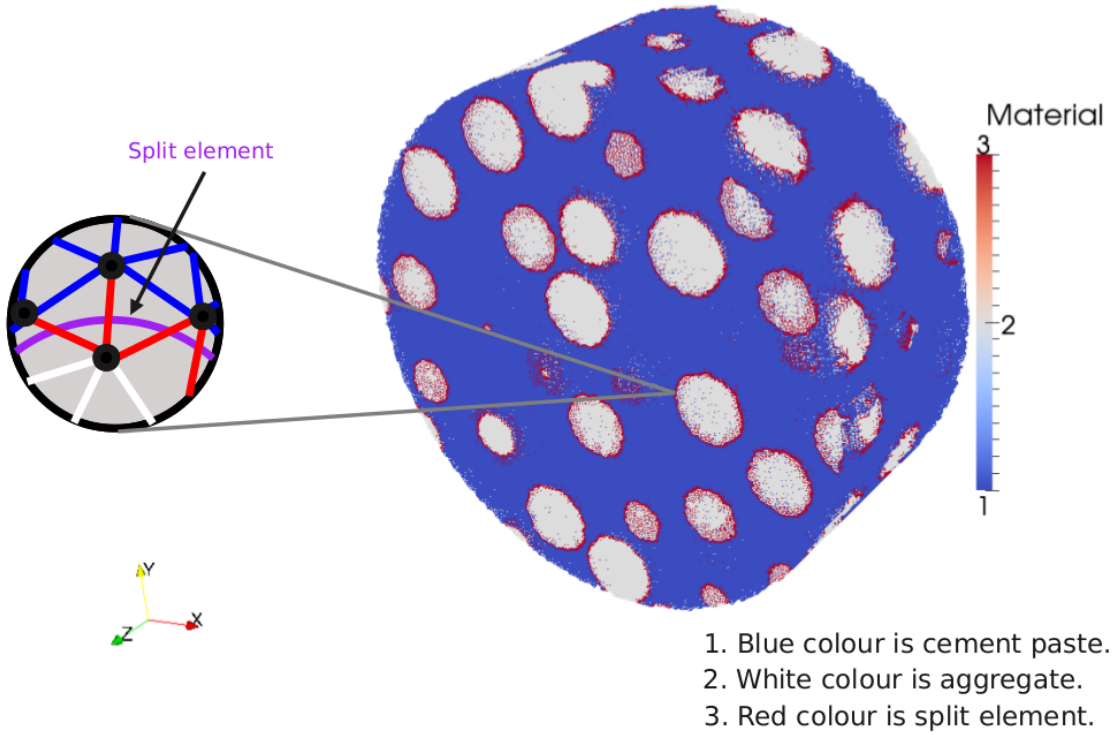

Figure 3.3: 3D representation of two-phase material for the simulations of the tensile splitting test.

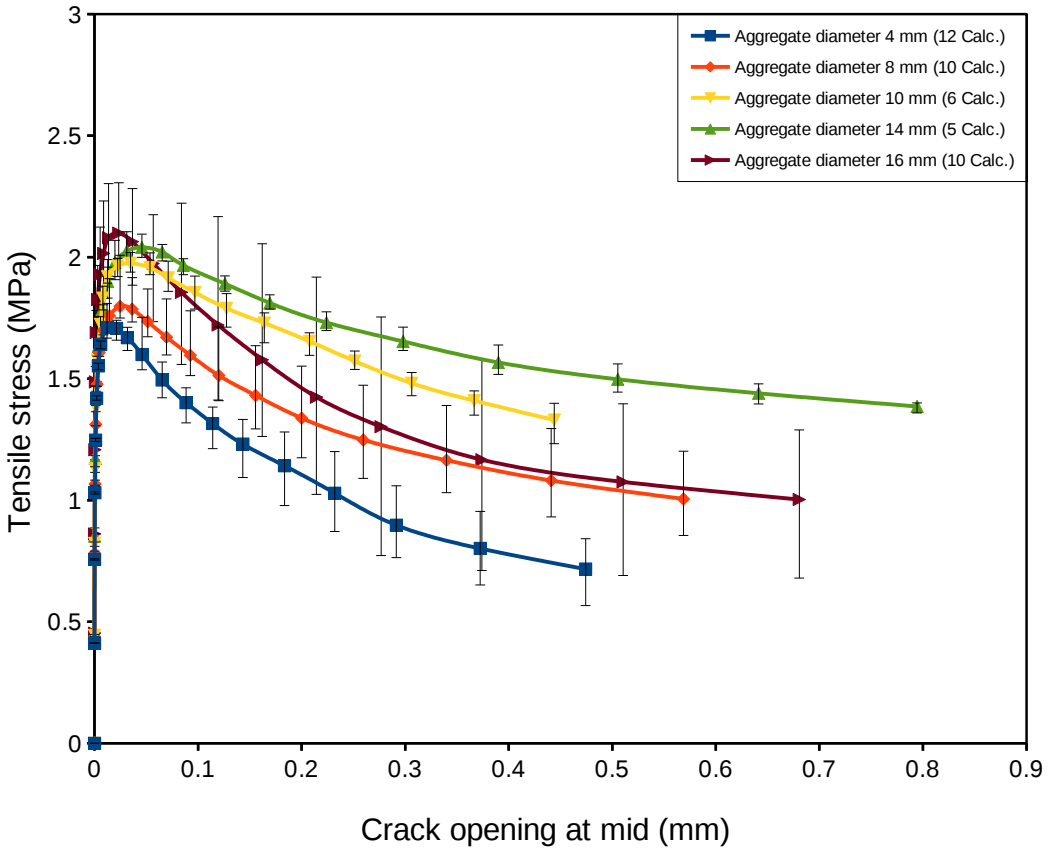

Figure 3.4: The tensile stress-crack opening at mid of cylinder specimens (volume of fraction is 20 %) with five aggregate diameters ranging from 4 to 16 mm. Simulations are carried out for five cylinder specimens.

3.2.2.1 Ultimate crack opening

The ultimate crack opening is defined as the crack corresponding to the ultimate tensile stress and it can be obtained from the stress-crack opening curve of concrete in the Brazilian splitting test, see Figure (3.2(b)). According to the present results, however, the results show an increase in ultimate crack opening with the increase in aggregate diameters. The reason may be that the crack path becomes larger through the cement paste and will change its path through the inerfaces when it connects with the aggregate particles, this means that the crack path is not a straight line (more tortuosity) with the increasing aggregate diameter. The numerical results show a significant influence of the aggregate diameter on the crack opening and by taking into account that the crack opening in x-direction and volume of fraction is constant. Therefore, the increase in the aggregates size results in a greater increase in the ultimate crack opening. The influence may be explained by the difference position of aggregate particles. The pathway of main crack take places in a cement paste or in the interfaces. Therefore the influence of the aggregates size is more significant.

Our results with some of the experimental works conducted by other researchers for examples: Mihashi et al. [Mihashi et al., 1991] who pointed out that the critical crack opening ($\boldsymbol{w_c}$) is increasing with the increase of aggregates size for the normal concrete, the reason of this increase is more heterogeneity when using largest aggregate sizes than the smallest aggregates size, it causes the expansion of the fracture process zone after applying the ultimate load with the increasing of absorption energy and therefore the critical crack will be increased. Mihashi et al. [Mihashi et al., 1991] offered that the increasing of critical is based on the tension softening diagrams because of the accumulation of microcracking over a wider nonlinear region. Li et al. [Li et al., 2004b] presented that the critical crack opening ($\boldsymbol{w_c}$) is increasing as according to the aggregates size for the dam concrete,

also, the specimens with larger aggregates size are more brittle than the specimens with smallest aggregates size. Elices et al. [Elices and Rocco, 2008] found the influence of the aggregates size on critical crack opening, it means the increasing of the aggregates size leads to an increase a critical crack opening.

Figure (3.5) shows the numerical meso-scale model, it can be seen the ultimate crack opening which measured at the peak of loading as function of aggregate diameters, also it shows a significant influence of the aggregate diameter on the ultimate crack opening.

As shown in Figures (3.6) and (3.7), 3D five cylinder specimens have been simulated for both front and isometric views respectively, the path of the crack is seen a straight line across the cylinder specimen with the aggregate diameter 4 mm and without discontinuities, while this path is more and tortuosity is seen in the specimens with the largest aggregate diameter. All the cracks took place at the cement paste and at the interfaces. All simulations pointed out at final step simulation.

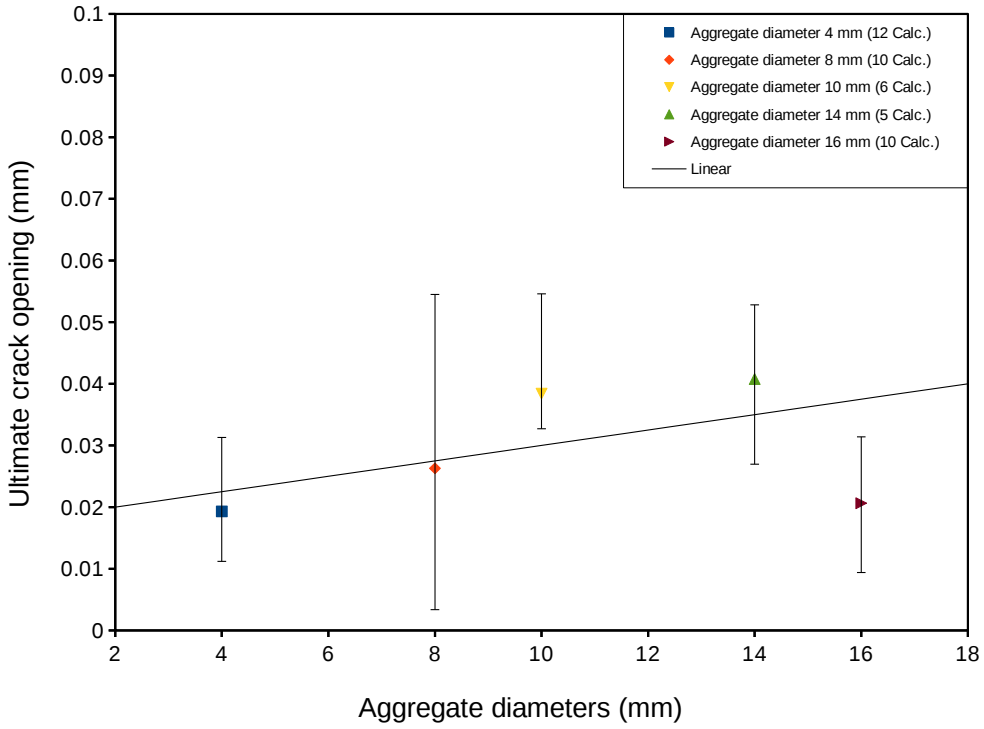

Figure 3.5: The effect of aggregate diameters on the ultimate crack opening (volume of fraction is 20 %) with five aggregate diameters ranging from 4 to 16 mm. Simulations are carried out for five cylinder specimens.

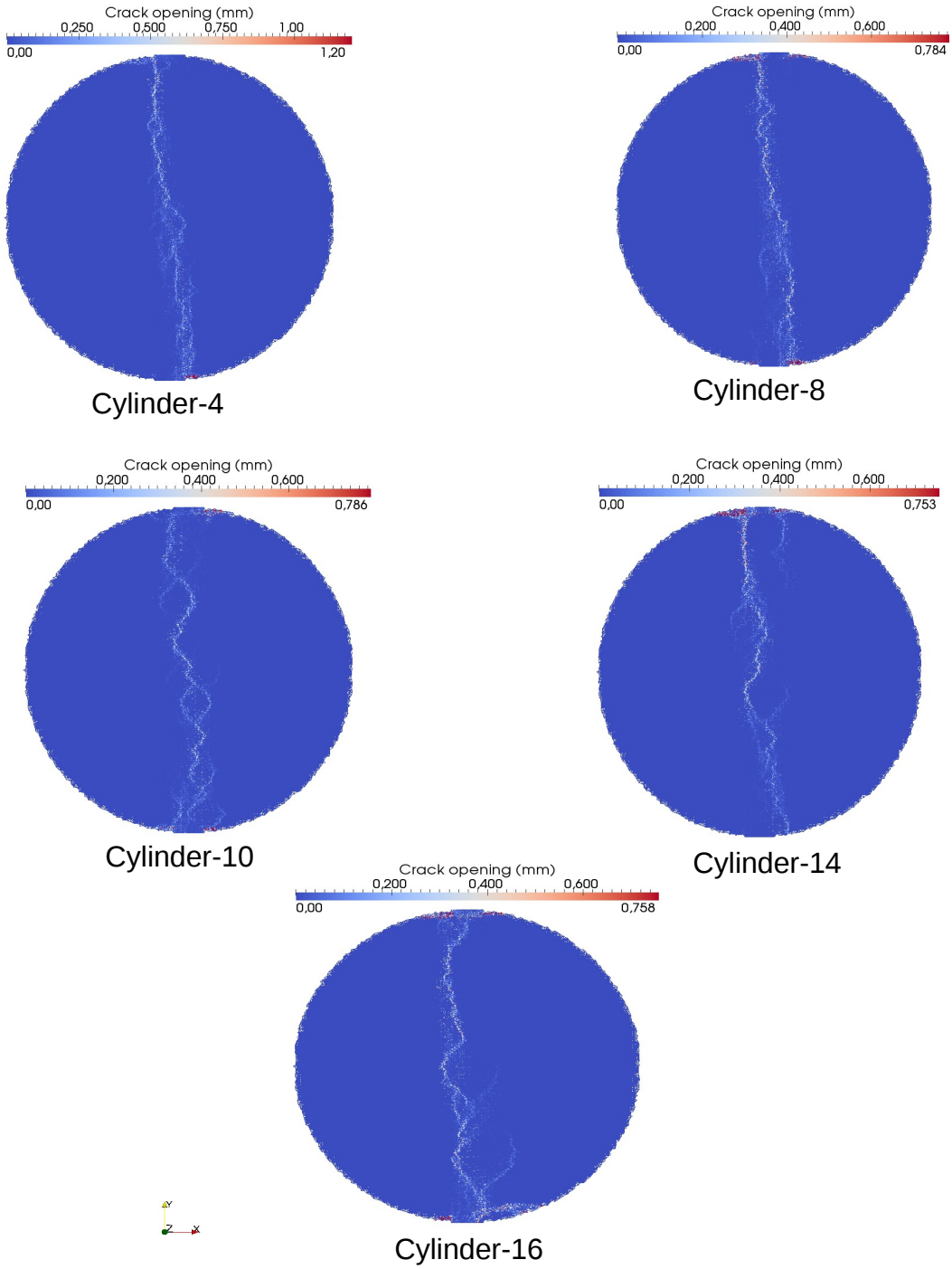

Figure 3.6: 3D front view of five cylinder specimens that are simulated with crack opening. Cylinders are of dimensions 50 x 110 mm of thickness and diameter, respectively.

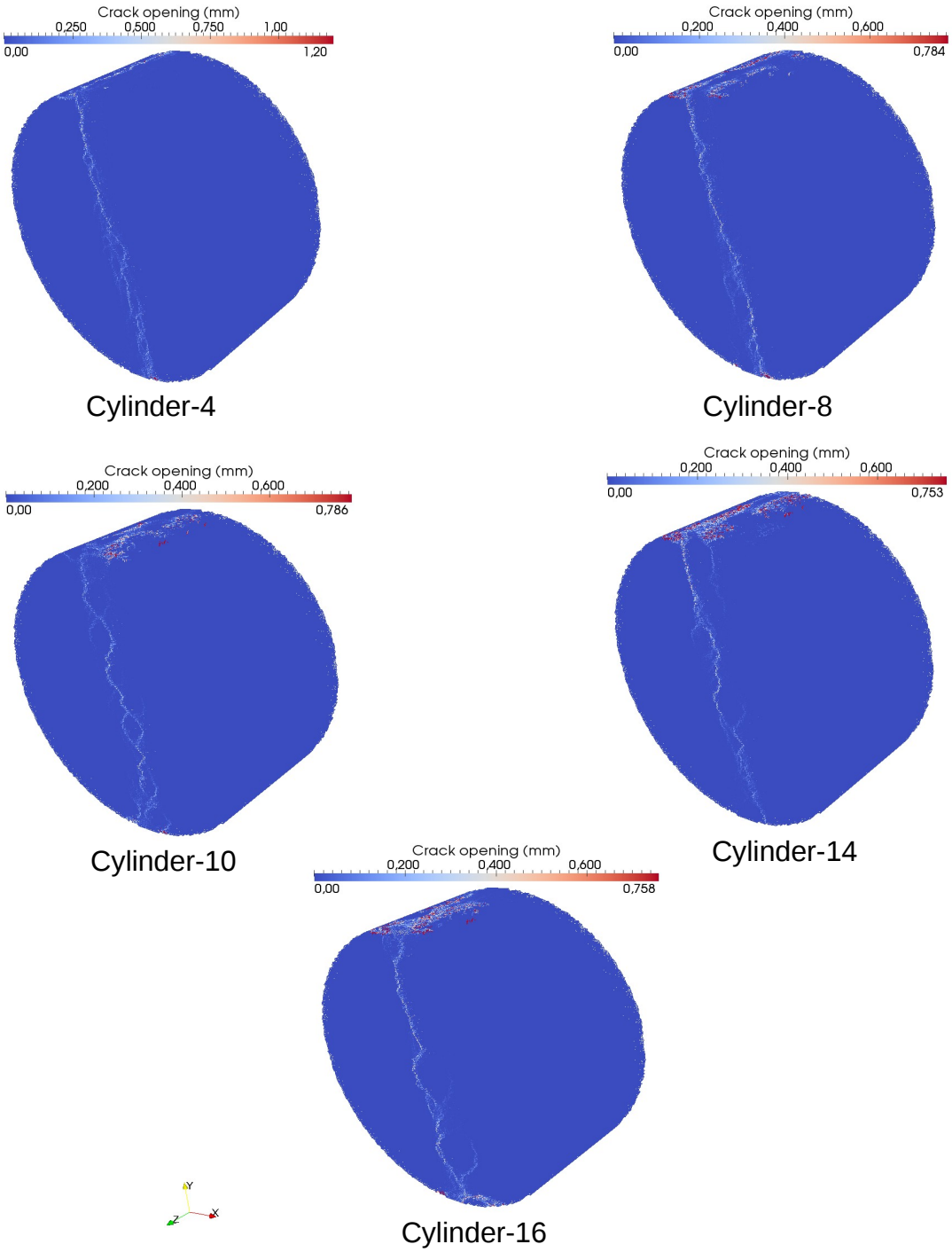

Figure 3.7: 3D isometric view of five cylinder specimens that are simulated with crack opening. Cylinders are of dimensions 50 x 110 mm of thickness and diameter, respectively.

3.2.2.2 Macroscopic ultimate tensile stress

The relationship between aggregate diameters and the ultimate splitting tensile stress for the five cylinder specimens are simulated, as shown in Figure (3.8), the ultimate tensile stress varied between 1.718 and 2.176 MPa. These results gave an indication of the behavior of concrete under tensile loading, it can be seen that an increasing of the tensile stress occurred when the aggregate diameters have been increased. This implies that the specimens with larger aggregate diameters are more brittle than the specimens with smallest aggregate diameters. Also, this behavior depends on the interface zone between the cement paste and aggregate particles. Figure (3.9) shows the ultimate tensile stress as a function of a specific surface area of aggregate for five cylinder specimens that are simulated. The surface area shows a reverse tendency with the ultimate tensile stress, it means that the increase of specific surface area leads to a decrease of the tensile stress in concrete. In addition, the volume of fraction is constant at 20 % for the five simulations. The specific surface area of smaller aggregate is higher than the area of specimens with largest aggregate. The results show that the geometry properties of the materials are controlling the crack location and position. Cracks take place either into the cement paste or on the interfaces, therefore the interfaces is higher with the smaller aggregate than the specimens with largest aggregate.

Concerning the effect of aggregates size, some researchers have recently shown the influence of the aggregates size on the mechanical behavior of concrete under loading. Rao et al. [Rao and Prasad, 2002] observed the increasing of the tensile stress with the increasing of aggregate size, also, it was found the debonding force at the interface zone was less due to the higher surface area of the smallest aggregate particles. Chen et al. [Chen and Liu, 2004] presented that the tensile strength of high-strengthed concrete is increasing with the aggregates size. Also, it was concluded that the bond stress at the interface zone between the aggregate

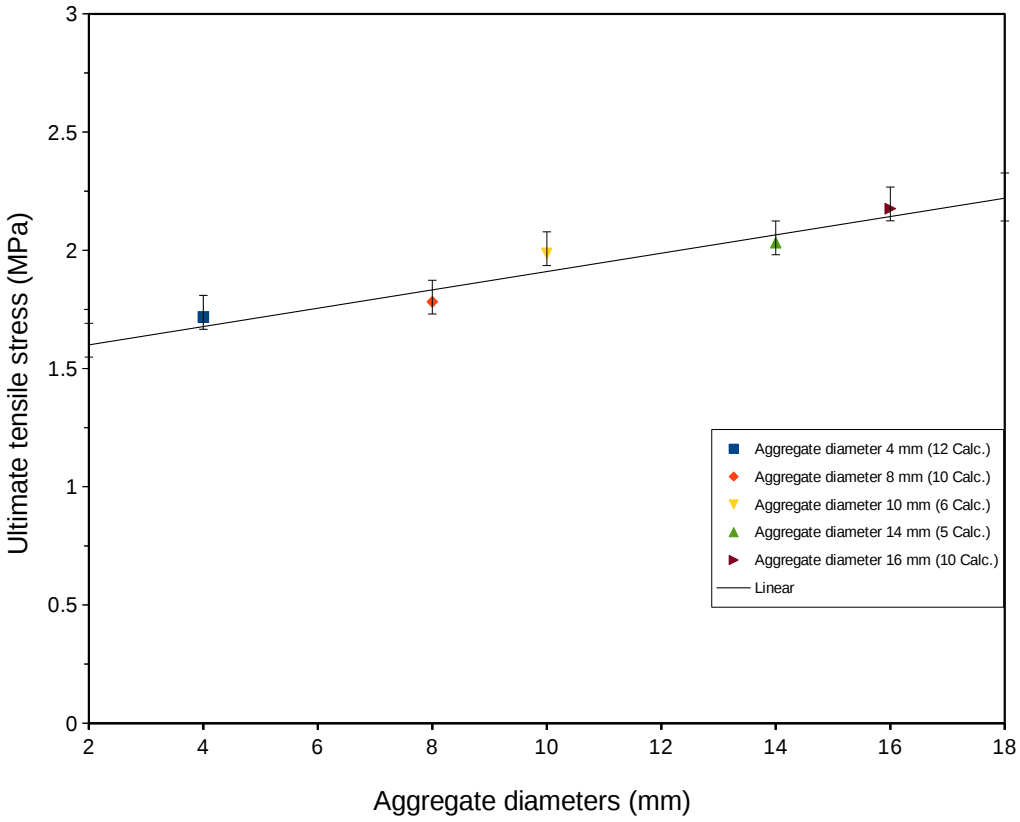

Figure 3.8: The effect of aggregate diameters on the ultimate tensile stress (volume of fraction is 20 %) with five aggregate diameters ranging from 4 to 16 mm. Simulations are carried out for five cylinder specimens.

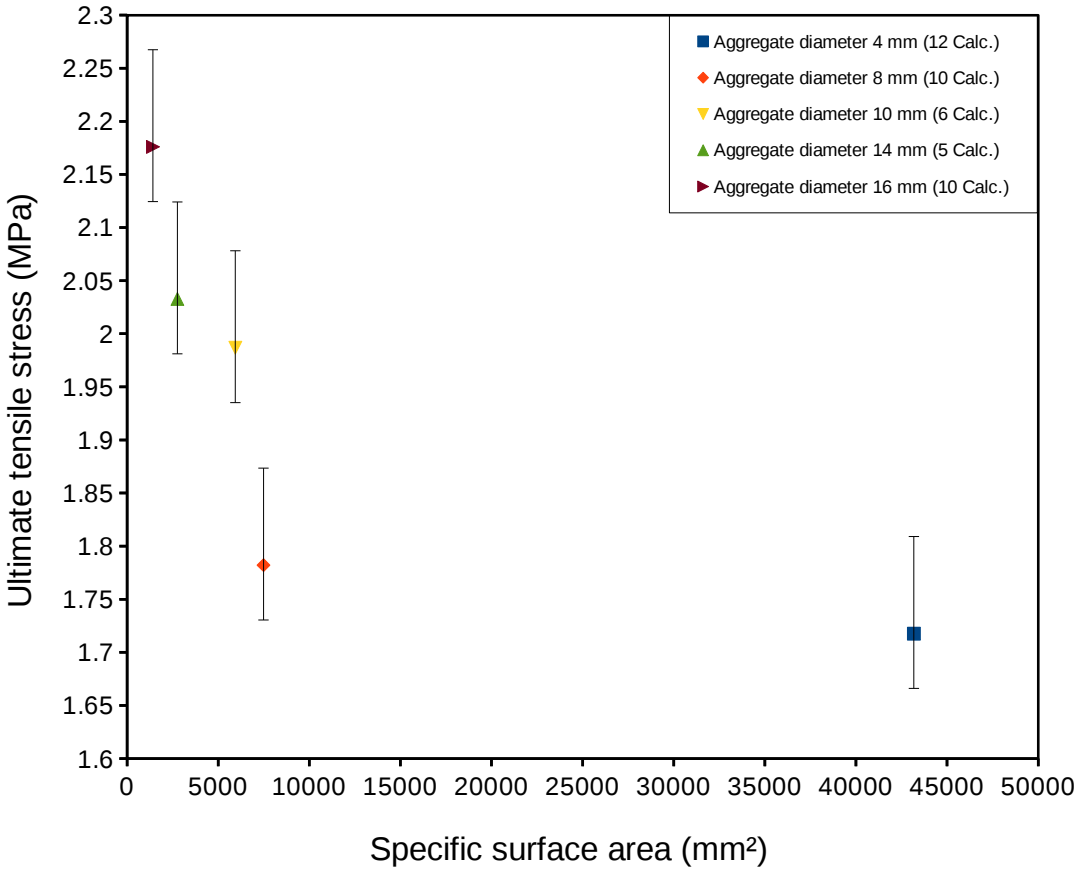

Figure 3.9: The effect of the specific area of aggregate on the ultimate tensile stress (volume of fraction is 20 %) with five aggregate diameters ranging from 4 to 16 mm. Simulations are carried out for five cylinder specimens.

and morter is weaking the matrix, therefore the crack paths were changed when it met with aggregate particles around the aggregate. While, the effect of aggregates size had a reverse tendency, i.e. the tensile strength decreased with the increasing of aggregates size ([Saouma et al., 1991], [Li et al., 2004b]).

3.2.2.3 Total dissipated energy

The mechanical behavior and fracture energy can be calculated for each simulation depending upon the correlation in the curve shown in Figure (3.10), by integrating the area under the curve (stress-imposed displacement). We obtained three phases: the first one is introduced from the micro cracks and the second one is introduced from connecting the micro cracks and the last phase is introduced from crack opening only. All areas under curves refer to dissipation energy while the areas after peak load refer to fracture energy. According to the present results, there is an increasing trends of the fracture energy with the increasing aggregate diameter, which is confirmed with the standard of CEB-FIP model code in [Code,]. Furthermore, the specific surface area of aggregate is influenced significantly on the fracture energy.

Figure (3.11) shows the fracture energy as a function of surface area for five cylinder specimens are simulated, it shows the effect of aggregate diameter on the fracture energy, i.e. the increasing of the aggregate diameter leads to an increase in the fracture energy. However, this can be explained that the behavior is similar for the dissipation energy as shown in Figure (3.12).

The numerical results explain the mechanical behavior under tensile loading for the increasing fracture energy and dissipation energy. The influence of the aggregate diameter on the dissipation energy is shown in Figure (3.10). The area under curves refers to the total dissipated energy, as the aggregate diameter becomes bigger, the energy is significantly increased. Furthermore, the slope of the curves

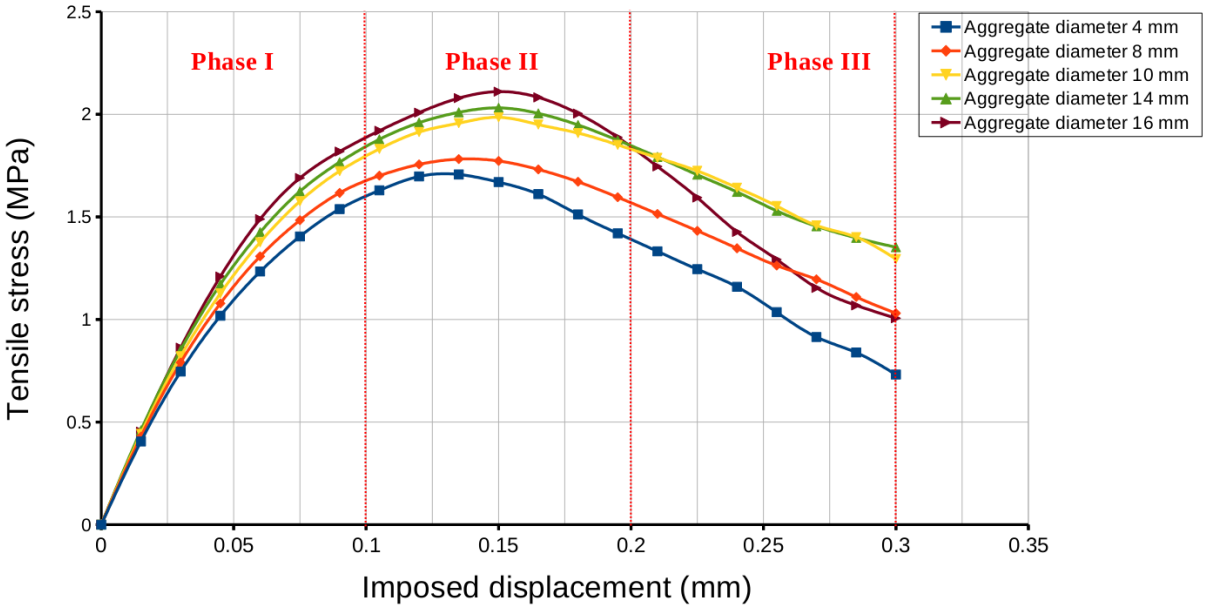

Figure 3.10: Relationship between tensile stress and imposed displacement for five cylinder specimens are simulated.

for aggregate diameters 16 and 14 mm respectively are wider than the slope of the curves for the aggregate diameters 10, 8 and 4 mm respectively after the maximum load. On the other hand, the degree of heterogeneity is based on the aggregate diameter, it means the increasing of heterogeneity with aggregate diameter 16 mm resulted a largest value of fracture energy. Therefore the aggregate diameter 4 mm resulted the lowest value of the energy. Our results are also consistent with several previous studies for examples, Petersson [Petersson, 1980], who shows that the fracture energy increases by 13 % with the type of aggregate and with the volume of fraction is 50 %, in this study, it was found that the increasing of fracture energy was based on type of aggregate, i.e. when the materials are stronger with the gravel aggregate will result a largest fracture energy, while the weaker materials with the limestone aggregate will result a smallest fracture energy. Mihashi et al. [Mihashi et al., 1989b] explained that the rate of the increasing of fracture

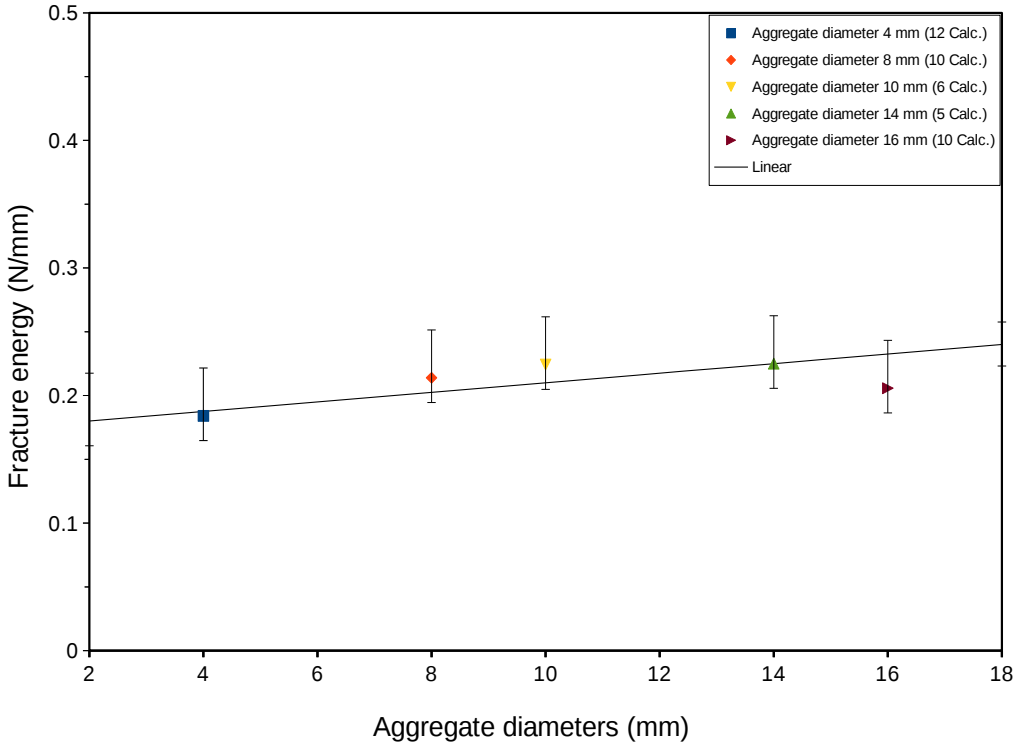

Figure 3.11: The effect of aggregate diameters on the fracture energy (volume of fraction is 20 %) with five aggregate diameters ranging from 4 to 16 mm. Simulations are carried out for five cylinder specimens.

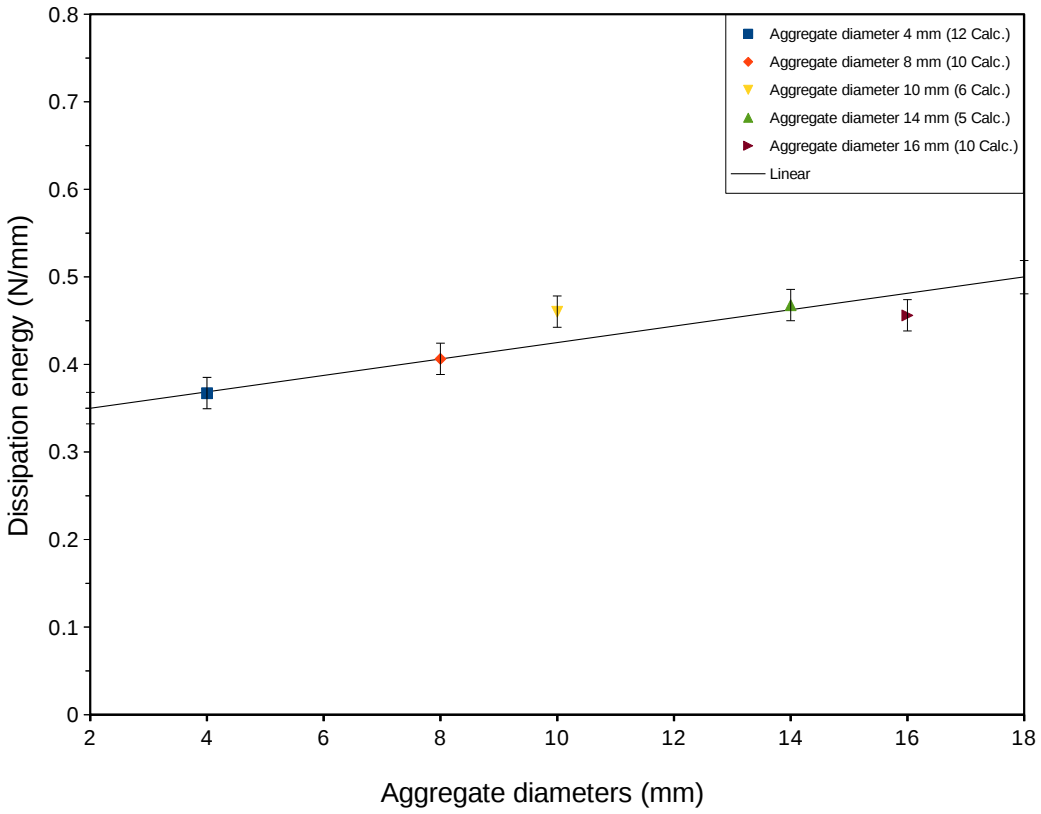

Figure 3.12: The effect of aggregate diameters on the dissipation energy (volume of fraction is 20 %) with five aggregate diameters ranging from 4 to 16 mm. Simulations are carried out for five cylinder specimens.

energy depends on degree of heterogeneity and the strength of matrix, i.e. the increasing of aggregates size leads to increase in the fracture energy by 40 % with volume of fraction 44 %. In addition, Mihashi et al. [Mihashi et al., 1991] observed the increasing of fracture energy was 46 % with the increasing of aggregates size with volume of fraction 44 %. The reason was the larger aggregates had created a wider fracture process zone.

In addition, Tasdemir et al. [Tasdemir et al., 1996] presented that an increase of the fracture energy by 34 % when there was an increase of the aggregates size with volume of fraction was 49 % this led to an increase of the fracture energy due to the availability of more brittle matrix when using bigger aggregates size and more volume of fraction, also Rao et al. [Rao and Prasad, 2002] pointed out that the energy was increased by 35 % for concrete without silica fume and was increased by 84 % for concrete with silica fume when the increased aggregates size with volume of fraction 44 %, the explanation of this increasing was influenced by the aggregates size and the size of nonhomogeneity when used largest aggregates size, it cased to a more stiffer materials also a higher bond strength between aggregate and the cement paste. Li et al. [Li et al., 2004b] carried out that the maximum aggregates size influences significantly upon the fracture energy, in another word, the increasing of the fracture energy by 17 % with the increasing of the aggregates size, it presented that this increasing was caused by the interlock force between the surface of the aggregate and the cement paste. However, in our study the increasing of both the fracture and dissipation energy are 12 and 24 %, respectively with the increasing of the aggregate diameter by using the volume of fraction to be 20 %.

3.2.3 Numerical simulations of the tensile splitting test: investigation of the volume fraction of aggregate

This section presents nine finite element simulations to investigate the behavior of concrete under diametral compression load in the context of the Brazilian splitting test. Nine cylinder specimens of concrete have been simulated with dimensions 50 x 110 mm of thickness and diameter, respectively. In addition, the effect of the volume fraction of aggregate and aggregates size on the mechanical behavior of heterogeneous material (such as concrete) are investigated. Three samples of representing the volume fractions of aggregate and another three samples of representing the sizes of aggregate were examined. The samples of representing the volume fractions were 10, 20 and 30 % volume fractions for each of the samples of representing the aggregates size at 10, 14 and 16 mm, respectively.

Figures (3.13, 3.14, 3.15) show the relation between the tensile stress and the crack opening at mid of specimens, can be observed a classic behavior of concrete under tensile stress. However, the finding from this work is that the net influence of increasing the volume fraction of aggregate to the increase of the tensile stress. In addition, it can be seen a significant effect of the aggregates size on the tensile stress in Figures (3.16, 3.17, 3.18).

The summarize of mechanical properties for each phase, is given in Table (3.2) for aggregate diameters 10, 14 and 16 mm.

Table 3.2: Mechanical properties of materials, ($\boldsymbol{E, \sigma_u, G_u}$) modulus of elasticity, tensile stress and fracture energy. Volume fractions of aggregate **10, 20** and **30** %.

Cement paste	**Aggregate**	**Interface**
$\boldsymbol{E_{cem}}$ = 35 GPa	$\boldsymbol{E_{agg}}$ = 100 GPa	-
$\boldsymbol{\sigma_u}$ = 3 MPa	-	$\boldsymbol{\sigma_u}$ = 3 MPa
$\boldsymbol{G_u}$ = 80 J/m$^{\mathbf{2}}$	-	$\boldsymbol{G_u}$ = 80 J/m$^{\mathbf{2}}$

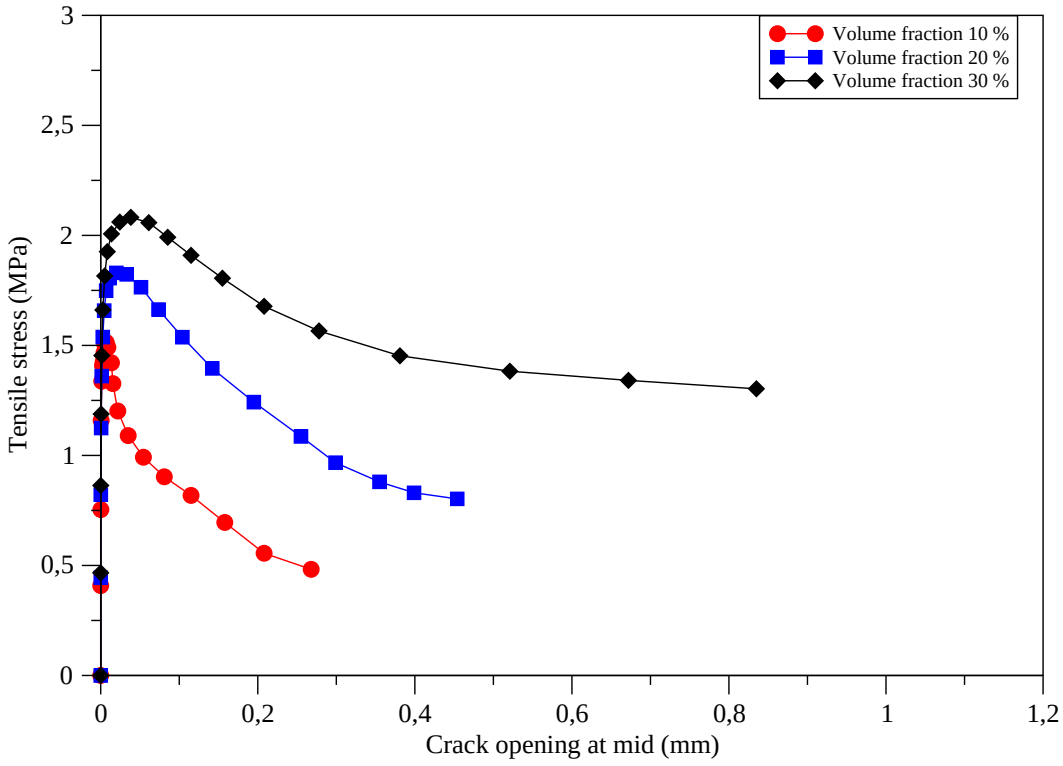

Figure 3.13: Relationship between the tensile stress and the crack opening at mid of specimens with aggregate diameter 10 mm and three volume fractions of aggregate 10, 20 and 30 %. Simulations are carried out for three cylinder specimens with dimensions 50 x 110 mm of thickness and diameter, respectively.

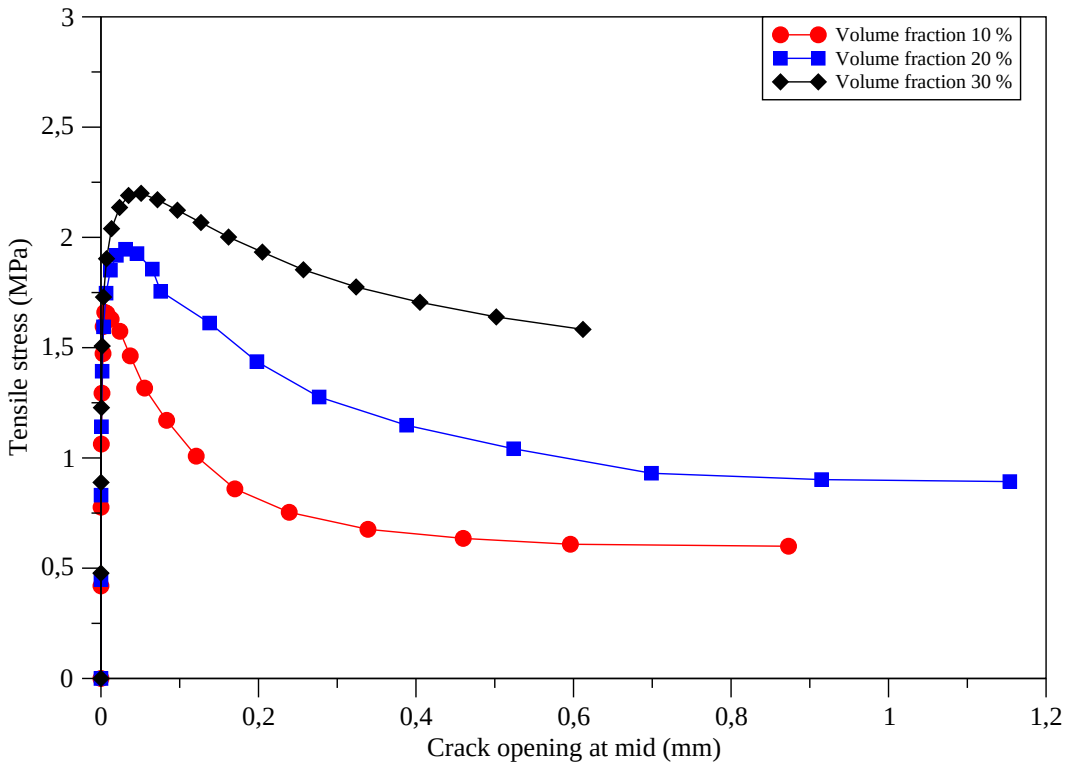

Figure 3.14: Relationship between the tensile stress and the crack opening at mid of specimens with aggregate diameter 14 mm and three volume fractions of aggregate 10, 20 and 30 %. Simulations are carried out for three cylinder specimens with dimensions 50 x 110 mm of thickness and diameter, respectively.

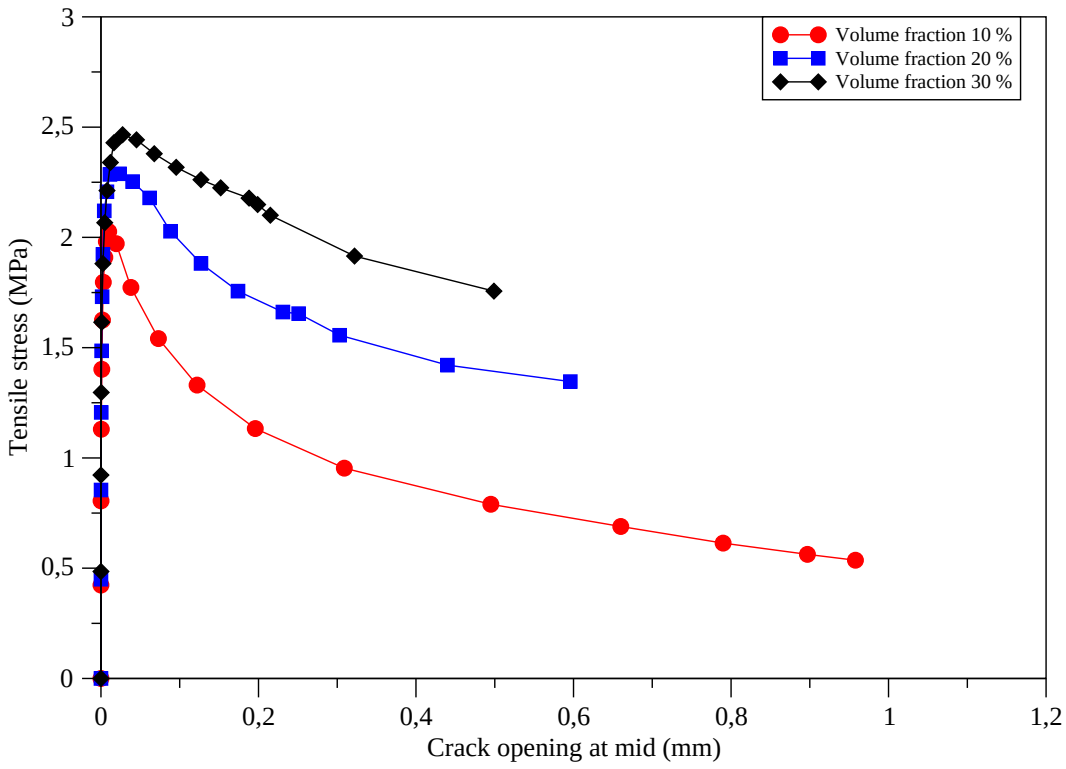

Figure 3.15: Relationship between the tensile stress and the crack opening at mid of specimens with aggregate diameter 16 mm and three volume fractions of aggregate 10, 20 and 30 %. Simulations are carried out for three cylinder specimens with dimensions 50 x 110 mm of thickness and diameter, respectively.

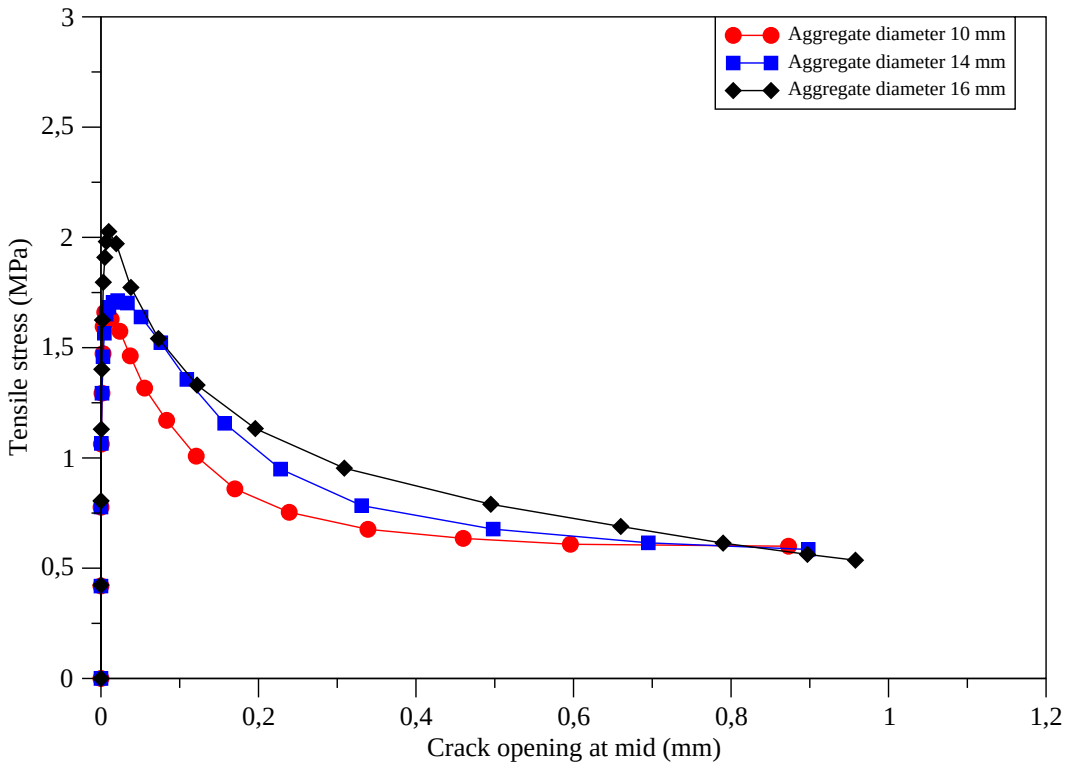

Figure 3.16: Relationship between the tensile stress and the crack opening at mid of specimens with volume fraction of aggregate 10 % and three diameters 10, 14, and 16 mm. Simulations are carried out for three cylinder specimens with dimensions 50 x 110 mm of thickness and diameter, respectively.

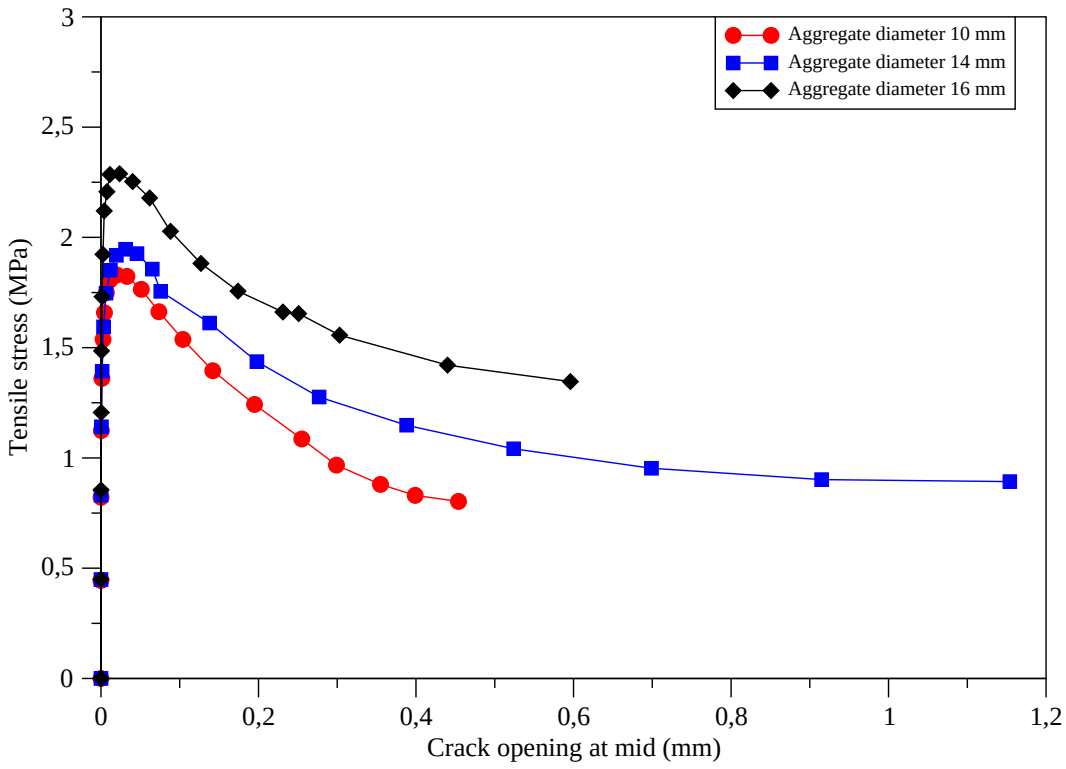

Figure 3.17: Relationship between the tensile stress and the crack opening at mid of specimens with volume fraction of aggregate 20 % and three diameters 10, 14, and 16 mm. Simulations are carried out for three cylinder specimens with dimensions 50 x 110 mm of thickness and diameter, respectively.

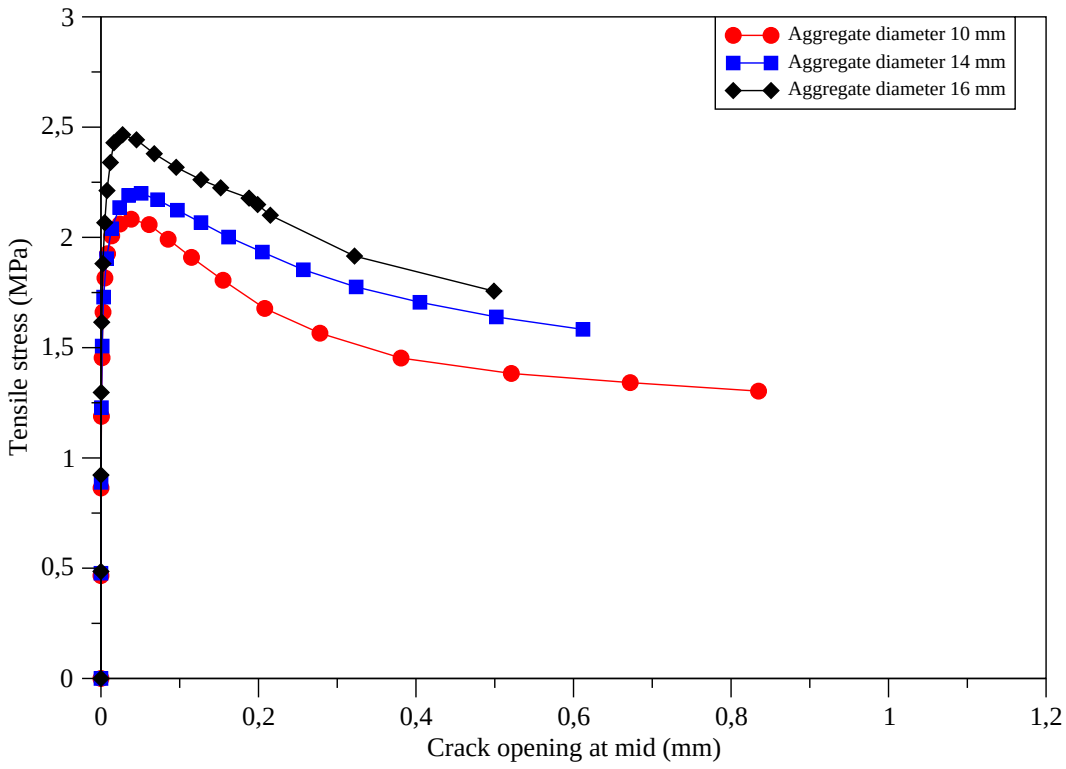

Figure 3.18: Relationship between the tensile stress and the crack opening at mid of specimens with volume fraction of aggregate 30 % and three diameters 10, 14, and 16 mm. Simulations are carried out for three cylinder specimens with dimensions 50 x 110 mm of thickness and diameter, respectively.

3.2.3.1 Ultimate crack opening

In this section, there is a focus to investigate the effect of the volume fraction and the aggregates size on the ultimate crack opening which is induced from the diametral loading. A meso-scale model is assigned the characterisation of the crack opening such as its dimensions, path and position. The numerical results of simulations are pointed out, there is a significant affecting relation between the volume fraction and the ultimate crack opening. In another word, there is an increase of ultimate crack opening with the increasing of the volume fraction of aggregate. To explain this indication, the volume fraction is larger (30 %), the interface zone will be more zone. In addition, the mechanism behavior of the heterogeneous material depends on the debonding force at the interface zone. Thus, as this zone is known to have reduced the mechanical bond strength between the cement paste and the aggregate. The second conception, when the volume fraction of aggregate 30 % is used, it led to a reduction in the spacing between the aggregate particles with taking into account the aggregates size is constant.

There are little studies had demonstrated the concerns about the influence of the volume fraction of aggregate on the crack width of concrete. Li et al. [Li et al., 2004b] observed the increasing of the critical crack width ($\boldsymbol{w_c}$) for dam concretes with the increasing the volume fraction of aggregate from 48 % to 69 %. While there are many studies that support the idea concerning the influence of the aggregates size on the mechanical behavior of concrete such as the crack width and its orentation and position of crack. Elices et al. [Elices and Rocco, 2008] presented the critical crack opening ($\boldsymbol{w_c}$) was increased as according to the aggregates size. Mihashi et al. [Mihashi et al., 1991] found the influence of the aggregates size on the critical crack opening for normal concrete, it means the increase of the aggregates size led to an increase the critical crack opening, high degree of heterogeneity that caused this development when used larger aggregates size than the smallest

aggregates size. Li et al. [Li et al., 2004b] offered the increasing of the critical crack was based on the aggregates size for dam concrete, therefore the specimens with larger aggregates size were more brittle than the specimens with smallest aggregate.

The numerical results for the ultimate crack opening which obtained at the peak tensile stress by simulating the Brazilian splitting tensile test for three volume fractions and three sizes of aggregate are shown in Figure (3.19).

Figures (3.20-3.25) show 3D simulation for three groups of cylinder specimens have been simulated in front and isometric views, with three sizes of aggregate. It can be noticed that the path of crack is more tortuosity in the specimens with the largest aggregate diameter, i.e. the orientation of crack varied when it connects with the aggregate particles, to explain this behavior, the cracks position are not only at the cement paste but also at the interface zone between the aggregate and cement paste. All simulations carried out at the final step simulation.

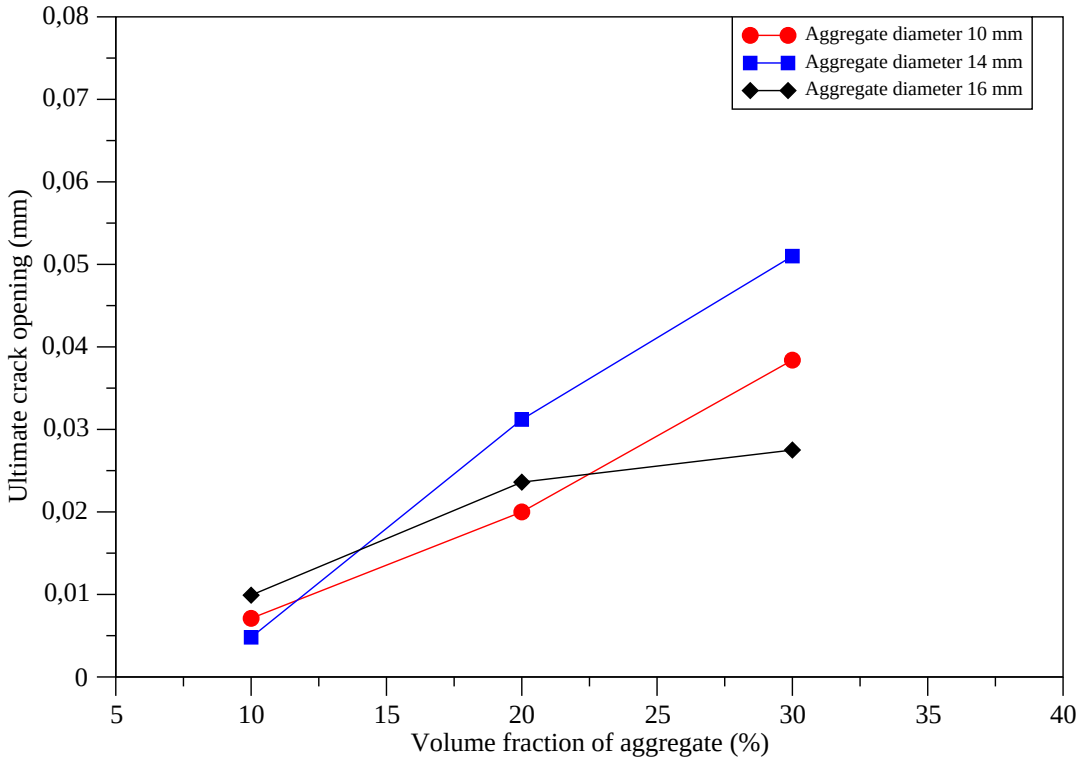

Figure 3.19: The effect of volume fraction and aggregates size on the ultimate crack opening with three aggregate diameters ranging from 10 to 16 mm. Simulations are carried out for nine cylinder specimens with dimensions 50 x 110 mm of thickness and diameter, respectively.

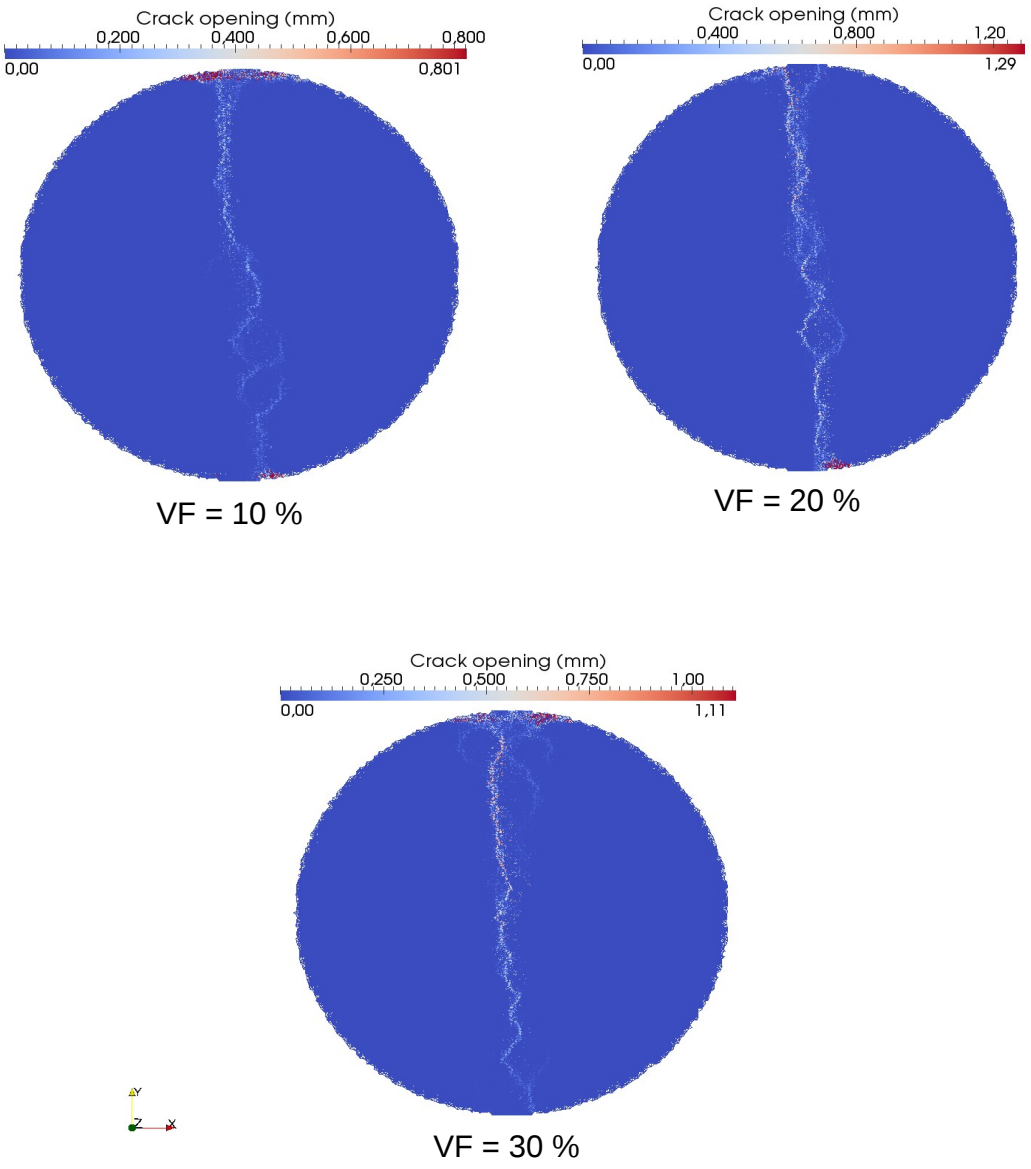

Figure 3.20: 3D front view of three cylinder specimens that are simulated with crack opening with aggregate diameter 10 mm. The specimens have dimensions 50 x 110 mm of thickness and diameter, respectively.

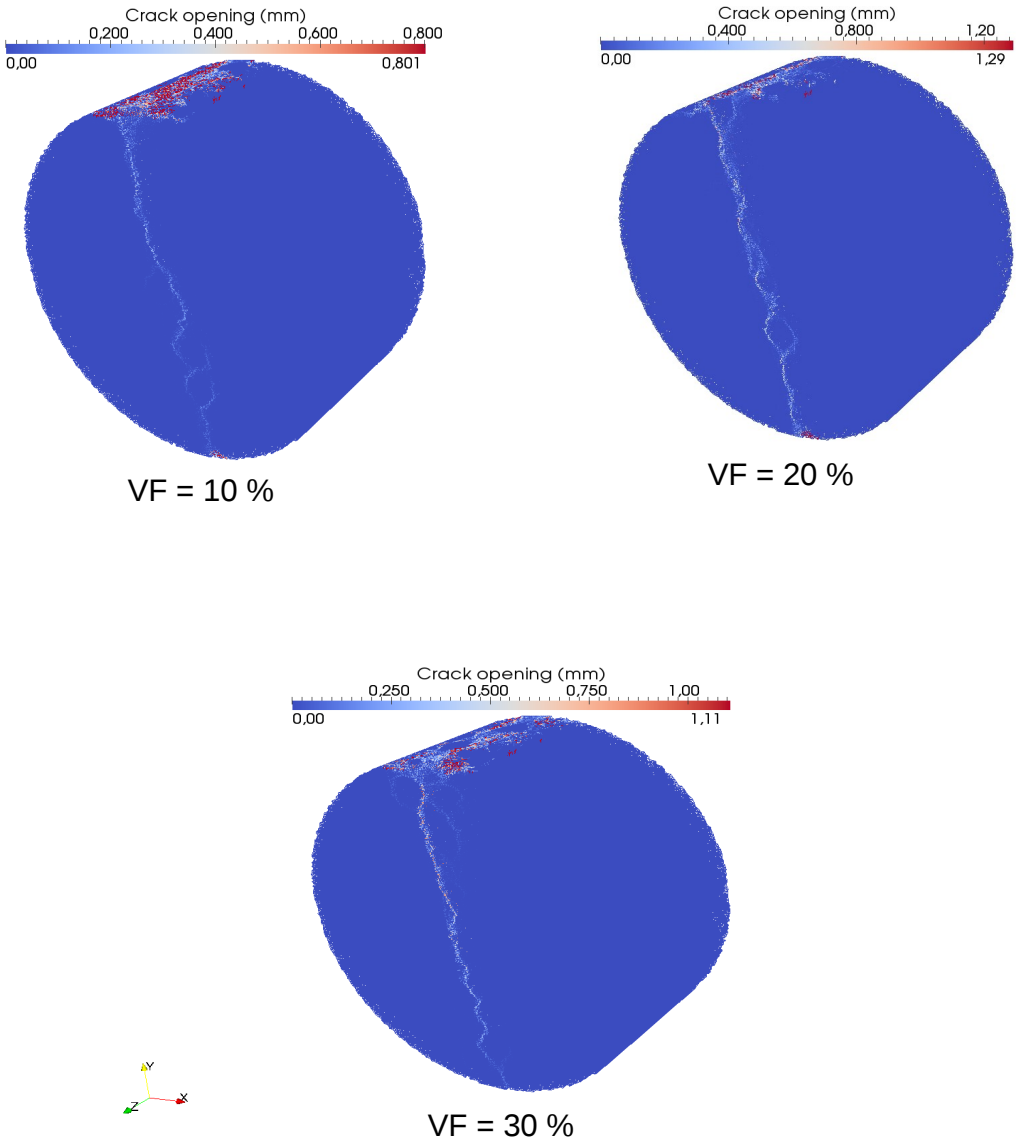

Figure 3.21: 3D isometric view of three cylinder specimens that are simulated with crack opening with aggregate diameter 10 mm. The specimens have dimensions 50 x 110 mm of thickness and diameter, respectively.

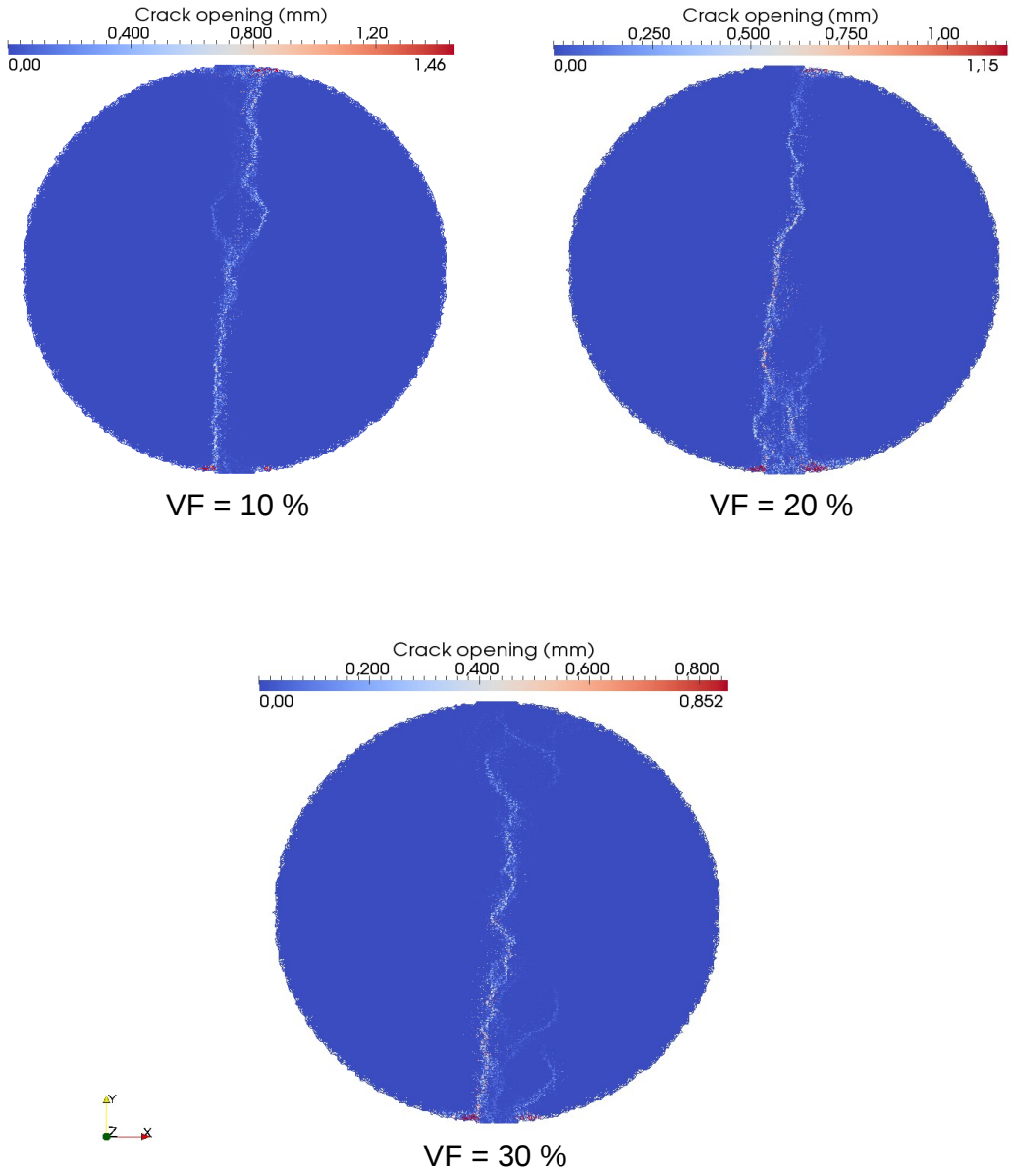

Figure 3.22: 3D front view of three cylinder specimens that are simulated with crack opening with aggregate diameter 14 mm. The specimens have dimensions 50 x 110 of thickness and diameter, respectively.

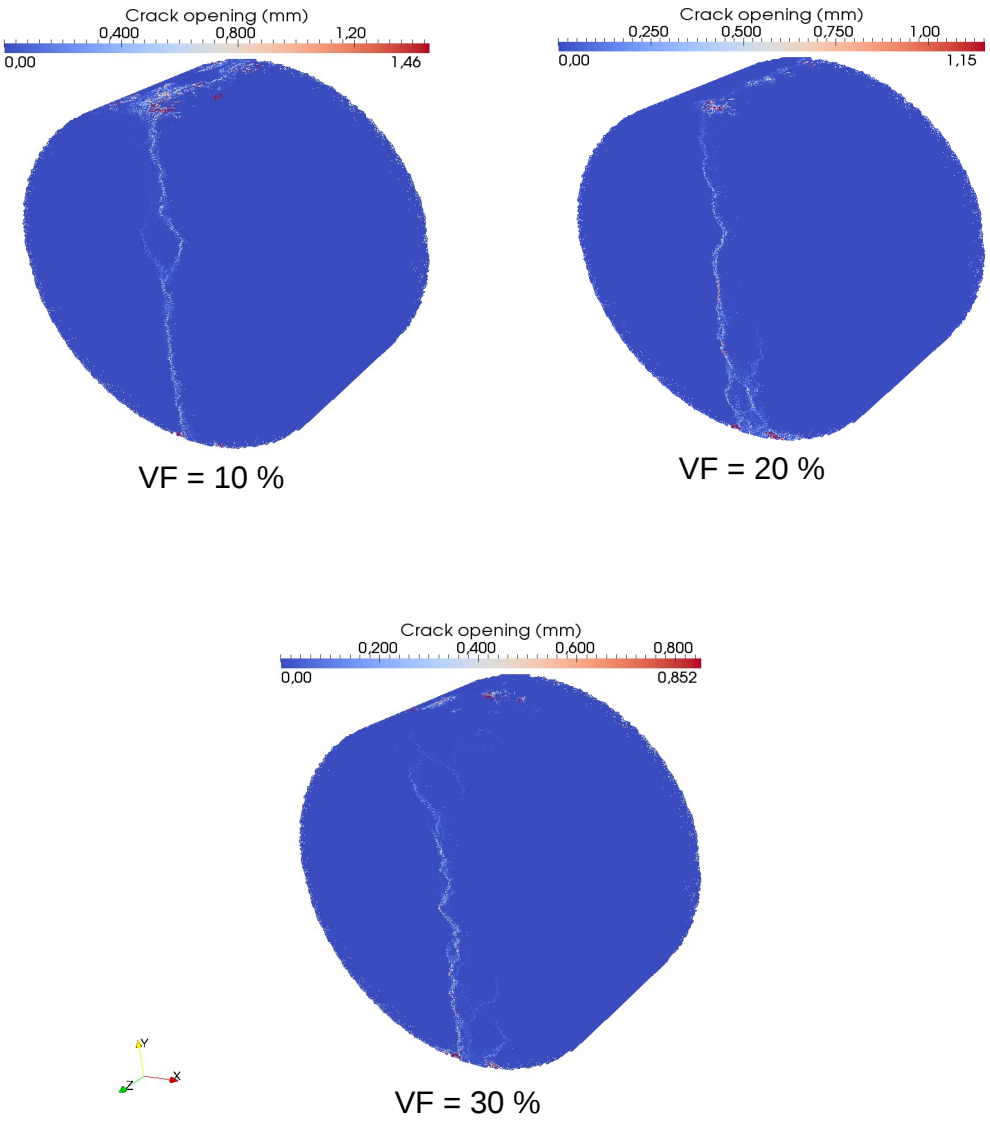

Figure 3.23: 3D isometric view of three cylinder specimens that are simulated with crack opening with aggregate diameter 14 mm. The specimens have dimensions 50 x 110 mm of thickness and diameter, respectively.

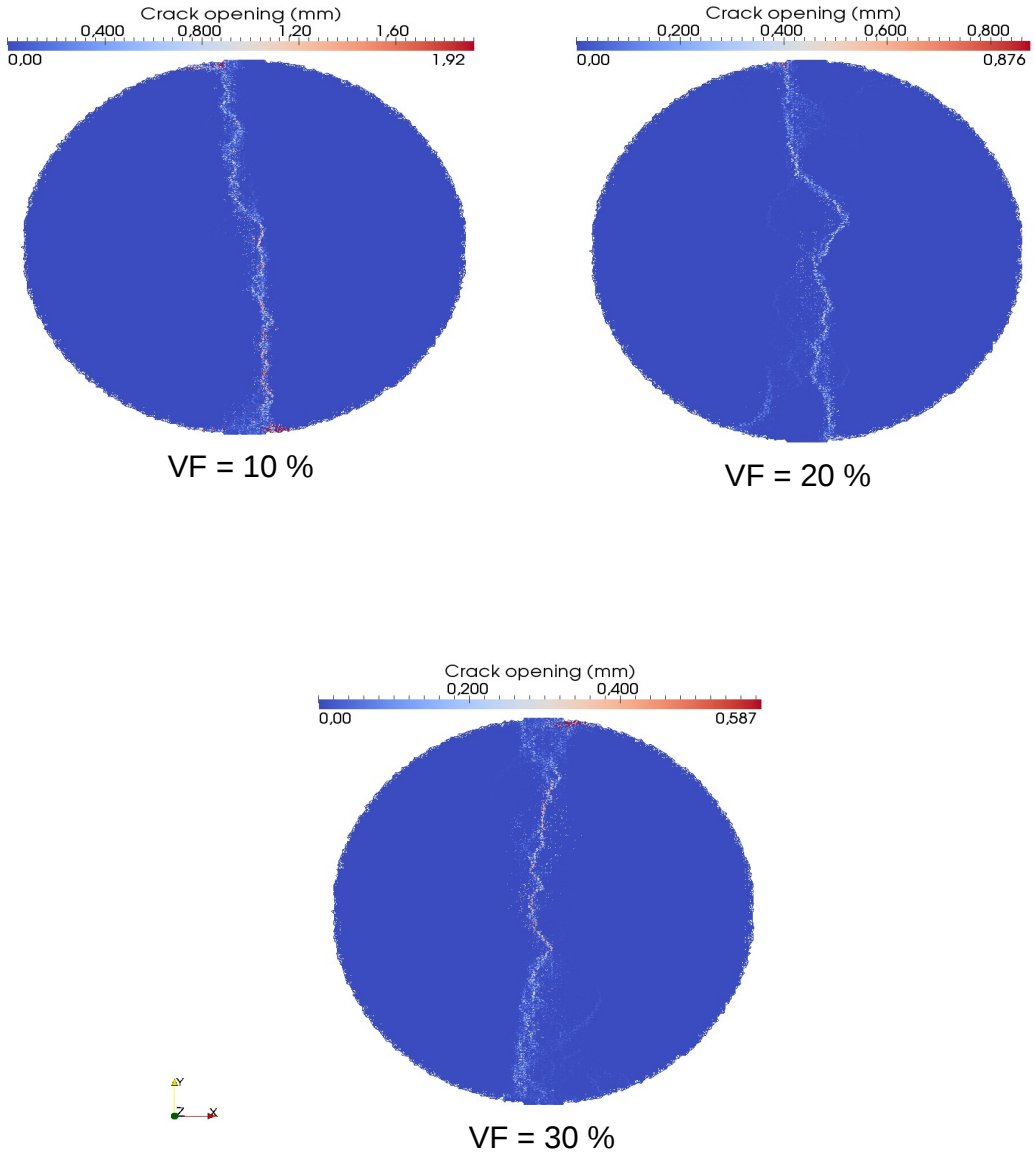

Figure 3.24: 3D front view of three cylinder specimens that are simulated with crack opening with aggregate diameter 16 mm. The specimens have dimensions 50 x 110 mm of thickness and diameter, respectively.

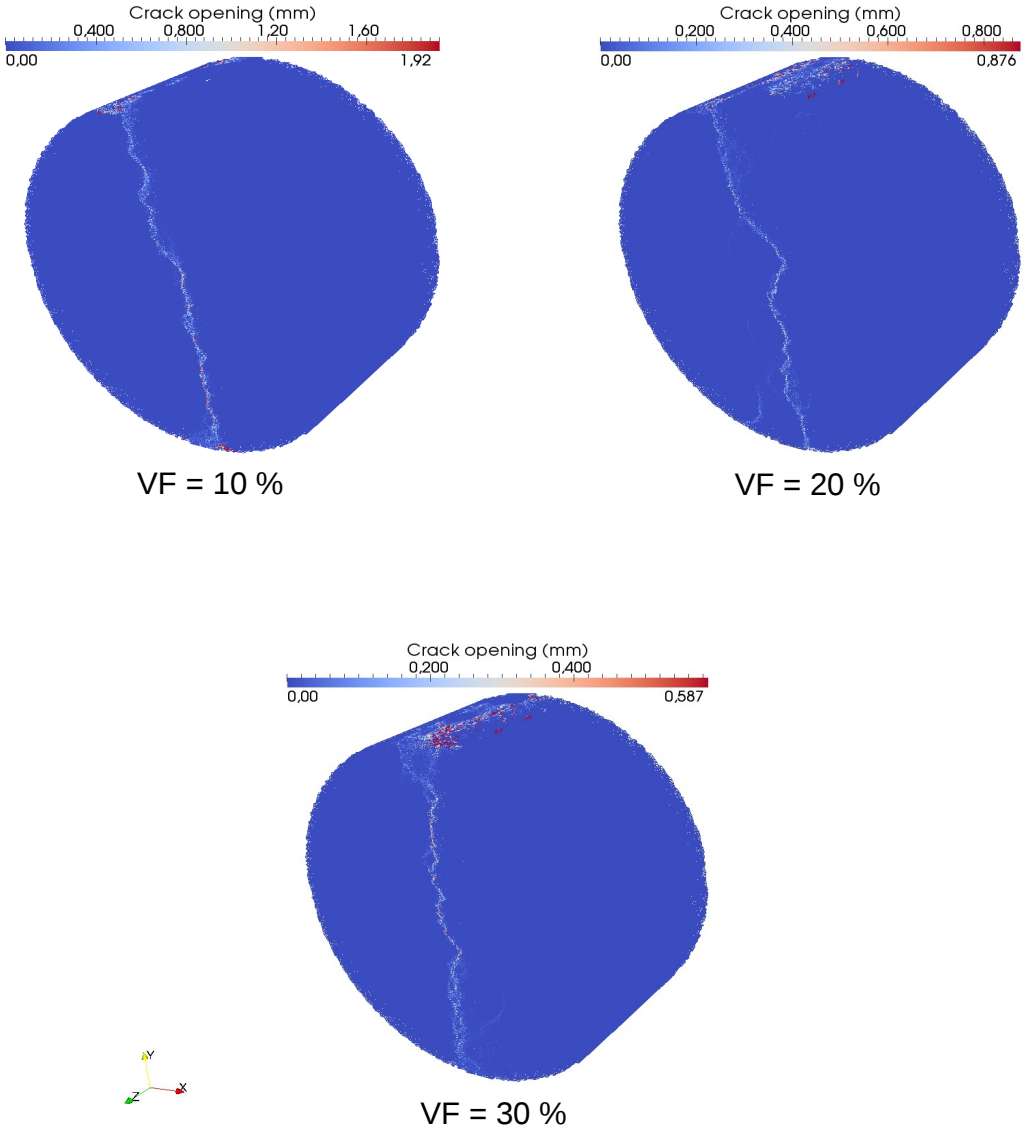

Figure 3.25: 3D isometric view of three cylinder specimens that are simulated with crack opening with aggregate diameter 16 mm. The specimens have dimensions 50 x 110 mm of thickness and diameter, respectively.

3.2.3.2 Macroscopic ultimate tensile stress

The influence of the volume fraction of aggregate on the ultimate tensile stress has been studied using three percentages of volume fraction 10, 20 and 30 % with three sizes of aggregate 10, 14 and 16 mm. The numerical simulations results show, that the ultimate tensile stress is increasing with the increasing of volume fraction of aggregate, also we noted that this increase depends on the aggregates size. This behavior can be explained by saying that, the heterogeneity of material with volume fraction 10 % is higher than those specimens with volume fraction 30 %. Furthermore, it has been observed that the specimen cylinders with larger size of aggregate are stronger than the specimens with smaller aggregate, i.e. the bonding strength between the aggregate particles and the cement paste depends on the aggregates size.

Figures (3.26) and (3.27) show the effect of the volume fraction and the aggregates diameter on the ultimate tensile stress, the relation between the specific surface area of aggregate with ultimate tensile stress. As have been shown, the ultimate stress increases as the volume fraction and aggregates size increase.

The influence of the volume fraction and the aggregates size on concrete behavior were reported from some of researchers, Burcu et al. [Akcay et al., 2012] concluded in their study, the splitting tensile stress increased, when increasing the volume fraction of aggregate. Tasdemir et al. [Tasdemir et al., 1996] carried out the effects of the volume fraction, increasing split tensile strength due to the increase of volume fraction of aggregate. Bayramov et al. [Bayramov et al., 2004] pointed out that increasing of splitting tensile strength was 37 % due to an increase in the volume of fraction from 40 to 66 %. They got that the specimens were stronger when the volume fraction of aggregate was higher. Ward M.A. [Ward, 1969] found the influence of the volume fraction on the tensile strength of concrete, i.e. the increasing of tensile strength with the increasing of the volume fraction of

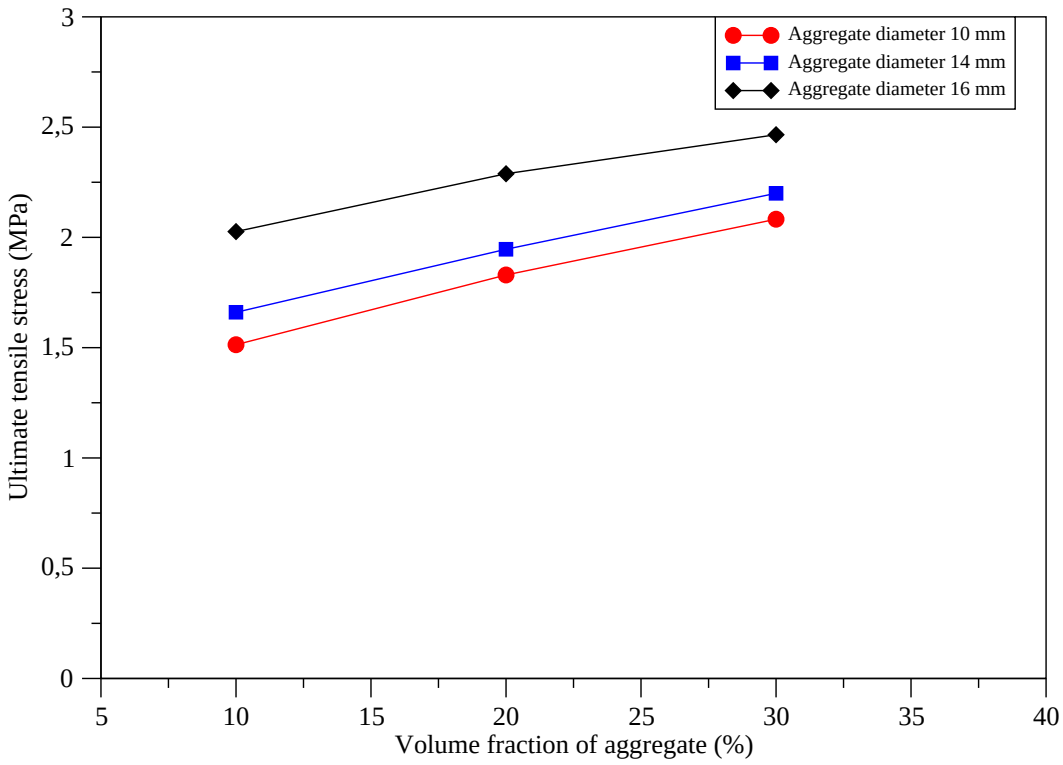

Figure 3.26: The effect of volume fraction of aggregate on the ultimate tensile stress with three aggregate diameters ranging from 10 to 16 mm. Simulations are carried out for nine cylinder specimens with dimensions 50 x 110 mm of thickness and diameter, respectively.

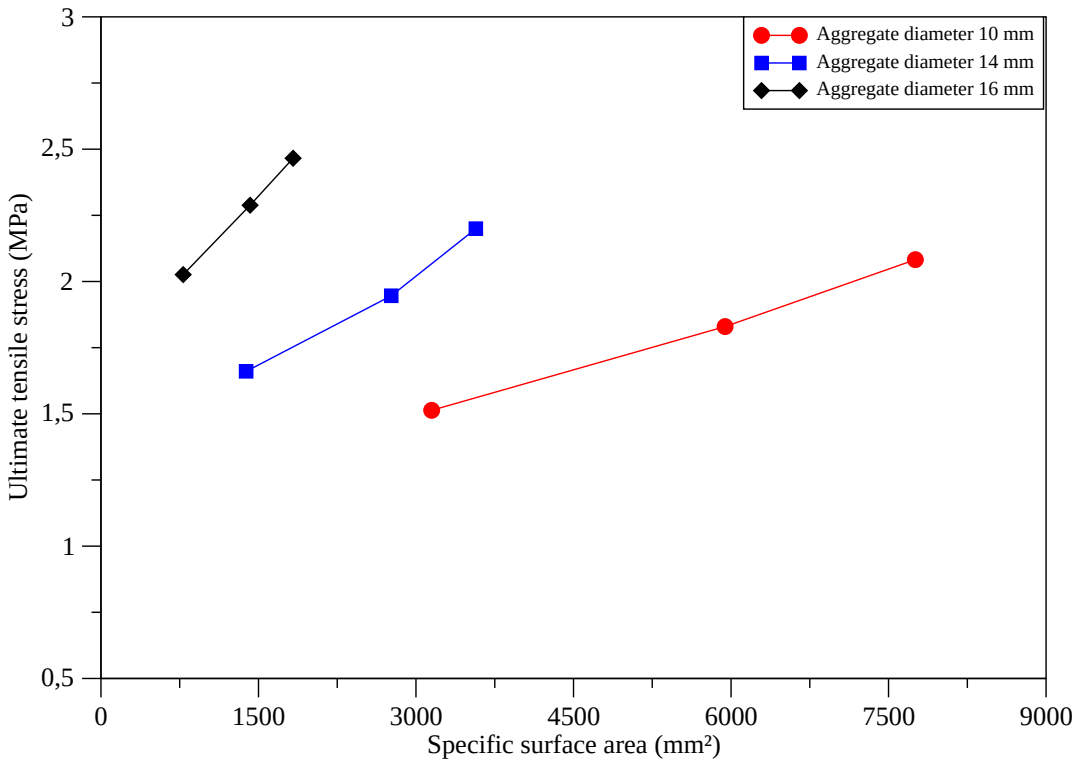

Figure 3.27: The effect of specific surface area of aggregate on the ultimate tensile stress with three volume fractions of aggregate 10, 20 and 30 %. Simulations are carried out for nine cylinder specimens with dimensions 50 x 110 mm of thickness and diameter, respectively.

aggregate.

While, Saouma et al. [Saouma et al., 1991] noted the opposite behavior for the splitting tensile loading with the volume fraction. On the other hand, the increasing of the volume fraction from 44 to 62 % has led to a decrease of the splitting tensile stress from 2.81 to 2.41 MPa. Johnston [Johnston, 1970] presented the experimental study by using the basalt aggregate, they observed the decreasing of the tensile strength with the increasing of the volume fraction.

Stock et al. [Stock et al., 1979] reported the influence of the volume fraction on the tensile strength, it got two indications: the first one was decreasing of the tensile strength by 25 % when the increasing of volume fraction from 0 to 20 % and the second indication was the increasing of tensile strength 34 % with the increasing of the volume fraction from 40 to 80 %.

However, some authors explained the effect of the aggregates size on the mechanical behavior of concrete such as tension or compression stress. Rao et al. [Rao and Prasad, 2002] reported that increasing the maximum aggregates size from 4.75 to 20 mm had led to an increase in the splitting tensile stress from 2.39 to 3.06 MPa, they noted that the surface area of aggregate was influenced on the debonding force at the interfaces zone between the aggregate and the cement paste, i.e. the debonding force was higher when the larger aggregates size was used. Chen et al. [Chen and Liu, 2004] pointed out during there experimental work that, the tensile stress was 2.04 MPa for the mortar, while it varied from 2.61 to 2.58 MPa when the aggregates size was ranged from 5-10 mm to 16-20 mm. That explained that the interfaces were influenced on the bonding stress for the high-strength concrete, that means the specimens have a larger aggregate are stronger than the mortar specimens, therefore the tortuosity of crack is increasing when it is connecting with the aggregate particles. Elices et al. [Elices and Rocco, 2008] obtained opposite results for the influence of aggregates size, i.e. the tensile strength for the

matrix was higher than the concrete specimens. The indication that, increasing the aggregates size led to decrease of the tensile stress was reported by Tasdemir et al. [Tasdemir et al., 1996] and Saouma et al. [Saouma et al., 1991] and Li et al. [Li et al., 2004b] and Petersson in [Petersson, 1980] and Johnston in [Johnston, 1970]. Otherwise, Mihashi et al. [Mihashi et al., 1991] offered the effect of the aggregates size on the tensile stress, they had explained that there was no clear behavior about the influence of the aggregates size on the tensile stress of concrete.

3.2.3.3 Total dissipated energy

In this section, two different parameters will be presented: the first one is the volume fraction of aggregate 10, 20 and 30 % and the second one is the aggregate diameter 10, 14 and 16 mm.

The fracture energy of the heterogeneous material can be calculated from measuring the surface area under the curve in Figure (3.2(b)), as above mentioned see section (3.2.2.3). In addition, this section offers the relationship between the volume fraction of aggregate with the dissipation energy which can be calculated depending on the relation of the stress-strain curve in Figure (3.2).

The mechanical-numerical results gave the formations that the correlation between the volume fraction and the aggregates size with the fracture energy of concrete. Also, the condition of this correlation is under tension stress for nine cylinder specimens are simulated in the context of the Brazilian splitting tensile test.

Figure (3.28) shows the fracture energy from the tensile stress versus strain curve for nine cylinder specimens are simulated, it can be seen that increasing the fracture energy with the increasing of that two parameters (volume fraction, aggregates size). In addition, as shown in Figure (3.29), the relationship between the dissipation energy with the volume fraction of aggregate for three aggregate

diameters 10, 14 and 16 mm, can be seen affecting the dissipation energy with the increasing two parameters (volume fraction, aggregates size), i.e. the results show an increase with the increasing volume fraction and aggregates size.

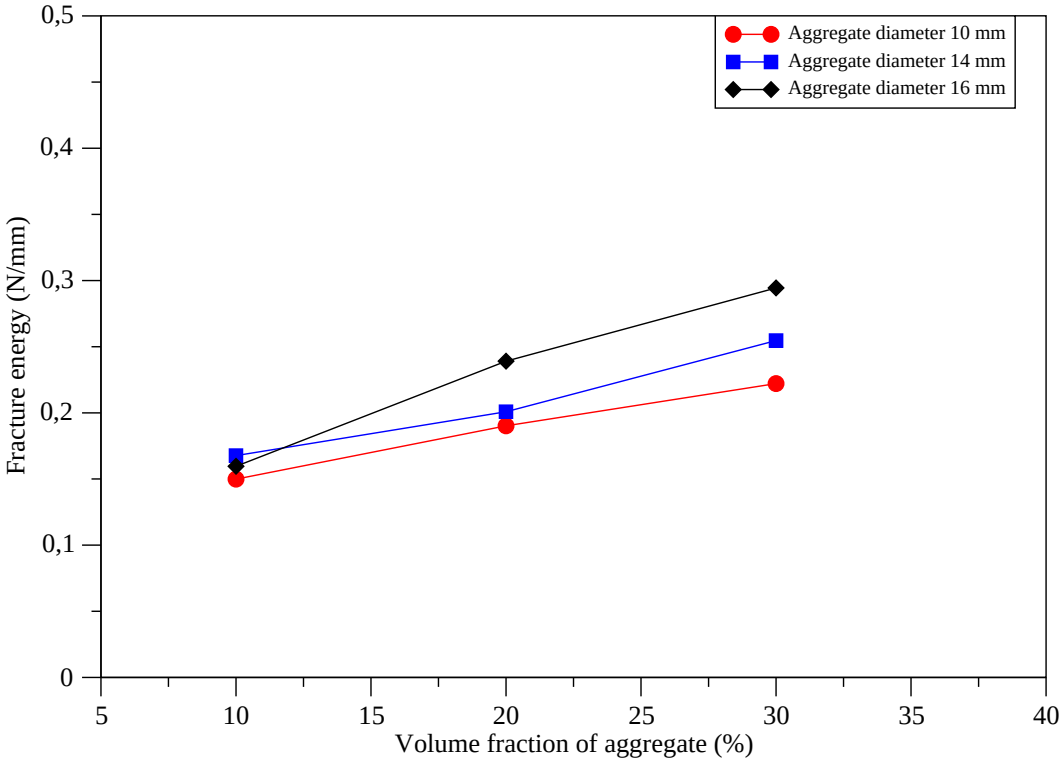

Figure 3.28: The effect of volume fraction and aggregates size on the fracture energy with three volume fractions of aggregate 10, 20 and 30 % and three aggregate diameters 10, 14 and 16 mm. Simulations are carried out for nine cylinder specimens with dimensions 50 x 110 mm of thickness and diameter, respectively.

These results are compared with the experimental results of other authors,

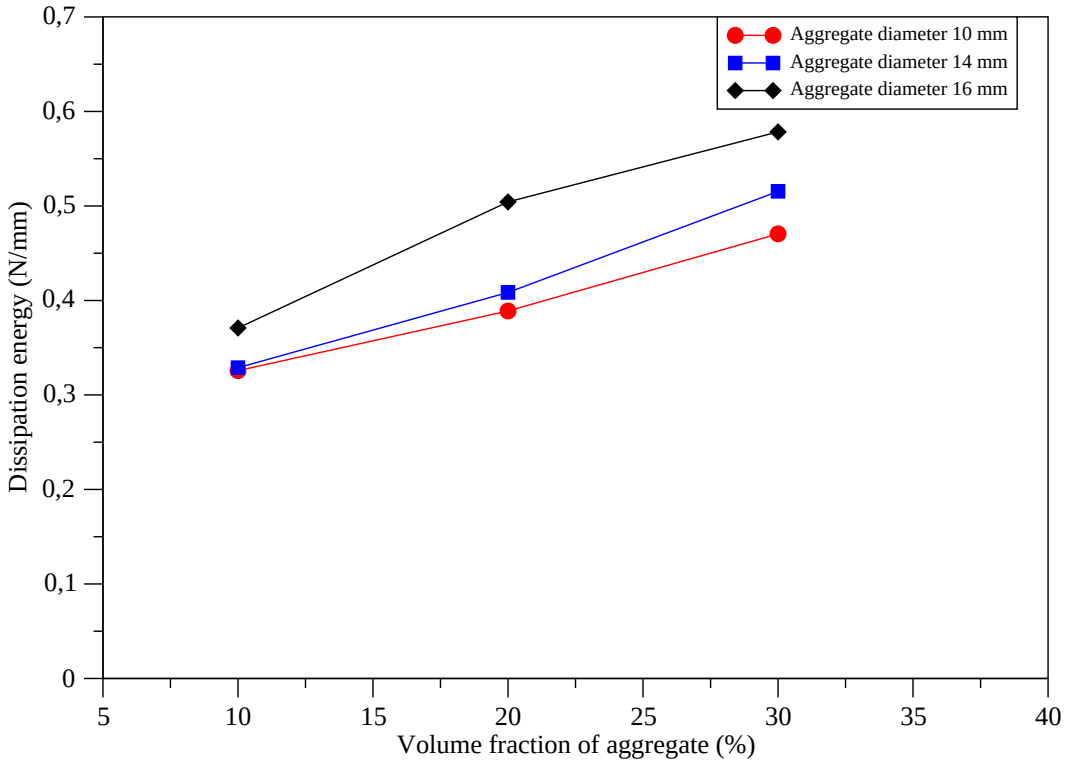

Figure 3.29: The effect of volume fraction and aggregates size on the dissipation energy with three volume fractions of aggregate 10, 20 and 30 % and three aggregate diameters 10, 14 and 16 mm. Simulations are carried out for nine cylinder specimens with dimensions 50 x 110 mm of thickness and diameter, respectively.

the results were agreement. Petersson in [Petersson, 1980] pointed out that the increasing of the volume fraction led to increase the fracture energy. Saouma et al. [Saouma et al., 1991] reported that the augmentation volume fraction of aggregate from 44 to 62 % caused to increase the fracture energy 31 %. Amparano et al. [Amparano et al., 2000] investigated the effects of aggregate content on the fracture energy by experimental study, in addition, they noted the fracture energy was decreased by 20 % as the volume fraction of aggregate increases from 45 to 55 %, however it increased by 35 % as the volume fraction of aggregate increased from 65 to 75 %, this results obtained under the conditions W/C ratio and the grading of aggregate were constants. Tasdemir et al. [Tasdemir et al., 1996] presented an experimental study and a meso-scale model to explain the influence of volume fraction of the aggregate on the fracture behavior of concrete under loading. Their results referred when the volume fraction varied from 0.0 to 0.6, the fracture energy was increased. Chen et al. [Chen and Liu, 2004] offered that the effect of volume fraction on the fracture properties of high performance concrete based on experimental work and it confirmed by the numerical study under meso level depended on the acoustic emission (AE) technique. They found that increasing the volume fraction of aggregate from 40 to 60 % resulted in an increase of the fracture energy for high-strength concrete. While, the fracture energy was decreased when the volume fraction increased from 60 to 80 %. For the low-strength concrete, the increase of the volume fraction caused to an increase of the fracture energy. The explanation of this indication was based on the strength of concrete, i.e. the bonding force at the interfaces between the aggregate and the cement paste was weaker than the force produced through the aggregate particles, thus the increase of the volume fraction means a higher interfaces around of aggregate particles and more a tortuosity of cracking, this indication produced a higher energy fracture, this explanation for low-strength concrete. However, the bond strength at the

interfaces was higher than the force produced through the aggregate particles for the high-strength concrete and the crack path through the aggregate particles in the same time, therefore when a higher volume fraction was used led to a decrease of tortuosity, i.e. a low energy fracture will be needed.

Furthermore, there is the influence of the aggregates size, there are many researchers discussed the relationship between the aggregates size and the fracture properties of concrete under service loads.

The influence of the aggregates size on the fracture energy was already discussed by Elices et al. [Elices and Rocco, 2008], they carried out that the bonding force between the aggregate and cement paste influenced significantly on the fracture energy. They found during a test made on concrete that the fracture energy was 35 J/m$^{\mathbf{2}}$ for the mortar, and the fracture energy was increased to 18 % when size 3 mm aggregate was used and this fracture energy increases 41 % when aggregate size 14 mm was used. This result agreed with the standard of CEB-FIP model code [Code,]. Kleinschrodt and Winkler in [Kleinschrodt and Winkler, 1986] had investigated that the fracture energy was 122.3 J/m$^{\mathbf{2}}$ when maximum aggregates size 8 mm was used, whereas it was 152.9 J/m$^{\mathbf{2}}$ when maximum aggregates size 16 mm was used. In addition, Zhang et al. [Zhang et al., 2005] observed the ranging of aggregates size from 7.5 to 22.5 mm led to an increase in the fracture energy to be 36 % for normal-strength concrete, whereas this increased to 26 % for high-strength concrete with aggregates size varied from 7.5 to 22.5 mm. Chen et al. [Chen and Liu, 2004] had explained that using the larger aggregates size caused to a higher fracture energy, and the mortar matrix was weaker than the aggregate particles, therefore more tortuosity of crack might apply when it is connected with the aggregate particles and more fracture energy is needed for the continuous path of crack. Saouma et al. [Saouma et al., 1991] demonstrated that the influence of the fracture energy by the aggregates size was based on the

roughness of the surface area of aggregate particles, on the other hand, the fracture energy increased to 31 % when the varying range of maximum aggregates size from 19 to 76 mm were used. Furthermore, Chen et al. [Chen and Liu, 2004] reported for high performance concrete, that the fracture energy was increased by 37 % when examined the mortar matrix and the concrete mixture with aggregates grading by 16-20 mm.

3.3 Meso-scale simulation of crack-induced permeability in the Brazilian splitting test

To investigate the coupling between crack opening and permeability, a numerical hydro-mechanical model is used. For readers interested in more details, a full description of the model, its numerical implementation and some examples can be found in [Jourdain et al., 2013]. For more details of numerical simulations, see **Appendix B**. Two investigations are given in this section. The first one is the interaction between crack opening and the permeability of fluids such as gas or water with the influence of aggregates size. The second one is the coupling between crack opening and permeability with the effect of the volume fraction of aggregate.

3.3.1 Hydro-mechanical coupling model

The coupling with permeability is made through a double porosity method. This method can also be found in [Djerbi et al., 2008] for diffusion problem in concrete, in [Zhou et al., 2006] for permeability problem in brittle rock and in [Dormieux and Kondo, 2004] in the framework of micromechanical model, meaning that the permeability of a cracked bar element is composed of two parts : the initial perme-

ability $\underline{\underline{\boldsymbol{k}}}^{\boldsymbol{i}}$ due to the initial permeability, and the crack permeability $\underline{\underline{\boldsymbol{k}}}^{\boldsymbol{c}}$. The total permeability is therefore $\underline{\underline{\boldsymbol{k}}}^{\boldsymbol{m}} = \underline{\underline{\boldsymbol{k}}}^{\boldsymbol{i}} + \underline{\underline{\boldsymbol{k}}}^{\boldsymbol{c}}$. Equation (3.4) is applied to each element with one going-through micro-crack and mass flow occurs parallelly to crack opening. We assume that the cracks are embedded into the porous medium and therefore connected to the pore network. In realistic situations, a certain amount of cracks may not contribute to the permeability variation because hydraulically isolated. Consequently, an overestimation of the real permeability is attended. The crack permeability is due to the crack opening $[|\boldsymbol{u}|]$ computed when solving the mechanical problem at the meso-scale and evolves with crack propagation. As the micro-crack distribution is dependent on the crack openings and orientations, the crack permeability induces an anisotropic character of fluid flow. Moreover, because the mechanical model is capable to model complete mechanical failure - coalescence of micro-cracks leading to a localized macro-crack - the crack permeability also takes into account the evolution from diffuse to localized (macro) crack.

Considering an incompressible fluid passing through a cracked media, the permeability tensor can be expressed such as

$$\underline{\underline{\boldsymbol{k}}}^{\boldsymbol{m}} = \boldsymbol{k^0}\underline{\underline{\mathbf{1}}} + \frac{[|\boldsymbol{u}|]^{\mathbf{3}}}{\mathbf{12}\boldsymbol{L}}(\underline{\underline{\mathbf{1}}} - \underline{\boldsymbol{n}} \otimes \underline{\boldsymbol{n}}) \tag{3.4}$$

where $\underline{\boldsymbol{n}}$ is the element bar unit normal vector, $\boldsymbol{k^0}$ is the initial permeability value of the material ($\simeq \mathbf{10^{-17}}$ $\mathbf{m^2}$ for ordinary concrete) and $\boldsymbol{L}$ is the length of a bar element including a strong discontinuity of magnitude $[|\boldsymbol{u}|]$. For details of the numerical simulations, see **Appendix B**.

3.3.2 Investigation of aggregates size

The crack openings [$|\boldsymbol{u}|$] in the meso-scale mechanical model were used in this investigation. Two parameters were studied in these simulations:

1. Firstly, the effect of aggregates size on gas permeability, i.e. five numerical simulations with aggregate diameters of 4, 8, 10, 14 and 16 mm were investigated and each simulation used one size of aggregate.

2. Secondly, the effect of crack opening on the flow of fluids such as gas or water (gas was used herein); the crack opening values were used from the cylinder specimens in the meso-scale mechanical model with dimensions of 110 diameter and 50 mm thickness.

In this study, the results show that the influence of aggregates size and crack opening on gas permeability became significantly more pronounced when the larger aggregate diameter was used. When the crack opening was smaller than **3** microns, there was no significant effect on the flow and permeability, while an increase in flow and permeability was limited to crack opening larger than **3** microns. Picandet et al. [Picandet et al., 2009] pointed out that when the crack opening was smaller than **3** microns, the increase in the total gas flow through cracked samples was due to diffuse damage in the specimen.

As shown in Figure (3.30), the relationships between gas permeability and the crack opening [$|\boldsymbol{u}|$] for five cylinder specimens were simulated. Clearly, gas permeability increases with the increase in the two parameters, aggregate diameter and crack opening, and the influence of crack opening is greater when it is more than **10** microns for all specimens.

Figure (3.31) shows the relationship between the permeability and crack opening for the cylinder specimen with an aggregate diameter of 4 mm compared with

the experimental results presented by Choinska et al. [Choinska et al., 2008a]. This experimental work considered four cylinder specimens in the context of the Brazilian splitting test (A, B, C and D) ranging in thickness from 30 to 50 mm with an aggregate diameter of 4 mm for all specimens. The numerical results tend to overestimate the experimental results when the crack opening is less than **50** microns and underestimate them when the crack opening is larger than **50** microns. Moreover, the permeability increased from approximately $\mathbf{3.0 \times 10^{-17}}$ to $\mathbf{1.0 \times 10^{-13}}$ $\mathbf{m^2}$ for both the numerical and the experimental results.

Figure (3.32) shows the 3D isometric views of cylinder specimens simulated for coupling between gas permeability and crack opening with five aggregate diameters of 4, 8, 10, 14 and 16 mm and the volume fraction is 20 %. We presented one simulation for each cylinder because there is no time to present a lot of simulations.

The published literature contains a vast number of studies on the influence of aggregates size and crack width on permeability. Gonilho Pereira et al. [Pereira et al., 2009] reported that the air permeability in concrete was higher than in the mortar fraction. Their explanation was that an increase in coarse aggregate led to an increase the path length for capillary pores and their interconnectivity, while this path had fewer capillary pores and less interconnectivity in mortar mixes. In addition, the increase in aggregates size resulted in more pores at the interface zone between the aggregates and the cement paste. These results are in agreement with other authors, Mehta [Mehta and Monteiro, 2006] and Wu et al. [Wu et al., 2015], who demonstrated an increase in gas permeability when increasing the maximum aggregates size. They explained that due to the microcracks density, widths, lengths and areas were increased when the aggregates size increased.

There are some of standards limitating the crack width which affects on the permeability. The ACI 318-95 Code limitations consider that as concrete structures deteriorate due to cracking, the crack opening should not exceed 0.33 mm

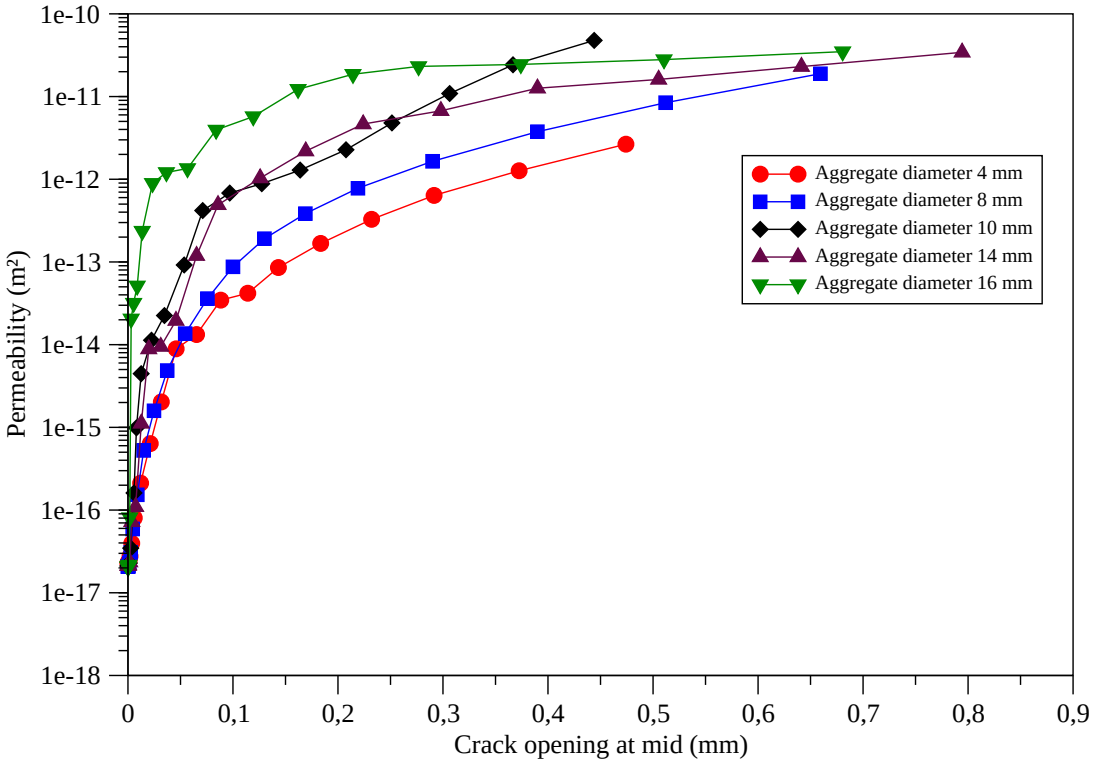

Figure 3.30: The effect of crack opening at mid of specimens on the permeability of concrete (volume fraction of 20 %) with five aggregate diameters ranging from 4 to 16 mm. Simulations are carried out for five cylinder specimens. The specimens have dimensions 50 x 110 mm of thickness and diameter, respectively.

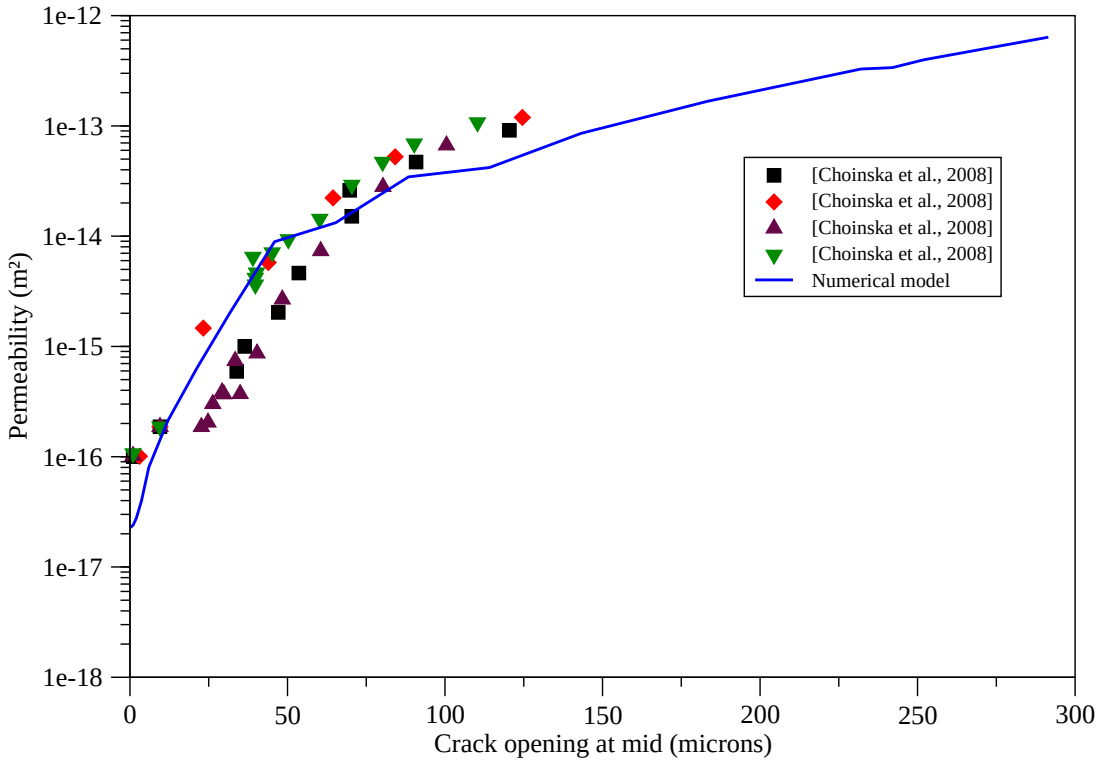

Figure 3.31: Permeability versus crack opening at mid of cylinder specimen with an aggregate diameter of 4 mm / experimental data [Choinska et al., 2008a]

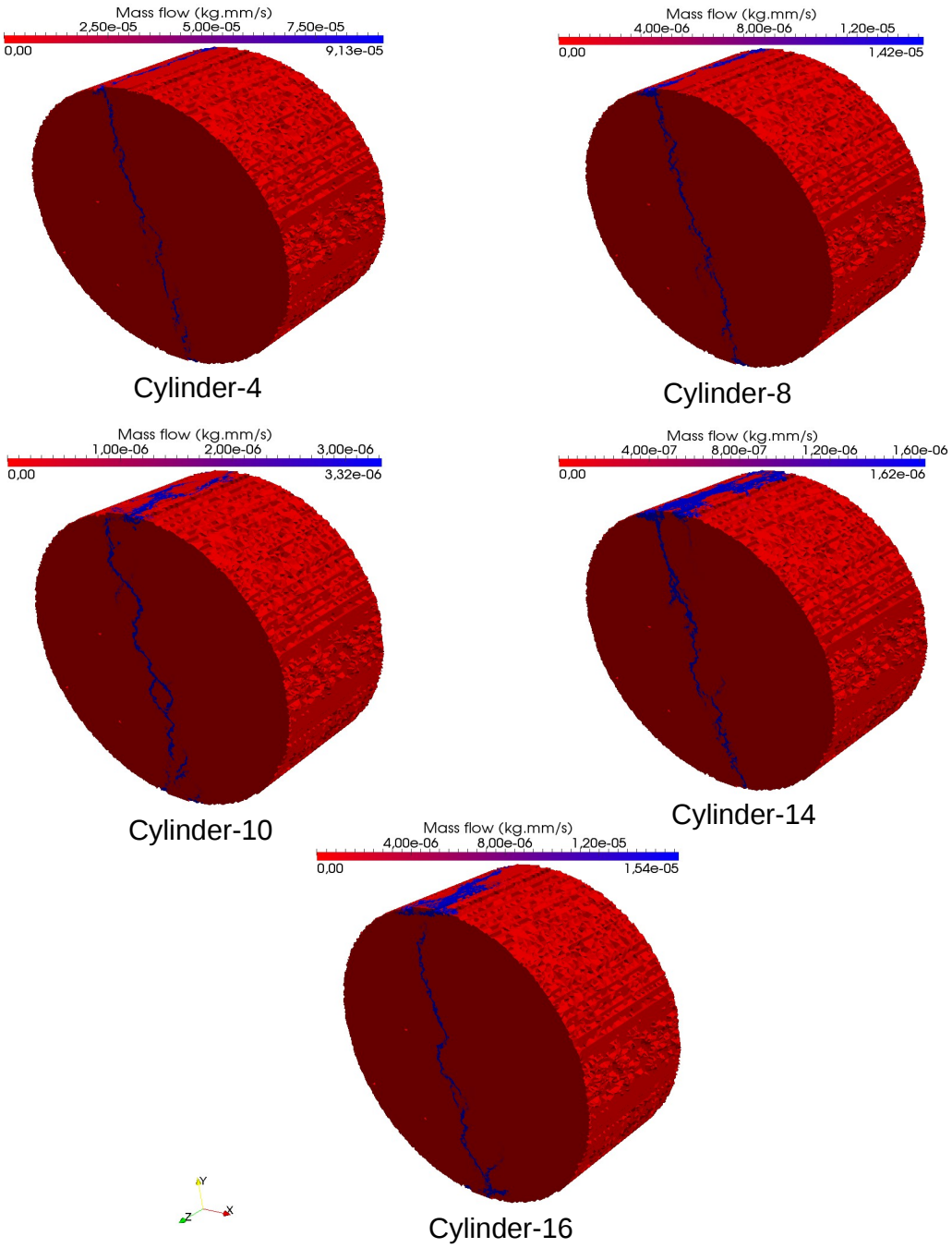

Figure 3.32: 3D isometric view of five cylinder specimens are simulated for coupling between permeability and crack opening with aggregate diameters 4, 8, 10, 14 and 16 mm. The specimens have dimensions 50 x 110 mm of thickness and diameter, respectively.

for member of structures with exterior exposure. ACI Committee 350 limits the crack width to 0.2 mm for structures exposed to very aggressive conditions. British Standards BS 8110-1997 states that the maximum crack width should not exceed 0.3 mm for the visible member of concrete structures and this crack should not weaken the performance of the concrete structure by affecting the corrosion of reinforcement steel bars. Eurocode 2 pointed out that the maximum crack width is 0.3 mm for the reinforced member or unbonded prestressed concrete and 0.2 mm for prestressed member with bonded tendons.

Wang et al. [Wang et al., 1997] pointed out the influence of crack width on water permeability for cylindrical concrete specimens under splitting tensile load. In this study, the crack width had no significant effect when it was less than 50 microns under loading, a significant effect between 50 and 200 microns, and then the water permeability became more steady when the crack width was larger than 200 microns. Aldea et al. [Aldea et al., 1999] explained the coupling between crack width and water permeability and they discussed the point, called the threshold effect, at which water flow increases, which was found to be at about 25-50 microns before unloading. On the other hand, Boulay et al. [Boulay et al., 2009] found there was no threshold effect on electrical conductance evolution under loading.

Gérard et al. [Gérard et al., 1996] demonstrated that water permeability increased when crack width increased. They noted that this behavior was due to the geometrical properties chosen and some initial experiments were performed to test crack paths in concrete, their orientation and micro cracks density. Seong-Tae Yi et al. [Yi et al., 2011] found that crack widths between 30 and 50 microns led to a decrease in water permeability for cylinder specimens of concrete as the time increased due to autogenous healing by physical and chemical closure within a crack surface. However, the permeability increased rapidly by about 190 times when the crack widths were 100 microns.

In the previous experimental studies, many parameters were taken into account for the effect of crack opening on permeability such as: crack roughness, aperture variation and tortuosity of cracks. Percolated threshold exist and depends on crack opening as well as crack density.

3.3.3 Investigation of the volume fraction of aggregate

In this investigation, the crack-induced permeability of gas in concrete is modeled to examine the interaction between the crack opening and permeability. Like in the previous example, the results of the meso-scale mechanical model were used for the crack opening $[|\boldsymbol{u}|]$. Two parameters were studied in these simulations:

1. Firstly, the influence of the aggregate volume fraction on the gas permeability of concrete nine numerical simulations with three aggregate volume fractions, 10, 20 and 30 % and three aggregate diameters of 10, 14 and 16 mm.

2. Secondly, the effect of crack opening on the flow of fluids such as gas or water (gas was used herein), was investigated using the Brazilian splitting test to obtain the cracked section with nine numerical simulations of cylinder specimens, 110 mm in diameter and 50 mm in thickness.

The results show a clear effect of the volume fraction on the gas permeability; increasing the aggregate volume fraction from 10 to 30 % resulted in a decrease in gas permeability, this tendency depends on the pores of aggregates particles and the increasing of tortuosity cause to decrease volume fraction. In addition, a significant trend in permeability with the crack opening and aggregates size was noted. To investigate one single controlled crack, we used the same example as in the mechanical part, which referred to the Brazilian splitting test to obtain a cracked section with nine numerical simulations of cylinder specimens, 110 mm in diameter and 50 mm in thickness.

Figures (3.33)-(3.35) refer to the relationship between the gas permeability and the crack opening [$|\boldsymbol{u}|$] for three groups of cylinder specimens are simulated. These results are in agreement with several previous studies in the literature.

Figures (3.36)-(3.38) show the 3D isometric views of cylinder specimens simulated for coupling between gas permeability and crack opening with three aggregate volume fractions of 10, 20 and 30 % and three aggregate diameters of 10, 14 and 16 mm, respectively.

Grassl et al. [Grassl et al., 2010] reported increasing permeability with increasing aggregate diameter and decreasing volume fraction. Wong et al. [Wong et al., 2009] showed that increasing the aggregate volume fraction in mortar from 0 to 70 % resulted in a decrease in the measured permeability of oxygen. Picandet et al. [Picandet et al., 2009] pointed out when the crack opening was smaller than 3 microns, an increase in the total gas flow through cracked samples was due to diffuse damage in the specimen. Care et al. [Care and Derkx, 2011] presented the correlation between aggregates size and volume fraction and the permeability of gas, i.e. gas permeability depended upon the aggregates size and its content.

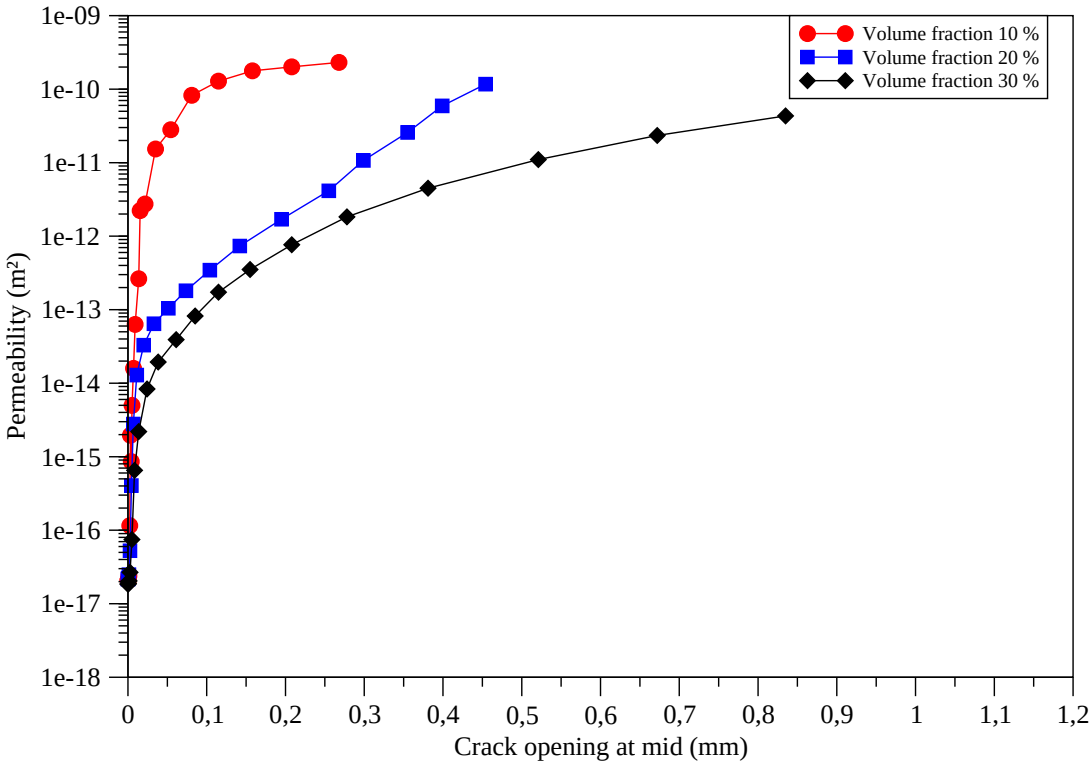

Figure 3.33: The effect of crack opening and volume fraction on permeability of concrete with three aggregate volume fractions and aggregate diameter 10 mm. Simulations are carried out for three cylinder specimens with dimensions 50 x 110 mm of thickness and diameter, respectively.

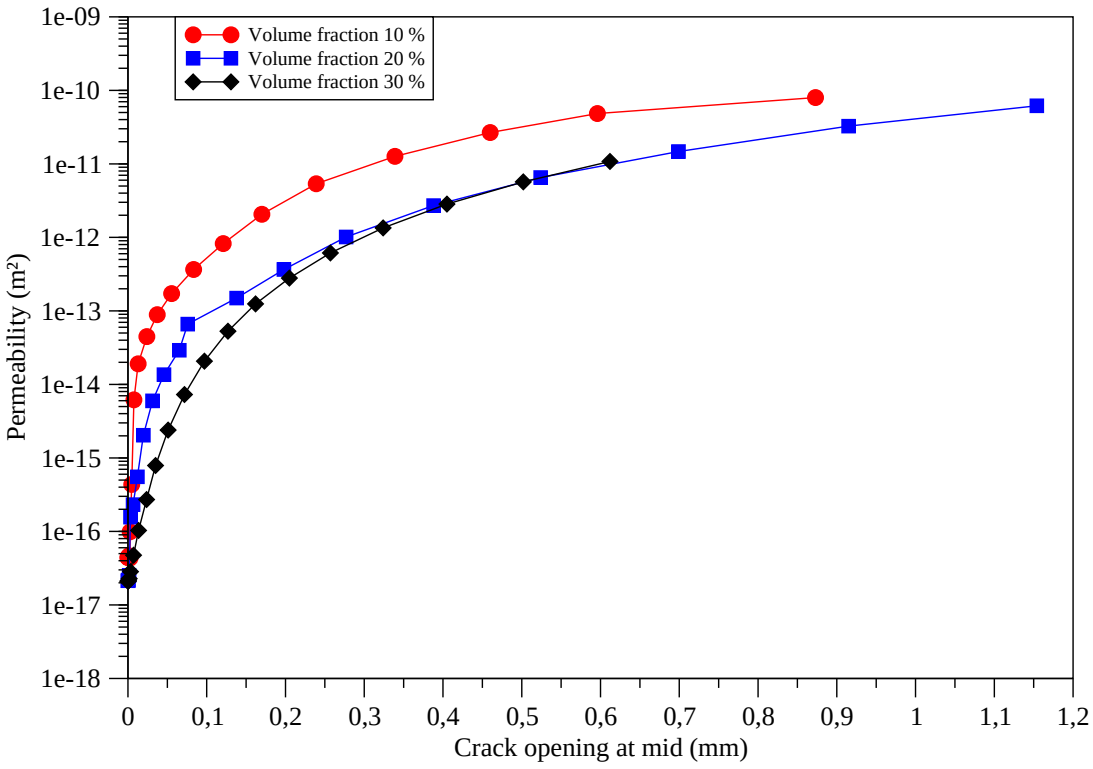

Figure 3.34: The effect of crack opening and volume fraction on permeability of concrete with three aggregate volume fractions and aggregate diameter 14 mm. Simulations are carried out for three cylinder specimens with dimensions 50 x 110 mm of thickness and diameter, respectively.

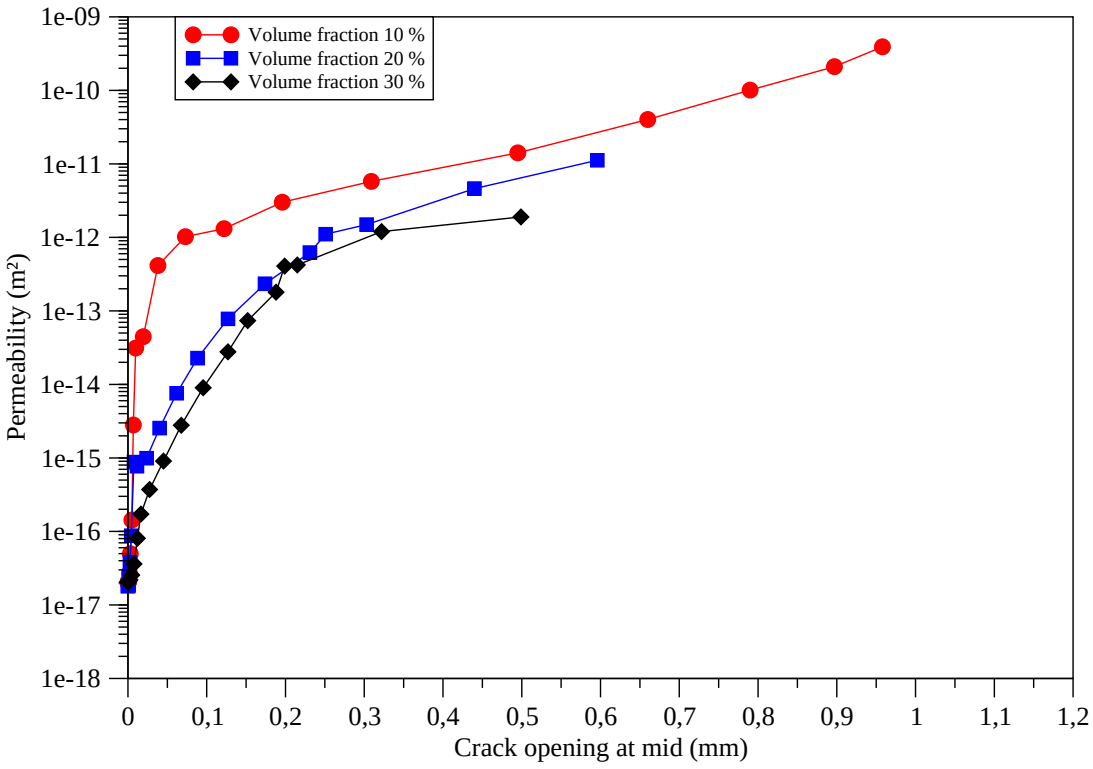

Figure 3.35: The effect of crack opening and volume fraction on permeability of concrete with three aggregate volume fractions and aggregate diameter 16 mm. Simulations are carried out for three cylinder specimens with dimensions 50 x 110 mm of thickness and diameter, respectively.

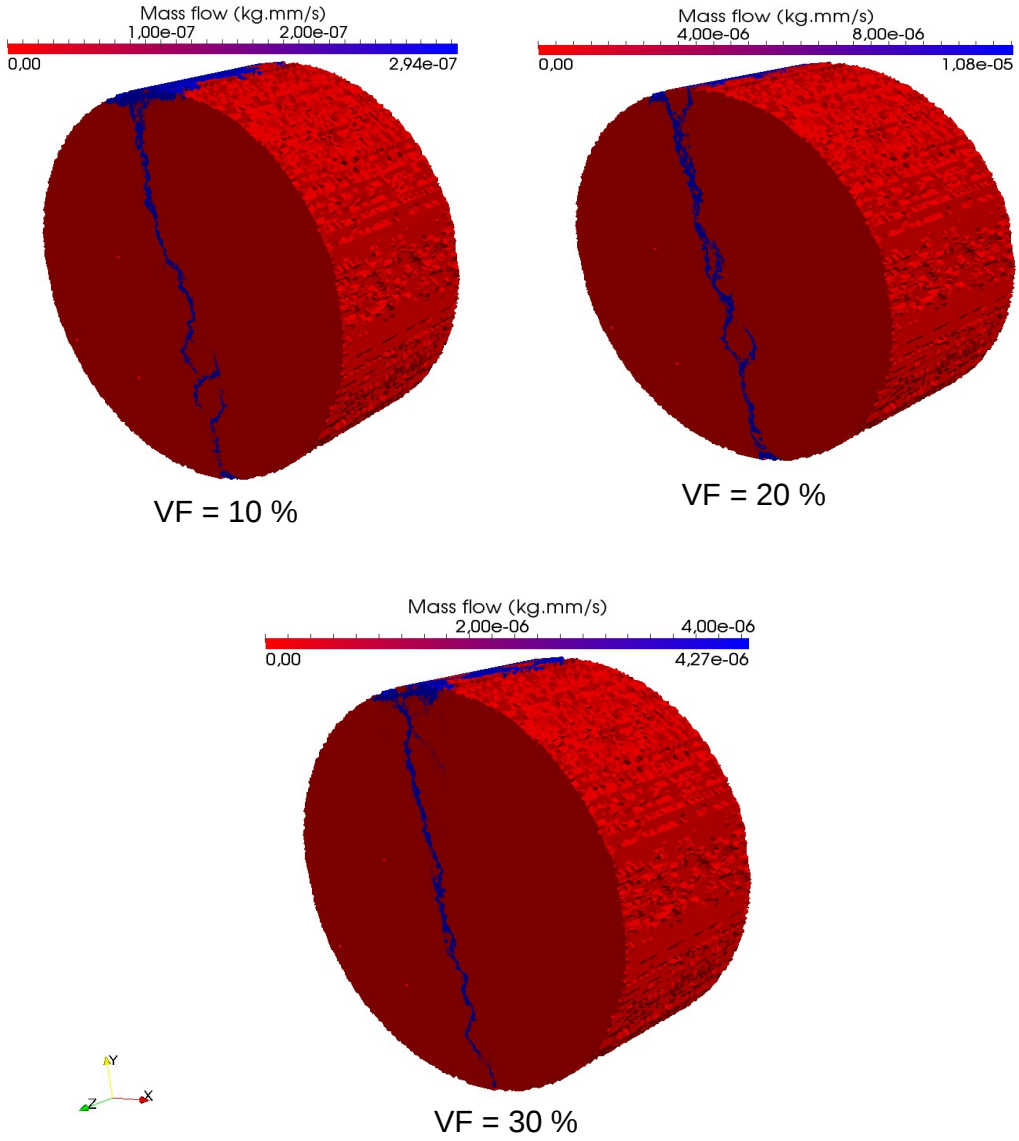

Figure 3.36: 3D isometric view of three cylinder specimens are simulated for coupling between permeability and crack opening with an aggregate diameter of 10 mm. The specimens have dimensions 50 x 110 mm of thickness and diameter, respectively.

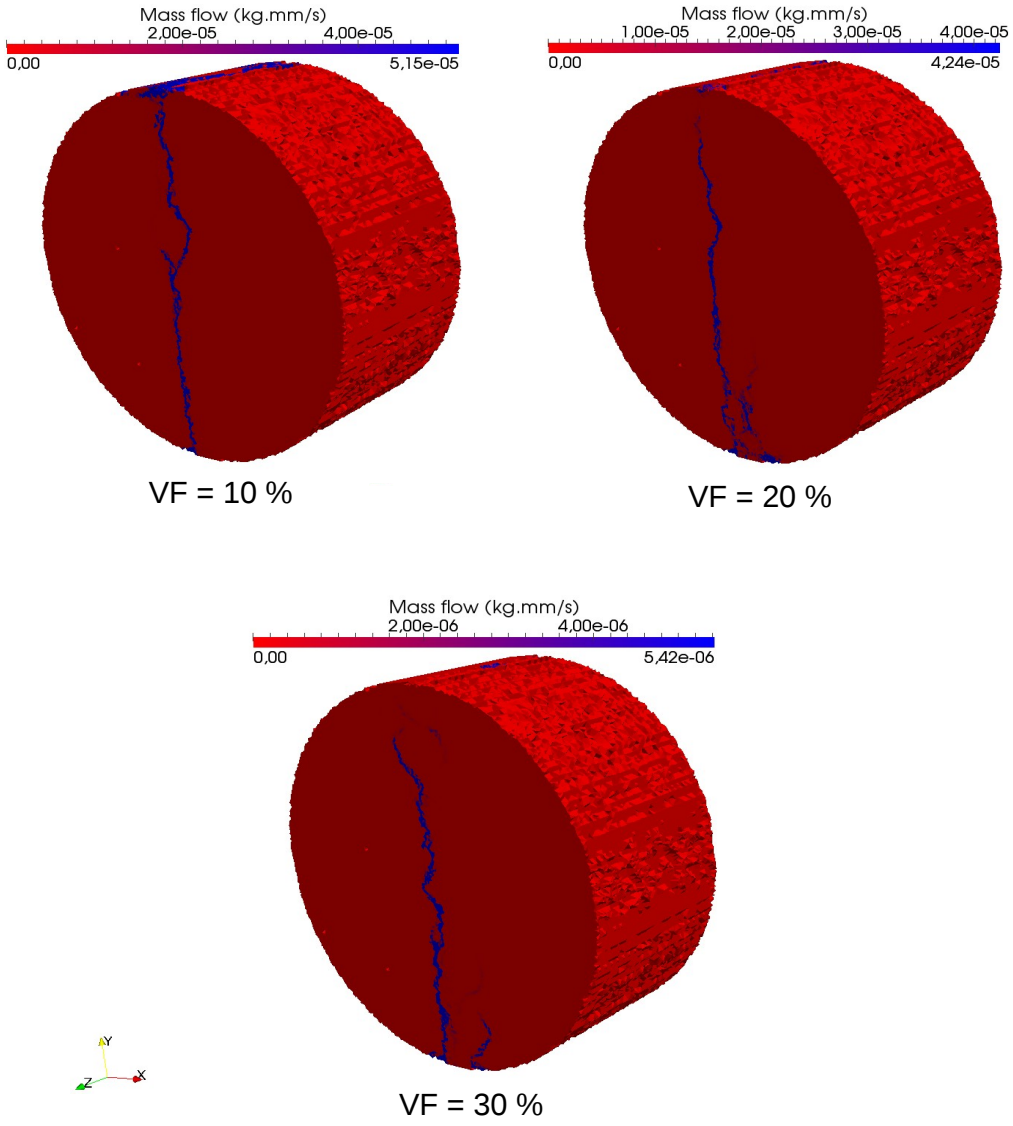

Figure 3.37: 3D isometric view of three cylinder specimens are simulated for coupling between permeability and crack opening with an aggregate diameter of 14 mm. The specimens have dimensions 50 x 110 mm of thickness and diameter, respectively.

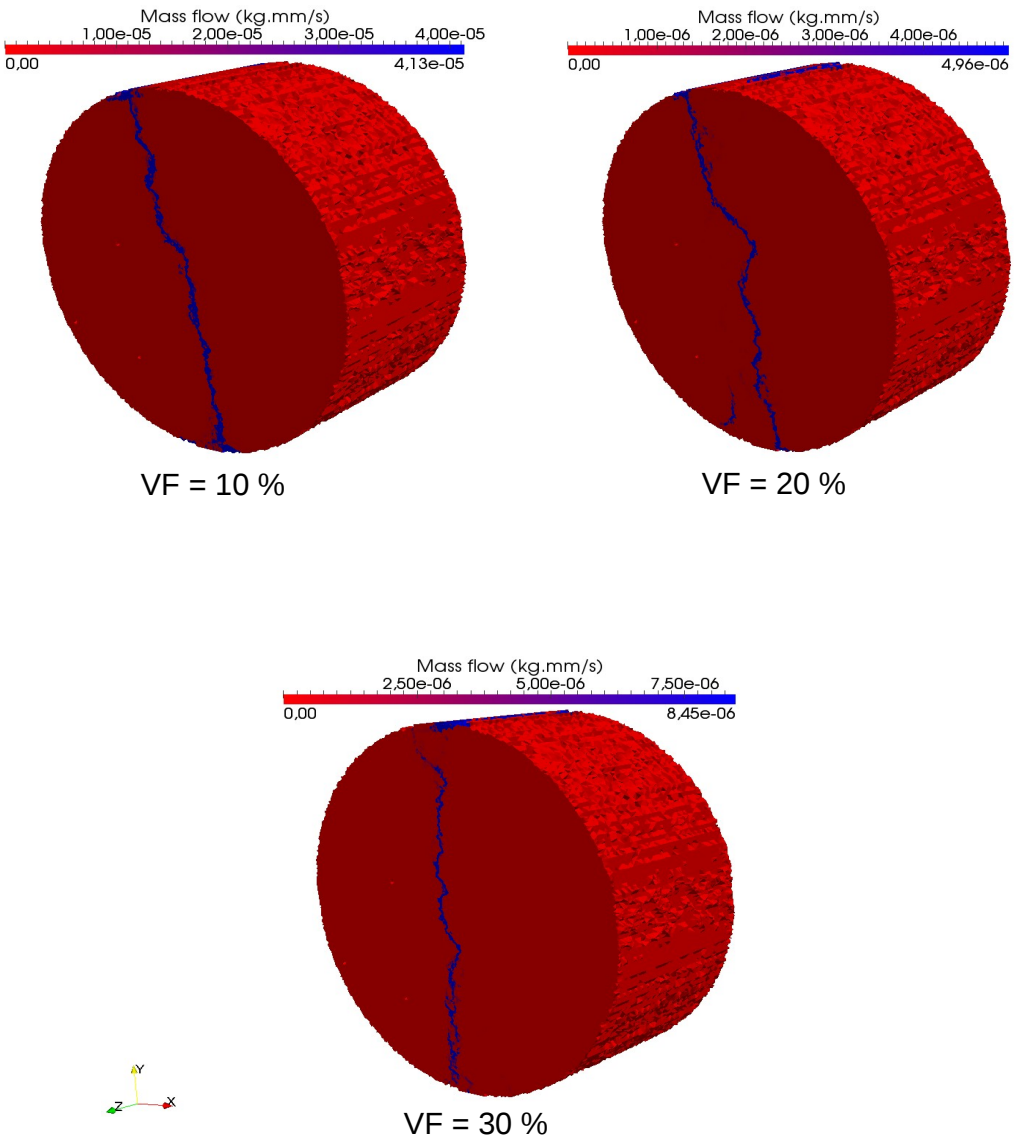

Figure 3.38: 3D isometric view of three cylinder specimens are simulated for coupling between permeability and crack opening with an aggregate diameter of 16 mm. The specimens have dimensions 50 x 110 mm of thickness and diameter, respectively.

3.4 Conclusions

The aim of this study is to understand the influence of aggregates size and volume fraction of aggregate on the hydro-mechanical behavior of concrete based on the numerical meso-scale model of heterogeneous material. Finite-element approach (E-FEM) was depended for this model. Five cylinder specimens were simulated with dimensions 50 x 110 mm, thickness and diameter respectively, according to the mechanical parameters and the properties of materials that were noted in Table (3.1) for five aggregate diameters 4, 8, 10, 14 and 16 mm. Also, nine cylinder specimens were simulated with similar dimensions. These specimens were simulated by varying both the volume fractions 10, 20 and 30 % and the aggregates size 10, 14 and 16 mm, so that they had the same mechanical parameters and properties of materials, as shown in Table (3.2).

The numerical simulations provided the hydro-mechanical behavior of concrete under diametral loading. From the numerical results it can be concluded:

1. The ultimate crack opening increases with the increasing of aggregate diameter and volume fraction.

2. Increasing of aggregate diameter and volume fraction led to an increase in the ultimate tensile stress.

3. The study pointed out that increasing of the fracture energy and the dissipation energy with respect to the aggregate diameter and volume fraction.

4. Mass flow and gas permeability are not significantly increased when the crack opening is less than **3** microns for all specimens, but there is a limited increase when the crack opening is larger than **3** microns and a clear increase at **10** microns.

5. Increasing the aggregates size leads to an increase in gas permeability.

6. Permeability decreases as the volume fraction increases.

7. We can not use our model for hall structures because we need more time to simulate the problem, in addition the simulations to take classical FEM Code. In order to run initial simulation and after to use meso-scale model only for cracked zone.

8. In the presented simulations, we have used linear elastic properties for aggregate, and cement paste properties for the interface between cement paste and aggregate. These hypothesis may be changed in future works: another properties for aggregate and for interface zone may be used in order to take under consideration non-benefic effects of aggregate due for example to restrained drying shrinkage.

9. My contributions in the numerical study principally concern parametric analysis and interpretation of aggregate size effects and volume fraction effects on hydro-mechanical behavior. In fact, as mechanical and hydro-mechanical models have already been set up ([Benkemoun et al., 2010], [Jourdain et al., 2013]), my work could rapidly provide simulations results.

Chapter 4

EXPERIMENTAL WORK

In this chapter, a experimental work is presented: mix design, preparation of materials and the specimens as well as experimental set-up. This work explains the influence of two parameters on the mechanical and hydro-mechanical behavior of concrete, the first one is the aggregates size and the second one is the crack opening. Four groups of cylinderical specimens have been realised within a water-to-cement ratio of 0.5, using glass beads particles as the coarse aggregate. One group is considered as reference: these specimens without coarse aggregates , mortar only. All manufactured cylinder specimens have the following dimensions: 110 mm of diameter and 220 mm of hight (110 x 220 mm). Three aggregate diameters are examined: 2, 6 and 10 mm, with the volume fraction of 20 %.

For the following works, from each cylinder, four discs are obtained by cutting with a diamond blade with dimensions 110 mm x 50 mm in diameter and thickness, respectively. These specimens are employed within 2 experimental set-up, one based on first mechanical BST loading and then CEMBUREAU permeability measurements after unloading,

and the second one the loading gas-permeability set-up (LGP), which presents to measur permeability value under BST loading. Effects of aggregates size, crack initiation opening, propagation, and as well as crack position are investigated.

Finally, the experimental results are compared with the mechanical meso-scale and hydro-mechanical models. The results show the interaction between the aggregates size and the crack opening with the gas permeability of concrete under loading. The increase of aggregates size from 2 to 10 mm leads to increase of gas permeability, as it is also in agreement with numerical results.

4.1 Introduction

Transport of fluids through the hardened concrete by a pressure gradient (permeability) plays a critical role in controlling of the serviceability of reinforced concrete structures, as for example: water reservoirs, water-retaining structures, nuclear reactors buildings, etc. Besides, the permeability is a parameter which may indirectly influence the durability of heterogeneous material such as concrete by governing the rate of penetration agents like chlorides or sulphates.

This chapter presents the experimental work for studying the interaction between crack opening and gas permeability. Furthermore, this work has three objectives. The first one concerns the effects of aggregates size on mechanical behavior under diametral loading in the Brazilian splitting tensile test. Four groups of cylinder specimens are investigated mortar only, mortar with 3 sizes of glass beads particles used as the coarse aggregates: 2, 6 and 10 mm in diameter. Each mixture has one size of aggregates (mono size) which different behavior with mlti-size aggregates. Tow mixtures have the same mortar. The second objective offers the

coupling between the crack opening, caused by loading, and the gas permeability and points out the influence of crack path and its width and aggregates size on permeability under loading and after loading time.

Finally, the third objective concerns the comparison and validation of the developed numerical models (mechanical and hydro-mechanical) by the obtained experimental results.

A heterogeneous material such as concrete is considered as a quasi-brittle material, for which under loading, crack occurs in the limited area of the structure: microcracks appear at the first stage of a loading, then this microcracks will be connected each other to form a macrocrack (main crack). The crack width and its position in the heterogeneous materials like concrete will be affected by different parameters such as: aggregates and cement type and content, aggregates size, type of loading, etc.

There are many researchers which focus on the influence of aggregates size on the mechanical properties of concrete. Bisschop and van Mier [Bisschop and Van Mier, 2002] investigated the effect of aggregates size on drying shrinkage microcracking in cement-based composites through on experimental study. Grabiec et al. [Grabiec et al., 2015] pointed out the influence of the type and maximum aggregates size on some properties of high strength concrete. By the way, Rao et al. [Rao and Prasad, 2002] presented the effect of surface type of aggregate on the fracture behavior of heterogeneous materials. However, other researchers demonstrated the influence of volume fraction on mechanical properties of concrete by a meso-mechanical approach and experimental works: Tasdemir et al. [Tasdemir et al., 1996] and Akcay et al. [Akcay et al., 2012].

On the other hand, some of studies explained the interaction between the crack opening and the permeability, Choinska et al. [Choinska et al., 2007] presented the permeability of concrete as a function of diffuse microcracking with the level of

damage from 0 to 15 % before the peak load, and as a function of the macrocrack opening after the peak load. Furthermore, these results have obtained a continuous permeability increase under loading in function of the global strain. Grassl et al. [Grassl et al., 2010] pointed out that the permeability of concrete increases with the increasing of crack width and increases with the aggregate diameter.

Picandet et al. [Picandet et al., 2009] demonstrated the coupling between the permeability and diffuse damages after unloading by experimental work. While Meziani et al. [Meziani and Skoczylas, 1999] and Choinska et al. [Choinska et al., 2007] studied the coupling under loading. Wu et al. [Wu et al., 2015] investigated the influence of microcracks on the transport properties and durability of concrete structures: they concluded that the gas permeability decreased with the decreasing of aggregates size.

The aggregates size is considered as one of the most important parameter which affects the mechanical properties of concrete. Bazant [Bažant, 2004] and Grassl et al. [Grassl et al., 2012] presented the effects of specimen size on mechanical behavior of concrete and demonstrated the size effects on the mechanical properties of concrete on the nominal strength, crack width and fracture process zone.

4.2 Experimental programme

This section presents the methodology of this study and materials composition with mix proportions, specimens preparation and curing method. In the following part of this section will be presented. The principles of mechanical device of the Brazilian splitting tensile test and the permeability devices.

4.2.1 Methodology

The experimental work highlights the effects of two factors on concrete behavior: the effects of aggregates size on mechanical behavior under diametral load in the Brazilian splitting tensile test (BSTT) and the effects of crack opening on gas permeability. For all mortar mixtures used, the volume of fraction was kept constant and equal to 20 %. Cylinder specimens with different aggregates sizes of 2, 6 and 10 mm are presented in Figure (4.1).

Figure 4.1: Three cylinder specimens of 110 mm of diameter and 220 mm of height with different aggregate sizes.

In this work, the experimental programme foucuses on underlining the effects of aggregates size on mechanical behavior in the context of the Brazilian splitting test and the influence of aggregates size on the permeability of a sound or damage

specimen. In the next sections will be presented the details of tested materials, mix proportions, preparation and drying of specimens, and then methods of mechanical and permeability tests.

4.2.2 Tested materials

Spherical glass beads are used as coarse aggregates, see Figure (4.2). The properties of these aggregates (glass beads) are given in Table (4.1). Three aggregate diameters studied are 2, 6 and 10 mm, while the volume of fraction for all aggregate diameters is 20 %.

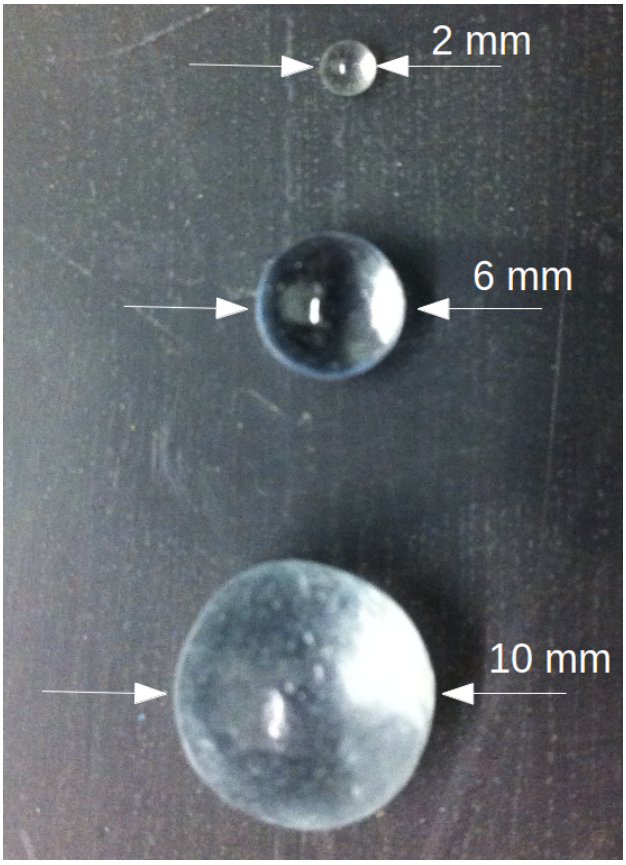

Figure 4.2: Three sizes of glass beads used in this study.

Table 4.1: Glass beads properties.

Glass bead	**Diameter (mm)**	**Specific weight (g/cm^3)**	**Young's modulus (GPa)**	**Crushing strength (kN)**
G-2	2±0.2	2.5±0.4	78	0.9
G-6	6±0.3	2.5±0.4	79	3.6
G-10	10±0.5	2.5±0.4	81	6.2

The fine aggregate is the Boulonnais sand which is limestone type, with the coefficient of absorption is 0.8 % and unit weight of 2900 kg/m^3. The type of cement used in this study is the Portland cement CEM I 52.5 N. The water-to-cement ratio is equal to 0.5. The composition of the cement is the following: 21.18 % SiO_2, Al_2O_3 3.56 %, Fe_2O_3 4.28 %, 64.76 % CaO, 0.81 % MgO, 0.25 % K_2, 0.16 % Na_2O and 2.55 % So_3. Its estimated Bogues composition is 88 % C_3S, 8.6 C_2S, 2.9 C_3A and 12.4 % C_4AF.

Tap water was used to prepare the mixtures for all the specimens. Neville [Neville, 2011] pointed out that PH ranging between 6.0 and 8.0 had no significant effect on the compressive strength of concrete.

4.2.3 Mix proportions

Two mix proportions used in this work are given in Table (4.2): **Mix A** corresponds to mortar only (without glass beads (GB)), **Mix B** corresponds to the same mortar but with glass beads (GB) inclusions. One size of aggregate was used for each mixture (mono size) and volume fraction was kept constant and equal to 20 %. A mechanical needle vibrator was used for compacting the concrete mixture within 3 layers.

Standard procedures NF P 18-422 propose the period of vibration according to the measured slump. In our tests, the period of vibration was reduced to 10 s

for the both mixtures.

Table 4.2: Details of two mixtures and mix proportions.

Mix ingredients (kg/m^3)	**Mix A**	**Mix B**
Sand Boulonnais, 0-4 mm	1757.8	1406
Portland Cement CEM I 52.5	585.94	469
Glass beads (2 or 6 or 10 mm)	-	382.9
Water	292.97	234.13
W/C ratio	0.5	0.5

Mix A has been defined according to the following computations for each cylinder:

$V_{\boldsymbol{mould}}$ = 0.0021 m^3

W/C = 0.5

Loss percentage = 20 %

Cement = 585.94 * 0.0021 * 1.2 = 1.477 kg

Sand = 1757.8 * 0.0021 * 1.2 = 4.430 kg

Water = 292.97 * 0.0021 * 1.2 = 0.738 kg

Mix B has been defined with glass bead (GB) studying for **20** % of volume fraction and has been computed as following:

$V_{\boldsymbol{GB}}$ = 0.2 * 0.0021 = 0.00042 m^3

W/C = 0.5

Cement = 1.477 * 0.8 = 1.182 kg

Sand = 4.430 * 0.8 = 3.544 kg

Water = 0.738 * 0.8 = 0.590 kg

$M_{\boldsymbol{GB}} = \boldsymbol{\rho_{GB}} * V_{\boldsymbol{GB}}$ = 2300 * 0.00042 = 0.966 kg

The mix proportions are given in Table (4.3) for each cylinder specimen with

three different aggregate sizes.

Table 4.3: Details of mix proportions in (kg) for each cylinder 110 mm x 220 mm specimen.

Specimens	Cement	Sand	Glass beads	Water
RS	1.477	4.430	-	0.738
RS-2mm	1.182	3.544	0.966	0.590
RS-6mm	1.182	3.544	0.966	0.590
RS-10mm	1.182	3.544	0.966	0.590

4.2.4 Specimens preparation

Three cylinderical specimens with dimensions 110 x 220 mm have been prepared for each mix. These specimens were cast in steel moulds. After casting, cylinder specimens were stored within the moulds in a humidity room for 24 h at 20 ℃ with 98 % relative humidity. Then, the specimens were put without moulds for curing in water at 20 ℃ during 28 days.

In the next step, each cylinder specimen was cut using a diamond blade saw. Four discs has been obtained see Figure (4.3) with dimensions about 110 x 50 mm. Two faces for all specimens were polished by using polishing machine, as shown in Figure (4.4). Finally, 48 110 x 50 mm cylinder specimens were obtained for two mixtures with different aggregates sizes and the final specimen dimensions were calculated with the accuracy of 0.1 mm. The No. 1 and 2 top and bottom specimens see Figure (4.3) were used in the following results for controlling test. Four cylinder specimens were prepared after cutting with dimensions 110 x 50 mm and aggregate diameters ranging from 2 to 10 mm.

Then, cylinder specimens were put in a non-ventilated drying oven and heated at 40 ℃ until their weights reached a constant value. Their weights were measured

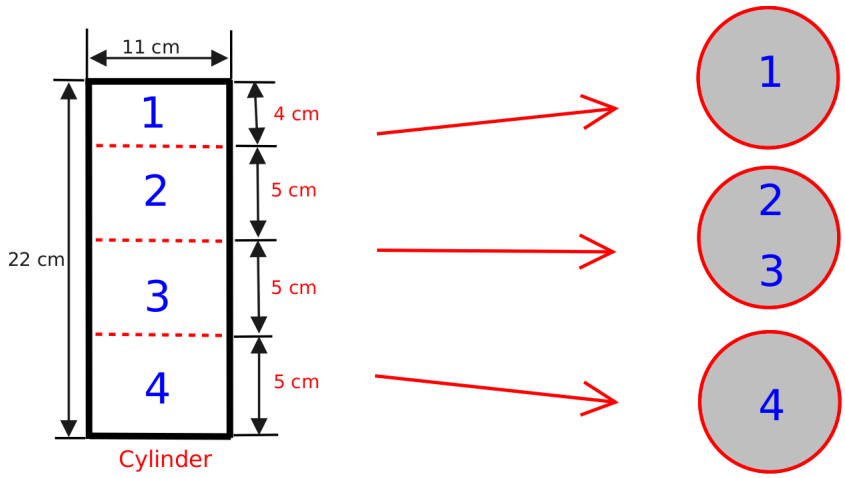

Figure 4.3: Schematic representation of four 110 mm x 50 mm discs within each cylinder specimen.

using a balance with an accuracy of 0.01 g. Figures (4.5, 4.6) represent respectively the relationships between the relative moisture loss and drying time, and moisture loss with the drying time. The data has been calculated using equation (4.1). It can be seen that the value of moisture loss is greater at the first days, while this value is decreasing with the time to become a constant beyond of 60 days in drying oven. However, the linear relationship between relative moisture loss and drying time was presented in Figure (4.7), this behavior as seems diffusion behavior. By the way, Picandet et al. [Picandet et al., 2001], Jacobs [Jacobs, 1998] and Abbas et al. [Abbas et al., 1999] pointed out that the water content in concrete specimen had a direct influence on the gas permeability measurments. All the dried specimens have been stored in plastic bags before permeability test and the curved surface of each specimen was covered within a self-adhesive aluminium film in order to ensure a one-dimensional gas flow inside the specimen when applying the pressure gradient.

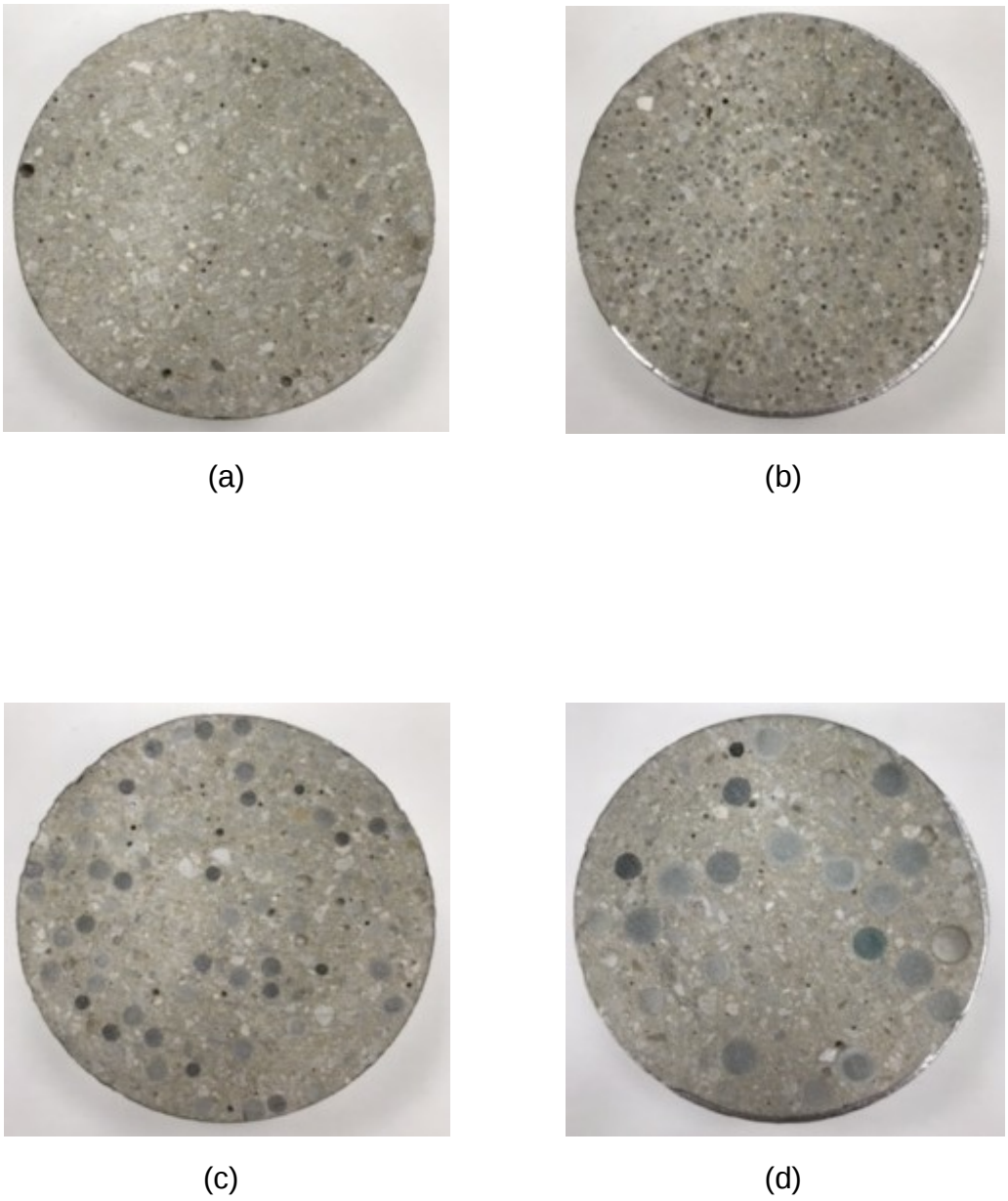

Figure 4.4: Sections of cylinder 110 mm x 50 mm specimens with different aggregate sizes: mortar (a) mortar with aggregates size of 2 mm (b) mortar with aggregates size of 6 mm (c) mortar with aggregates size of 10 mm (d).

$$\boldsymbol{RM\%} = \frac{\boldsymbol{W_w - W_d}}{\boldsymbol{W_w}} \times \mathbf{100} \tag{4.1}$$

where $\boldsymbol{RM}$ is relative moisture loss in (%), $\boldsymbol{W_w}$ is wet weight of the specimen in (kg) and $\boldsymbol{W_d}$ is dry weight of the specimen in (kg).

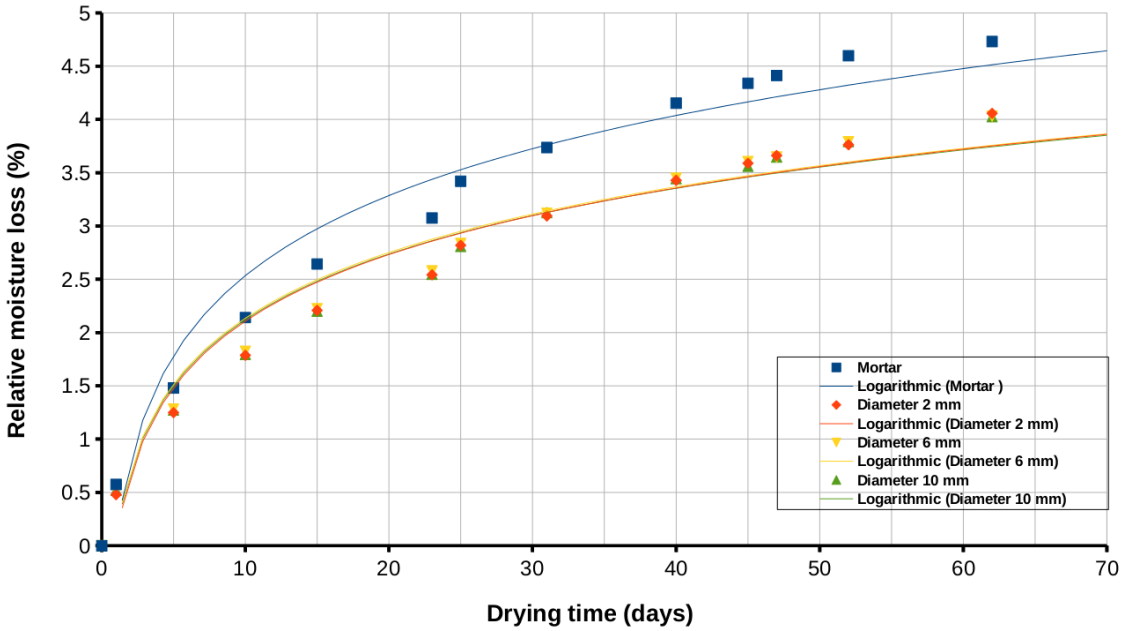

Figure 4.5: Relationship between relative moisture loss and drying time for cylinder 110 mm x 50 mm specimens.

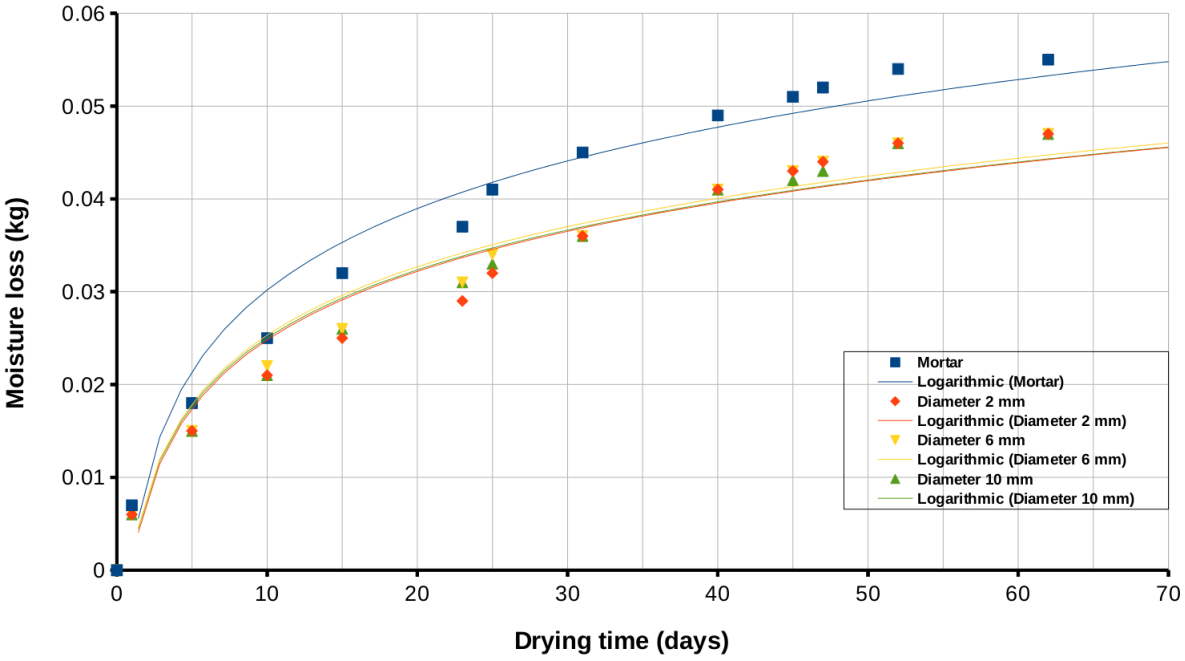

Figure 4.6: Relationship between absolut moisture loss and drying time for cylinder 110 mm x 50 mm specimens.

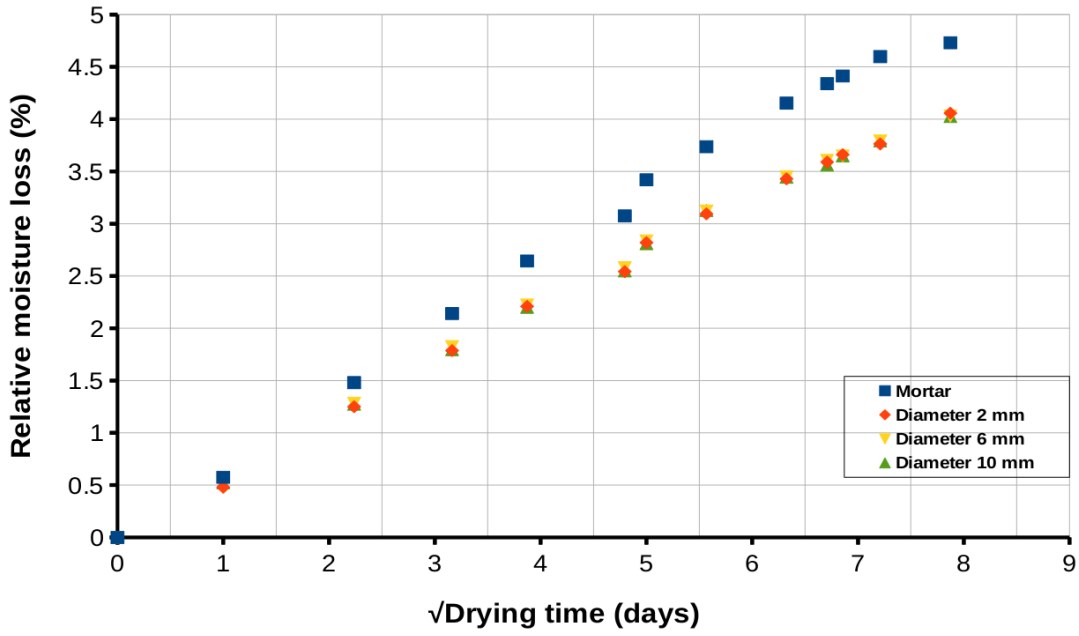

Figure 4.7: Relationship between relative moisture loss and square root of drying time for cylinder 110 mm x 50 mm specimens.

4.2.5 Mechanical damage procedures

For studying the behavior of concrete under loading, tensile tests on concrete are classified into direct and indirect ones. Direct tensile test has been realised by other researchers by applying an axial tension force to the concrete specimen. Mechtcherine et al. [Mechtcherine and Müller, 1998] developed this test using dog-bone specimens as un-notched element and prism as notched one. Also, Cunha et al. [Cunha et al., 2011] developed this test by molding specimen with embedded steel bars. These bars were used to apply the tensile force to the concrete.

The literature review show that most of researchers prefer to use indirect tensile methods, i.e. the Brazilian splitting tensile test (BSTT) and flexural tests. This two tests are easier to carry out than the direct ones and have been standardized in several Codes, the ASTM and Eurocodes.

The Brazilian splitting test set-up and load distribution are shown in Figures (4.8 a and b). The correlation between tensile strength and applied load can be defined by equation (4.2) for a cylinder specimen, where $\boldsymbol{\sigma_t}$ is the splitting tensile strength in (MPa) at the failure due to the ultimate diametral loading $\boldsymbol{P_u}$ in (N), and $\boldsymbol{D}$ is the diameter of the cylinder specimen in (mm) and $\boldsymbol{B}$ is the specimen thickness in (mm).

$$\boldsymbol{\sigma_t = \frac{2P_u}{\pi BD}} \tag{4.2}$$

Cylinder specimens with dimensions 110 x 50 mm were used to induce one main crack in each mortar specimen by applying diametral loading in the Brazilian splitting tensile test (BSTT) using a computerized hydraulic MTS machine with maximum capacity of 1000 kN equipped with a special 250 kN loading cell, as shown in Figure (4.9).

Figure (4.10) shows a cylinderical specimen between two platens of a testing MTS machine and loaded in diametral direction in the context of the Brazilian splitting tensile test (BSTT).

4.2.6 CEMBUREAU gas permeability test procedure

The gas permeability was computed based on the principles of Hagen-Poiseuille relationship for laminar flow of a compressible fluid such as nitrogen through a porous media with the small capillary pores under steady-state conditions. As shown in equation (4.3), the apparent permeability $\boldsymbol{k_a}$ in ($\mathbf{m^2}$) can be determined as following:

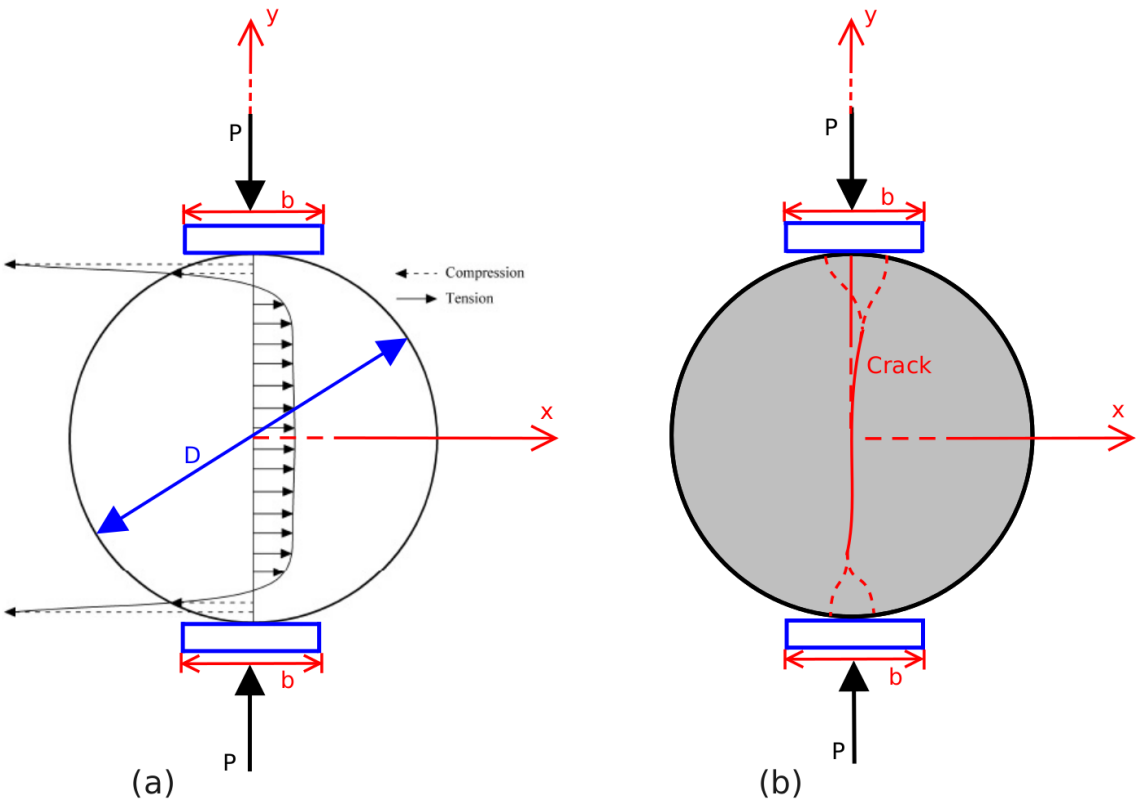

Figure 4.8: Behavior description for a cylinder specimen under loading in the BSTT. Distribution of stress [ASTM C496, 1996] (a) load application and crack pattern (b).

Figure 4.9: Hydraulic MTS machine with a cylinder specimen.

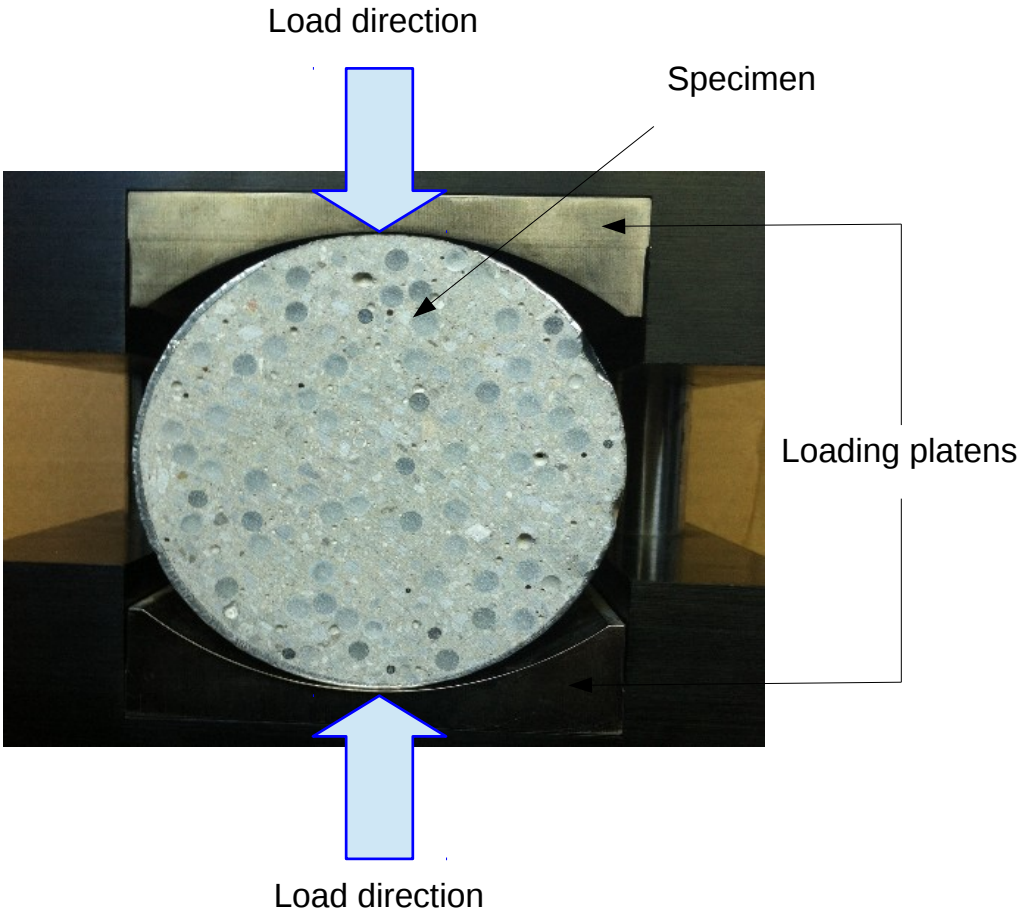

Figure 4.10: Set-up for the Brazilian splitting test.

$$k_a = \frac{Q}{A} \frac{2\mu B P_{atm}}{(P_i^2 - P^2{}_{atm})} \tag{4.3}$$

where Q is the measured gas flow in (m^3/s), B is the thickness of the cylinder specimen in (m), A is the cross-sectional area in (m^2), μ is the coefficient of viscosity (1.7 x 10^{-5} Pa.s for nitrogen gas at 20 ℃), P_i is the inlet pressure in (Pa), and P_{atm} is the atmospheric pressure in (Pa).

Kollek [Kollek, 1989] was first to presented a study for measuring the apparent coefficient permeability using the CEMBUREAU method. This method is convenient for porous media as concrete. The experimental set-up developed in our laboratory permits to measur the apparent permeability (k_a), and the determine the intrinsic permeability (k_v) of sound or damaged concrete.

The boundary conditions in the permeability testing room were 20 $\pm$ 1 ℃ and 50 $\pm$ 5 % RH, temperature and relative humidity, respectively.

The gas permeability set-up shown in Figure (4.11), works with nitrogen supply reserve fitted with a pressure valve from 0 to 15 bars, precision pressure regulator from 0 to 6 bars, digital pressure gauge for measuring the inlet pressure P_i with accuracy 100 Pa (1.10^{-3} bar), mass flow meters, and the permeability cell as shown in Figure (4.12).

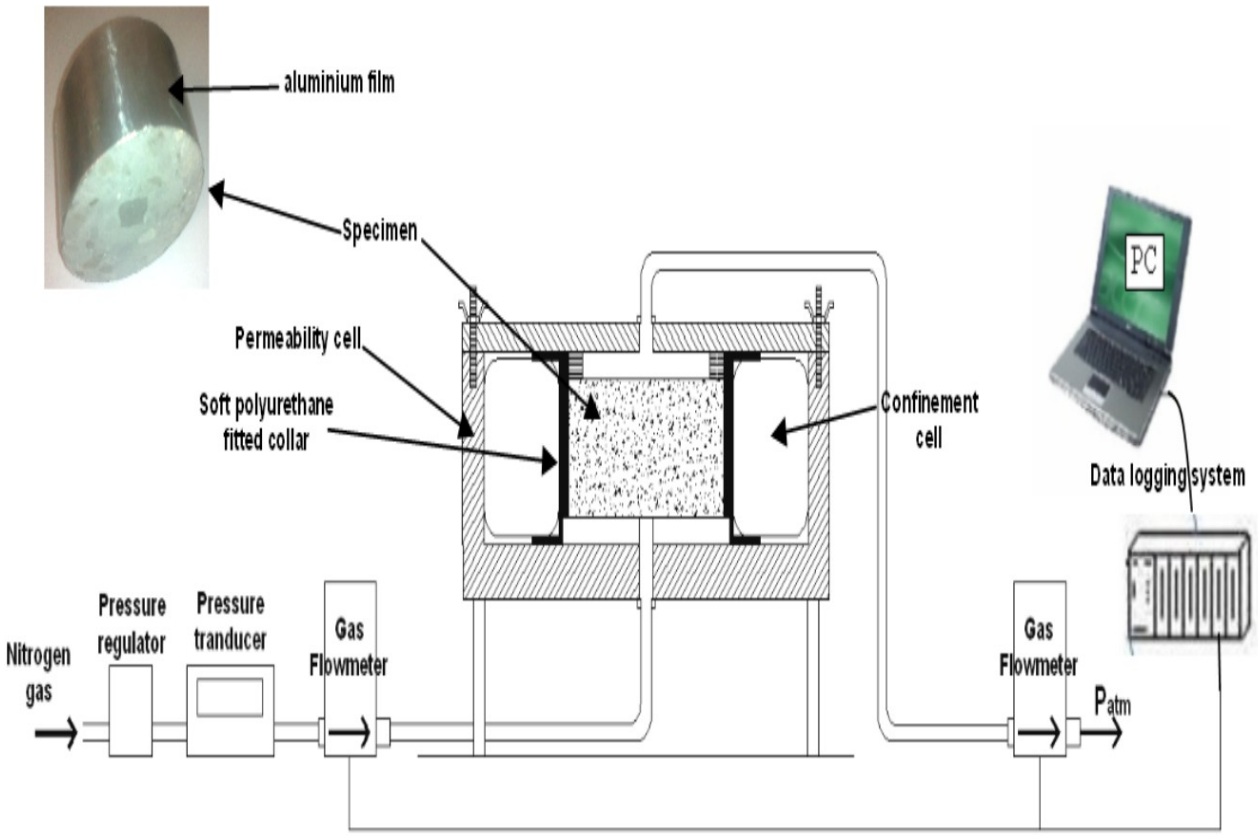

Figure 4.11: Schematic layout of the gas permeability set-up with the CEMBUREAU cell.

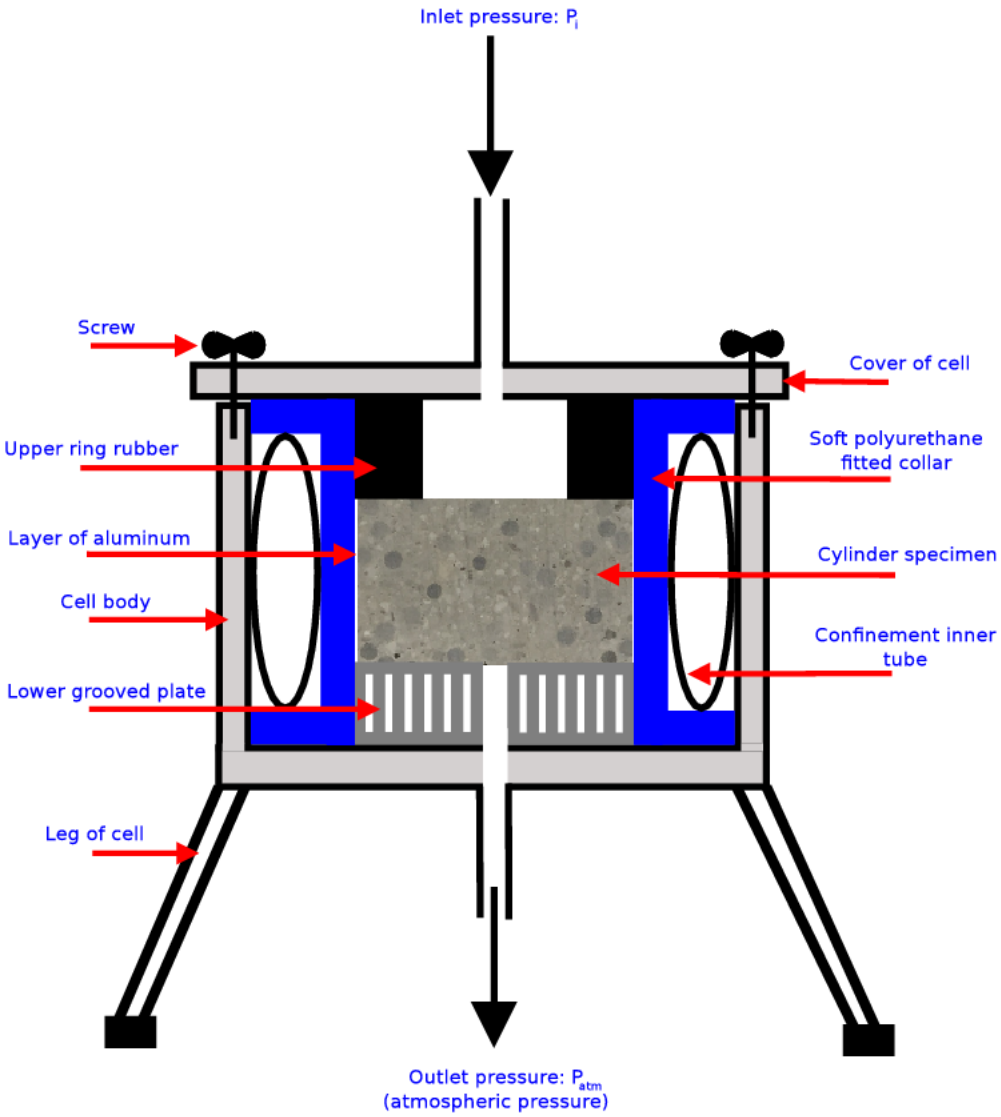

Figure 4.12: Schematic presentation of the permeability cell with a test specimen.

4.2.7 Loading-gas permeability (LGP) set-up and testing procedure

The second method to permeability estimation is the loading-gas permeability (LGP) set-up shown in Figure (4.13). It permits to realise permeability measurements loading and at the same time, i.e. investigate the influence of cracked section on gas permeability. Two hollow aluminium cylinders may be used to apply gas pressure gradient. They have 4 mm in thickness. In addition it was used two flat rubber rings with thickness 5 mm which were placed between hollow aluminium cylinder and specimen to avoid gas leakage during test, see Figures (4.14 a and b). The hollow aluminium cylinders were used due to their negligible effect on the cylinder specimens behavior under the Brazilian splitting tensile tests. Figure (4.15) shows general views of this test.

4.3 Mechanical behavior

This section presents the behavior of concrete specimens with dimensions 110 x 50 mm diameter and thickness, respectively under applied loading that based on the Brazilian splitting test.

4.3.1 Aggregates size-ultimate tensile stress relationship

The hydraulic MTS machine was used with unaxial loading capacity of 1000 kN, equipped with a loading cell of 250 kN, and computerized unit controller for measuring the mechanical values such as: load, displacement-strain as well as time, etc. For applying load, the components of this set-up represent two plates: the first one is the upper plate for applying loading and the second one is lower plate for fixing the cylinder specimen. Figure (4.16) shows this set-up, we can see two

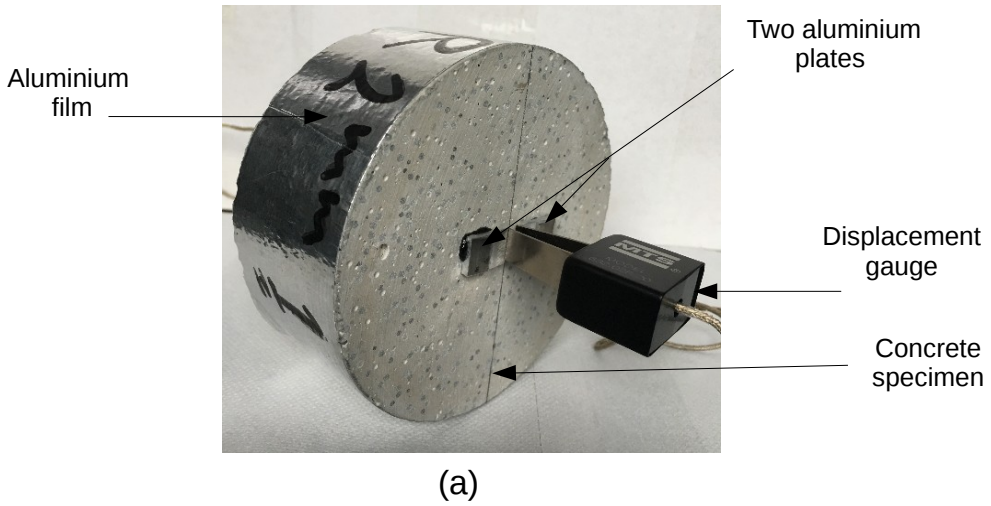

Figure 4.13: The test set-up for the mechanical behavior illustration and permeability.

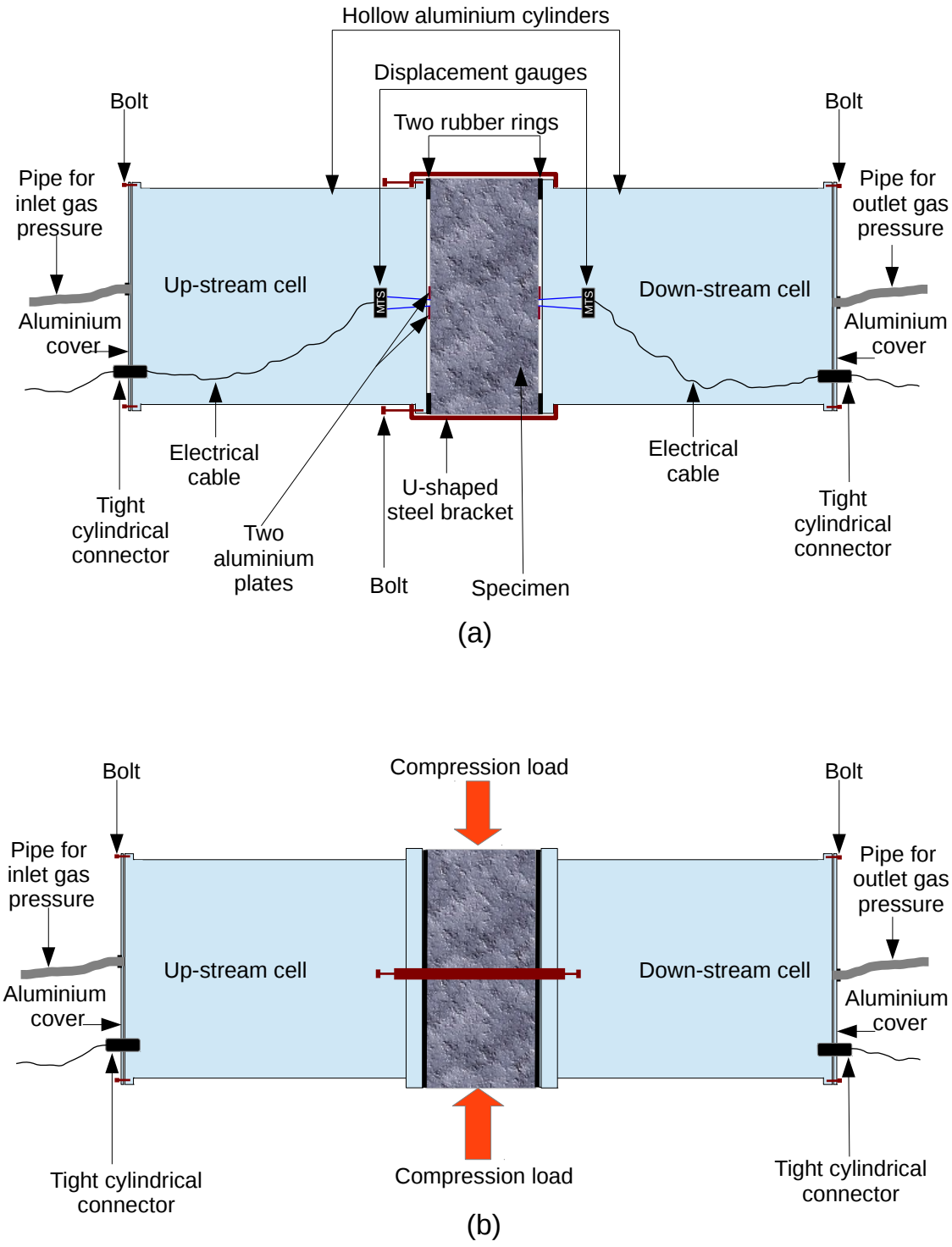

Figure 4.14: Schematic (a) top view (b) side view of the loading-gas permeability (LGP) set-up.

Figure 4.15: Experimental set-up of the coupling between the gas permeability and crack opening. Bottle of nitrogen with pressure regulator (1) datalogger and power (2) mass flow measur system (3) pressure gauge (4) pressure control (5) concrete specimen under applied loading and gas pressure (6).

kinds of cracks at the failure test: the main crack is one at mid of specimen and the second one is secondary crack which appeared after main crack. In our study, we used in the initiation phase to measur gas permeability.

Figure 4.16: Cylinder specimen under loading in the MTS machine.

As shown in Figure (4.17), the relationship between the ultimate tensile stress and aggregate diameters is globally decreasing, while the results from the numerical model show a reverse tendency: with tensile stress is increasing with the increasing of aggregate diameters.

The results show the ultimate tensile stress of mortar with GB inclusions (6 and

10 mm) lower than the corresponding reference mortar, and that the tensile stress seems to decrease as the aggregates size increases, i.e. the concrete specimens have larger porosity when using bigger aggregates size. However, the results show that the distribution of aggregates and its position affect on the ultimate tensile stress of concrete. In addition, the ultimate tensile stress for specimens which have been in relative humidity 90 % and were put in oven at temperature 40 ℃. Otherwise, this indication explains that when the time of curing is longer in humidity room at RH 90 %, due to the amount of water, it is enough to fill the voids and coat the cement grains which enable a greater hydration of cement and leads to greater ultimate tensile stress for concrete specimens, as shown in Figure (4.17).

The results are in general agreement with previous studies that had investigated for relationship between the tensile stress with the aggregates size. Elices and Rocco [Elices and Rocco, 2008] reported that the tensile strength for concrete was lower than the tensile strength of matrix, and the tensile strength was decreased with the increasing of the aggregates size. Zhang et al. [Zhang et al., 2005] presented the influence of coarse aggregates size on the tensile stress for normal and high-strength concrete, the increasing of aggregates size caused to decrease of tensile strength of concrete. Saouma et al. [Saouma et al., 1991] and Li et al. [Li et al., 2004b] observed the increasing in aggregates size caused to decrease tensile strength in dam concrete. Furthermore, Petersson [Petersson, 1980], Tasdemir et al. [Tasdemir et al., 1996] and Chen et al. [Chen and Liu, 2004] pointed out the influence of the aggregates size which is increasing leads to decrease the tensile strength of concrete. While Mihashi et al. [Mihashi et al., 1989a], [Mihashi et al., 1991] showed no clear trend, i.e. the tensile stress for mortar specimens was greater than the specimens with aggregates size between 15-20 mm, while was less than the specimens with aggregates size between 20-30 mm.

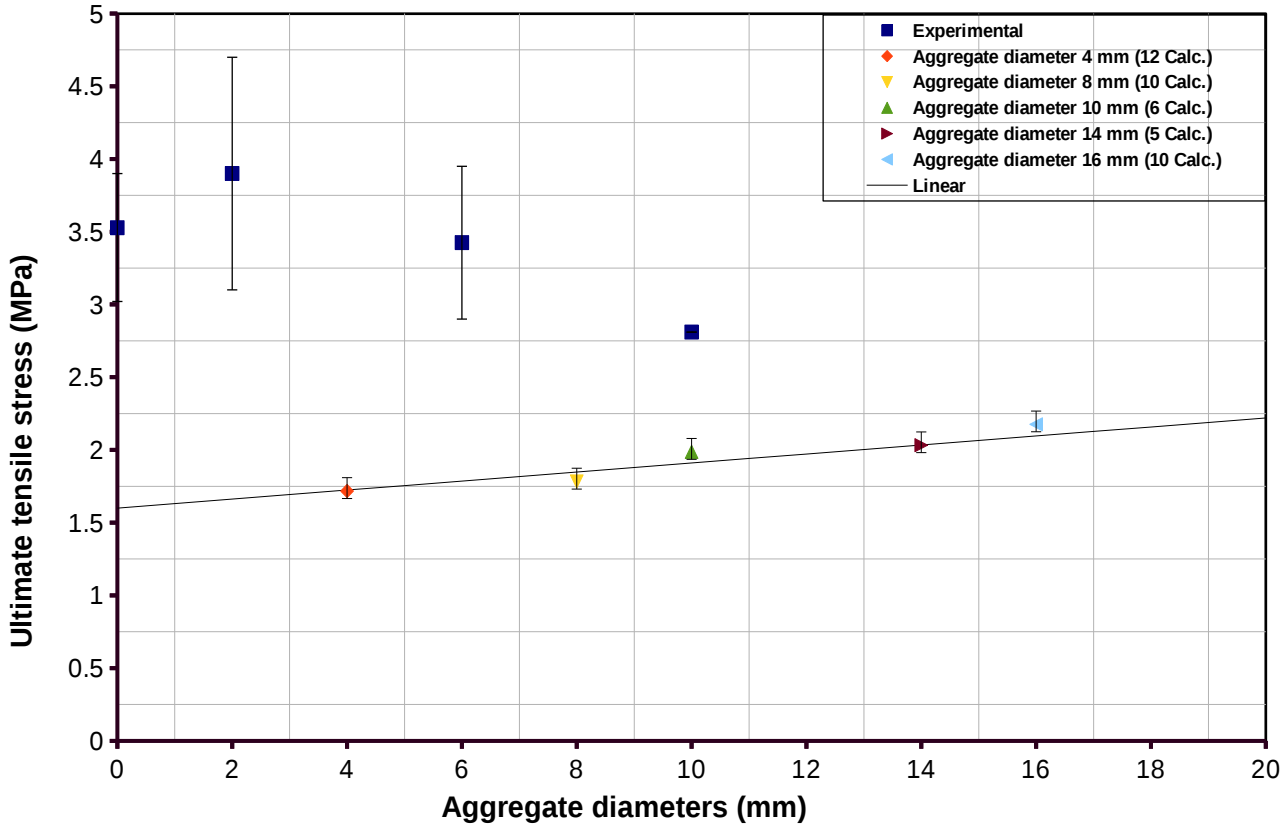

Figure 4.17: Effect of aggregates size on ultimate tensile stress for cylinder specimens. Comparison with numerical model results.

4.3.2 Observation of crack patterns

During the process loading and investigation the crack characteristics, the tested cylinders gave two indications: the first one was the primary crack that appeared at the center of specimens during splitting test and had been grown toward the edges of specimens; this indication is an agreement with studies of Wang [Wang, 1994], Choinska [Choinska, 2006] and Picandet [Picandet, 2001]. The second indication was the secondary crack appeared before the primary crack for some of the specimens under loading. By the way, it can be seen two types of cracks in Figure (4.18).

The results showed the right main crack (primary crack) for the reference specimens (without GB aggregate) occurs for the specimens with GB aggregate of 2 mm of the same crack pattern was obtained: crack position at the center of specimen, without tortuosity and developed toward the edges of specimen. In addition, this path of crack was the straight line without discontinuities, as shown in Figures (4.18 and 4.19 a). Therefore, for the cylinder specimens with the aggregate diameters 6 mm and 10 mm it was noticed that the primary crack appeared at the center of the specimen and propagated towards the edges under loading while the crack path was not a straight line (tortuosity), i.e. this crack trended to go around the aggregate particles which placed on the path of crack, and it was frequently slightly discontinuous, as shown in Figures (4.19 b and c). Also, there is some glass beads removed by cutting and during loading test. The micro-cracks are introduced in the cement paste specimens due to shrinkage restrained that cause to weakness mechanical behavior of specimens, see Figure (4.20 a and b).

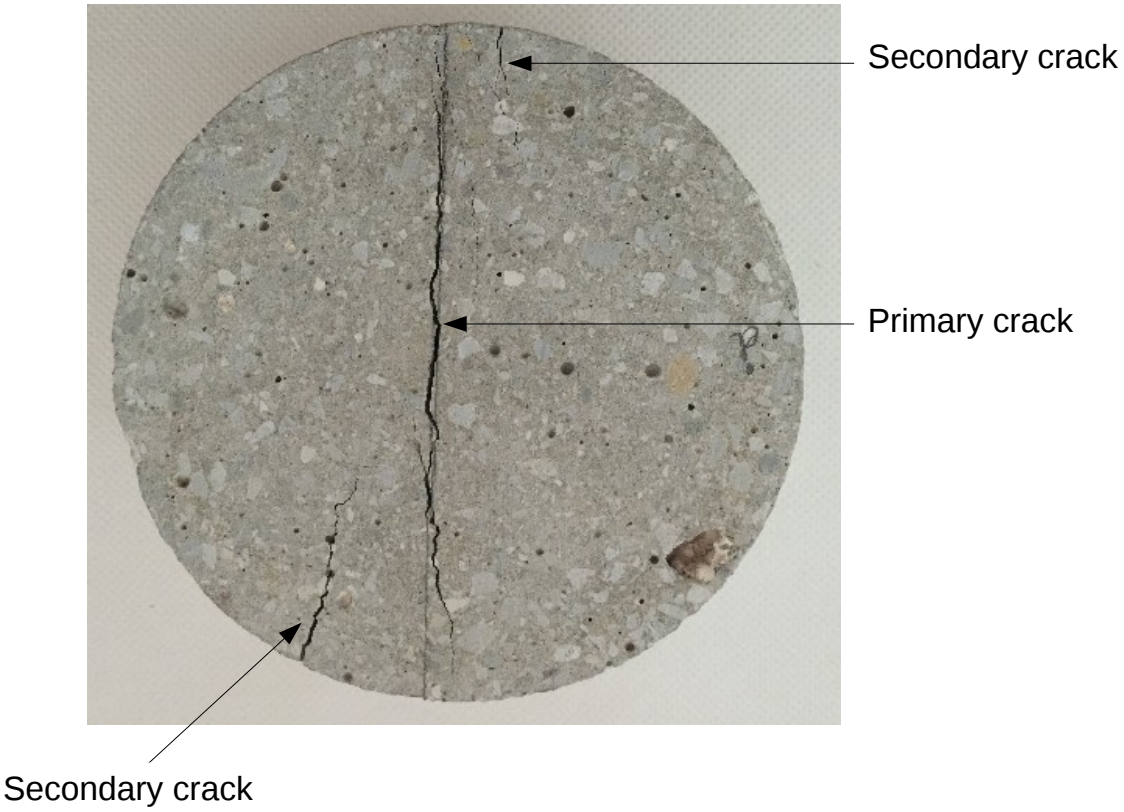

Figure 4.18: Mortar cylinder 110 mm x 50 mm specimen with two types of cracks.

(a)

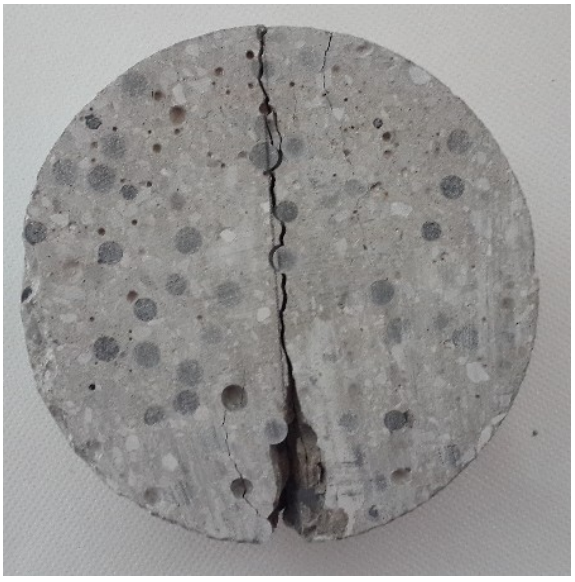

(b) (c)

Figure 4.19: Cylinder 110 mm x 50 mm specimens. Aggregate diameter 2 mm (a) aggregate diameter 6 mm (b) aggregate diameter 10 mm (c).

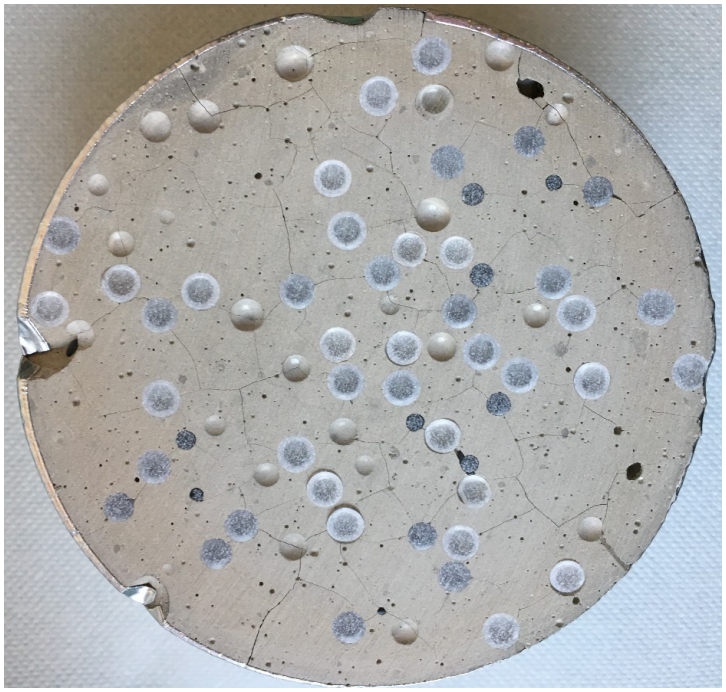

(a)

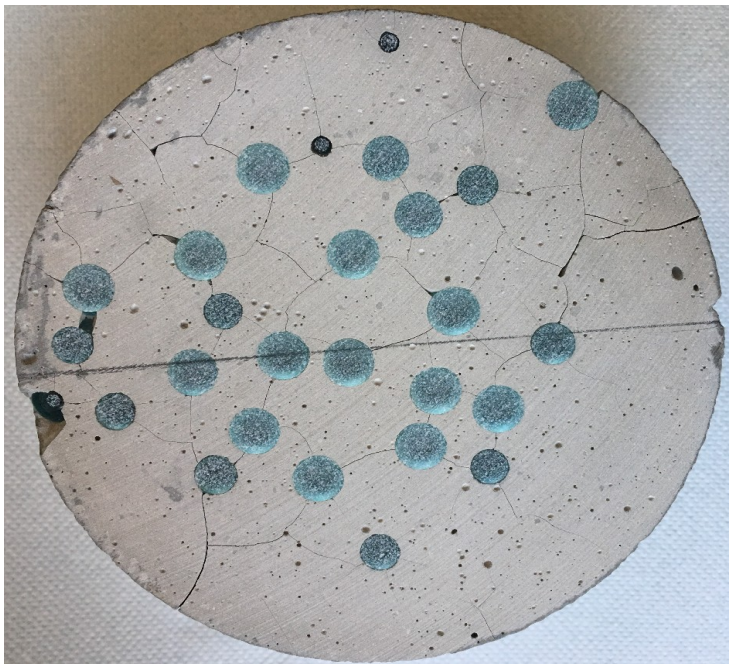

(b)

Figure 4.20: Cylinder 110 mm x 50 mm cement paste specimens. Aggregate diameter 6 mm (a) aggregate diameter 10 mm (b) .

4.3.3 Load-COD relationship

To investigate the crack opening displacement (COD) under loading, cylinder specimens were examined, 110 mm diameter and 50 mm thickness. These specimens were tested in diameteral loading. The distribution of load was through two compression platens of the MTS machine. There are many parameters that affect this test and permit or not to get complete pre-peak as well as post-peak behavior. The complete behavior that we want to get is observed in Figure (4.22) and named ***TypeI***. Therefore, ***TypeII*** test, with snap-back means for us failed tests. In order to understand how to get ***TypeI*** response, the effects of attachment size, sensors numbers and attachment type have been investigated in this study. Furthermore, the loading machine parameters have also been analyzed in order to get ***TypeI*** response (by PID regulation).

4.3.3.1 Effect of the COD sensors attachment size

Two electrical displacement gauges with accuracy of 0.02 microns were used in this test, as shown in Figure (4.21). Each one was fixed on each side of the specimen by using two aluminum plates like knifes which were glued by mixing epoxy. When the load was applied, two types of response under loading were then noticed, one where the COD always increased and the other with a snap-back, that means the COD decreased with the loading. On the other hand, the type of response depends on the specimen geometry and the loading set-up. The previous mentioned behaviors depend on the size and position of two aluminium plates, see Figure (4.23), i.e. when the aluminium plates were nearby the center of specimen that will be resulted behavior ***TypeI***, while these plates were faraway the center which will be resulted behavior ***TypeII***.

Figure (4.24) shows the relationship between the applied load and crack opening

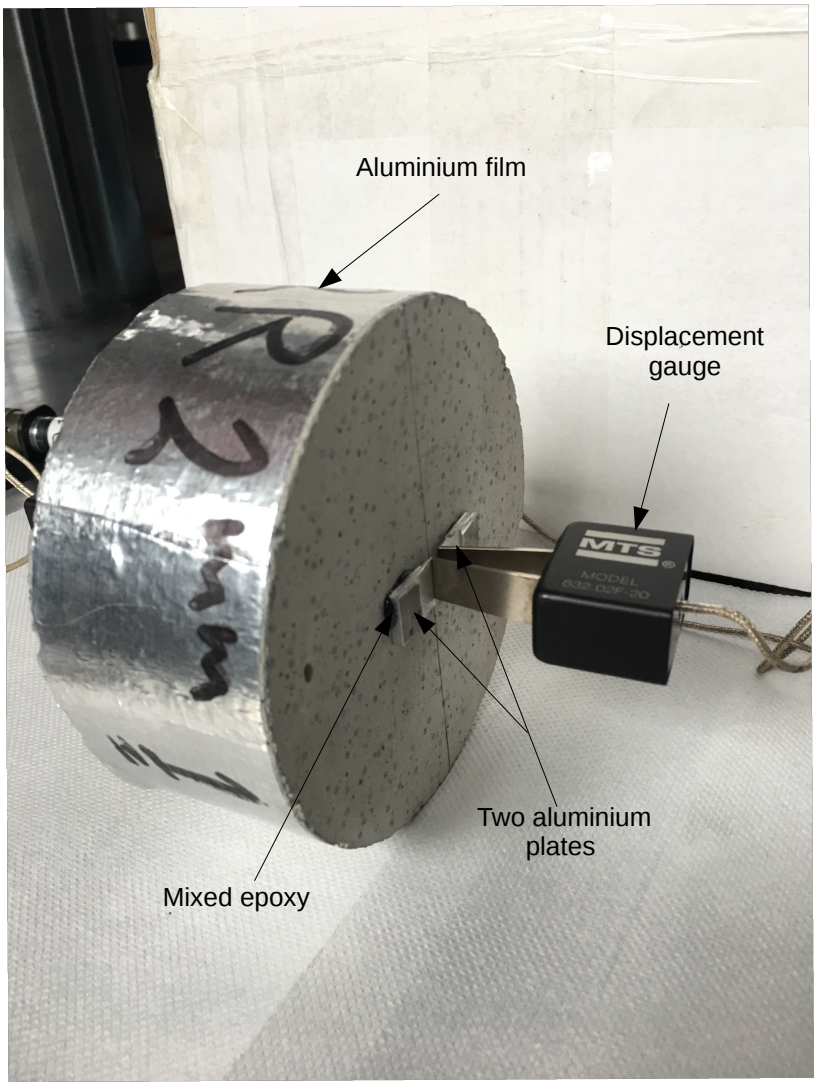

Figure 4.21: Cylinder 110 mm x 50 mm specimen within the set-up of the electrical displacement gauges and aluminium plates present on 2 specimen's sides.

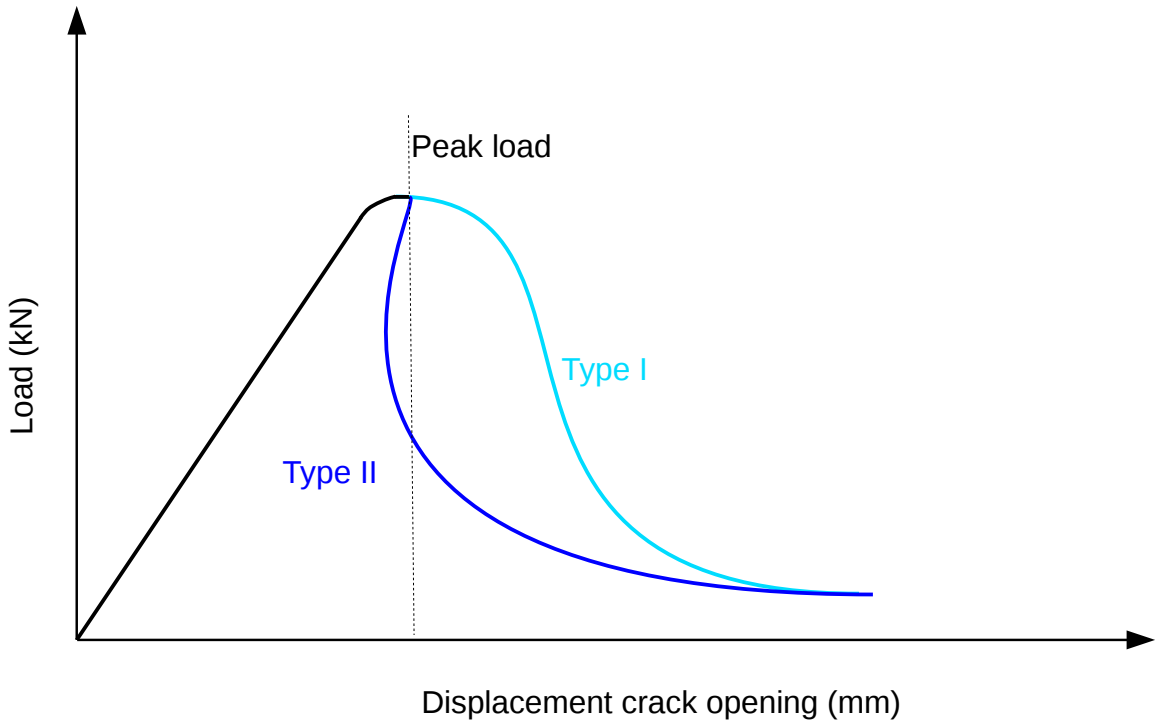

Figure 4.22: Relationship between the applied load and displacement crack opening. Two types of response for cylinder specimen according to aluminium plates' position.

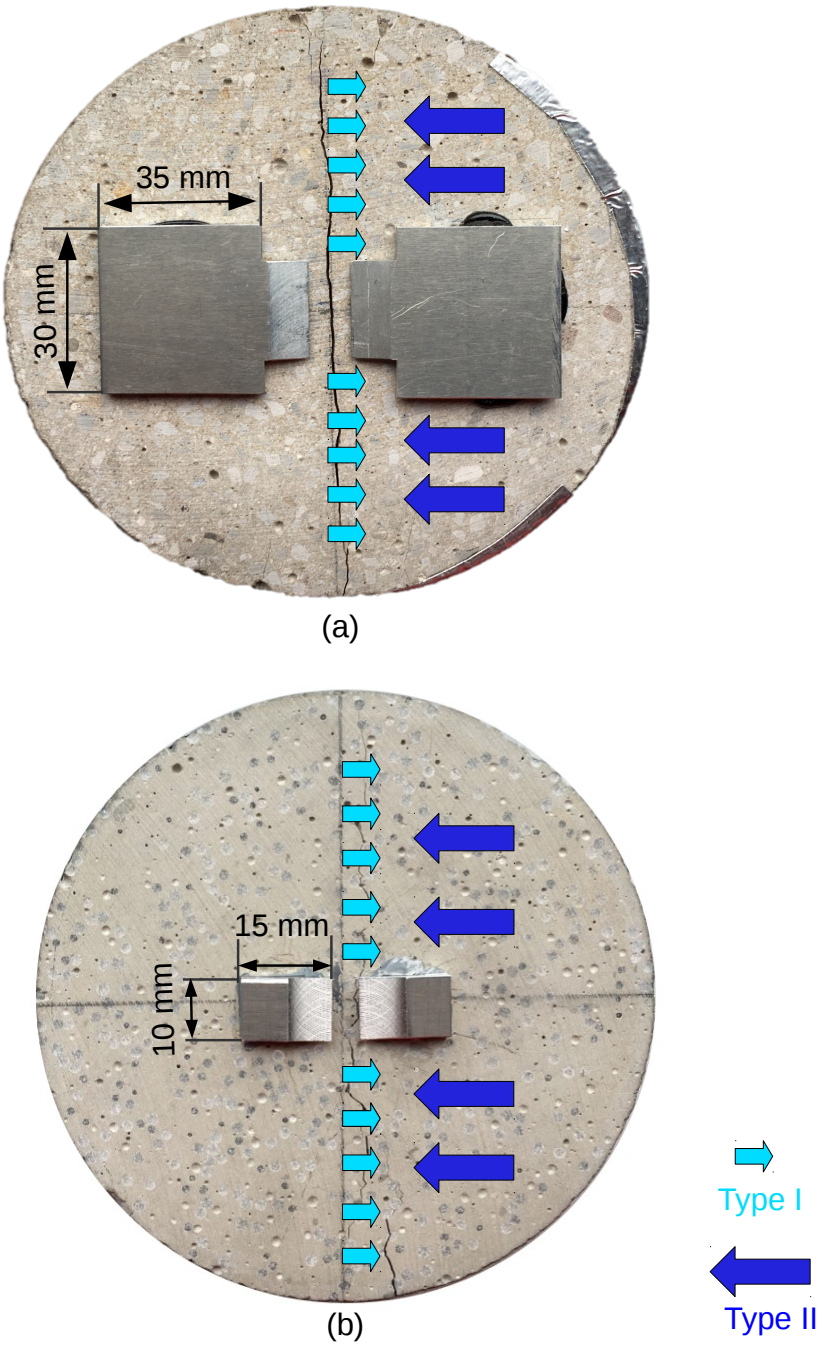

Figure 4.23: Cylinder 110 mm x 50 mm specimens with representation the two types of response for concrete beyond the peak loading.

displacement (COD1) for cyclic loading tests with small aluminium plates with dimensions 10 x 15 mm. The crack opening displacements (COD1 and COD2) at two faces of cylinder specimen were digital calculated. The control parameter, the average loading, was increased at a constant rate of 0.1 kN/s. The test results were plotted by the curves of the crack opening displacement (COD1 and COD2) as a function of the applied load. It can be observed that the slope of the loading and unloading phases decreased after each cyclic loading, that means the stiffness of the concrete was decreased due to cracking. We noticed that the slope for the aluminium plates with dimensions 30 x 35 mm is lower than for small plates, i.e. the crack opening displacement (COD2) is twice of COD1 for the same load level, and the same specimen, as shown in Figure (4.25).

Figure (4.26) shows the relationship between the crack opening displacement and the applied load with two size of plates. Here, we remark that the slope of the curves were reduced with cyclic loading for two faces probably due to the micro cracking. In addition, this slope for small plates $(\boldsymbol{S})$ was more steep than for the big ones $(\boldsymbol{B})$. That means that behavior of material depends on the geometrical properties of plates and their position within the splitting tensile test. While the deformation between two plates were gave nearly the same behavior in the elastic phase for two size of plates, see Figure (4.27).

Figure (4.28) shows the relationship between the crack opening displacement and the applied loading for two specimens of the same mixture. The notation $(\boldsymbol{R})$ refers to the cylinder specimen under loading without the two hollow aluminium cylinders, while $(\boldsymbol{SS})$ refers to the cylinder specimen with two aluminium cylinders. This relationship shows that the mechanical behavior of the cylinder specimen is independant on the hollow aluminium cylinders. By this test permits to validate our set-up. In the following test, we choose small plates, which permit to get crack opening without integration of the elastic behavior of the zones placed

for a way from crack position.

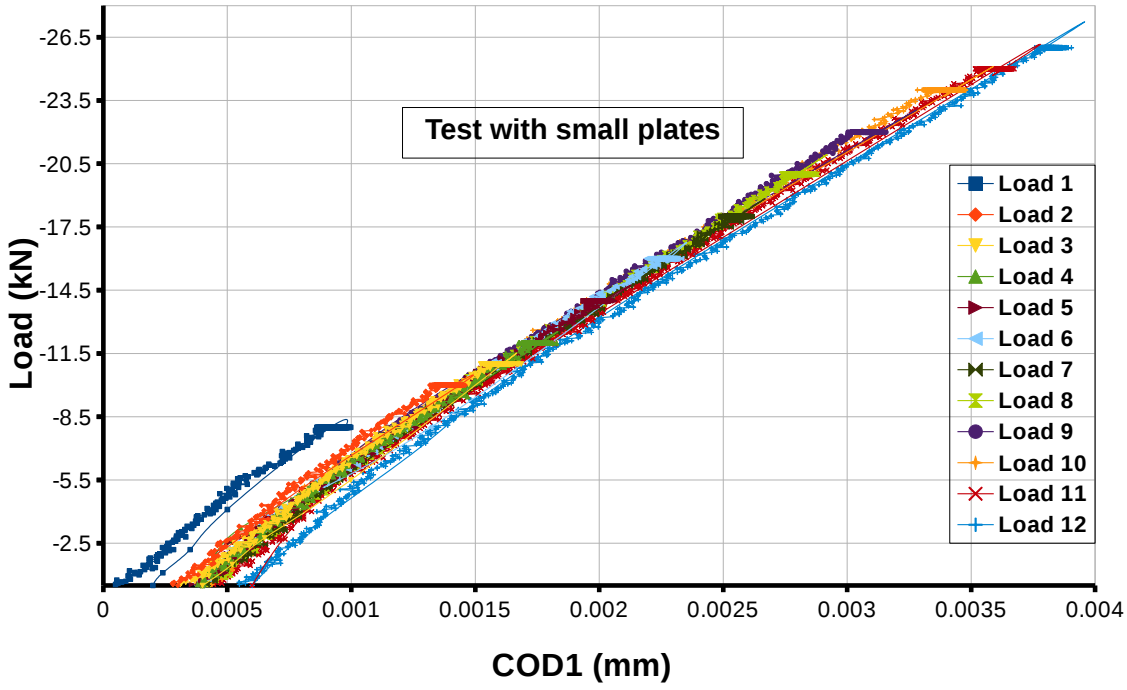

Figure 4.24: Relationship between the applied load and COD1 for twelve cyclic loading tests on the same specimen with two aluminium plates with dimensions 10 x 15 mm.

4.3.3.2 Effect of the COD sensors attachment type (epoxy)

Through this test, was noted the influence of the epoxy type before loading on the crack opening displacement (COD), caused by sliding of two aluminium plates on concrete surface exposed to humidity and temperature laboratory conditions.

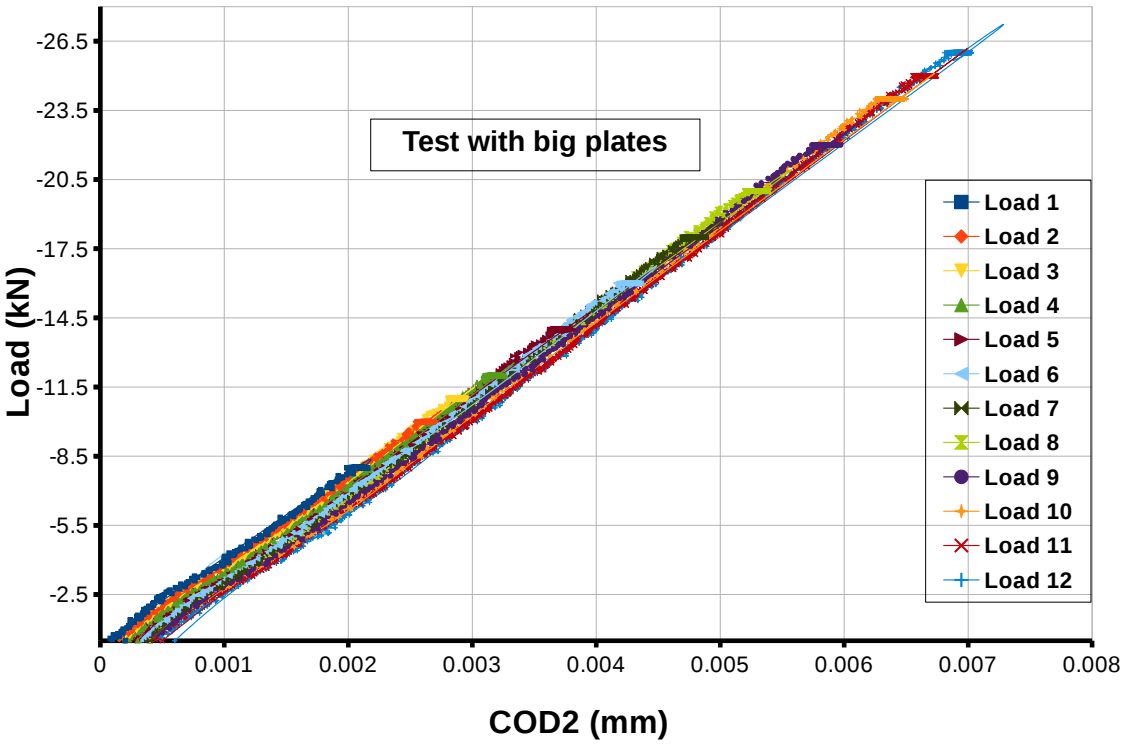

Figure 4.25: Relationship between the applied load and COD2 for twelve cyclic loading tests on the same specimen with two aluminium plates with dimensions 30 x 35 mm.

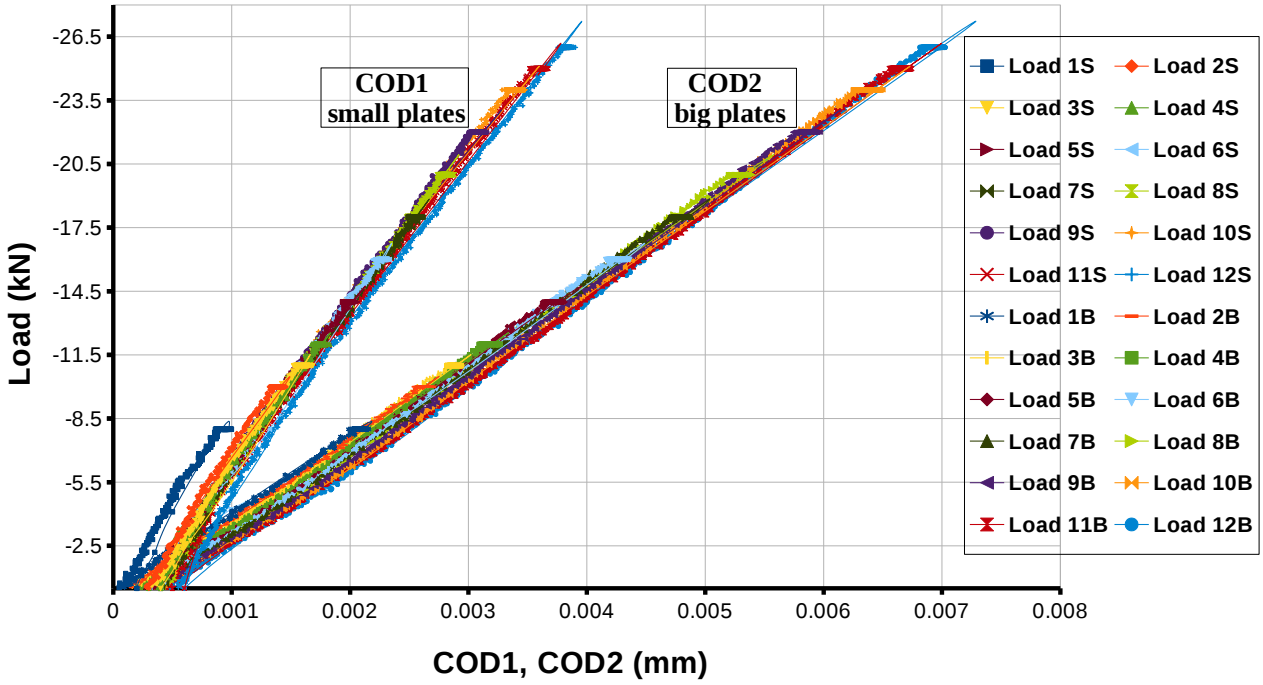

Figure 4.26: Relationship between the applied load and COD1-COD2 for twelve cyclic loading tests on the same specimen with two sizes of aluminium plates, small ones $(\boldsymbol{S})$ with dimensions 10 x 15 mm and big ones $(\boldsymbol{B})$ with dimensions 30 x 35 mm.

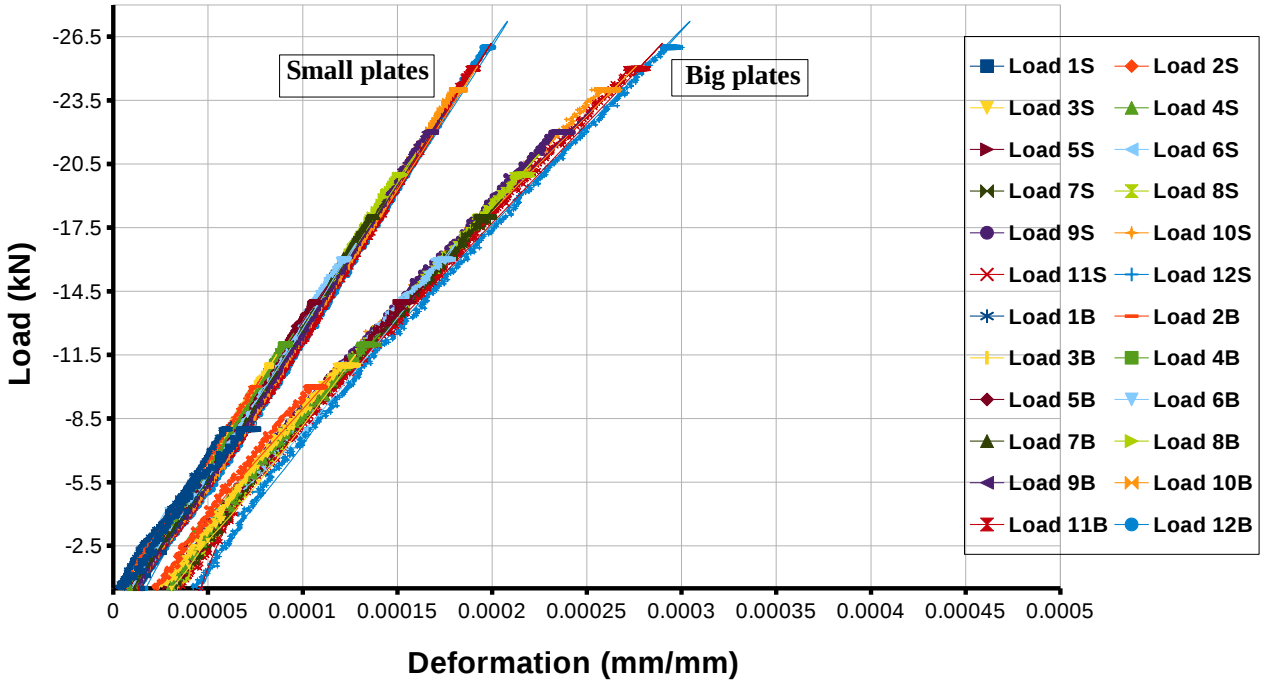

Figure 4.27: Relationship between the applied load and deformation for twelve cyclic loading tests on the same specimen with two sizes aluminium plates, small ones $(\boldsymbol{S})$ with dimensions 10 x 15 mm and big ones $(\boldsymbol{B})$ with dimensions 30 x 35 mm.

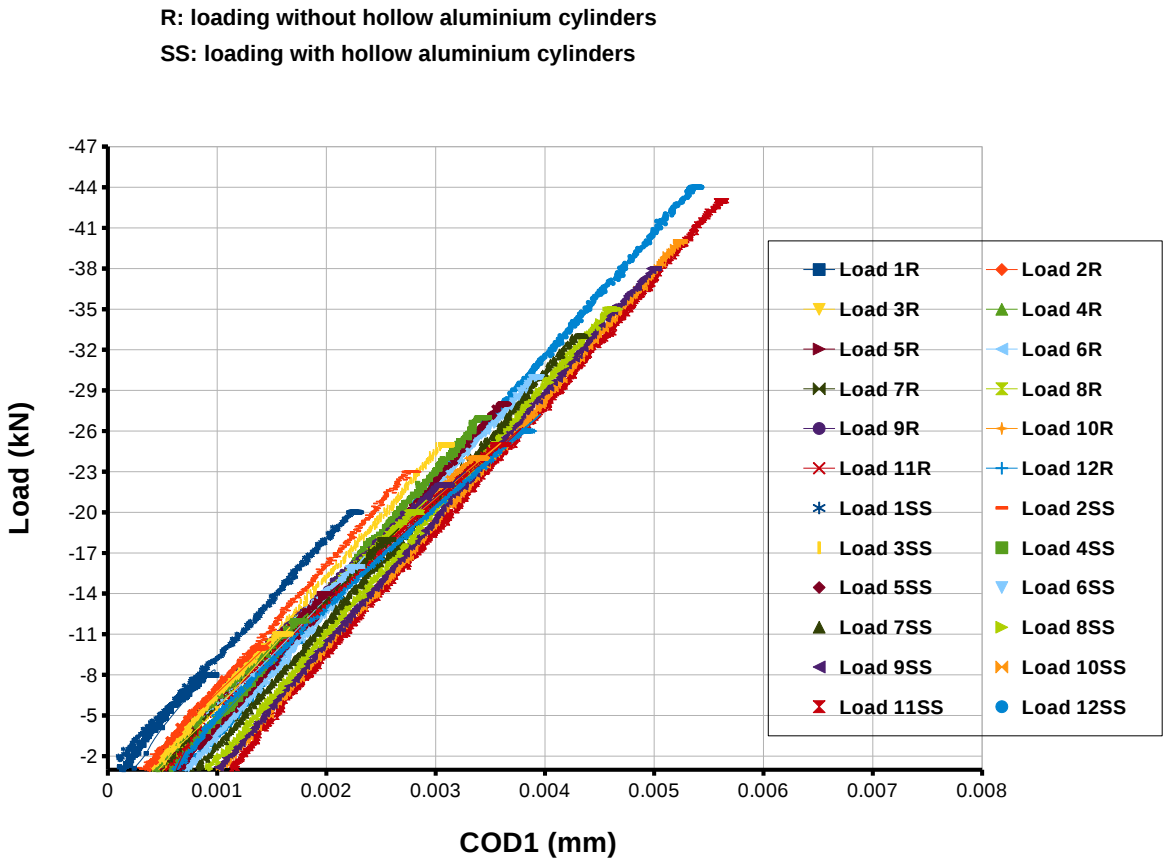

Figure 4.28: Relationship between the applied load and COD1 for twelve cyclic loading tests on the two specimens of one mix, with and without hollow aluminium cylinders.

Figure (4.29) shows the relationship between the COD with time for two types of mixed epoxy at two sides of a specimen. The first one is POLYFIX (epoxy A) that contents methylene diphenyl diisocyanate (isomers and homoloques) and the second one is LOCTITE EA 3450 (epoxy B). One can see that the COD for the epoxy $\boldsymbol{B}$ is much lower than epoxy $\boldsymbol{A}$. COD for epoxy $\boldsymbol{B}$ becomes is stable beyond **250000** s ($\approx$ 2 days). For epoxy $\boldsymbol{A}$, the COD value becomes stable beyond **262000** s ($\approx$ 3 days). However, we prefer to use epoxy $\boldsymbol{A}$ for practical reasons related to plates remove and recycling it for the next tests.

In order to get ***TypeI*** responses, we have choose to use 2 gauges. The two gauges were perpendicular to the loading direction on the two sides of a specimen, where the crack opening displacement at sides one and two were noted as COD1 and COD2, respectively. COD1, COD2 and the average COD were recorded during loading test period.

The test results are plotted by curves of COD1, COD2 and the average COD in function of time of loading, see Figure (4.30). It can be observed that the behavior of a specimen under diametral load is similar at the two sides in the early pre-peak phase see Figure (4.26). In addition, the average COD values are between the values of COD1 and COD2, therefore this data give good indications to carry a Brazilian splitting test (BSTT), the average COD. Figure (4.31) shows the relation of the tensile loading as a function of average COD under sequential loading. This data refers the decreasing in the modulus of elasticity with the increasing of the intensity and of number of cycles.

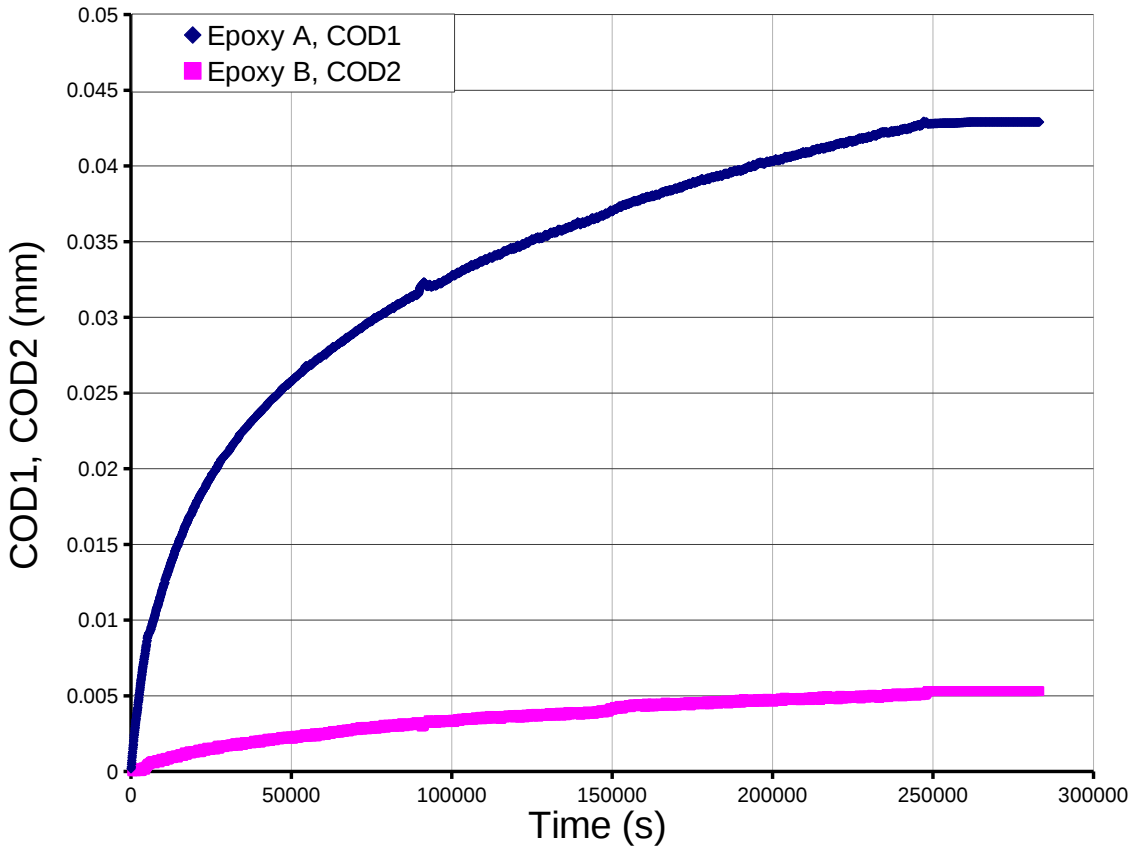

Figure 4.29: Relationship between the displacement crack opening for two types of epoxy (A and B) and time, before loading the specimen.

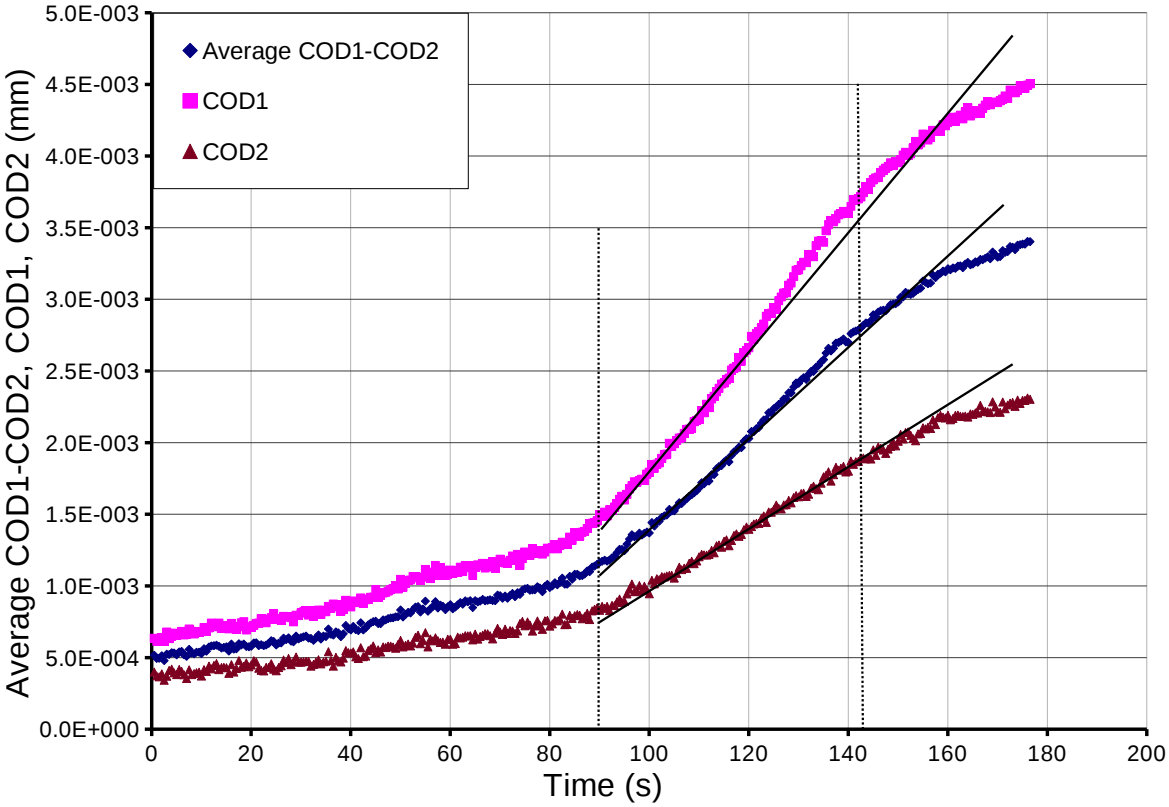

Figure 4.30: Relationship between the displacement crack opening for two gauges placed at each specimen side and their average (epoxy ***A***) during loading.

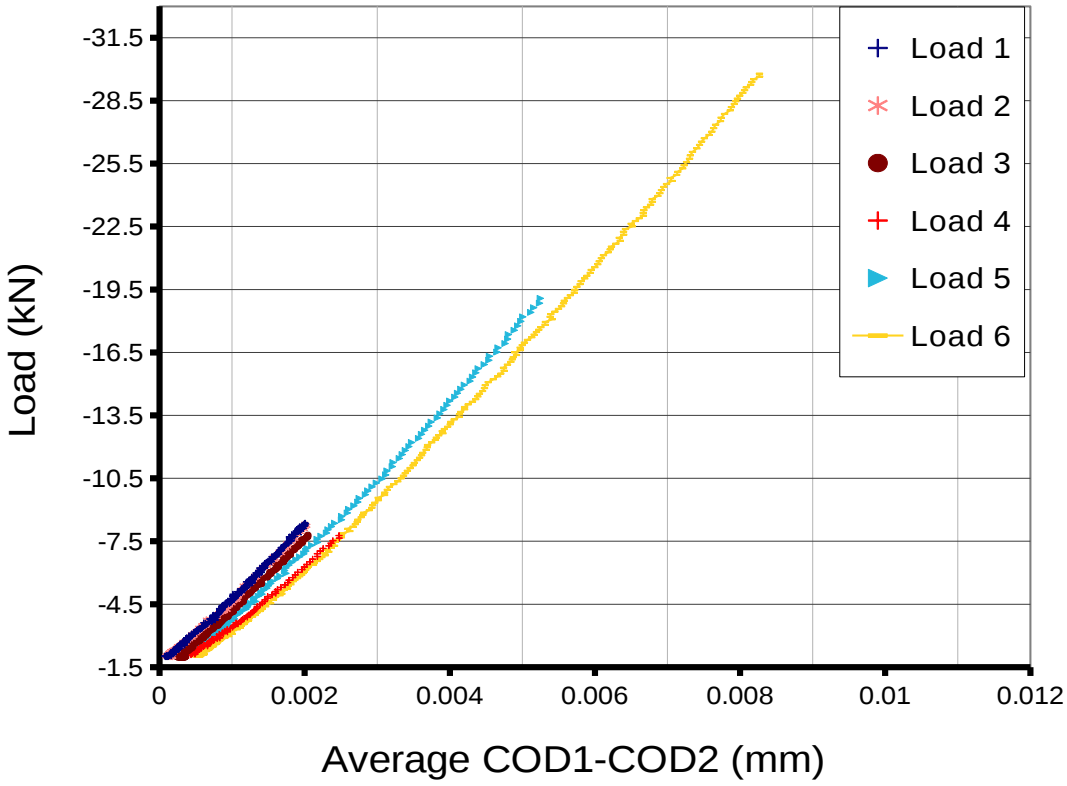

Figure 4.31: Relationship between the applied load and displacement crack opening for six sequential loading tests on the same specimen.

4.3.3.3 PID control

Closed-loop control (CLC) can be defined simply as the process by which a desired response is continuously obtained from a system by adequately modifying its input [Gettu et al., 1996]. Figures (4.32 a and b) show respectively a flowchart of a OLC (open loop control) and of a CLC system. To obtain a desired response ***TypeI***, (see Figure (4.22)), a testing machine with CLC system should be used. In literature can be found the first testing machines using the CLC system, (see Hudson et al. [Hudson et al., 1972]), which may control load, loading rates, displacement, and displacement rates. This type of testing controlled machines has been developed and led to the increased using in experimental works for testing brittle materials, such as concrete and rock that fail suddenly under loading at the peak-load.

A commonly used configuration is the PID controller, where the letters stand for the proportional, integral, and derivative actions generated by the controller, see Gettu et al. [Gettu et al., 1996]. Equation (4.4) refers to the general control signal:

$$\boldsymbol{u(t) - K_P e(t) + K_I \int e(t)dt + K_D \frac{d}{dt} e(t)} \tag{4.4}$$

where $\boldsymbol{t}$ is the time, $\boldsymbol{u(t)}$ is the controlled signal, $\boldsymbol{e(t)}$ is error signal, $\boldsymbol{K_P}$ is the proportional gain, $\boldsymbol{K_I}$ is the integral gain and $\boldsymbol{K_D}$ is the derivative gain. However, Equation (4.5) gives the error signal as shown below:

$$\boldsymbol{e(t) = r(t) - c(t)} \tag{4.5}$$

where $\boldsymbol{r(t)}$ is the reference input, $\boldsymbol{c(t)}$ is the output of the controlled variable.

Figure (4.33) represents concrete behavior obtained using average COD as the controlled signal $\boldsymbol{u(t)}$. This response has been obtained after the MTS machine PID manual regulation for a constant loading rate of 0.2 $\boldsymbol{\mu m/s}$ (0.2 $*\mathbf{10^{-3}}$ mm/s). One may observe the presence of the pre-peak and post-peak behavior without brittle failure. Furthermore, the peak average COD is about **6** microns, as already obtained by other researchers (see Choinska et al. [Choinska et al., 2008b], Wang et al. [Wang et al., 1997] and Rastiello et al. [Rastiello et al., 2015].

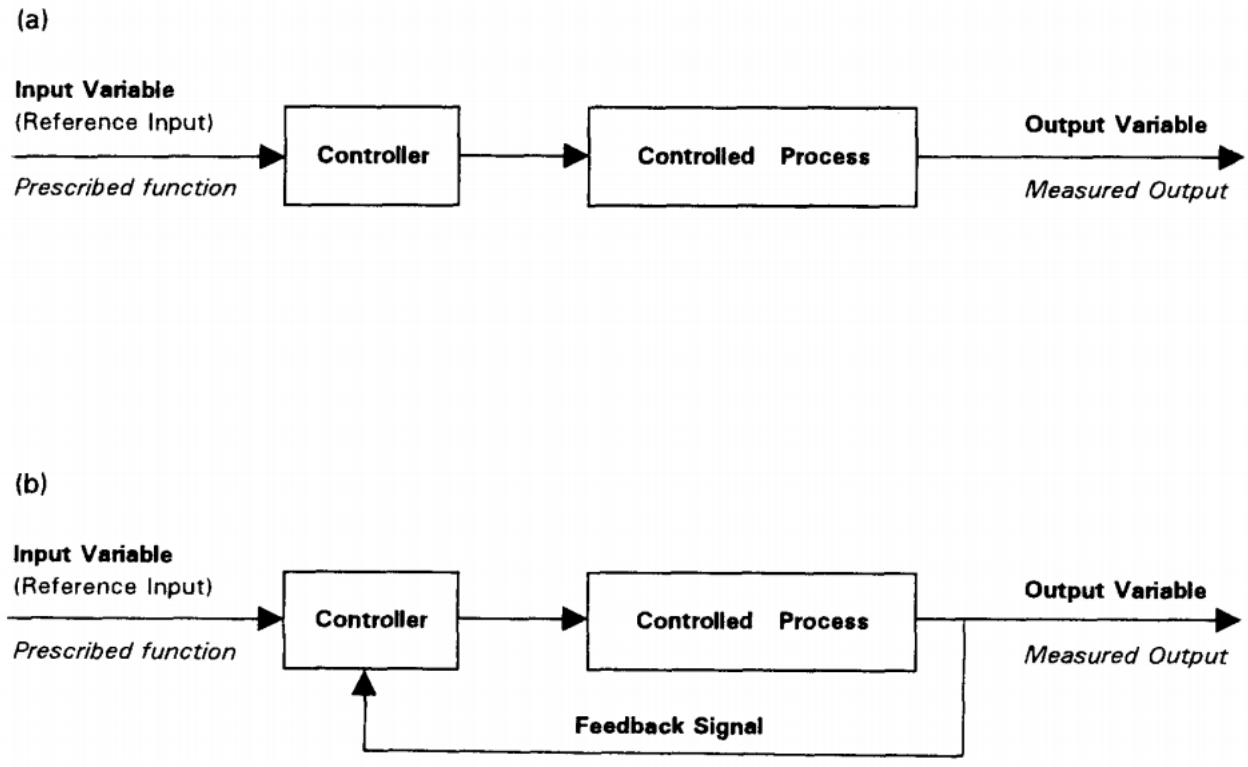

Figure 4.32: Open loop control (a); closed loop control, [Gettu et al., 1996].

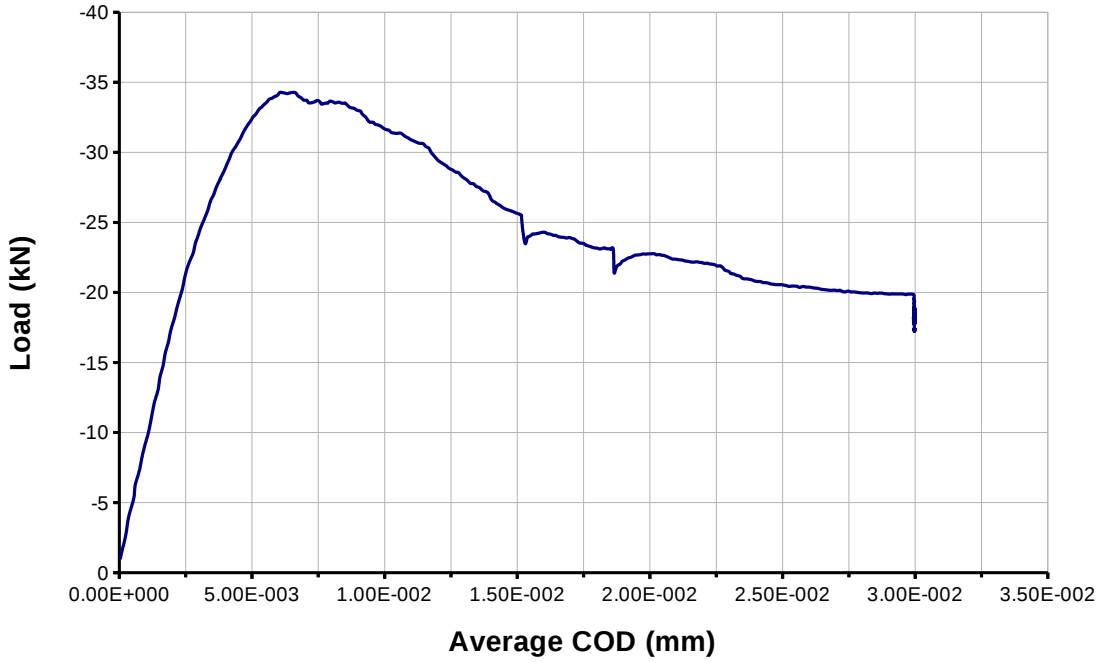

Figure 4.33: Relationship between the applied load and the average COD for cylinder concrete specimen within a COD-controlled, BSTT.

4.4 Hydro-mechanical behavior (force-controlled)

Force-controlled method is used in this study due to technical problems with the MTS machine. To investigate crack-permeability interaction with aggregate diameters ranging from 2 to 10 mm for cylinder specimens with dimensions 50 x 110 mm thickness and diameter respectively, the permeability of gas is measured for all specimens before loading (uncracked section) and the second measure is carried

out after loading (cracked section), then it compared with the reference specimens (without GB aggregate). All specimens were tested in air-conditioned room of 20 ± 1 ℃ temperature and 50 % RH.

A gas permeability test is performed to measure apparent permeability ($\boldsymbol{k_a}$) depending on equation (4.3) for uncracked specimens, then the intrinsic gas permeability ($\boldsymbol{k_v}$) is determined according to the Klinkenberg's principles for different pressures. At this stage is investigated the influence of aggregates size on the intrinsic permeability ($\boldsymbol{k_v}$) for unloaded specimens.

The specimens have been loaded in the BSTT as a cyclic loading between 50 and 90 % of ultimate loading. Then, they were submitted to CEMBUREAU permeability tests and $\boldsymbol{k_v}$ was obtained. The experimental results are compared with numerical results for hydro-mechanical model. Herein, the intrinsic gas permeability ($\boldsymbol{k_v}$) based on the CEMBUREAU and loading-gas permeability (LGP) are compared for uncracked sections. Then, the apparent permeability ($\boldsymbol{k_a}$) was measured at each stage of loading later.

4.4.1 Intrinsic gas permeability (k_v) of uncracked specimen

All specimens were oven dried at a temperature of 40 ± 1 ℃ for a period of 60 days, to remove evaporable water which could influence the test results. According to Klinkenberg's theory and equation (4.3), the intrinsic permeability can be computed by applying four different pressures varying for example between $\mathbf{0.5, 1.0, 2.0}$ and $\mathbf{3.0}$ bars. As shown in Figure (4.34), the linear relationships between the apparent gas permeabilities ($\boldsymbol{k_a}$) and inverse of pressure ($\boldsymbol{1/P_m}$) exist. Therefore, the determination of the intrinsic gas permeability ($\boldsymbol{k_v}$) according to Klinkenberg theory is possible.

According to the results for specimens with three sizes of GB aggregate, it can

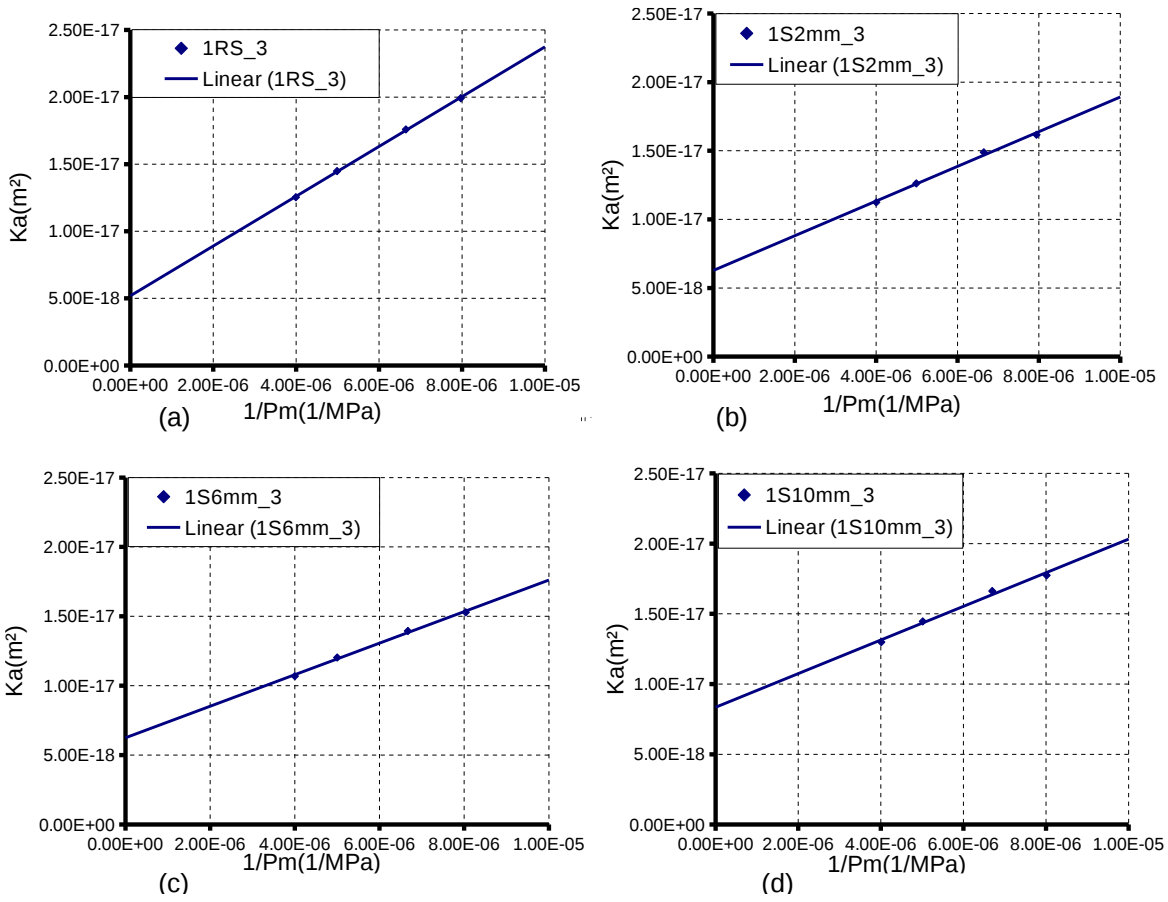

Figure 4.34: Determination of the intrinsic gas permeability ($\boldsymbol{k_v}$) from the measurment of the apparent gas permeability ($\boldsymbol{k_a}$) for four inlet gas pressures 0.5, 1.0, 2.0 and 3.0 bar. According to the Klinkenberg's principles and considering the lower inlet gas pressures. Four cylinder specimens are tested: mortar (a) aggregate diameter 2 mm (b) aggregate diameter 6 mm (c) aggregate diameter 10 mm (d).

be showed that the influence of aggregates size on $\boldsymbol{k_v}$ is not very significant but in agreement with literature review, see Grassl et al. [Grassl et al., 2010]. In the other words, the increasing of aggregate diameter leads to increase of the intrinsic gas permeability, i.e. the capillary pores are surrounding the larger aggregates more than that surrounding the smaller aggregate and the path of flow in cylinder specimens with larger aggregate is shorter than for the specimens with the smaller aggregate. These experimental results are concordance with experimental mechanical evolution see Figure (4.17). Figure (4.35) presents the relation between the intrinsic gas permeability ($\boldsymbol{k_v}$) with aggregate diameters for four groups of cylinder specimens and is compared with the numerical model, for which permeability values are nearly independant on aggregates size.

Some of previous studies have presented the influence of aggregates size on permeability of concrete see for example which of [Fabien, 2012] who explained the gas permeability is increasing according to increase of aggregates size, also the permeability for specimens when used cement type CEM III is more than that the specimens with cement type CEM I. The reason of this increasing due to the W/C ratio, i.e. cement type CEM III is more sensitive under the dry conditions than the cement type CEM I. Grassl et al. [Grassl et al., 2010] reported the increase of permeability with the increase of aggregates size. Peng [Peng, 2009] explained this increase due to increase of microcracks surrounding the larger aggregate caused by the shrinkage effects more than for the smaller aggregates. Basheer et al. [Basheer et al., 2005] found the air permeability increases with the increase of aggregates size and explained this tendency by two reasons: firstly the reduction in the tortuosity of the flow path occurs due to increase of aggregates size, secondly higher W/C ratio with larger aggregate would result in a higher porosity. Therefore, the increase of fine-to-coarse aggregate ratio from 0.5 to 0.7 leads to decrease of the air permeability of the concrete. Pereira et al. [Pereira

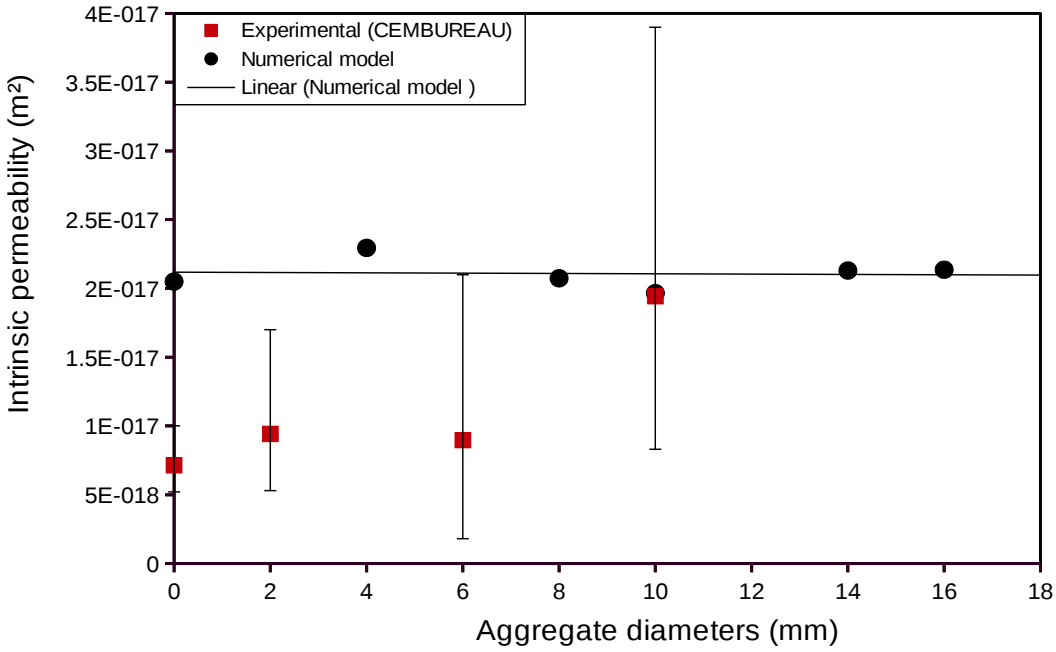

Figure 4.35: Relationship of intrinsic gas permeability ($\boldsymbol{k_v}$) from the measurment of the apparent permeability ($\boldsymbol{k_a}$) for four groups of cylinder specimens with aggregate diameters 2, 6, 10 mm and mortar. According to the Klinkenberg's principles and considering the lower inlet gas pressures.

et al., 2009] pointed out that the concrete mixtures produced higher porosity and air permeability when used larger aggregates size and it explained the reason of this behavior since the increasing of the aggregates size contributes not only to the increase of interconnectivity of capillary pores and its path length, but also to the increase of porosity at the interface zone between the cement paste and aggregate. This results are also in agreement with the study of Mehta [Mehta and Monteiro, 2006].

4.4.2 Coupling between the gas permeability and crack opening

To study the interaction between the mass flow and geometrical properties of crack, two methods are used in this study to measure the apparent permeability to nitrogen as a neutral percolating gas. These methods are the following: the CEMBUREAU one see Figure (4.11) performed after unloading of the specimens, and the LGP one performed under loading see Figure (4.15).

4.4.2.1 CEMBUREAU method (after unloading)

Figure (4.11) shows details of this method. The gas permeability tests were performance on the cracked specimens by controlling loads using the Brazilian splitting test. The specimens were then placed in the permeability cell and gas pressure gradient of **1** bar (0.1 MPa was applied) for a uncracked and cracked specimens and **2** bars (0.2 MPa) in confinement cell, see Figure (4.12). The gas pressure gradient (1 bar) was applied for 30-minutes to reach steady state, then flow rate was recorded from the test beginning and gas permeability was calculated depending on equation (4.3). The cracked specimens were obtained by applying up to 5-cycles loading of 50-90 % the ultimate loading maintained for 1-minute before unloading.

COD1 and COD2 are recorded after all the cycles of loading and unloading, and then is calculated the cumulative average COD.

After up to 5-cycles loading, the specimen was then put in permeability cell as shown in Figure (4.12) during 5-minutes, time needed to place a specimen in the cell. The gas permeability test then started. Each gas permeability test consists of apparent permeability ($\boldsymbol{k_a}$) measurements under **1** bar of pressure gradient see equation (4.3). The test results are plotted with the relationship between the gas permeability and the average COD in Figure (4.36). It is observed that the uncracked mortar specimens have lower permeability than the other specimens, i.e. gas permeability increases with the increase of aggregates size for sound specimens. Exactly as for the results presented in Figure (4.35), we explain this phenomenon due to more porosity and shorter flow path through specimens with bigger aggregates. It may be also noticed that gas permeability increases as respect to the crack opening, see Figure (4.36).

4.4.2.2 Loading-gas permeability (LGP) method (after unloading)

Figure (4.15) shows details of experimental test for the coupling between gas permeability and crack opening. Furthermore, the specific pressure regulators were used according to the pressure range, herein it is only **1** bar and the inlet gas pressure was read using a digital pressure gauge with an accuracy of 100 Pa.

Permeability measurements were carried out in an air-conditioned room (20 ± 1 ℃). Each gas permeability test consists of apparent permeability ($\boldsymbol{k_a}$) measurements with **1** bar pressure gradient see equation (4.3). The outlet gas percolating through the concrete specimen was computed in atmospheric pressure conditions using a gas flow meter, see Figure (4.15). Establishing a steady state of gas flow before actual computations requires a significant amount of time, varying from 15 to 30 min for cracked and uncracked specimen. Herein, the inlet flow was used to

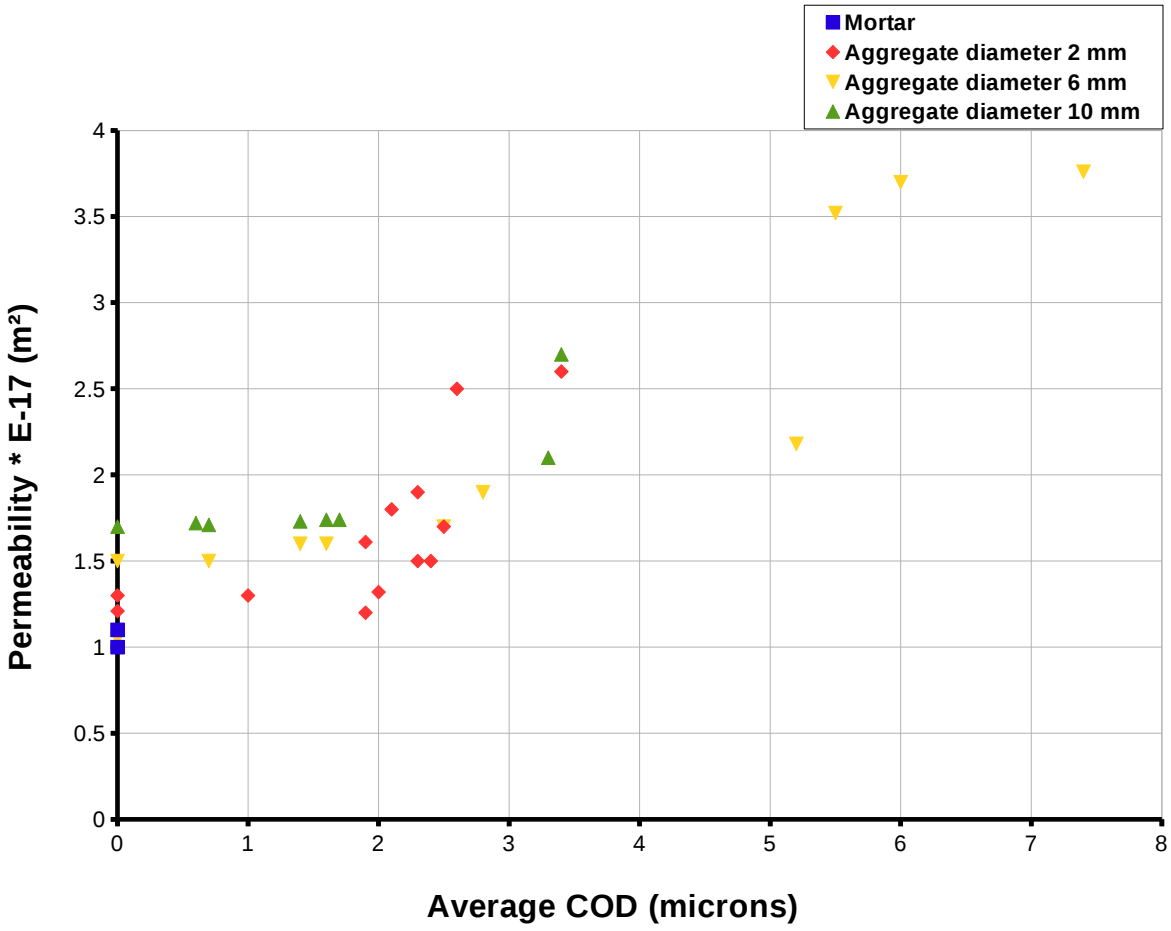

Figure 4.36: Relationship between gas permeability and the average COD for four groups of cylinder specimens with aggregate diameters (glass beads) of 2, 6, 10 mm and mortar using the CEMBUREAU method (after loading).

determine gas permeability at end of 10-minutes interval after attending the steady state flow. The cracked specimens were obtained by applying up to 5-cycles loading of 50-90 % the ultimate loading maintained for 1-minute before unloading. COD1 and COD2 are recorded after all the cycles of loading and unloading, and then is calculated the cumulative average COD.

As for the CEMBUREAU method (see section 4.4.2.1), 1-minute after unloading, the average COD decreases by few microns. In addition, it was noted the COD2 placed on the inlet specimen face increased about **0.3** microns when the gas pressure was starting then it was steady after few minutes. This increasing is due to that this side of specimen is under inlet pressure see Figure (4.41).

To investigate the coupling between gas permeability and crack opening, four groups of specimens were tested by varying GB aggregates diameter from 2 to 10 mm and comparing to the reference mortar specimens. Figure (4.37) shows the relationship between the apparent gas permeability (under 1 bar of relative gas pressure) and different cracks openings (COD average unloading). It was observed that for the mortar specimens have lower permeability than the other specimens with GB aggregates. Furthermore, the average COD influences on the gas permeability. It means that the increasing of the aggregates size and crack opening lead to an increase in gas permeability. The increase of aggregates size causes to increase of pores around the aggregate particle. In addition, the path of flow is smaller than for the specimens with small aggregates size. On the other hand, the increasing specific surface area for each aggregates particle increases the porosity between cement paste and aggregates and the distance that the transporting species has to travel across the matrix is decreased. The permeability increase is also due to the connectivity of microcracks. Therefore, the results from this experimental work also support findings from the numerical model, see Figure (3.30). Here, the coupling between crack opening and gas permeability is in agreement

with the other authors, for example, Grassl et al. [Grassl et al., 2010] who observed, permeability increase with the increasing of the aggregate diameter and decreasing of volume fraction. Picandet et al. [Picandet et al., 2009] pointed out that is the crack opening is smaller than 3 microns, thus the increase in the total gas flow through cracked samples is due to diffuse damage of the specimen. Care et al. [Care and Derkx, 2011] presented the correlation between the aggregate size and volume fraction with the permeability of gas, i.e. gas permeability depends upon aggregate size and its content. Peng [Peng, 2009] found the increasing microcracks surrounding the aggregate particles with the increasing aggregates size. Fabien [Fabien, 2012] pointed out that the gas permeability is increasing according to increase of aggregates size which used limestone crushed aggregates while in this study is used glass (siliceous) aggregates with smooth surface.

Finally, Table (4.4) presents the apparent permeabilities ($\boldsymbol{k_a}$) for uncracked specimens may be measured for two methods (CEMBUREAU and LGP). It may be observed that mortar specimens have an average permeability of **1.05** and **1.024** $\mathbf{m^2}$ for two methods, respectively under 1 bar gas pressure. Therefore, the average permeability increases from **1.255** to **1.7** $\mathbf{m^2}$ with increases aggregates size from 2 to 10 mm using CEMBUREAU method, and from **1.044** to **2.04** $\mathbf{m^2}$ using LGP (loading-gas permeability) method.

Table 4.4: The apparent permeability ($\boldsymbol{k_a * 10^{-17}\ m^2}$) under **1** bar gas pressure for uncracked cylinder specimens (initial permeabilities).

Specimens	**CEMBUREAU**	**LGP**
RS	1.1, 1.0	1.08, 0.967
RS-2mm	1.3, 1.21	1.13, 0.957
RS-6mm	1.05, 1.5	1.12, 1.34, 1.73
RS-10mm	1.7	2.3, 1.78

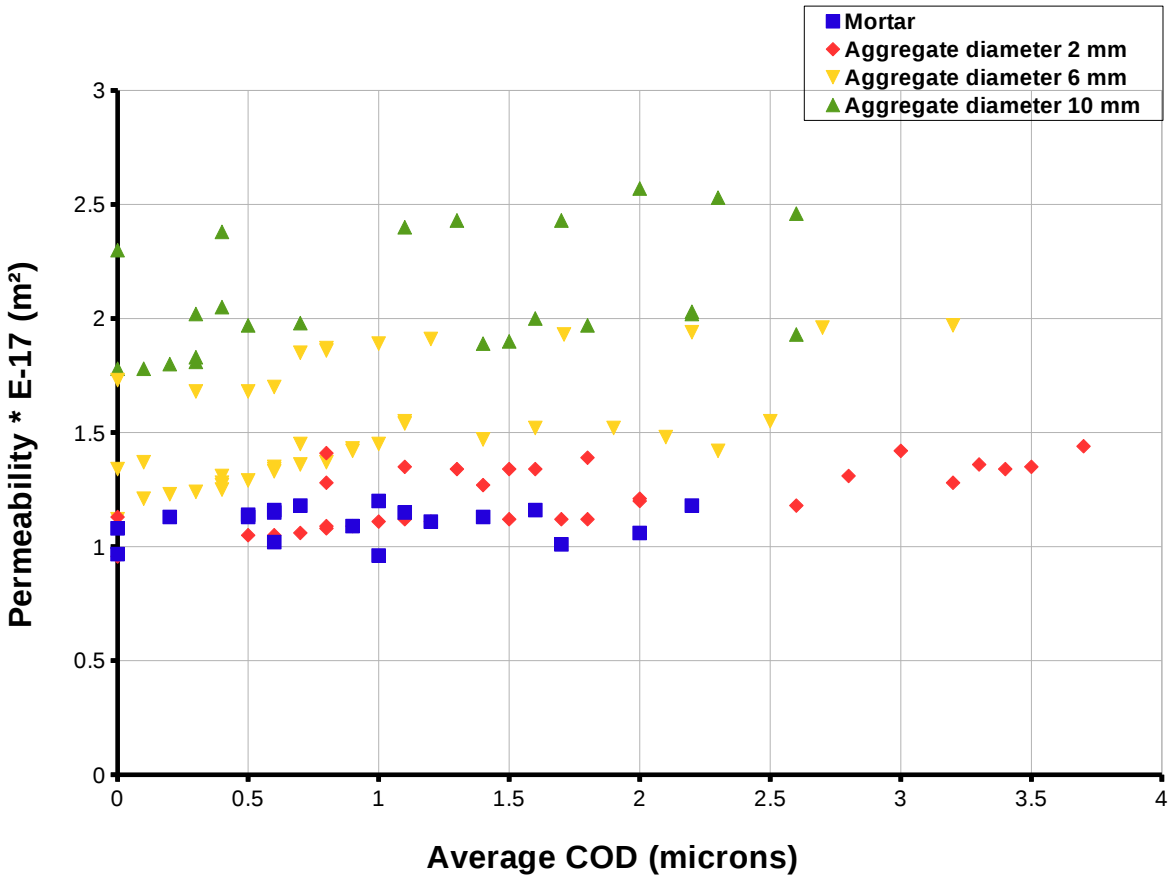

Figure 4.37: Relationship between gas permeability and the average COD for four groups of cylinder specimens with aggregate diameters (glass beads) of 2, 6, 10 mm and mortar using loading-gas permeability (LGP) method (after unloading).

4.5 Hydro-mechanical behavior (COD-controlled)

In this section, the influence of crack opening on gas permeability of concrete specimens is presented using the COD-controlled tests. That means the investigating of hydro-mechanical properties of concrete under splitting tensile test and gas pressure injection at the same time. Herein, the method of gas permeability determination under loading using the LGP set-up is employed. The experimental procedure is denoted in the next section (4.5.1). Then, the results are compared with obtained in the previous section concerning the force-controlled hydro-mechanical behavior.

4.5.1 Load-COD relationship within the LGP set-up

Figure (4.38) shows the relationship between the applied load and the average COD for a CEM I microconcrete specimen with natural crushed limestone aggregates ranging from 4 to 12 mm in diameter (see formulation according to Fabien [Fabien, 2012]. This Figure presents two parts: the first one pre-peak phase up to **42** kN (2.8 MPa) (peak load), and the average COD up to about **7** microns. In this phase, gas permeability was measured using the LGP method at the initial state (average COD equal to 0 microns), and then at the peak load see Figure (4.38). The second phase corresponds to the post-peak phase, for which the loading globally decreases for increasing average COD value up to **45** microns see Figure (4.38). In this second phase gas permeability was also measured using the same LGP method. Once the desired value of the average COD obtained, the latter was maintained during the permeability test to the gas injection at **1** bar of pressure. After permeability measurment, gas pressure was removed and loading was continued up to next desired average COD value. We have choosen a step of about $\mathbf{3-5}$ microns between each permeability measurement.

The observed vertical decreasing parts of the load-average COD curve provide a relaxation effects, accompanied by loading decrease, during gas injection and permeability test. Another observation concerns the decrease of the slope of the loading curve between the two mentioned parts: pre and post-peak ones. This behavior is due to damage phenomena (see Figure (2.5) according to Terrien [Terrien, 1980]).

The data from the two specimen sides (see Figures 4.38 and 4.39) show that the crack opening (COD2) is greater than on the other side (COD1). This means that the crack generally initiates and open on one specimen side (COD2) first and then propagates to the other side (see Figures 4.39 and 4.40). Therefore, one may observe that concrete specimen behavior under BSTT is 3D. The behavior is almost 2D in the early pre-peak phase and the becomes 2D at the final post-peak phase (see Figure 4.40 for average COD larger than **40** microns). This is the reason for which the meso-scale modeling is needed to predict 3D crack initiation and propagation in concrete. Furthermore, this 3D behavior is influenced by the aggregates size and position, as well as gas pressure. The latter will be designed in the next section (4.5.2).

4.5.2 Crack opening-gas permeability relationship

To investigate the influence of crack opening on gas permeability, the loading-gas permeability (LGP) method is used, for details see Figure (4.15). The behavior of unloaded concrete specimen under **1** bar of nitrogen gas pressure is shown in Figure (4.41 a), as pressure and flow evolution are shown in Figure (4.41 b). It may be noticed that the mass flow increases aspect to increase of gas pressure and it becomes constant latter. Gas is injected on the COD1 specimen side supplied with the up-stream cell (see Figures 4.14 a and b). Herein, the positive sign of COD1 and COD2 values shows that the pressure induces elastic extension on this

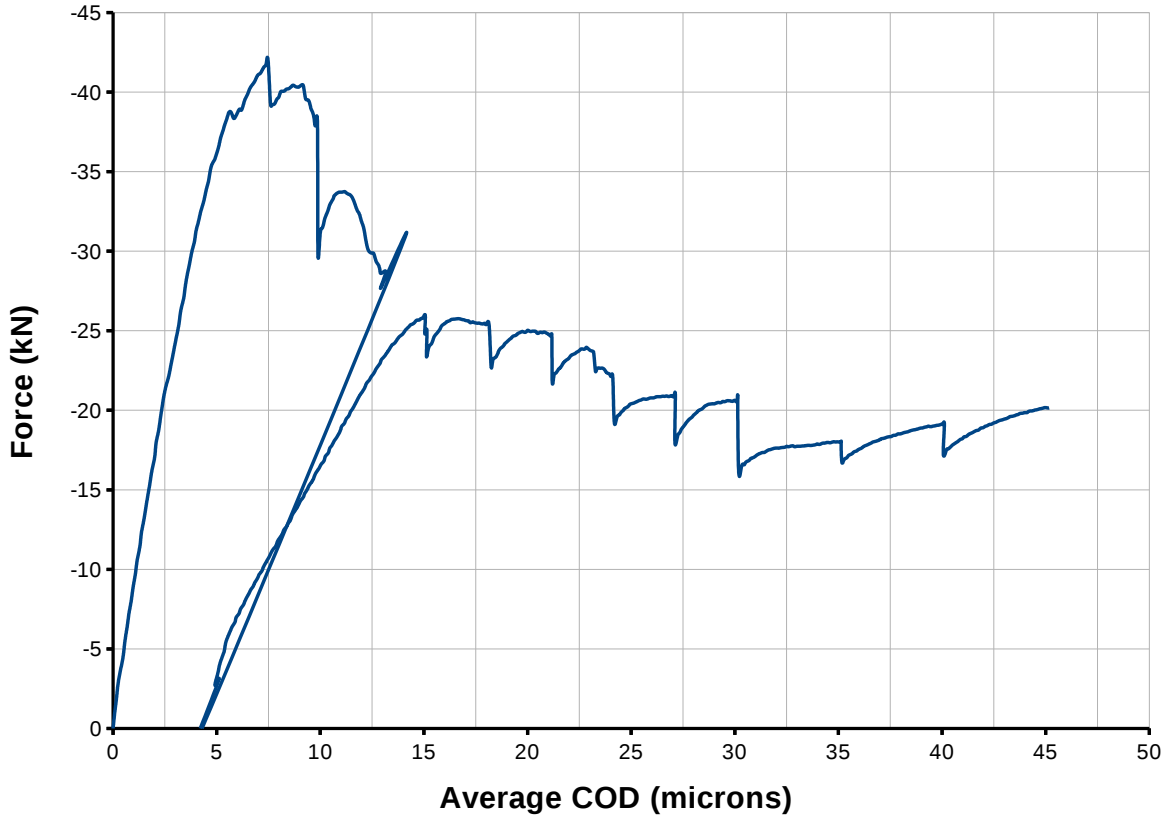

Figure 4.38: Relationship between the applied load and the average COD for cylinder concrete specimen within a COD-controlled, BSTT.

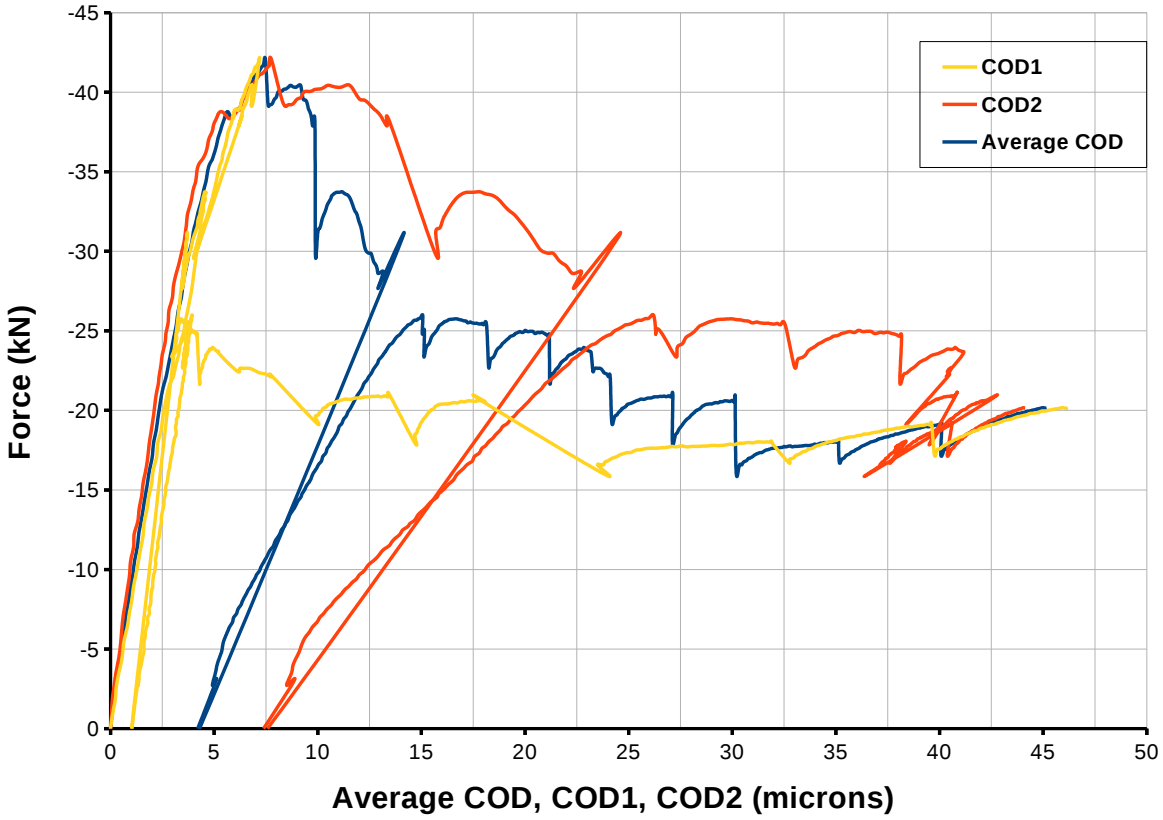

Figure 4.39: Relationship between the applied load and the average COD, COD1 and COD2 for cylinder concrete specimen for two phases within a COD-controlled, BSTT.

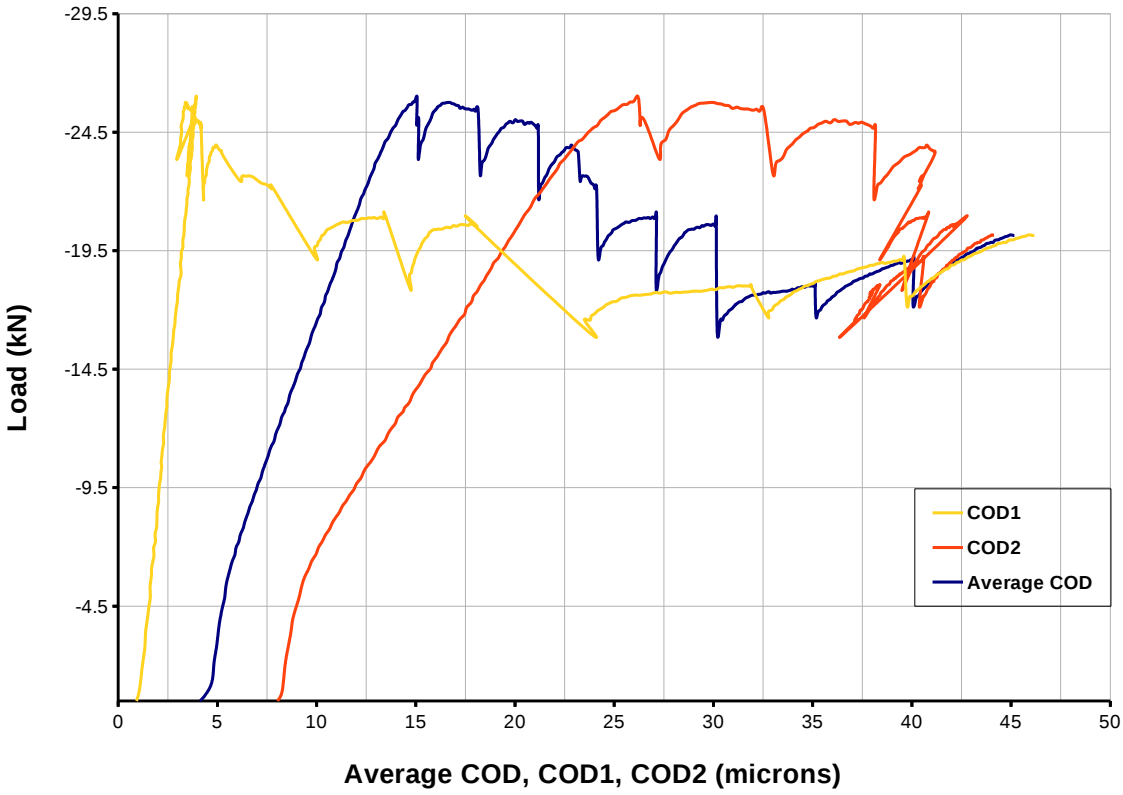

Figure 4.40: Relationship between the applied load and the average COD, COD1 and COD2 for cylinder concrete specimen within a COD-controlled, BSTT.

side. COD1 evolution is due to two reasons: the first one is pressure force effects on two metallic plates leading first to COD1 opening (= COD1 increase = extension) and the second one is the temperature decrease due to nitrogen properties (cool) resulting in epoxy shortening and therefore COD1 closing (= COD1 decrease = shortening). This behavior is in computation competition with the COD1 opening beyond **800** s, (see Figure 4.41 a) when the pores flow starts, (see mass-flow evolution in Figure 4.41 b). The COD1 evolution tends to get stable beyond **3000** s. COD2 evolution provides first opening probably caused by structural flexural effects of pressure, and then remains constant. Two stages were considered for gas permeability determinations: the first stage corresponds to unloaded specimen to measure initial apparent permeability under **1** bar gas pressure. This permeability is called $\boldsymbol{k_{init.}}$ and for microconcrete studied here was $\mathbf{0.411 * 10^{-17}}$ $\mathbf{m^2}$. The second stage corresponds to permeability measurements beyond the peak.

In fact, when the load dropped beyond the peak load the BSTT was continued up to different average COD values, (see Figures 4.38 and 4.39 in section 4.5.1). Once gas injected through a specimen at different post-peak loading levels, permeability was then calculated and the results presented in Table (4.5). As already mentioned in the previous section we have chosen to determine permeability evolution for every 3-5 microns of average COD value. Figure (4.42) shows the behavior of a cylinder specimen under applying load and gas pressure. The curve shows sigmoid-type evolution with 3 different kinetics: the first one ($\boldsymbol{A}$) produces due to micro-cracks development, the second one ($\boldsymbol{B}$) results from the connectivity of micro-cracks and cracks propagation and opening and the last one ($\boldsymbol{C}$) is probably due to cracks opening only. These indications are in agreement with other researchers Choinska et al. [Choinska et al., 2007], [Choinska et al., 2008a] Wang et al. [Wang et al., 1997], see Figures (4.43) and (4.44). It needs to be noticed that the 3-kinetics sigmoidal behavior is observed after tensile behavior as well as

for compressive behavior.

Figure (4.45) shows the relationship between the relative gas permeability and the average COD, COD1 and COD2. It may be noticed the gas permeability is globally increasing with crack opening values. Furthermore, beyond average COD of **40** microns, (see Table 4.5) all three evolutions fall on the same master curve. This behavior is in agreement with the mechanical model, (see Figure 4.40) and due to 2D behavior. However, the observed evolutions in Figure (4.45) provide us hydro-mechanical modeling of the permeability-crack opening relation in concrete. In fact, the risk of over-estimation or under-estimation of concrete permeability appears. By the way, it is important to note that the k-COD1 evolution don't provide sigmoidal behavior.

Table 4.5: Cracks opening values with gas permeability under **1** bar gas pressure for cylinder specimens.

COD1 (μm)	**COD2 (μm)**	**Av. COD (μm)**	**k_a (10^{-17} m^2)**
0	0	0	0.411
4	15.8	9.9	1.0
3.1	23.5	13.3	1.28
3.7	26.5	15.1	1.4
3.7	32.5	18.1	1.71
4.2	38	21.1	1.96
9.7	38.6	24.1	5.33
14.0	40.1	27.1	13
22.6	37.4	30.1	56
32.3	37.8	35.1	135
39.8	40.2	40.1	212
46.4	43.8	45.1	314

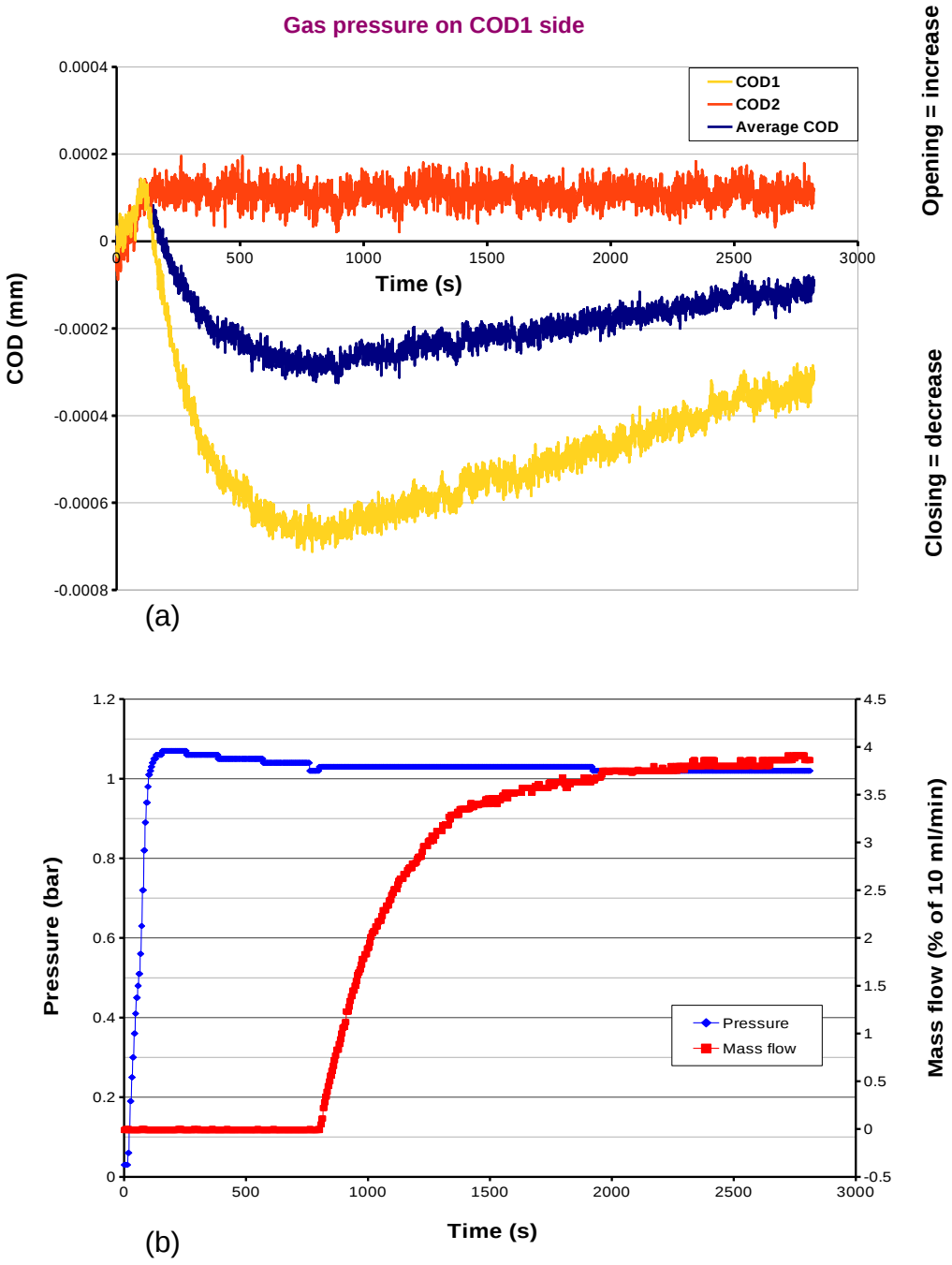

Figure 4.41: Relationships between the average COD, COD1 and COD2 and time (a) gas pressure and time (b) for cylinder concrete specimen under **1** bar gas pressure within a COD-controlled, BSTT.

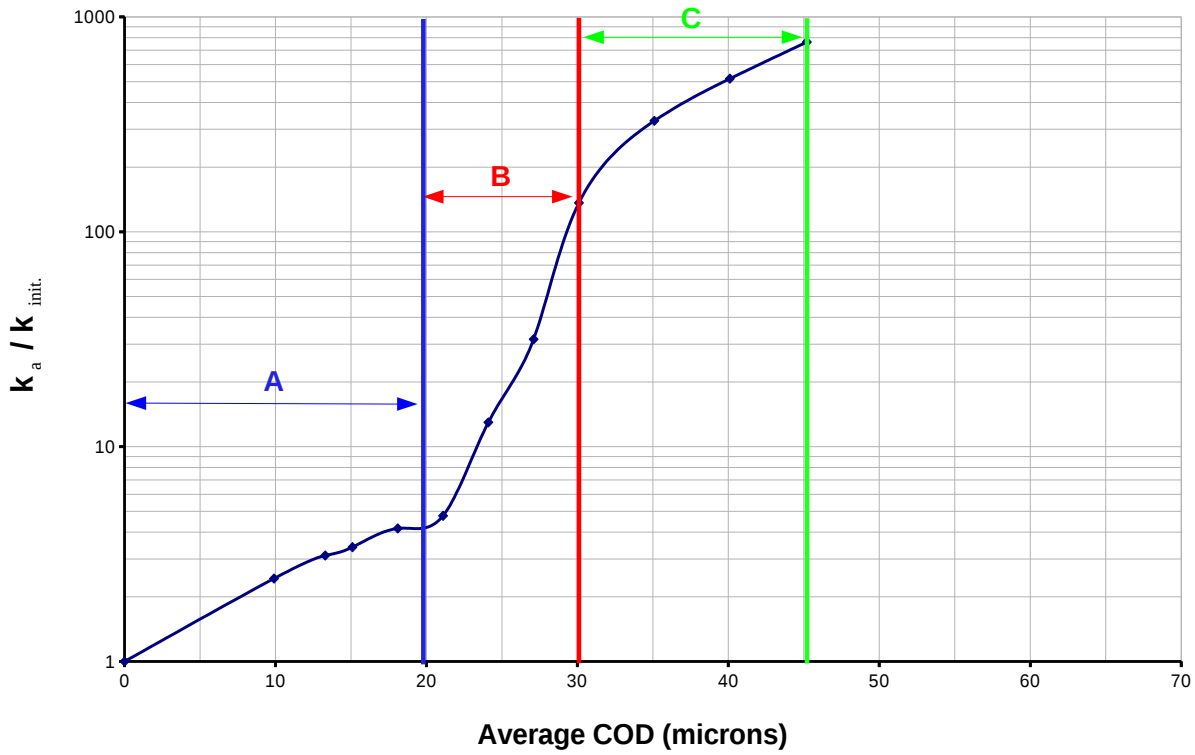

Figure 4.42: Relationship between the relative increases gas permeability and the average COD for cylinder concrete specimen within a COD-controlled, BSTT.

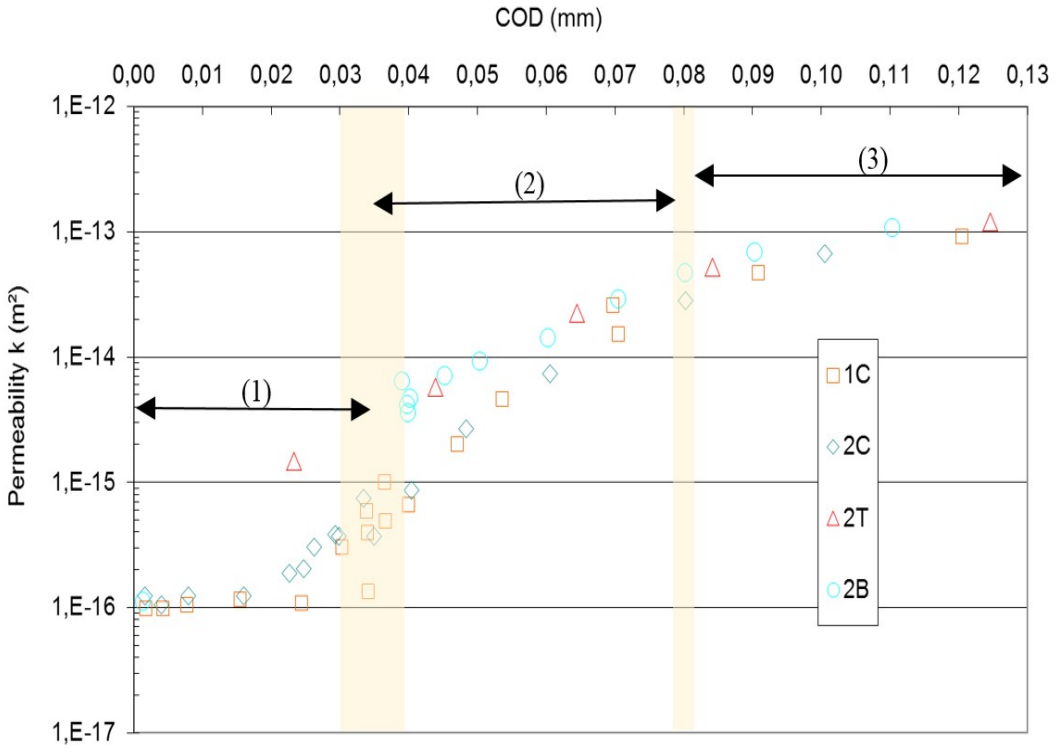

Figure 4.43: Relationship between gas permeability and the COD for cylinder concrete specimen under splitting tensile test [Choinska et al., 2008a].

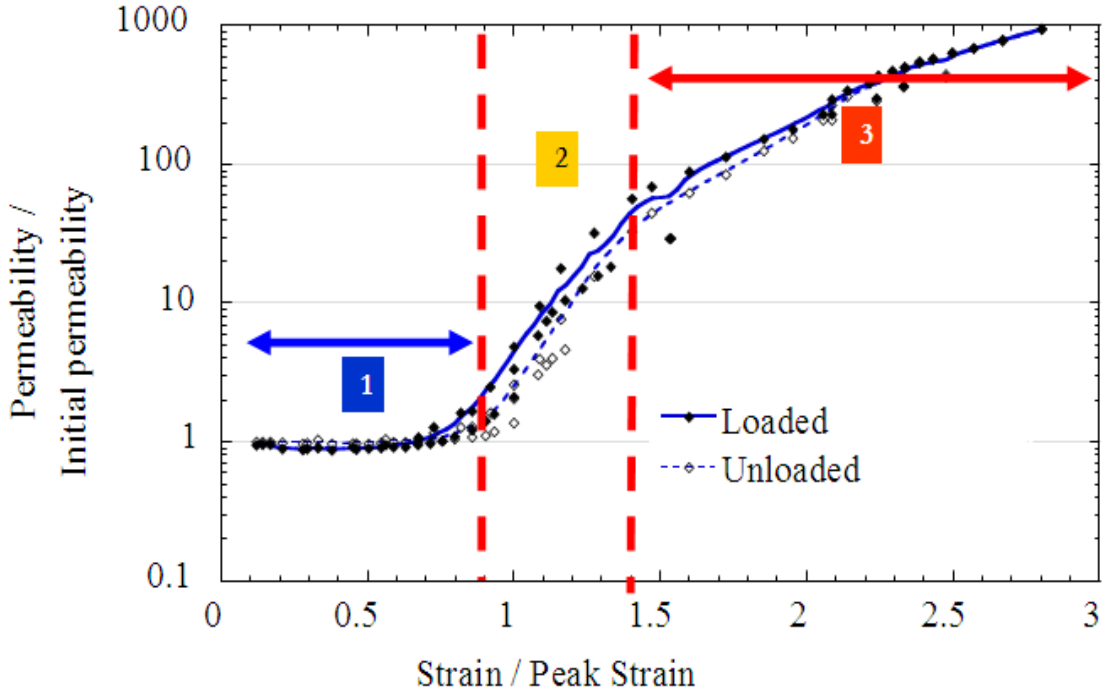

Figure 4.44: Relationship between the relative increases gas permeability and the relative strain for cylinder concrete specimen under unaxial compression test [Choinska et al., 2007].

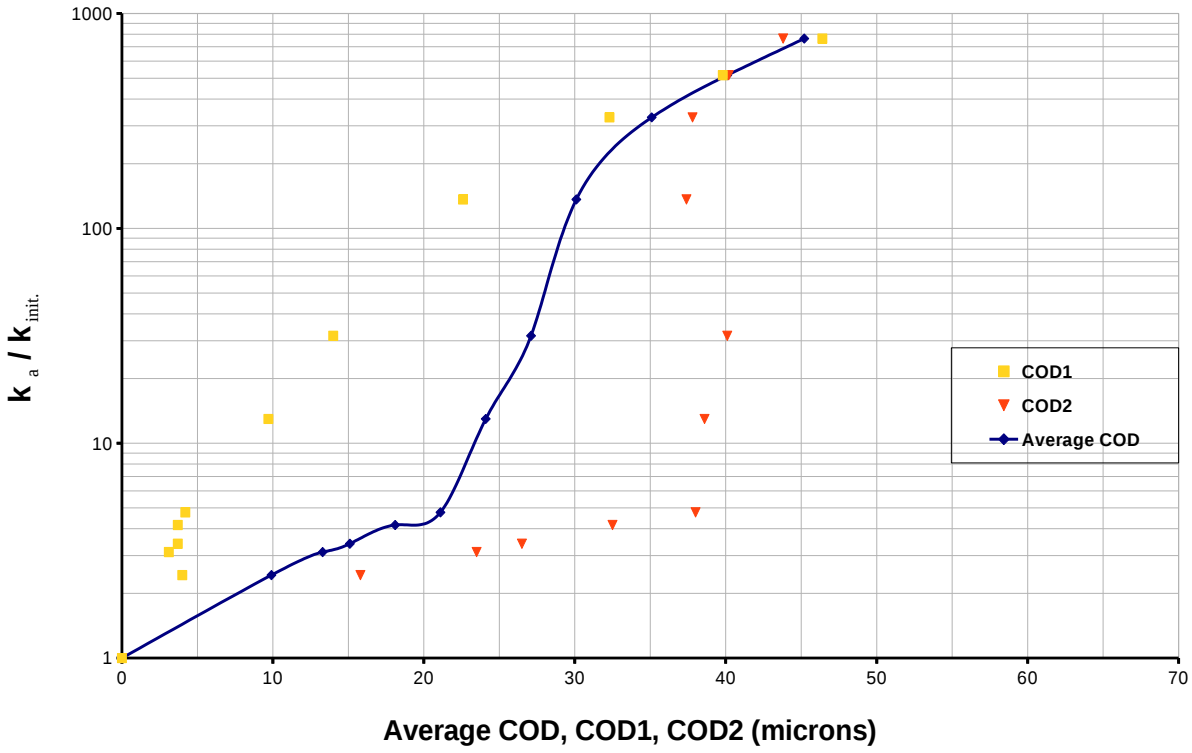

Figure 4.45: Relationship between the relative increases gas permeability and the average COD, COD1 and COD2 for cylinder concrete specimen within a COD-controlled, BSTT.

4.6 Conclusions

This experimental study presents and permits to understand the effects of crack initiation, propagation and opening of the aggregates size on the hydro-mechanical behavior of concrete. The present study has been realised on mortar containing 20 % volume fraction and aggregates particles (glass beads) ranging from 2 to 10 mm in diameter as well as on concrete with natural limestone crushed aggregates ranging from 4 to 12 mm in diameter. We were taken into account the context of the Brazilian splitting indirect tensile test in order to improve the numerical modeling. The main conclusions are the following:

1. The aggregates size influences the moisture loss in concrete under drying conditions of 40 ℃ .

2. The results show that ultimate tensile stress increases when the aggregates size decreases. This behavior is not found with our numerical modeling (see Figure 4.17).

3. The crack pattern depends on the aggregates size and position, which is in agreement with our numerical model (see Figures 3.6 and 3.7).

4. The aggregates size slightly affect the intrinsic permeability ($\boldsymbol{k_v}$) at the initial state. Therefore, the intrinsic permeability of mortar with glass beads aggregates diameter at 10 mm is higher than those with smaller aggregates even without glass beads aggregates. Our numerical model provides almost the same permeability values for each aggregates size (see Figure 4.35).

5. The results indicate that the apparent gas permeability ($\boldsymbol{k_a}$) of concrete specimens increases with aggregates size and crack opening (see Figures 4.36

and 4.37). This behavior is in agreement with the numerical model (see Figure 3.30).

6. The developed loading LGP method is validated and permits to get nearly the same results as the CEMBUREAU method for uncracked concrete initial permeability (see Table 4.4). However, this method permits to study permeability evolution under loading, in pre-peak as well as in post-peak loads.

7. The permeability-COD evolution is sigmoidal one, and in according to other studies, for tensile test but even for compressive tests. However, our model needs to be improved to represent sigmoidal evolution, especially in the first stage (A) (see Figure 3.31).

8. Cause to technical problem is occurred in MTS machine at the first time, we used cylinder specimens with limestone aggregates. In future work will be investigated more specimens with glass beads (GB).

Chapter 5

General conclusions and perspectives

5.1 General conclusions

To study and analyze the effects of aggregates size and volume fraction on the transfer properties of cracked concrete structures, two models were used: the first one is a meso-scale mechanical model to represent the crack opening [$|\boldsymbol{u}|$] and the second one is a hydro-mechanical model for coupling the crack opening and gas permeability. These models presented in **Chapter 3**.

In this chapter, two examples were presented to validate and provide the two models: the first one was the effect of aggregates size on the gas permeability of cracked concrete while the second example explained the influence of the aggregate volume fraction on the gas permeability of cracked concrete.

Whereas, to investigate and validate the numerical models we presented the experimental work in **Chapter 4**. Herein, the observed size effects of aggregates and geometrical crack opening on the gas permeability in concrete specimens.

From the results presented earlier on the study on mechanical and hydro-

mechanical properties by affecting aggregates size, volume fraction and crack opening on concrete cylinder specimens in the context the Brazilian splitting test, the following general conclusions are offered:

5.1.1 Numerical models

1. The results show that the effect of aggregates size is more pronounced of mechanical behavior with the largest aggregate diameter (higher specific surface area).

2. The study shows the mechanical behavior is influenced by the volume fraction of aggregate, i.e. that means the amount of aggregates has more relevant and important for the durability of concrete structures.

3. The crack opening dimensions $\boldsymbol{w_c}$ are depending significantly on the aggregates size, i.e. the ultimate crack opening increases with the increasing of aggregate diameter, for example the ultimate crack opening was **0.0193** mm with the aggregate diameter 4 mm, while it was **0.0206** mm with the aggregate diameter 16 mm and.

4. The specimens that contained more aggregate particles, it had wider crack opening, i.e. increasing the volume of fraction led to an increase in the ultimate crack opening, for example the maximum crack opening was **0.0071** mm with the volume fraction 10 % while it was **0.0384** mm with the volume fraction 30 %, these specimens have aggregate diameter 10 mm. In addition, the specimens have aggregate diameter 16 mm and the volume fraction 10 % led to the ultimate crack opening was **0.0099** mm while it was **0.0275** mm with the volume fraction 30 %. These results are agreement with with many experimental work in the literature review.

5. Increasing of ultimate tensile stress with the increasing of aggregate diameter, when the applied stresses were varied from **1.718** to **2.176** MPa with aggregate diameters 4 and 16 mm respectively. This behavior caused be the higher interfacial transition zone for smallest aggregate diameter and volume of fraction was constant 20 %.

6. Increasing of the volume fraction led to an increase the ultimate tensile stress, for example the ultimate tesile stresses were increased from **1.513** to **2.082** MPa when the volume fractions were varied from 10 to 30 % for the specimen has 10 mm aggregate diameter while this increasing of stresses were varied from **1.661** to **2.199** MPa for the specimen has 14 mm aggregate diameter. This result was supported from some of previous studies.

7. The study pointed out that increasing of the fracture energy and the dissipation energy with respect to the aggregate diameter, this increasing were varied from **0.184** to **0.206** N/mm for fracture energy and aggregate diameters were changed from 4 to 16 mm, while the dissipation energy was increased from **0.367** to **0.456** N/mm with aggregate diameters were increased from 4 to 16 mm. These findings were supported from another researchers.

8. The fracture energy and dissipation energy increase as the volume fraction increases, for example the fracture energy was varied from **0.150** to **0.222** N/mm when the volume fractions were increased from 10 to 30 % for the specimen has aggregate diameter 10 mm, while the fracture energy was increased from **0.160** to **0.294** N/mm for the specimen has 16 mm aggregate diameter. In addition, were varied the volume fractions from 10 to 30 % led to an increase the dissipation energy from **0.326** to **0.470** N/mm and **0.371** to **0.578** N/mm with the aggregate diameters 10 and 16 mm respectively.

9. The hydro-mechanical behavior influenced by the aggregates size and volume

fraction.

10. Mass flow and gas permeability are not significantly increased when the crack opening is less than **3** microns for all specimens, but there is a limited increase when the crack opening is larger than **3** microns and a clear increase at **10** microns. Moreover, the numerical simulations show a significant increase in permeability from **3.0** x $\mathbf{10^{-17}}$ to **1.0** x $\mathbf{10^{-13}}$ $\mathbf{m^2}$ when the crack opening is upto **50** microns.

11. Increasing the aggregates size leads to an increase in gas permeability, for example from **4.19** x $\mathbf{10^{-14}}$ to **5.73** x $\mathbf{10^{-12}}$ $\mathbf{m^2}$ when the aggregates size varies from 4 to 16 mm and the crack opening is **100** microns for all specimens.

12. Permeability decreases as the volume fraction increases, for example from **1.29** x $\mathbf{10^{-10}}$ to **1.73** x $\mathbf{10^{-13}}\mathbf{m^2}$ when the volume fraction increases from 10 to 30 % with an aggregate diameter of 10 mm and a crack opening of **100** microns for all specimens.

5.1.2 Experimental work

1. The aggregate content influences on the moisture loss in concrete under drying conditions in 40 $\mathring{C}$, i.e. the moisture loss during first week for mortar specimens was **0.018** kg while it was **0.015** kg for specimens with the aggregates.

2. The results of the Brazilian splitting tensile test showed that the ultimate tensile stress decreases as the aggregates size increases, for example **3.90, 3.43** and **2.81** MPa when the aggregates size are 2, 6 and 10 mm, respectively.

This behavior confirms that the specimens with the aggregates size 10 mm have higher porosity than the mortar specimens.

3. The position and shape of crack patterns presented the same results for the cylinder specimen (mortar) and specimens with the aggregates size 2 mm, the crack path started at the center toward the edges with a straight line without tortuosity during loading. Whereas, the cylinder specimens with the aggregates size 6 mm and 10 mm observed by developing from a center of a cylinder toward the edges with tortuosity and discontinuities when reached the aggregate particles.

4. The aggregate size slightly affects on the intrinsic permeability $\boldsymbol{k_v}$, that is, the intrinsic permeability for specimens with aggregate diameter 10 mm was higher than those of without aggregate (mortar specimens), we obtained intrinsic permeability **7.13** x $\mathbf{10^{-18}}$ $\mathbf{m^2}$ for mortar specimens and it was **1.94** x $\mathbf{10^{-17}}$ $\mathbf{m^2}$. In addition, the apparent permeability $\boldsymbol{k_a}$ was **3.26** x $\mathbf{10^{-17}}$ $\mathbf{m^2}$ for cylinder specimens with aggregate diameter 10 mm while it was **2.17** x $\mathbf{10^{-17}}$ $\mathbf{m^2}$ for mortar specimens.

5. The experimental results showed that the specimens contained aggregates size 10 mm, it had more apparent gas permeability ($\boldsymbol{k_a}$). In addition, the increasing of crack opening leads to increase the apparent gas permeability ($\boldsymbol{k_a}$).

5.2 Perspectives

The following perspectives may be drawn for future research:

5.2.1 Numerical study

1. Investigating the influence of aggregates size on the hydro-mechanical behavior with different aggregates size in the same specimen.

2. Studying the effect of volume fraction 60-75 % on the hydro-mechanical properties of concrete.

5.2.2 Experimental study

1. Using different aggregates size for the same specimen and volume fraction more than 20 % (GB), to investigate how these two parameters effects on hydro-mechanical behavior.

2. Using different aggregates shapes and nature (physical properties, E, k) to understand crack initiation and propagation in the cement paste and interface.

Appendix A

3D MESO-SCALE MECHANICAL MODEL

A.1 Hu-Washizu variational formulation with three fields

Remark: this section presents the method which was used by Nathan Benkemoun in [Benkemoun, 2010].

In the mechanical behavior, particularly for using Embedded Finite Element Method (E-FEM), a so-called weak form of the equilibrium equation of the displacement formulations. Therefore, Hw-Washizu in [Washizu, 1982] demonstrated three-field variational formulation is compatible to understand the kinematic enhancement for representing the displacement, i.e. to solve this mechanical problem he used this type of formulation which considers the displacement, strain and stress field – as addressed $\boldsymbol{u}$, $\boldsymbol{\varepsilon}$ and $\boldsymbol{\sigma}$, respectively, – as independant. However, each field was presented on the domain $\boldsymbol{\Omega}$ which consists of two parts: the first one is $\boldsymbol{S_t}$ and the second one is $\boldsymbol{S_u}$. This two parts follow the surface forces and the

displacements were imposed. As shown in equations (A.1), (A.2) and (A.3), three mathematical formulations for equilibrium equation of the stress field and the enhancement kinematic relationship between the strain and displacement field were introduced as follow:

Find $(\boldsymbol{u}, \boldsymbol{\varepsilon}, \boldsymbol{\sigma}) \in (\boldsymbol{V}, \boldsymbol{E}, \boldsymbol{T})$ so that $\forall(\boldsymbol{\delta u}, \boldsymbol{\delta\varepsilon}, \boldsymbol{\delta\sigma}) \in (\boldsymbol{V_0}, \boldsymbol{E}, \boldsymbol{T})$:

$$\boldsymbol{HW_u}(\boldsymbol{u}, \boldsymbol{\varepsilon}, \boldsymbol{\sigma}; \boldsymbol{\delta u}) = \int_{\boldsymbol{\Omega}} \boldsymbol{\partial \delta u} : \boldsymbol{\sigma}\, \boldsymbol{d\Omega} - \int_{\boldsymbol{\Omega}} \boldsymbol{\delta u} \,.\, \boldsymbol{b}\, \boldsymbol{d\Omega} - \int_{\boldsymbol{S_t}} \boldsymbol{\delta u} \,.\, \bar{\boldsymbol{t}}\, \boldsymbol{dS} = \boldsymbol{0} \quad \text{(A.1)}$$

$$\boldsymbol{HW_\sigma}(\boldsymbol{u}, \boldsymbol{\varepsilon}, \boldsymbol{\sigma}; \boldsymbol{\delta\sigma}) = \int_{\boldsymbol{\Omega}} \boldsymbol{\delta\sigma} : (\boldsymbol{\partial u} - \boldsymbol{\varepsilon})\, \boldsymbol{d\Omega} = \boldsymbol{0} \quad \text{(A.2)}$$

$$\boldsymbol{HW_\varepsilon}(\boldsymbol{u}, \boldsymbol{\varepsilon}, \boldsymbol{\sigma}; \boldsymbol{\delta\varepsilon}) = \int_{\boldsymbol{\Omega}} \boldsymbol{\delta\epsilon} : (\tilde{\boldsymbol{\sigma}}(\boldsymbol{\varepsilon}) - \boldsymbol{\sigma})\, \boldsymbol{d\Omega} = \boldsymbol{0} \quad \text{(A.3)}$$

with

$\boldsymbol{V} = \{\boldsymbol{u} \mid \boldsymbol{u} \in \boldsymbol{H^1}(\boldsymbol{\Omega}), \boldsymbol{u} = \bar{\boldsymbol{u}} \text{ on } \boldsymbol{S_u}\}$

$\boldsymbol{V_0} = \{\boldsymbol{\delta_u} \mid \boldsymbol{\delta_u} \in \boldsymbol{H^1}(\boldsymbol{\Omega}), \boldsymbol{\delta_u} = \boldsymbol{0} \text{ on } \boldsymbol{S_u}\}$

$\boldsymbol{E} = \{\boldsymbol{\varepsilon} \mid \boldsymbol{\varepsilon} \in \boldsymbol{L_2}(\boldsymbol{\Omega})\}$

$\boldsymbol{T} = \{\boldsymbol{\sigma} \mid \boldsymbol{\sigma} \in \boldsymbol{L_2}(\boldsymbol{\Omega})\}$

where $\tilde{\boldsymbol{\sigma}}$ refers to stress field that is according to the constitutive law on the domain $\boldsymbol{\Omega}$, $\boldsymbol{b}$ is the internal force on the field $\boldsymbol{\Omega}$ and $\bar{\boldsymbol{t}}$ is the traction vector imposed on the surface $\boldsymbol{S_t}$.

Jirásek in [Jirásek, 2000] pointed out that the finite element discretization for representing the weak form was based on the principle of the Hu-Washizu variational, this problem can be solved corresponding to the interpolation estimates for the three unknown fields $(\boldsymbol{u}, \boldsymbol{\varepsilon}, \boldsymbol{\sigma})$ as:

$$\boldsymbol{u} \approx \boldsymbol{Nd} + \boldsymbol{N_c d_c} \quad \text{(A.4)}$$

$$\boldsymbol{\varepsilon \approx B\, d \,+\, G\, a} \tag{A.5}$$

$$\boldsymbol{\sigma \approx S\, s} \tag{A.6}$$

where $\boldsymbol{N}$ refers to the standard displacement interpolation matrix (including the usual shape functions), $\boldsymbol{B = \partial N}$ is the standard strain interpolation matrix (containing the derivatives of the shape functions) and $\boldsymbol{N_c}$ and $\boldsymbol{G}$ refer to the matrices including some enrichment terms for displacements and strains, respectively. In addition, $\boldsymbol{S}$ refers to the stress interpolation matrix, the vectors $\boldsymbol{d, d_c, a, s}$ refer to obtaining the degrees of freedom according to nodal displacements, enhanced displacement modes (better displacements), enhanced strain modes (better strain), and stress parameters, respectively.

Substituting the equations (A.4)-(A.6) into the formulation of Hu-Washizu (A.1)-(A.3) and taking into account the independant of the three virtual fields $\boldsymbol{(\delta_u, \delta_\varepsilon, \delta_\sigma)}$, we obtain:

$$\int_{\Omega} \boldsymbol{B^T \tilde{\sigma}(B\, d + G\, a)\, d\Omega = f_{ext}} \tag{A.7}$$

$$\int_{\Omega} \boldsymbol{G^T \tilde{\sigma}(B\, d + G\, a)\, d\Omega} - \int_{\Omega} \boldsymbol{G^T S\, d\Omega\, s = 0} \tag{A.8}$$

$$\int_{\Omega} \boldsymbol{S^T B_c\, d\Omega d_c} - \int_{\Omega} \boldsymbol{S^T G\, d\Omega\, a = 0} \tag{A.9}$$

$$\int_{\Omega} \boldsymbol{B_c^T S\, d\Omega s = f_{ext,c}} \tag{A.10}$$

with

$$\boldsymbol{f_{ext}} = \int_{\Omega} \boldsymbol{N^T b\, d\Omega} + \int_{\boldsymbol{S_t}} \boldsymbol{N^T \bar{t}\, dS} \tag{A.11}$$

$$\boldsymbol{f_{ext,c}} = \int_{\Omega} \boldsymbol{N_c^T b}\, d\boldsymbol{\Omega} + \int_{\boldsymbol{S_t}} \boldsymbol{N_c^T \bar{t}}\, d\boldsymbol{S} \tag{A.12}$$

In equation (A.12) is the vector of external forces $\boldsymbol{f_{ext,c}} = 0$, in order to simplify the solving procedure.

From the literature it can be found that there is three techniques of the kinematic enhancements in order to obtain the matrices $\boldsymbol{N_c}$ and $\boldsymbol{G}$, they based on the Hu-Washizu formulations.

This three techniques are as follow:

1. **Statically Optimal Symmetric Formulation (SOS):** this technique considered the strain field is enhanced, whereas the interpolation of the displacement field is not enhanced. Then, all the parameters $\boldsymbol{d_c}$, $\boldsymbol{N_c}$ and $\boldsymbol{B_c}(= \boldsymbol{\partial N_c})$ in equations (A.7-A.10) can be deleted. Then, deriving the equation (A.9) with taking into account the parameter $\boldsymbol{d_c}$ is variable, can be obtained:

$$\int_{\Omega} \boldsymbol{S^T G}\, d\boldsymbol{\Omega}\, \boldsymbol{a} = \boldsymbol{0} \tag{A.13}$$

According to the statical considerations (patch test), to reproduce the interpolation matrix of strain enhancement respecting the zero mean condition brings continuity to the stress field $\boldsymbol{S}$ is $\boldsymbol{S} = \boldsymbol{I}$, where $\boldsymbol{I}$ is the unit matrix. Equation (A.13) becomes:

$$\int_{\Omega} \boldsymbol{G}\, d\boldsymbol{\Omega}\, \boldsymbol{a} = \boldsymbol{0} \tag{A.14}$$

Can be modified $\boldsymbol{G}$ matrix in equation (A.14) this case applied when condition of zero mean was not satisfied. Then, for any value of parameter $\boldsymbol{a}$ in equation (A.9) has been satisfied.

$$\int_{\Omega} \boldsymbol{G}\, d\boldsymbol{\Omega} = \boldsymbol{0} \tag{A.15}$$

On the other hand, the stress parameters $\boldsymbol{s}$ are disapeared in the equation (A.8) is now a zero matrix. The equations can write , finily:

$$\int_{\Omega} \boldsymbol{B}^{\boldsymbol{T}} \tilde{\boldsymbol{\sigma}} (\boldsymbol{B}\ \boldsymbol{d} + \boldsymbol{G}\ \boldsymbol{a})\ d\boldsymbol{\Omega} = \boldsymbol{f_{ext}} \tag{A.16}$$

$$\int_{\Omega} \boldsymbol{G}^{\boldsymbol{T}} \tilde{\boldsymbol{\sigma}} (\boldsymbol{B}\ \boldsymbol{d} + \boldsymbol{G}\ \boldsymbol{a})\ d\boldsymbol{\Omega} = \boldsymbol{0} \tag{A.17}$$

2. **Kinematically Optimal Symmetric Formulation (KOS):** this technique deals with modifying the enhanced interpolation process. The kinematic enhancement in the displacement field is constructed with some suitable interpolation matrix. All the parameters $\boldsymbol{d_c}, \boldsymbol{N_c}$ and $\boldsymbol{B_c}(= \boldsymbol{\partial N_c})$ can not be removed. Therefore, the assumption by Ibrahimbegovic [Ibrahimbegovic and Wilson, 1991] can be followed, which constructed the parameter $\boldsymbol{\partial N_c}$ by setting the parameters $\boldsymbol{G} = \boldsymbol{B_c}$ and $\boldsymbol{d_c} = \boldsymbol{a}$. This equal leads to the same form of governing equations as before, i.e. (A.16-A.17):

$$\int_{\Omega} \boldsymbol{B}^{\boldsymbol{T}} \tilde{\boldsymbol{\sigma}} (\boldsymbol{B}\ \boldsymbol{d} + \boldsymbol{G}\ \boldsymbol{a})\ d\boldsymbol{\Omega} = \boldsymbol{f_{ext}} \tag{A.18}$$

$$\int_{\Omega} \boldsymbol{G}^{\boldsymbol{T}} \tilde{\boldsymbol{\sigma}} (\boldsymbol{B}\ \boldsymbol{d} + \boldsymbol{G}\ \boldsymbol{a})\ d\boldsymbol{\Omega} = \boldsymbol{0} \tag{A.19}$$

For the two techniques (SOS) and (KOS), it show that the stress parameter were $\boldsymbol{s}$ completely disappeared from the formulation, in addition they both gave the same equations for equilibrium with the only difference that the matrix $\boldsymbol{G}$ in equation (A.15) has to be constructed by $\boldsymbol{G} = \boldsymbol{B_c}$.

Jirásek presented that the two techniques (SOS) and (KOS) can act as an example of the finite localization band based on Constant-strains triangle (CST) [Jirásek, 2000].

3. **Statically and Kinematically Optimal Nonsymmetric Formulation (SKON):** this technique carried out by Dvorkin et al. [Dvorkin et al., 1990], it was modified by Simo [Simo and Oliver, 1994], however this method did not used the variational formulation, but it depended upon the test functions that were different from trial functions corresponding a weak form. In addition, this technique presented two point: the first one it used $\boldsymbol{G} = \boldsymbol{B_c}$ in the strain field, see equation (A.5), and the second point it replaced the matrix $\boldsymbol{G}$ by $\tilde{\boldsymbol{G}}$ in equation (A.19), therefore the equations became:

$$\int_{\Omega} \boldsymbol{B}^{\boldsymbol{T}} \tilde{\boldsymbol{\sigma}} (\boldsymbol{B}\, \boldsymbol{d} + \boldsymbol{G}\, \boldsymbol{a})\, d\boldsymbol{\Omega} = \boldsymbol{f_{ext}} \tag{A.20}$$

$$\int_{\Omega} \tilde{\boldsymbol{G}}^{\boldsymbol{T}} \tilde{\boldsymbol{\sigma}} (\boldsymbol{B}\, \boldsymbol{d} + \boldsymbol{G}\, \boldsymbol{a})\, d\boldsymbol{\Omega} = \boldsymbol{0} \tag{A.21}$$

The SKON technique includes both the kinematic and static aspects properly, i.e. it represented the two methods (SOS) and (KOS), the condition of continuity for the traction vector had provided the kinematic of discontinuities was reflected perfectly. In the other word, the matrix $\tilde{\boldsymbol{G}}$ that did not transpose $\boldsymbol{B_c}$. The results led to linearize the formulations with the non symmetrical system.

A.2 Method of Incompatible Modes

The method of incompatible modes was pointed out by Wilson et al. [Wilson et al., 1973], then it was developed in some studies. This section, will presente explain the Method of Incompatible Modes, this method is based on the framework of the three-field Hu-Washizu variational principle, **this part is presented by Benkemoun in** [Benkemoun, 2010]. The original concept of this method was

constructed based on the enhancement at the strain field, directly. It also, was constructed as an orthogonal complement to the enhanced strain field for three fields displacement, strain and stress.

According to the formulation of the three-field Hu-Washizu variational principle, actual three fields $(\boldsymbol{u}, \boldsymbol{\varepsilon}, \boldsymbol{\sigma})$ are independents for displacement field, strain field and stress field, respectively. They are replaced by the virtual three fields $(\boldsymbol{\omega}, \boldsymbol{\gamma}, \boldsymbol{\tau})$ are also independents for displacement, strain and stress fields, respectively.

Therefore the formulation of the three-field Hu-Washizu variational principle corresponding to the virtual fields can be written as:

Find $(\boldsymbol{u}, \boldsymbol{\varepsilon}, \boldsymbol{\sigma}) \in (\boldsymbol{V}, \boldsymbol{E}, \boldsymbol{T})$ so that $\forall(\boldsymbol{\omega}, \boldsymbol{\gamma}, \boldsymbol{\tau}) \in (\boldsymbol{V_0}, \boldsymbol{E}, \boldsymbol{T})$:

$$\boldsymbol{HW_u}(\boldsymbol{u}, \boldsymbol{\varepsilon}, \boldsymbol{\sigma}; \boldsymbol{\omega}) = \int_{\boldsymbol{\Omega}} \boldsymbol{\partial\omega} : \boldsymbol{\sigma}\, \boldsymbol{d\Omega} - \int_{\boldsymbol{\Omega}} \boldsymbol{\omega} \,.\, \boldsymbol{b}\, \boldsymbol{d\Omega} - \int_{\boldsymbol{S_t}} \boldsymbol{\omega} \,.\, \bar{\boldsymbol{t}}\, \boldsymbol{dS} = \boldsymbol{0} \quad \text{(A.22)}$$

$$\boldsymbol{HW_\sigma}(\boldsymbol{u}, \boldsymbol{\varepsilon}, \boldsymbol{\sigma}; \boldsymbol{\tau}) = \int_{\boldsymbol{\Omega}} \boldsymbol{\tau} : (\boldsymbol{\partial u} - \boldsymbol{\varepsilon})\, \boldsymbol{d\Omega} = \boldsymbol{0} \quad \text{(A.23)}$$

$$\boldsymbol{HW_\varepsilon}(\boldsymbol{u}, \boldsymbol{\varepsilon}, \boldsymbol{\sigma}; \boldsymbol{\gamma}) = \int_{\boldsymbol{\Omega}} \boldsymbol{\gamma} : (\tilde{\boldsymbol{\sigma}}(\boldsymbol{\varepsilon}) - \boldsymbol{\sigma})\, \boldsymbol{d\Omega} = \boldsymbol{0} \quad \text{(A.24)}$$

with

$\boldsymbol{V} = \{\boldsymbol{u} \mid \boldsymbol{u} \in \boldsymbol{H^1}(\boldsymbol{\Omega}), \boldsymbol{u} = \bar{\boldsymbol{u}} \text{ on } \boldsymbol{S_u}\}$

$\boldsymbol{V_0} = \{\boldsymbol{\omega} \mid \boldsymbol{\omega} \in \boldsymbol{H^1}(\boldsymbol{\Omega}), \boldsymbol{\omega} = \boldsymbol{0} \text{ on } \boldsymbol{S_u}\}$

$\boldsymbol{E} = \{\boldsymbol{\varepsilon} \mid \boldsymbol{\varepsilon} \in \boldsymbol{L_2}(\boldsymbol{\Omega})\}$

$\boldsymbol{T} = \{\boldsymbol{\sigma} \mid \boldsymbol{\sigma} \in \boldsymbol{L_2}(\boldsymbol{\Omega})\}$

where $\tilde{\boldsymbol{\sigma}}$ refers to the stress field that according to the constitutive law on the domain $\boldsymbol{\Omega}$, $\boldsymbol{b}$ is the internal force on the field $\boldsymbol{\Omega}$ and $\bar{\boldsymbol{t}}$ is the traction vector imposed on the surface $\boldsymbol{S_t}$.

However, the method of incompatible modes showed a good enhancement for both actual and virtual for the strain fields which noted by $(\tilde{\boldsymbol{\varepsilon}}, \tilde{\boldsymbol{\gamma}})$, respectively.

Can be obtained:

$$\boldsymbol{\varepsilon} = \boldsymbol{\partial u} \; + \; \tilde{\boldsymbol{\varepsilon}} \tag{A.25}$$

$$\boldsymbol{\gamma} = \boldsymbol{\partial \omega} \; + \; \tilde{\boldsymbol{\gamma}} \tag{A.26}$$

The two previous equations (A.25) and (A.26) are substituted directly into the three-field Hu-Washizu variational formulations with equations (A.22)-(A.24), can be written as:

$$\int_{\boldsymbol{\Omega}} \boldsymbol{\partial \omega} : \boldsymbol{\sigma} \; \boldsymbol{d\Omega} - \int_{\boldsymbol{\Omega}} \boldsymbol{\omega} \; . \; \boldsymbol{b} \; \boldsymbol{d\Omega} - \int_{\boldsymbol{S_t}} \boldsymbol{\omega} \; . \; \bar{\boldsymbol{t}} \; \boldsymbol{dS} = \mathbf{0} \tag{A.27}$$

$$\int_{\boldsymbol{\Omega}} \boldsymbol{\tau} : \tilde{\boldsymbol{\varepsilon}} \; \boldsymbol{d\Omega} = \mathbf{0} \tag{A.28}$$

$$\int_{\boldsymbol{\Omega}} \boldsymbol{\partial \omega} : (\tilde{\boldsymbol{\sigma}}(\boldsymbol{\varepsilon}) - \boldsymbol{\sigma}) \; \boldsymbol{d\Omega} + \int_{\boldsymbol{\Omega}} \tilde{\boldsymbol{\gamma}} : (\tilde{\boldsymbol{\sigma}}(\boldsymbol{\varepsilon}) - \boldsymbol{\sigma}) \; \boldsymbol{d\Omega} = \mathbf{0} \tag{A.29}$$

In addition, it should be remarked for the improving strains must be separated the two strains, i.e. the two parameters $(\boldsymbol{\omega}, \tilde{\boldsymbol{\gamma}})$ are independants variables. Therefore, the equations (A.27)-(A.29) can be written:

$$\int_{\boldsymbol{\Omega}} \boldsymbol{\partial \omega} : \boldsymbol{\sigma} \; \boldsymbol{d\Omega} - \int_{\boldsymbol{\Omega}} \boldsymbol{\omega} \; . \; \boldsymbol{b} \; \boldsymbol{d\Omega} - \int_{\boldsymbol{S_t}} \boldsymbol{\omega} \; . \; \bar{\boldsymbol{t}} \; \boldsymbol{dS} = \mathbf{0} \tag{A.30}$$

$$\int_{\boldsymbol{\Omega}} \boldsymbol{\tau} : \tilde{\boldsymbol{\varepsilon}} \; \boldsymbol{d\Omega} = \mathbf{0} \tag{A.31}$$

$$\int_{\boldsymbol{\Omega}} \boldsymbol{\partial \omega} : (\tilde{\boldsymbol{\sigma}}(\boldsymbol{\varepsilon}) - \boldsymbol{\sigma}) \; \boldsymbol{d\Omega} = \mathbf{0} \tag{A.32}$$

$$\int_{\boldsymbol{\Omega}} \tilde{\boldsymbol{\gamma}} : (\tilde{\boldsymbol{\sigma}}(\boldsymbol{\varepsilon}) - \boldsymbol{\sigma}) \; \boldsymbol{d\Omega} = \mathbf{0} \tag{A.33}$$

By substituting the equation (A.32) into equation A.30), the previous equations become:

$$\int_{\Omega} \boldsymbol{\partial\omega} : \tilde{\boldsymbol{\sigma}}(\varepsilon)\, \boldsymbol{d\Omega} - \int_{\Omega} \boldsymbol{\omega} \,.\, \boldsymbol{b}\, \boldsymbol{d\Omega} - \int_{\boldsymbol{S_t}} \boldsymbol{\omega} \,.\, \bar{\boldsymbol{t}}\, \boldsymbol{dS} = \mathbf{0} \tag{A.34}$$

$$\int_{\Omega} \boldsymbol{\tau} : \tilde{\boldsymbol{\varepsilon}}\, \boldsymbol{d\Omega} = \mathbf{0} \tag{A.35}$$

$$\int_{\Omega} \boldsymbol{\partial\omega} : (\tilde{\boldsymbol{\sigma}}(\varepsilon) - \boldsymbol{\sigma})\, \boldsymbol{d\Omega} = \mathbf{0} \tag{A.36}$$

$$\int_{\Omega} \tilde{\boldsymbol{\gamma}} : (\tilde{\boldsymbol{\sigma}}(\varepsilon) - \boldsymbol{\sigma})\, \boldsymbol{d\Omega} = \mathbf{0} \tag{A.37}$$

For the above mentioned, the incompatible modes formulation had demonstrated that the stress fields $\boldsymbol{\sigma}$ and $\boldsymbol{\tau}$, in addition strain fields $\tilde{\boldsymbol{\varepsilon}}$ and $\tilde{\boldsymbol{\gamma}}$ were modified such as orthogonal. That modification is avoided many constraints of fields into the final formulation. This method can be used to the non-linear constitutive material laws, however it is obtained the solving of stress via the calculation of strains as:

$$\int_{\Omega} \boldsymbol{\tau} : \tilde{\boldsymbol{\varepsilon}}\, \boldsymbol{d\Omega} = \mathbf{0} \quad \text{and} \quad \int_{\Omega} \tilde{\boldsymbol{\gamma}} : \boldsymbol{\sigma}\, \boldsymbol{d\Omega} = \mathbf{0} \tag{A.38}$$

Hence, by integrating the previous equation into equations (A.34)-(A.37), it can be written:

$$\int_{\Omega} \boldsymbol{\partial\omega} : \tilde{\boldsymbol{\sigma}}(\varepsilon)\, \boldsymbol{d\Omega} - \int_{\Omega} \boldsymbol{\omega} \,.\, \boldsymbol{b}\, \boldsymbol{d\Omega} - \int_{\boldsymbol{S_t}} \boldsymbol{\omega} \,.\, \bar{\boldsymbol{t}}\, \boldsymbol{dS} = \mathbf{0} \tag{A.39}$$

$$\int_{\Omega} \boldsymbol{\partial\omega} : (\tilde{\boldsymbol{\sigma}}(\varepsilon) - \boldsymbol{\sigma})\, \boldsymbol{d\Omega} = \mathbf{0} \tag{A.40}$$

$$\int_{\Omega} \tilde{\boldsymbol{\gamma}} : \tilde{\boldsymbol{\sigma}}(\varepsilon)\, \boldsymbol{d\Omega} = \mathbf{0} \tag{A.41}$$

Equations (A.40) and (A.41) are considered to be a strong form, therefore to produce convergence in this method, the patch test should be used for enrichment, on the other hand, the stress field is considered constant which becomes more simplified in equation (A.41) $\tilde{\boldsymbol{\sigma}}(\boldsymbol{\varepsilon}) = \tilde{\boldsymbol{\sigma}}_{\boldsymbol{c}}$, the compatiblity equation can be written:

$$\tilde{\boldsymbol{\sigma}}_{\boldsymbol{c}} \int_{\boldsymbol{\Omega}} \tilde{\gamma}\, \boldsymbol{d\Omega} = \mathbf{0} \Rightarrow \int_{\boldsymbol{\Omega}} \tilde{\gamma}\, \boldsymbol{d\Omega} = \mathbf{0}, \tag{A.42}$$

For representing both actual and virtual stain fields according to the E-FEM formulation, the formulas can be written:

$$\boldsymbol{\varepsilon} = \boldsymbol{B}\,\boldsymbol{d} + \boldsymbol{G}\,\boldsymbol{a} \quad \text{and} \quad \boldsymbol{\gamma} = \boldsymbol{B}\,\boldsymbol{d} + \tilde{\boldsymbol{G}}\,\boldsymbol{a} \tag{A.43}$$

where $\boldsymbol{B} = \boldsymbol{\partial N}$ refers to the standard strain interpolation matrix (including the derivatives of the shape functions), $\boldsymbol{G}$, $\tilde{\boldsymbol{G}}$ are matrices including the enrichment terms for actual and virtual strains, respectively, which are noted incompatible modes terms. $\boldsymbol{a}$ is the vector which containing the degrees of freedom corresponding to the enhanced strain field.

The hypothesis of $\boldsymbol{\partial u}$ and $\boldsymbol{\partial \omega}$ are in the same manner for the equation (A.43), therefore $\boldsymbol{B} \bigcap \boldsymbol{G} = \boldsymbol{\emptyset}$ and $\boldsymbol{B} \bigcap \tilde{\boldsymbol{G}} = \boldsymbol{\emptyset}$ can be chosen. Corresponding the equation (A.42) of the condition zero mean, $\tilde{\boldsymbol{G}}$ is modified, $\int_{\boldsymbol{\Omega}} \tilde{\boldsymbol{G}}\, \boldsymbol{d\Omega} = \mathbf{0}$.

By substituting equation (A.43) into equations (A.40) and (A.41), the formulations can be obtained are as the SKON formulations, but they are according to **the Method of Incompatible Modes** are as shown:

$$\int_{\boldsymbol{\Omega}} \boldsymbol{B}^{\boldsymbol{T}} \tilde{\boldsymbol{\sigma}} (\boldsymbol{B}\,\boldsymbol{d} + \boldsymbol{G}\,\boldsymbol{a})\, \boldsymbol{d\Omega} = \boldsymbol{f_{ext}} \tag{A.44}$$

$$\int_{\boldsymbol{\Omega}} \tilde{\boldsymbol{G}}^{\boldsymbol{T}} \tilde{\boldsymbol{\sigma}} (\boldsymbol{B}\,\boldsymbol{d} + \boldsymbol{G}\,\boldsymbol{a})\, \boldsymbol{d\Omega} = \mathbf{0} \tag{A.45}$$

The previous equations (A.44) and (A.45) are written as the finite element formulations as shown:

$$\boldsymbol{A}_{e=1}^{n_{elm}}[\boldsymbol{f}_{int}^{e} - \boldsymbol{f}_{ext}^{e}] = \boldsymbol{0} \tag{A.46}$$

$$\int_{\Omega_e} \tilde{\boldsymbol{G}}^{T}\tilde{\boldsymbol{\sigma}}(\boldsymbol{B}\,\boldsymbol{d} + \boldsymbol{G}\,\boldsymbol{a})\,d\boldsymbol{\Omega} = \boldsymbol{0} \quad \forall\, \boldsymbol{e} \in [\boldsymbol{1}, \boldsymbol{n_{elm}}] \tag{A.47}$$

where

$$\boldsymbol{f}_{int}^{e} = \int_{\Omega_e} \boldsymbol{B}^{T}\tilde{\boldsymbol{\sigma}}(\boldsymbol{B}\,\boldsymbol{d} + \boldsymbol{G}\,\boldsymbol{a})\,d\boldsymbol{\Omega} \tag{A.48}$$

A.3 Weak discontinuity

In this section the focus is made on the application of incompatible modes method as the finite element method for implementing the heterogeneous material such as concrete (aggregate melts into mortar). As shown in Figure (A.1), 2D discretization with non-adapted mesh for heterogeneous material.

By using the equations (A.46)-(A.48), they are applying the finite elements depending on the method of incompatible modes for the bar element which divided into two parts, these formulations in strain field (weak discontinuity). In bar element, there are no matrix $\boldsymbol{G}$, but as a scalar function which noted $\boldsymbol{G_1}^{1/2}$, in addition, the parameter $\boldsymbol{a}$ is noted $[|\varepsilon|]$.

As shown in Figure (A.2), the bar element with two nodes according to the method of incompatible modes, it represents two-phase materials: phase 1 refers to the cement paste or mortar and phase 2 refers to the aggregate particle.

As $\boldsymbol{G_1}^{1/2}$ refers to the strain-displacement function which equals to the $\tilde{\boldsymbol{G}}_{\boldsymbol{1}}^{1/2}$ in the bar element, it can be written:

$$\boldsymbol{G_1}^{1/2} = \tilde{\boldsymbol{G}}_{\boldsymbol{1}}^{1/2} = \begin{cases} \boldsymbol{G_1}^{1} = -\frac{1}{\theta\ell}\,, & \boldsymbol{x} \in [\boldsymbol{0}, \boldsymbol{\theta\ell}] \\ \boldsymbol{G_1}^{2} = \frac{1}{(1-\theta)\ell}\,, & \boldsymbol{x} \in [\boldsymbol{\theta\ell}, \boldsymbol{\ell}] \end{cases} \tag{A.49}$$

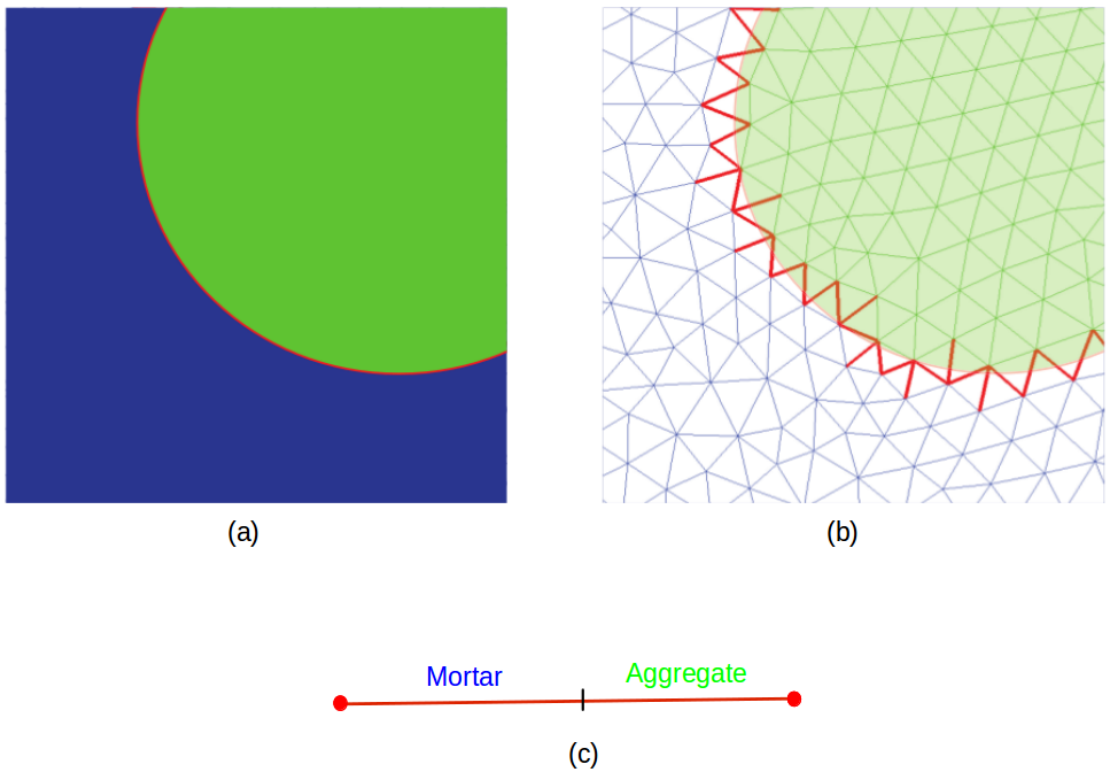

Figure A.1: 2D discretization with non-adapted mesh : aggregate melts into mortar (a) discretization finite elements (b) bar element cut in two parts (c) by Benkemoun in [Benkemoun, 2010].

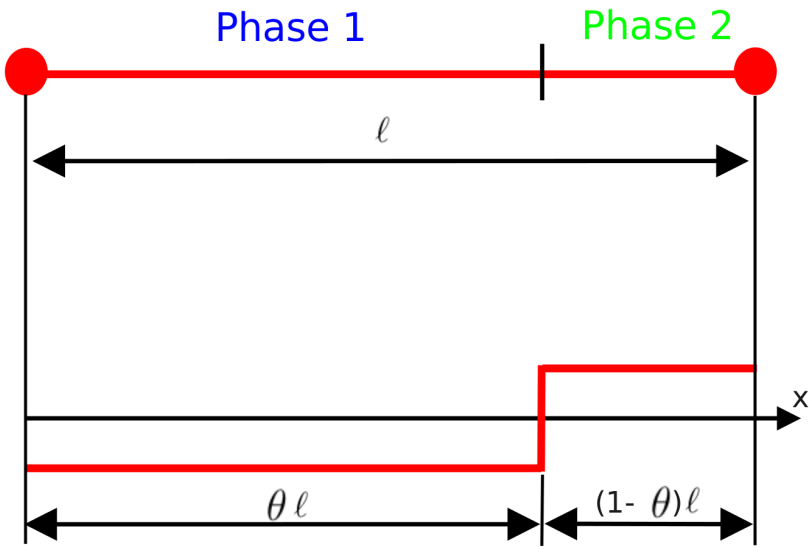

Figure A.2: Bar element for representing two-phase materials at weak discontinuity by Benkemoun in [Benkemoun, 2010].

where $\boldsymbol{\ell}$ is the length of the bar element and $\boldsymbol{\theta}$ is a dimensionless parameter.

By deriving the shape functions for two nodes $\boldsymbol{N_1}$ and $\boldsymbol{N_2}$ the following vector can be obtained:

$$\boldsymbol{B} = [\boldsymbol{N_1}, \boldsymbol{N_2}] = [-\frac{\mathbf{1}}{\boldsymbol{\ell}}, \frac{\mathbf{1}}{\boldsymbol{\ell}}] \tag{A.50}$$

in addition, $\boldsymbol{d}$ refers to the unknown vector:

$$\boldsymbol{d} = \begin{bmatrix} \boldsymbol{u_1} \\ \boldsymbol{u_2} \end{bmatrix} \tag{A.51}$$

For representing the strain field for bar element $\boldsymbol{e}$ as shown in relation:

$$\boldsymbol{\varepsilon} = \sum_{\boldsymbol{a=1}}^{\mathbf{2}} \boldsymbol{B_a^e}\, \boldsymbol{d_a^e} = \boldsymbol{B}\, \boldsymbol{d} \tag{A.52}$$

According to the relation into equation (A.43) and taking into account that $\boldsymbol{G_1}^{1/2}$ is applied for two phases (aggregate and mortar), and by considering each phase is independant, this equation can be obtained:

$$\boldsymbol{\varepsilon}^{1} = \boldsymbol{B}\,\boldsymbol{d} + \boldsymbol{G_1}^{1}[|\boldsymbol{\varepsilon}|], \quad \boldsymbol{\varepsilon}^{2} = \boldsymbol{B}\,\boldsymbol{d} + \boldsymbol{G_1}^{2}[|\boldsymbol{\varepsilon}|] \tag{A.53}$$

When applying the constitutive laws for each material (aggregate or mortar), i.e. the individual elastic moduli of each phase is $\boldsymbol{E_1}$ or $\boldsymbol{E_2}$ as:

$$\begin{cases} \tilde{\boldsymbol{\sigma}}^{1}(\boldsymbol{B}\,\boldsymbol{d} + \boldsymbol{G_1}^{1}[|\boldsymbol{\varepsilon}|]) = \boldsymbol{E_1}\,\boldsymbol{\varepsilon}^{1} = \boldsymbol{E_1}(\boldsymbol{B}\,\boldsymbol{d} + \boldsymbol{G_1}^{1}[|\boldsymbol{\varepsilon}|]) \\ \tilde{\boldsymbol{\sigma}}^{2}(\boldsymbol{B}\,\boldsymbol{d} + \boldsymbol{G_1}^{2}[|\boldsymbol{\varepsilon}|]) = \boldsymbol{E_2}\,\boldsymbol{\varepsilon}^{2} = \boldsymbol{E_2}(\boldsymbol{B}\,\boldsymbol{d} + \boldsymbol{G_1}^{2}[|\boldsymbol{\varepsilon}|]) \end{cases} \tag{A.54}$$

For simplicity the equation above (A.54), can be written:

$$\begin{cases} \tilde{\boldsymbol{\sigma}}^{1}(\boldsymbol{B}\,\boldsymbol{d} + \boldsymbol{G_1}^{1}[|\boldsymbol{\varepsilon}|]) = \tilde{\boldsymbol{\sigma}}^{1}(\boldsymbol{d}, [|\boldsymbol{\varepsilon}|]) \\ \tilde{\boldsymbol{\sigma}}^{2}(\boldsymbol{B}\,\boldsymbol{d} + \boldsymbol{G_1}^{2}[|\boldsymbol{\varepsilon}|]) = \tilde{\boldsymbol{\sigma}}^{2}(\boldsymbol{d}, [|\boldsymbol{\varepsilon}|]) \end{cases} \tag{A.55}$$

By using equation (A.37) and replacing the function $\tilde{\boldsymbol{G}_1}^{1/2}$ by the function $\boldsymbol{G_1}^{1/2}$ for two domains: firstly is $\boldsymbol{\Omega_1}$ for the phase 1, secondly is $\boldsymbol{\Omega_2}$ for the phase 2, in addition, from the relation $\boldsymbol{\Omega_1} \bigcup \boldsymbol{\Omega_2}$ we can obtain:

$$\int_{\boldsymbol{\Omega_{1,e}}} \tilde{\boldsymbol{G}_1}^{1}\boldsymbol{E_1}(\boldsymbol{Bd}+\boldsymbol{G_1}^{1}[|\boldsymbol{\varepsilon}|])\boldsymbol{d\Omega_1} + \int_{\boldsymbol{\Omega_{2,e}}} \tilde{\boldsymbol{G}_1}^{2}\boldsymbol{E_2}(\boldsymbol{Bd}+\boldsymbol{G_1}^{2}[|\boldsymbol{\varepsilon}|])\boldsymbol{d\Omega_2} = \boldsymbol{0}\forall \boldsymbol{e} \in [\boldsymbol{1}, \boldsymbol{n_{elm}}] \tag{A.56}$$

From the equation (A.49), and the values of $\tilde{\boldsymbol{G}_1}^{1}$ and $\tilde{\boldsymbol{G}_1}^{2}$ are equal to $-\frac{\boldsymbol{1}}{\boldsymbol{\theta\ell}}$ and $\frac{\boldsymbol{1}}{\boldsymbol{(1-\theta)\ell}}$, respectively, and the integration we obtain:

$$-\frac{\boldsymbol{1}}{\boldsymbol{\theta\ell}}\boldsymbol{E_1}(\boldsymbol{Bd}+\boldsymbol{G_1}^{1}[|\boldsymbol{\varepsilon}|])\boldsymbol{A\theta\ell} + \frac{\boldsymbol{1}}{\boldsymbol{(1-\theta)\theta}}\boldsymbol{E_2}(\boldsymbol{Bd}+\boldsymbol{G_1}^{2}[|\boldsymbol{\varepsilon}|])\boldsymbol{A(1-\theta)\ell} = \boldsymbol{0}\forall \boldsymbol{e} \in [\boldsymbol{1}, \boldsymbol{n_{elm}}] \tag{A.57}$$

after simplify the equation (A.57) and making rearrangement, we obtain:

$$-\boldsymbol{E}_1(\boldsymbol{B}\,\boldsymbol{d}+\boldsymbol{G_1}^1[|\varepsilon|])\boldsymbol{A}+\boldsymbol{E}_2(\boldsymbol{B}\,\boldsymbol{d}+\boldsymbol{G_1}^2[|\varepsilon|])\boldsymbol{A}=\boldsymbol{0}\ \ \forall\,\boldsymbol{e}\in[\boldsymbol{1},\boldsymbol{n_{elm}}] \tag{A.58}$$

where $\boldsymbol{A}$ is the cross section of the bar element, in addition the stress for each phase is as shown below:

$$\tilde{\boldsymbol{\sigma}}^1(\boldsymbol{d},[|\varepsilon|]+\tilde{\boldsymbol{\sigma}}^2(\boldsymbol{d},[|\varepsilon|])=\boldsymbol{0} \tag{A.59}$$

According to the equations (A.46)-(A.48), for the bar element with two-phase materials, new formulations can be obtained:

$$\boldsymbol{A}_{e=1}^{n_{elm}}[\boldsymbol{f}_{int}^{e}(\boldsymbol{d},[|\varepsilon|])-\boldsymbol{f}_{ext}^{e}]=\boldsymbol{0} \tag{A.60}$$

$$\boldsymbol{h}_{[||\varepsilon|]}=\tilde{\boldsymbol{\sigma}}^1(\boldsymbol{d},[|\varepsilon|]+\tilde{\boldsymbol{\sigma}}^2(\boldsymbol{d},[|\varepsilon|])=\boldsymbol{0} \tag{A.61}$$

where

$$\boldsymbol{f}_{int}^{e}=\int_{\Omega_{1,e}}\boldsymbol{B}^T\boldsymbol{E}_1(\boldsymbol{B}\,\boldsymbol{d}+\boldsymbol{G_1}^1[|\varepsilon|])\,d\Omega_1+\int_{\Omega_{2,e}}\boldsymbol{B}^T\boldsymbol{E}_2(\boldsymbol{B}\,\boldsymbol{d}+\boldsymbol{G_1}^2[|\varepsilon|])\,d\Omega_2=\boldsymbol{0} \tag{A.62}$$

From the above mentioned, can be considered a weak discontinuity is one of kinematic enhancement that was used to implement the multi-phase materials which did not need a change in the adapted meshes, a set of bar of elements placed at the interfaces between the aggregate and the cement paste, i.e. each part has its modulus of elasticity, the first part is placed into the cement paste, and the second part is placed into the aggregate particles.

According to the equation (A.61), that refers to a linear equation, the next subsection presents linearization for the equations (A.60)-(A.62) corresponding

the relation of $\boldsymbol{d}$ and $[|\boldsymbol{\varepsilon}|]$ to obtain a matrix or a system which can be solved. The general linearization equation is as given below:

$$\boldsymbol{\Psi}(\boldsymbol{\chi}) = \boldsymbol{\chi}\Big|_{n+1}^{(k)} + \sum_i \frac{\partial \boldsymbol{\chi}}{\partial \boldsymbol{\Xi_i}}\Big|_{n+1}^{(k)} \boldsymbol{\Delta\Xi_i}\Big|_{n+1}^{(k+1)} = \mathbf{0} \tag{A.63}$$

where $\boldsymbol{n}$ is time step, $\boldsymbol{k}$ is the itteration for the convergence of problem and $\boldsymbol{\Xi_i}$ is the variable.

A.3.1 Linearization of weak discontinuity equation

According to the equation (A.63) the linearization of equation (A.60) will be found and this result can be obtained:

$$\begin{aligned}
\boldsymbol{A}_{e=1}^{n_{elm}}\Big[&\int_{\Omega_{1,e}} \boldsymbol{B}^T \boldsymbol{E}_1 \frac{\partial(\boldsymbol{B}\,\boldsymbol{d} + \boldsymbol{G_1}^1[|\boldsymbol{\varepsilon}|])}{\partial \boldsymbol{d}}\Big|_{n+1}^{(k)} \boldsymbol{\Delta d}_{n+1}^{(k+1)} d\Omega_1 \\
&+ \int_{\Omega_{2,e}} \boldsymbol{B}^T \boldsymbol{E}_2 \frac{\partial(\boldsymbol{B}\,\boldsymbol{d} + \boldsymbol{G_1}^2[|\boldsymbol{\varepsilon}|])}{\partial \boldsymbol{d}}\Big|_{n+1}^{(k)} \boldsymbol{\Delta d}_{n+1}^{(k+1)} d\Omega_2 \\
&+ \int_{\Omega_{1,e}} \boldsymbol{B}^T \boldsymbol{E}_1 \frac{\partial(\boldsymbol{B}\,\boldsymbol{d} + \boldsymbol{G_1}^1[|\boldsymbol{\varepsilon}|])}{\partial [|\boldsymbol{\varepsilon}|]}\Big|_{n+1}^{(k)} \boldsymbol{\Delta}[|\boldsymbol{\varepsilon}|]_{n+1}^{(k+1)} d\Omega_1 \\
&+ \int_{\Omega_{2,e}} \boldsymbol{B}^T \boldsymbol{E}_2 \frac{\partial(\boldsymbol{B}\,\boldsymbol{d} + \boldsymbol{G_1}^2[|\boldsymbol{\varepsilon}|])}{\partial [|\boldsymbol{\varepsilon}|]}\Big|_{n+1}^{(k)} \boldsymbol{\Delta}[|\boldsymbol{\varepsilon}|]_{n+1}^{(k+1)} d\Omega_2\Big] \\
&= -\boldsymbol{A}_{e=1}^{n_{elm}}[\boldsymbol{f}_{int}^e - \boldsymbol{f}_{ext}^e]\Big|_{n+1}^{(k)}
\end{aligned} \tag{A.64}$$

By deriving this formulation according to the relation $(\boldsymbol{d}, [|\boldsymbol{\varepsilon}|])$, we obtain:

$$\begin{aligned}
\boldsymbol{A}_{e=1}^{n_{elm}}\Big[&\int_{\Omega_{1,e}} \boldsymbol{B}^T \boldsymbol{E}_1 \boldsymbol{B} \boldsymbol{\Delta d}_{n+1}^{(k+1)} d\Omega_1 + \int_{\Omega_{2,e}} \boldsymbol{B}^T \boldsymbol{E}_2 \boldsymbol{B} \boldsymbol{\Delta d}_{n+1}^{(k+1)} d\Omega_2 \\
&+ \int_{\Omega_{1,e}} \boldsymbol{B}^T \boldsymbol{E}_1 \boldsymbol{G_1}^1 \boldsymbol{\Delta}[|\boldsymbol{\varepsilon}|]_{n+1}^{(k+1)} d\Omega_1 + \int_{\Omega_{2,e}} \boldsymbol{B}^T \boldsymbol{E}_2 \boldsymbol{G_1}^2 \boldsymbol{\Delta}[|\boldsymbol{\varepsilon}|]_{n+1}^{(k+1)} d\Omega_2\Big] \\
&= -\boldsymbol{A}_{e=1}^{n_{elm}}[\boldsymbol{f}_{int}^e - \boldsymbol{f}_{ext}^e]\Big|_{n+1}^{(k)}
\end{aligned} \tag{A.65}$$

By integrating the domains $\boldsymbol{\Omega_1}$ and $\boldsymbol{\Omega_2}$ ($[\mathbf{0}, \boldsymbol{\theta\ell}]$, $[\boldsymbol{\theta\ell}, \boldsymbol{\ell}]$, respectively, with substituting the previous equation corresponding the functions $\boldsymbol{G_1}^1$ and $\boldsymbol{G_1}^2$ become:

$$\begin{aligned} \boldsymbol{A}_{e=1}^{n_{elm}}[\int_{\Omega_{1,e}} \boldsymbol{B}^T \boldsymbol{E_1} \boldsymbol{B}\ \boldsymbol{A}\theta\ell\boldsymbol{\Delta d}_{n+1}^{(k+1)} + \boldsymbol{B}^T \boldsymbol{E_2} \boldsymbol{B}\ \boldsymbol{A}(1-\theta)\ell\boldsymbol{\Delta d}_{n+1}^{(k+1)} \\ - \boldsymbol{B}^T \boldsymbol{E_1} \boldsymbol{A}\boldsymbol{\Delta}[|\varepsilon|]_{n+1}^{(k+1)} + \boldsymbol{B}^T \boldsymbol{E_2} \boldsymbol{A}\boldsymbol{\Delta}[|\varepsilon|]_{n+1}^{(k+1)}] \\ = -\boldsymbol{A}_{e=1}^{n_{elm}}[\boldsymbol{f}_{int}^e - \boldsymbol{f}_{ext}^e]\Big|_{n+1}^{(k)} \end{aligned} \tag{A.66}$$

By using the general linearization equation (A.63) the linearization of equation (A.61) will be obtained as shown below:

$$\begin{aligned} &- \boldsymbol{E_1} \frac{\partial(\boldsymbol{B}\,\boldsymbol{d} + \boldsymbol{G_1}^1[|\varepsilon|])}{\partial \boldsymbol{d}}\Big|_{n+1}^{(k)} \boldsymbol{A}\boldsymbol{\Delta}\boldsymbol{d}_{n+1}^{(k+1)} + \boldsymbol{E_2} \frac{\partial(\boldsymbol{B}\,\boldsymbol{d} + \boldsymbol{G_1}^2[|\varepsilon|])}{\partial \boldsymbol{d}}\Big|_{n+1}^{(k)} \boldsymbol{A}\boldsymbol{\Delta}\boldsymbol{d}_{n+1}^{(k+1)} \\ &- \boldsymbol{E_1} \frac{\partial(\boldsymbol{B}\,\boldsymbol{d} + \boldsymbol{G_1}^1[|\varepsilon|])}{\partial [|\varepsilon|]}\Big|_{n+1}^{(k)} \boldsymbol{A}\boldsymbol{\Delta}[|\varepsilon|]_{n+1}^{(k+1)} + \boldsymbol{E_2} \frac{\partial(\boldsymbol{B}\,\boldsymbol{d} + \boldsymbol{G_1}^2[|\varepsilon|])}{\partial [|\varepsilon|]}\Big|_{n+1}^{(k)} \boldsymbol{A}\boldsymbol{\Delta}[|\varepsilon|]_{n+1}^{(k+1)} \\ &= -\boldsymbol{A}\boldsymbol{h}_{[|\varepsilon|]}\Big|_{n+1}^{(k)} \end{aligned} \tag{A.67}$$

By deriving the previous formulation (A.67) according to the relation $(\boldsymbol{d}, [|\varepsilon|])$ and dividing on $\boldsymbol{A}$, it becomes:

$$\begin{aligned} &- \boldsymbol{E_1}\boldsymbol{B}\boldsymbol{\Delta}\boldsymbol{d}_{n+1}^{(k+1)} + \boldsymbol{E_2}\boldsymbol{B}\boldsymbol{\Delta}\boldsymbol{d}_{n+1}^{(k+1)} - \boldsymbol{E_1}\boldsymbol{G_1}^1\boldsymbol{\Delta}[|\varepsilon|]_{n+1}^{(k+1)} + \boldsymbol{E_2}\boldsymbol{G_1}^2\boldsymbol{\Delta}[|\varepsilon|]_{n+1}^{(k+1)} \\ &= -\boldsymbol{h}_{[|\varepsilon|]}\Big|_{n+1}^{(k)} \end{aligned} \tag{A.68}$$

For representing the equations (A.66) and (A.68) as a matrix, can be written:

$$\begin{pmatrix} \boldsymbol{K} & \boldsymbol{F} \\ \boldsymbol{F}^T & \boldsymbol{b} \end{pmatrix}_{n+1}^{(k)} \begin{pmatrix} \boldsymbol{\Delta d} \\ \boldsymbol{\Delta}[|\varepsilon|] \end{pmatrix}_{n+1}^{(k+1)} = \begin{pmatrix} -\boldsymbol{A}_{e=1}^{n_{elm}}[\boldsymbol{f}_{int}^e - \boldsymbol{f}_{ext}^e] \\ -\boldsymbol{h}_{[|\varepsilon|]} \end{pmatrix}_{n+1}^{(k)} \tag{A.69}$$

where

$$\begin{aligned} \boldsymbol{K} &= \boldsymbol{A}_{e=1}^{n_{elm}}[\boldsymbol{B}^{\boldsymbol{T}}\boldsymbol{E}_{\boldsymbol{1}}\boldsymbol{B}\ \boldsymbol{A}\boldsymbol{\theta}\boldsymbol{\ell} + \boldsymbol{B}^{\boldsymbol{T}}\boldsymbol{E}_{\boldsymbol{2}}\boldsymbol{B}\ \boldsymbol{A}(\boldsymbol{1}-\boldsymbol{\theta})\boldsymbol{\ell}] \\ \boldsymbol{F} &= \boldsymbol{B}^{\boldsymbol{T}}[-\boldsymbol{E}_{\boldsymbol{1}} + \boldsymbol{E}_{\boldsymbol{2}}]\boldsymbol{A} \\ \boldsymbol{b} &= \boldsymbol{E}_{\boldsymbol{1}}\boldsymbol{G}_{\boldsymbol{1}}{}^{\boldsymbol{1}} + \boldsymbol{E}_{\boldsymbol{2}}\boldsymbol{G}_{\boldsymbol{1}}{}^{\boldsymbol{2}} = \frac{\boldsymbol{E}_{\boldsymbol{1}}}{\boldsymbol{\theta}\boldsymbol{\ell}} + \frac{\boldsymbol{E}_{\boldsymbol{2}}}{(\boldsymbol{1}-\boldsymbol{\theta})\boldsymbol{\ell}} \end{aligned} \tag{A.70}$$

A.4 Strong discontinuity

This type of enhancement deals with the quasi-brittle material, therefore the failure mechanism is triggered under a loading that is leading to a crack opening (broken element) in the domain $\boldsymbol{\Omega_e}$, which is splitted to two parts $\boldsymbol{\Omega_1}$ and $\boldsymbol{\Omega_2}$. Therefore, for implementing this kinematic enhancement we are depending on the E-FEM and the method of incompatible modes. So we, by strong discontinuity, are able to explicit the geometrical properties of the crack opening in the heterogeneous material such as: the dimensions of crack, its position and its pathway.

However, the equations (A.46)-(A.48) as the weak discontinuity was used in the previous section. Herein, this type of enrichment is taking into account both enhancements: the first one is according to the incompatible modes for strain field as shown below:

$$\boldsymbol{\varepsilon} = \boldsymbol{\partial u} + \tilde{\boldsymbol{\varepsilon}}_{\boldsymbol{1}} = \boldsymbol{B}\ \boldsymbol{d} + \boldsymbol{G}_{\boldsymbol{1}}^{\boldsymbol{1/2}}[|\boldsymbol{\varepsilon}|] \tag{A.71}$$

where $\boldsymbol{G}_{\boldsymbol{1}}^{\boldsymbol{1/2}}$ is the function according to the method of incompatible modes as the weak discontinuity.

The second enhancement refers to the strain field, also, while it represented the actual displacement it has been noted $\tilde{\boldsymbol{\varepsilon}}_{\boldsymbol{2}} = \boldsymbol{G}_{\boldsymbol{2}}[|\boldsymbol{u}|]$, where $\boldsymbol{G}_{\boldsymbol{2}}$ is the second incompatible mode which divided into two parts, it is a regular part $\bar{\boldsymbol{G}}_{\boldsymbol{2}}$ and a

non-regular part $\bar{\bar{G}}_2$ [Ibrahimbegovic, 2006]. Therefore, the equation (A.71) can be re-written with two strains as shown below:

$$\varepsilon = \partial + \tilde{\varepsilon}_1 + \tilde{\varepsilon}_2 \tag{A.72}$$

As shown in Figure (A.3), the bar element with strong discontinuity, which was placed at the interfaces between aggregate and cement. In addition, the second incompatible mode function G_2 can be written as:

$$G_2 = -\frac{1}{\ell} + \delta_\Gamma \tag{A.73}$$

where ℓ is the length of the bar element, θ is the dimensionless parameter, $-\frac{1}{\ell}$ refers to $\bar{G}_2$ and δ_Γ refers to $\bar{\bar{G}}_2$. The last one refers to the Dirac function which was placed at the interfaces between the aggregate and mortar. From function G_2 the crack at the interfaces can be measured when the bar element is placed into this zone. In the bar element is $G_2 = \tilde{G}_2$.

The previous vector G, can be re-written with two incompatible modes as:

$$G = [G_1^{1/2}, G_2] \tag{A.74}$$

and the vector a has local unknowns is formed as:

$$a = \begin{bmatrix} [|\varepsilon|] \\ [|u|] \end{bmatrix} \tag{A.75}$$

For representing the mechanical behavior of crack opening in two-phase materials by using the Discrete Strong Discontinuity Approach, two behaviors are taken into account. Firstly, it should be considered that the two parts are continuum. Secondly, the two domains Ω_1 and Ω_2 have been considered to have an elastic properties. In addition, the strain fields can be written for each phase as:

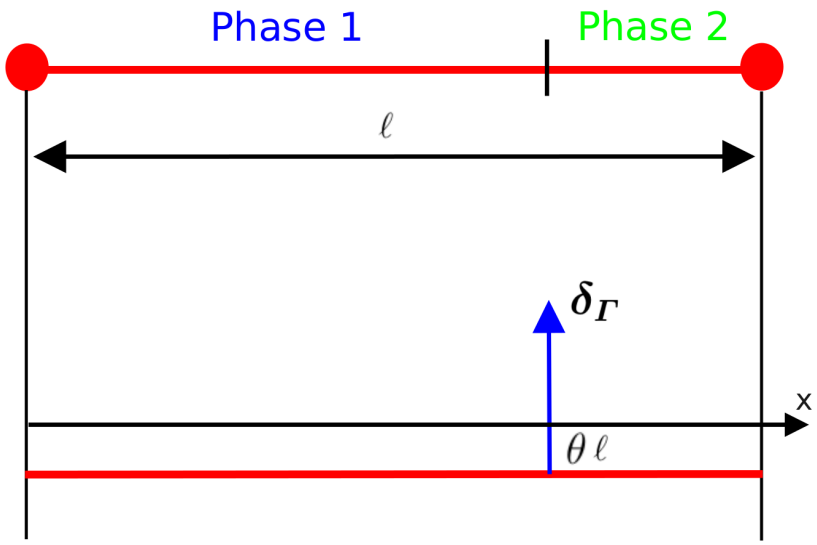

Figure A.3: Bar element for representing the crack opening at strong discontinuity into interface zone by Benkemoun in [Benkemoun, 2010].

$$\varepsilon^1 = \boldsymbol{B}\,\boldsymbol{d} + \boldsymbol{G_1}^1[|\varepsilon|] + \bar{\boldsymbol{G}}_2[|\boldsymbol{u}|], \quad \varepsilon^2 = \boldsymbol{B}\,\boldsymbol{d} + \boldsymbol{G_1}^2[|\varepsilon|] + \bar{\boldsymbol{G}}_2[|\boldsymbol{u}|] \tag{A.76}$$

For the above mentioned, the behavior of two materials have been elastic, can be obtained:

$$\begin{cases} \tilde{\boldsymbol{\sigma}}^1(\boldsymbol{B}\,\boldsymbol{d} + \boldsymbol{G_1}^1[|\varepsilon|] + \bar{\boldsymbol{G}}_2[|\boldsymbol{u}|]) = \boldsymbol{E}_1\,\varepsilon^1 = \boldsymbol{E}_1(\boldsymbol{B}\,\boldsymbol{d} + \boldsymbol{G_1}^1[|\varepsilon|] + \bar{\boldsymbol{G}}_2[|\boldsymbol{u}|]) \\ \tilde{\boldsymbol{\sigma}}^2(\boldsymbol{B}\,\boldsymbol{d} + \boldsymbol{G_1}^2[|\varepsilon|] + \bar{\boldsymbol{G}}_2[|\boldsymbol{u}|]) = \boldsymbol{E}_2\,\varepsilon^2 = \boldsymbol{E}_2(\boldsymbol{B}\,\boldsymbol{d} + \boldsymbol{G_1}^2[|\varepsilon|] + \bar{\boldsymbol{G}}_2[|\boldsymbol{u}|]) \end{cases} \tag{A.77}$$

therefore, the simplify of previous equation can be written as:

$$\begin{cases} \tilde{\boldsymbol{\sigma}}^1(\boldsymbol{B}\,\boldsymbol{d} + \boldsymbol{G_1}^1[|\varepsilon|] + \bar{\boldsymbol{G}}_2[|\boldsymbol{u}|]) = \tilde{\boldsymbol{\sigma}}^1(\boldsymbol{d}, [|\varepsilon|], [|\boldsymbol{u}|]) \\ \tilde{\boldsymbol{\sigma}}^2(\boldsymbol{B}\,\boldsymbol{d} + \boldsymbol{G_1}^2[|\varepsilon|] + \bar{\boldsymbol{G}}_2[|\boldsymbol{u}|]) = \tilde{\boldsymbol{\sigma}}^2(\boldsymbol{d}, [|\varepsilon|], [|\boldsymbol{u}|]) \end{cases} \tag{A.78}$$

By substituting the equation (A.78) in the equations (A.46)-(A.48) the finite element discretization of bar element can be obtained as:

$$\boldsymbol{A}_{e=1}^{n_{elm}}[\boldsymbol{f}_{int}^{e}(\boldsymbol{d},[|\varepsilon|],[|\boldsymbol{u}|]) - \boldsymbol{f}_{ext}^{e}] = \boldsymbol{0} \tag{A.79}$$

$$\int_{\Omega_e} \tilde{\boldsymbol{G}}_{\boldsymbol{1}}^{\boldsymbol{1/2}}\tilde{\boldsymbol{\sigma}}^{\boldsymbol{1/2}}(\boldsymbol{d},[|\varepsilon|],[|\boldsymbol{u}|])\, d\boldsymbol{\Omega} = \boldsymbol{0} \quad \forall\, \boldsymbol{e} \in [\boldsymbol{1}, \boldsymbol{n_{elm}}] \tag{A.80}$$

$$\int_{\Omega_e} \tilde{\boldsymbol{G}}_{\boldsymbol{2}}\tilde{\boldsymbol{\sigma}}^{\boldsymbol{1/2}}(\boldsymbol{d},[|\varepsilon|],[|\boldsymbol{u}|])\, d\boldsymbol{\Omega} = \boldsymbol{0} \quad \forall\, \boldsymbol{e} \in [\boldsymbol{1}, \boldsymbol{n_{elm}}] \tag{A.81}$$

where

$$\begin{aligned} \boldsymbol{f}_{int}^{e} = &\int_{\Omega_{1,e}} \boldsymbol{B}^{T}\boldsymbol{E}_{\boldsymbol{1}}(\boldsymbol{B}\,\boldsymbol{d} + \boldsymbol{G}_{\boldsymbol{1}}{}^{\boldsymbol{1}}[|\varepsilon|] + \bar{\boldsymbol{G}}_{\boldsymbol{2}}[|\boldsymbol{u}|])\, d\boldsymbol{\Omega}_{\boldsymbol{1}} \\ &+ \int_{\Omega_{2,e}} \boldsymbol{B}^{T}\boldsymbol{E}_{\boldsymbol{2}}(\boldsymbol{B}\,\boldsymbol{d} + \boldsymbol{G}_{\boldsymbol{1}}{}^{\boldsymbol{2}}[|\varepsilon|] + \bar{\boldsymbol{G}}_{\boldsymbol{2}}[|\boldsymbol{u}|])\, d\boldsymbol{\Omega}_{\boldsymbol{2}} \end{aligned} \tag{A.82}$$

According to the equations (A.79)-(A.82), a new formulation can be obtained for the bar element with two-phase materials and corresponding the relation $[|\boldsymbol{u}|]$. After replacing $\tilde{\boldsymbol{G}}_{\boldsymbol{1}}^{\boldsymbol{1/2}}$ by $\boldsymbol{G}_{\boldsymbol{1}}^{\boldsymbol{1/2}}$ and $\tilde{\boldsymbol{G}}_{\boldsymbol{2}}$ by $\boldsymbol{G}_{\boldsymbol{2}}$. This leads to:

$$\boldsymbol{h}_{[|\varepsilon|]} = -\tilde{\boldsymbol{\sigma}}^{\boldsymbol{1}}(\boldsymbol{d},[|\varepsilon|],[|\boldsymbol{u}|]) + \tilde{\boldsymbol{\sigma}}^{\boldsymbol{2}}(\boldsymbol{d},[|\varepsilon|],[|\boldsymbol{u}|]) = \boldsymbol{0} \tag{A.83}$$

then,

$$\int_{\Omega_e} \tilde{\bar{\boldsymbol{G}}}_{\boldsymbol{2}}\tilde{\boldsymbol{\sigma}}^{\boldsymbol{1/2}}(\boldsymbol{d},[|\varepsilon|],[|\boldsymbol{u}|])d\boldsymbol{\Omega} + \int_{\Omega_e} \bar{\bar{\boldsymbol{G}}}_{\boldsymbol{2}}\tilde{\boldsymbol{\sigma}}^{\boldsymbol{1/2}}(\boldsymbol{d},[|\varepsilon|],[|\boldsymbol{u}|])d\boldsymbol{\Omega} = \boldsymbol{0} \forall \boldsymbol{e} \in [\boldsymbol{1}, \boldsymbol{n_{elm}}] \tag{A.84}$$

However, in equation (A.73) the functions $\tilde{\bar{\boldsymbol{G}}}_{\boldsymbol{2}} = -\frac{\boldsymbol{1}}{\boldsymbol{\ell}}$ and $\bar{\bar{\boldsymbol{G}}}_{\boldsymbol{2}} = \boldsymbol{\delta}_{\boldsymbol{\Gamma}}$, therefore this leads to:

$$\int_{\Omega_e} -\frac{1}{\ell}\tilde{\boldsymbol{\sigma}}^{1/2}(\boldsymbol{d},[|\boldsymbol{\varepsilon}|],[|\boldsymbol{u}|])d\boldsymbol{\Omega}+\int_{\Omega_e}\boldsymbol{\delta}_{\boldsymbol{\Gamma}}\tilde{\boldsymbol{\sigma}}^{1/2}(\boldsymbol{d},[|\boldsymbol{\varepsilon}|],[|\boldsymbol{u}|])d\boldsymbol{\Omega}=\mathbf{0}\forall\boldsymbol{e}\in[\mathbf{1},\boldsymbol{n}_{elm}] \tag{A.85}$$

According to the Dirac function and its integration can be written:

$$\int_{\boldsymbol{\Omega}}\boldsymbol{\delta}_{\boldsymbol{\Gamma}}\boldsymbol{\alpha}_{\mathbf{0}}\,d\boldsymbol{\Omega}=\int_{\boldsymbol{\Gamma}}\boldsymbol{\alpha}_{\mathbf{0}}\,d\boldsymbol{\Gamma}\quad\forall\,\boldsymbol{\alpha}_{\mathbf{0}}\in\boldsymbol{C}_{\mathbf{0}}^{\infty}(\boldsymbol{\Omega}) \tag{A.86}$$

$$\int_{\Omega_e} -\frac{1}{\ell}\tilde{\boldsymbol{\sigma}}^{1/2}(\boldsymbol{d},[|\boldsymbol{\varepsilon}|],[|\boldsymbol{u}|])\,d\boldsymbol{\Omega}+\int_{\boldsymbol{\Gamma}}\tilde{\boldsymbol{\sigma}}^{1/2}(\boldsymbol{d},[|\boldsymbol{\varepsilon}|],[|\boldsymbol{u}|])|_{\boldsymbol{\Gamma}}\,d\boldsymbol{\Gamma}=\mathbf{0}\,\forall\boldsymbol{e}\in[\mathbf{1},\boldsymbol{n}_{elm}] \tag{A.87}$$

where $\tilde{\boldsymbol{\sigma}}^{1/2}(\boldsymbol{d},[|\boldsymbol{\varepsilon}|],[|\boldsymbol{u}|])|_{\boldsymbol{\Gamma}}$ refers to the traction vector $\boldsymbol{t}_{\boldsymbol{\Gamma}}$, can be re-written:

$$\int_{\Omega_e} -\frac{1}{\ell}\tilde{\boldsymbol{\sigma}}^{1/2}(\boldsymbol{d},[|\boldsymbol{\varepsilon}|],[|\boldsymbol{u}|])\,d\boldsymbol{\Omega}+\int_{\boldsymbol{\Gamma}}\boldsymbol{t}_{\boldsymbol{\Gamma}}d\boldsymbol{\Gamma}=\mathbf{0}\quad\forall\,\boldsymbol{e}\in[\mathbf{1},\boldsymbol{n}_{elm}] \tag{A.88}$$

However, by dividing the equation (A.87) for the two domains $\boldsymbol{\Omega}_{\mathbf{1}}$ and $\boldsymbol{\Omega}_{\mathbf{2}}$ corresponding two-phase materials, the formula can be re-written:

$$\begin{aligned}&\int_{\Omega_{1,e}} -\frac{1}{\ell}\tilde{\boldsymbol{\sigma}}^{1}(\boldsymbol{d},[|\boldsymbol{\varepsilon}|],[|\boldsymbol{u}|])\,d\boldsymbol{\Omega}_{\mathbf{1}}+\int_{\Omega_{2,e}} -\frac{1}{\ell}\tilde{\boldsymbol{\sigma}}^{2}(\boldsymbol{d},[|\boldsymbol{\varepsilon}|],[|\boldsymbol{u}|])\,d\boldsymbol{\Omega}_{\mathbf{2}}\\&+\int_{\boldsymbol{\Gamma}}\boldsymbol{t}_{\boldsymbol{\Gamma}}d\boldsymbol{\Gamma}=\mathbf{0}\quad\forall\,\boldsymbol{e}\in[\mathbf{1},\boldsymbol{n}_{elm}]\end{aligned} \tag{A.89}$$

By injecting the equation (A.77) into the equation (A.88), can be obtained:

$$\begin{aligned}&\int_{\Omega_{1,e}} -\frac{1}{\ell}\boldsymbol{E}_{\mathbf{1}}(\boldsymbol{B}\,\boldsymbol{d}+\boldsymbol{G}_{\mathbf{1}}{}^{1}[|\boldsymbol{\varepsilon}|]+\bar{\boldsymbol{G}}_{\mathbf{2}}[|\boldsymbol{u}|])\,d\boldsymbol{\Omega}_{\mathbf{1}}\\&+\int_{\Omega_{2,e}} -\frac{1}{\ell}\boldsymbol{E}_{\mathbf{2}}(\boldsymbol{B}\,\boldsymbol{d}+\boldsymbol{G}_{\mathbf{1}}{}^{2}[|\boldsymbol{\varepsilon}|]+\bar{\boldsymbol{G}}_{\mathbf{2}}[|\boldsymbol{u}|])\,d\boldsymbol{\Omega}_{\mathbf{2}}\\&+\int_{\boldsymbol{\Gamma}}\boldsymbol{t}_{\boldsymbol{\Gamma}}d\boldsymbol{\Gamma}=\mathbf{0}\quad\forall\,\boldsymbol{e}\in[\mathbf{1},\boldsymbol{n}_{elm}]\end{aligned} \tag{A.90}$$

After the integration of equation(A.89) for the two domains $\boldsymbol{\Omega_{1,e}}$ and $\boldsymbol{\Omega_{2,e}}$, $[\boldsymbol{0}, \boldsymbol{\theta\ell}]$ and $[\boldsymbol{\theta\ell}, \boldsymbol{\ell}]$, respectively, we obtain:

$$\begin{aligned} &\boldsymbol{E_1}(\boldsymbol{B}\,\boldsymbol{d} + \boldsymbol{G_1^{1/2}}[|\varepsilon|] + \boldsymbol{\bar{G}_2}[|\boldsymbol{u}|])\,\boldsymbol{A}\,\boldsymbol{\theta} \\ &+ \boldsymbol{E_2}(\boldsymbol{B}\,\boldsymbol{d} + \boldsymbol{G_1^{1/2}}[|\varepsilon|] + \boldsymbol{\bar{G}_2}[|\boldsymbol{u}|])\,\boldsymbol{A}(\boldsymbol{1}-\boldsymbol{\theta}) \\ &+ \boldsymbol{t_\Gamma}\boldsymbol{A} = \boldsymbol{0} \quad \forall\, \boldsymbol{e} \in [\boldsymbol{1}, \boldsymbol{n_{elm}}] \end{aligned} \tag{A.91}$$

By dividing on $\boldsymbol{A}$, this leads to:

$$\begin{aligned} &\boldsymbol{E_1}(\boldsymbol{B}\,\boldsymbol{d} + \boldsymbol{G_1^{1/2}}[|\varepsilon|] + \boldsymbol{\bar{G}_2}[|\boldsymbol{u}|])\,\boldsymbol{\theta} \\ &+ \boldsymbol{E_2}(\boldsymbol{B}\,\boldsymbol{d} + \boldsymbol{G_1^{1/2}}[|\varepsilon|] + \boldsymbol{\bar{G}_2}[|\boldsymbol{u}|])(\boldsymbol{1}-\boldsymbol{\theta}) \\ &+ \boldsymbol{t_\Gamma} = \boldsymbol{0} \quad \forall\, \boldsymbol{e} \in [\boldsymbol{1}, \boldsymbol{n_{elm}}] \end{aligned} \tag{A.92}$$

By using the equation (A.78) for each phase, can be re-written:

$$-\boldsymbol{\theta}\tilde{\boldsymbol{\sigma}}^{\boldsymbol{1}}(\boldsymbol{d}, [|\boldsymbol{\varepsilon}|], [|\boldsymbol{u}|]) - (\boldsymbol{1}-\boldsymbol{\theta})\tilde{\boldsymbol{\sigma}}^{\boldsymbol{2}}(\boldsymbol{d}, [|\boldsymbol{\varepsilon}|], [|\boldsymbol{u}|]) + \boldsymbol{t_\Gamma} = \boldsymbol{0} \forall \boldsymbol{e} \in [\boldsymbol{1}, \boldsymbol{n_{elm}}] \tag{A.93}$$

Finally, from the equations (A.79)-(A.82) which discretizied the bar element with two-phase materials and previous equation (A.91), can be re-written:

$$\boldsymbol{A}_{\boldsymbol{e=1}}^{\boldsymbol{n_{elm}}}[\boldsymbol{f}_{\boldsymbol{int}}^{\boldsymbol{e}}(\boldsymbol{d}, [|\boldsymbol{\varepsilon}|], [|\boldsymbol{u}|]) - \boldsymbol{f}_{\boldsymbol{ext}}^{\boldsymbol{e}}] = \boldsymbol{0} \tag{A.94}$$

$$\boldsymbol{h}_{[|\boldsymbol{\varepsilon}|]} = -\tilde{\boldsymbol{\sigma}}^{\boldsymbol{1}}(\boldsymbol{d}, [|\boldsymbol{\varepsilon}|], [|\boldsymbol{u}|]) + \tilde{\boldsymbol{\sigma}}^{\boldsymbol{2}}(\boldsymbol{d}, [|\boldsymbol{\varepsilon}|], [|\boldsymbol{u}|]) = \boldsymbol{0} \quad \forall\, \boldsymbol{e} \in [\boldsymbol{1}, \boldsymbol{n_{elm}}] \tag{A.95}$$

$$\boldsymbol{h}_{[|\boldsymbol{u}|]} = -\boldsymbol{\theta}\tilde{\boldsymbol{\sigma}}^{\boldsymbol{1}}(\boldsymbol{d}, [|\boldsymbol{\varepsilon}|], [|\boldsymbol{u}|]) - (\boldsymbol{1}-\boldsymbol{\theta})\tilde{\boldsymbol{\sigma}}^{\boldsymbol{2}}(\boldsymbol{d}, [|\boldsymbol{\varepsilon}|], [|\boldsymbol{u}|]) + \boldsymbol{t_\Gamma} = \boldsymbol{0}\, \forall \boldsymbol{e} \in [\boldsymbol{1}, \boldsymbol{n_{elm}}] \tag{A.96}$$

where

$$\begin{aligned} \boldsymbol{f}_{\boldsymbol{int}}^{\boldsymbol{e}} = & \int_{\boldsymbol{\Omega}_{1,e}} \boldsymbol{B}^{\boldsymbol{T}} \boldsymbol{E}_{\mathbf{1}} (\boldsymbol{B}\, \boldsymbol{d} + \boldsymbol{G}_{\mathbf{1}}{}^{\mathbf{1}} [|\boldsymbol{\varepsilon}|] + \bar{\boldsymbol{G}}_{\mathbf{2}} [|\boldsymbol{u}|])\, \boldsymbol{d\Omega}_{\mathbf{1}} \\ & + \int_{\boldsymbol{\Omega}_{2,e}} \boldsymbol{B}^{\boldsymbol{T}} \boldsymbol{E}_{\mathbf{2}} (\boldsymbol{B}\, \boldsymbol{d} + \boldsymbol{G}_{\mathbf{1}}{}^{\mathbf{2}} [|\boldsymbol{\varepsilon}|] + \bar{\boldsymbol{G}}_{\mathbf{2}} [|\boldsymbol{u}|])\, \boldsymbol{d\Omega}_{\mathbf{2}} \end{aligned} \tag{A.97}$$

As shown in Figure (A.4), the classical behavior of concrete under loading. In addition, the traction vector $\boldsymbol{t}_{\boldsymbol{\Gamma}}$ can be found according to the equation (A.96) at the discontinuity. This equation becomes activated when introducing the discontinuity surface. The heterogeneous material such as concrete is considered a quasi-brittle material, therefore in this work the crack opening due to the applied load is a mode **I**, see Figure (2.1).

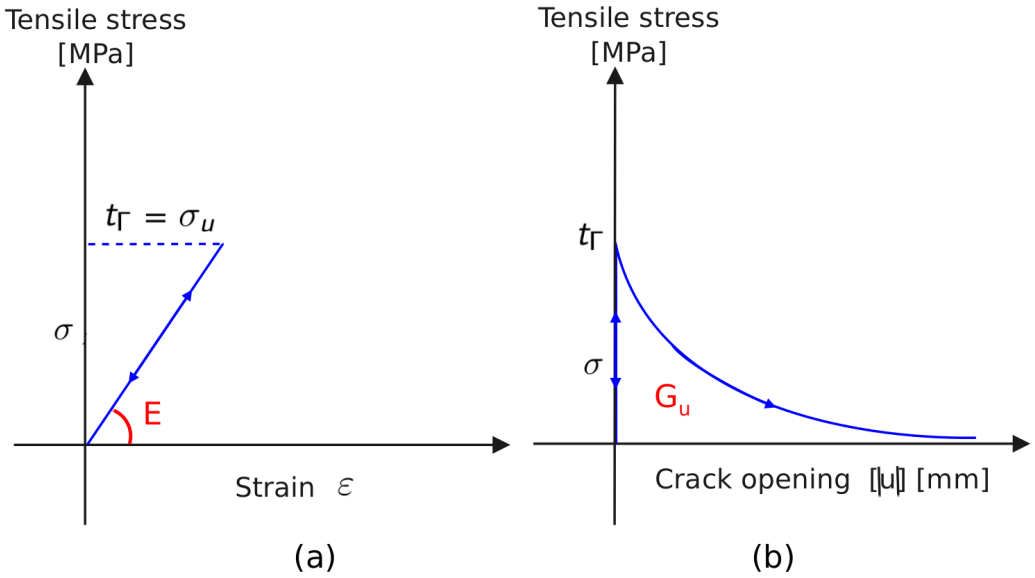

Figure A.4: Elastic-quasi-brittle-behavior: outside the discontinuity (a) at the discontinuity (b) [Benkemoun, 2010].

According to the yield function, $\boldsymbol{\Phi}(\boldsymbol{t}_{\boldsymbol{\Gamma}}, \boldsymbol{q})$ is considered to be the governing equation for linking between the traction stress $\boldsymbol{t}_{\boldsymbol{\Gamma}}$ and the magnitude of crack opening $[|\boldsymbol{u}|]$ as shown below:

$$\boldsymbol{\Phi(t_\Gamma, q) = t_\Gamma - (\sigma_u - q)} \tag{A.98}$$

where $\boldsymbol{t_\Gamma}$ is the tensile stress at the discontinuity in (MPa), $\boldsymbol{\sigma_u}$ is the fracture tensile stress in (MPa), it is equal to $\boldsymbol{\theta\tilde{\sigma}^1(d, [|\varepsilon|], [|u|]) + (1-\theta)\tilde{\sigma}^2(d, [|\varepsilon|], [|u|])}$ and $\boldsymbol{q}$ is the hardening function as shown in equation (A.99) which decrease the experimental relation according to the crack opening value, while it becomes **zero** at the discontinuity therefore, $\boldsymbol{\Phi(t_\Gamma, q) = 0}$. $\boldsymbol{G_u}$ refers to the fracture energy, it can be computed from the area under the stress-crack curve in Figure (A.4(b)), i.e. the amount of energy which is needed to introduce a fully crack opening per meter square.

$$\boldsymbol{q = \sigma_u\left(1 - exp(-\frac{\sigma_u}{G_u}[|u|])\right)} \tag{A.99}$$

A.4.1 Linearization of strong discontinuity equation

According to the formulations (A.94)-(A.97) with inserting $\boldsymbol{\Phi(t_\Gamma, q) = 0}$ at the discontinuity, the formula can be rearranged:

$$\boldsymbol{A_{e=1}^{n_{elm}}[f_{int}^e(d, [|\varepsilon|], [|u|]) - f_{ext}^e] = 0} \tag{A.100}$$

$$\boldsymbol{-\tilde{\sigma}^1(d, [|\varepsilon|], [|u|]) + \tilde{\sigma}^2(d, [|\varepsilon|], [|u|]) = 0 \quad \forall\, e \in [1, n_{elm}]} \tag{A.101}$$

$$\boldsymbol{-\theta\tilde{\sigma}^1(d, [|\varepsilon|], [|u|]) - (1-\theta)\tilde{\sigma}^2(d, [|\varepsilon|], [|u|]) + t_\Gamma = 0 \quad \forall\, e \in [1, n_{elm}]} \tag{A.102}$$

$$\boldsymbol{\Phi(t_\Gamma, [|u|] = 0 \quad \forall\, e \in [1, n_{elm}]} \tag{A.103}$$

To simplify the previous equations (A.100)-(A.103), they have four unknowns $\boldsymbol{d}$, $[|\boldsymbol{\varepsilon}|]$, $[|\boldsymbol{u}|]$ and $\boldsymbol{t_\Gamma}$, where the equation (A.102) refers to $\boldsymbol{t_\Gamma}$ to be a function of $\boldsymbol{d}$, $[|\boldsymbol{\varepsilon}|]$ and $[|\boldsymbol{u}|]$, the equation can be re-written:

$$\boldsymbol{A}_{e=1}^{n_{elm}}[\boldsymbol{f}_{int}^{e}(\boldsymbol{d},[|\boldsymbol{\varepsilon}|],[|\boldsymbol{u}|])-\boldsymbol{f}_{ext}^{e}]=\boldsymbol{0} \tag{A.104}$$

$$-\tilde{\boldsymbol{\sigma}}^{1}(\boldsymbol{d},[|\boldsymbol{\varepsilon}|],[|\boldsymbol{u}|])+\tilde{\boldsymbol{\sigma}}^{2}(\boldsymbol{d},[|\boldsymbol{\varepsilon}|],[|\boldsymbol{u}|])=\boldsymbol{0}\quad\forall\,\boldsymbol{e}\in[\boldsymbol{1},\boldsymbol{n_{elm}}] \tag{A.105}$$

$$\boldsymbol{\Phi}(\boldsymbol{t_\Gamma},[|\boldsymbol{u}|]=\boldsymbol{0}\quad\forall\,\boldsymbol{e}\in[\boldsymbol{1},\boldsymbol{n_{elm}}] \tag{A.106}$$

According to the general linearization equation that is given in equation (A.63), and the equations (A.104)-(A.106), the linearization of equation (A.104) will be presented with relation to $\boldsymbol{d}$, $[|\boldsymbol{\varepsilon}|]$ and $[|\boldsymbol{u}|]$, this equation can be obtained:

$$\begin{aligned}
\boldsymbol{A}_{e=1}^{n_{elm}}\Big[&\int_{\Omega_{1,e}}\boldsymbol{B}^{T}\boldsymbol{E}_{1}\frac{\partial(\boldsymbol{B}\,\boldsymbol{d}+\boldsymbol{G_1}^{1}[|\boldsymbol{\varepsilon}|]+\bar{\boldsymbol{G}}_{2}[|\boldsymbol{u}|]}{\partial\boldsymbol{d}}\Big|_{n+1}^{(k)}\boldsymbol{\Delta}\boldsymbol{d}_{n+1}^{(k+1)}d\Omega_{1}\\
&+\int_{\Omega_{2,e}}\boldsymbol{B}^{T}\boldsymbol{E}_{2}\frac{\partial(\boldsymbol{B}\,\boldsymbol{d}+\boldsymbol{G_1}^{2}[|\boldsymbol{\varepsilon}|]+\bar{\boldsymbol{G}}_{2}[|\boldsymbol{u}|])}{\partial\boldsymbol{d}}\Big|_{n+1}^{(k)}\boldsymbol{\Delta}\boldsymbol{d}_{n+1}^{(k+1)}d\Omega_{2}\\
&+\int_{\Omega_{1,e}}\boldsymbol{B}^{T}\boldsymbol{E}_{1}\frac{\partial(\boldsymbol{B}\,\boldsymbol{d}+\boldsymbol{G_1}^{1}[|\boldsymbol{\varepsilon}|]+\bar{\boldsymbol{G}}_{2}[|\boldsymbol{u}|])}{\partial[|\boldsymbol{\varepsilon}|]}\Big|_{n+1}^{(k)}\boldsymbol{\Delta}[|\boldsymbol{\varepsilon}|]_{n+1}^{(k+1)}d\Omega_{1}\\
&+\int_{\Omega_{2,e}}\boldsymbol{B}^{T}\boldsymbol{E}_{2}\frac{\partial(\boldsymbol{B}\,\boldsymbol{d}+\boldsymbol{G_1}^{2}[|\boldsymbol{\varepsilon}|]+\bar{\boldsymbol{G}}_{2}[|\boldsymbol{u}|])}{\partial[|\boldsymbol{\varepsilon}|]}\Big|_{n+1}^{(k)}\boldsymbol{\Delta}[|\boldsymbol{\varepsilon}|]_{n+1}^{(k+1)}d\Omega_{2}\\
&+\int_{\Omega_{1,e}}\boldsymbol{B}^{T}\boldsymbol{E}_{1}\frac{\partial(\boldsymbol{B}\,\boldsymbol{d}+\boldsymbol{G_1}^{1}[|\boldsymbol{\varepsilon}|]+\bar{\boldsymbol{G}}_{2}[|\boldsymbol{u}|])}{\partial[|\boldsymbol{u}|]}\Big|_{n+1}^{(k)}\boldsymbol{\Delta}[|\boldsymbol{u}|]_{n+1}^{(k+1)}d\Omega_{1}\\
&+\int_{\Omega_{2,e}}\boldsymbol{B}^{T}\boldsymbol{E}_{2}\frac{\partial(\boldsymbol{B}\,\boldsymbol{d}+\boldsymbol{G_1}^{2}[|\boldsymbol{\varepsilon}|]+\bar{\boldsymbol{G}}_{2}[|\boldsymbol{u}|])}{\partial[|\boldsymbol{u}|]}\Big|_{n+1}^{(k)}\boldsymbol{\Delta}[|\boldsymbol{u}|]_{n+1}^{(k+1)}d\Omega_{2}\Big]\\
&=-\boldsymbol{A}_{e=1}^{n_{elm}}[\boldsymbol{f}_{int}^{e}-\boldsymbol{f}_{ext}^{e}]\Big|_{n+1}^{(k)}
\end{aligned} \tag{A.107}$$

By deriving the equation (A.107) according to its relation to $\boldsymbol{d}, \boldsymbol{d}, [|\boldsymbol{\varepsilon}|]$ and $[|\boldsymbol{u}|]$ we obtain:

$$\begin{aligned}
&\boldsymbol{A}_{e=1}^{n_{elm}}[\int_{\Omega_{1,e}} \boldsymbol{B}^{\boldsymbol{T}}\boldsymbol{E}_{\boldsymbol{1}}\,\boldsymbol{B}\boldsymbol{\Delta}\boldsymbol{d}_{n+1}^{(k+1)}d\boldsymbol{\Omega}_{\boldsymbol{1}} + \int_{\Omega_{2,e}} \boldsymbol{B}^{\boldsymbol{T}}\boldsymbol{E}_{\boldsymbol{2}}\,\boldsymbol{B}\boldsymbol{\Delta}\boldsymbol{d}_{n+1}^{(k+1)}d\boldsymbol{\Omega}_{\boldsymbol{2}} \\
&\quad + \int_{\Omega_{1,e}} \boldsymbol{B}^{\boldsymbol{T}}\boldsymbol{E}_{\boldsymbol{1}}\,\boldsymbol{G_1}^{\boldsymbol{1}}\boldsymbol{\Delta}[|\boldsymbol{\varepsilon}|]_{n+1}^{(k+1)}d\boldsymbol{\Omega}_{\boldsymbol{1}} + \int_{\Omega_{2,e}} \boldsymbol{B}^{\boldsymbol{T}}\boldsymbol{E}_{\boldsymbol{2}}\,\boldsymbol{G_1}^{\boldsymbol{2}}\boldsymbol{\Delta}[|\boldsymbol{\varepsilon}|]_{n+1}^{(k+1)}d\boldsymbol{\Omega}_{\boldsymbol{2}} \\
&\quad + \int_{\Omega_{1,e}} \boldsymbol{B}^{\boldsymbol{T}}\boldsymbol{E}_{\boldsymbol{1}}\,\bar{\boldsymbol{G}}_{\boldsymbol{2}}\boldsymbol{\Delta}[|\boldsymbol{u}|]_{n+1}^{(k+1)}d\boldsymbol{\Omega}_{\boldsymbol{1}} + \int_{\Omega_{2,e}} \boldsymbol{B}^{\boldsymbol{T}}\boldsymbol{E}_{\boldsymbol{2}}\,\bar{\boldsymbol{G}}_{\boldsymbol{2}}\boldsymbol{\Delta}[|\boldsymbol{u}|]_{n+1}^{(k+1)}d\boldsymbol{\Omega}_{\boldsymbol{2}}] \\
&\quad = -\boldsymbol{A}_{e=1}^{n_{elm}}[\boldsymbol{f}_{\boldsymbol{int}}^{\boldsymbol{e}} - \boldsymbol{f}_{\boldsymbol{ext}}^{\boldsymbol{e}}]\Big|_{n+1}^{(k)}
\end{aligned} \tag{A.108}$$

By substituting the functions $\boldsymbol{G_1}^{\boldsymbol{1}}, \boldsymbol{G_1}^{\boldsymbol{2}}$ and $\bar{\boldsymbol{G}}_{\boldsymbol{2}}$ with integrating in the two domains $\boldsymbol{\Omega_1}$ and $\boldsymbol{\Omega_2}$, $[\boldsymbol{0}, \boldsymbol{\theta\ell}]$ and $[\boldsymbol{\theta\ell}, \boldsymbol{\ell}]$, respectively, as:

$$\begin{aligned}
&\boldsymbol{A}_{e=1}^{n_{elm}}[\boldsymbol{B}^{\boldsymbol{T}}\boldsymbol{E}_{\boldsymbol{1}}\,\boldsymbol{B}\;\boldsymbol{A}\;\boldsymbol{\theta\ell}\boldsymbol{\Delta}\boldsymbol{d}_{n+1}^{(k+1)} + \boldsymbol{B}^{\boldsymbol{T}}\boldsymbol{E}_{\boldsymbol{2}}\,\boldsymbol{B}\;\boldsymbol{A}(\boldsymbol{1}-\boldsymbol{\theta})\boldsymbol{\ell}\boldsymbol{\Delta}\boldsymbol{d}_{n+1}^{(k+1)} \\
&\quad - \boldsymbol{B}^{\boldsymbol{T}}\boldsymbol{E}_{\boldsymbol{1}}\;\boldsymbol{A}\boldsymbol{\Delta}[|\boldsymbol{\varepsilon}|]_{n+1}^{(k+1)} + \boldsymbol{B}^{\boldsymbol{T}}\boldsymbol{E}_{\boldsymbol{2}}\;\boldsymbol{A}\boldsymbol{\Delta}[|\boldsymbol{\varepsilon}|]_{n+1}^{(k+1)} \\
&\quad - \boldsymbol{B}^{\boldsymbol{T}}\boldsymbol{E}_{\boldsymbol{1}}\;\boldsymbol{A}\;\boldsymbol{\theta}\boldsymbol{\Delta}[|\boldsymbol{u}|]_{n+1}^{(k+1)} - \boldsymbol{B}^{\boldsymbol{T}}\boldsymbol{E}_{\boldsymbol{2}}\;\boldsymbol{A}(\boldsymbol{1}-\boldsymbol{\theta})\boldsymbol{\Delta}[|\boldsymbol{u}|]_{n+1}^{(k+1)}] \\
&\quad = -\boldsymbol{A}_{e=1}^{n_{elm}}[\boldsymbol{f}_{\boldsymbol{int}}^{\boldsymbol{e}} - \boldsymbol{f}_{\boldsymbol{ext}}^{\boldsymbol{e}}]\Big|_{n+1}^{(k)}
\end{aligned} \tag{A.109}$$

After, linearization of equation (A.105), can be given:

$$
\begin{aligned}
&- \boldsymbol{E_1}\frac{\partial(\boldsymbol{B}\,\boldsymbol{d}+\boldsymbol{G_1}^{1}[|\varepsilon|]+\bar{\boldsymbol{G}}_{\boldsymbol{2}}[|\boldsymbol{u}|]}{\partial \boldsymbol{d}}\Big|_{n+1}^{(k)}\boldsymbol{A}\,\boldsymbol{\Delta d}_{n+1}^{(k+1)}\\
&+ \boldsymbol{E_2}\frac{\partial(\boldsymbol{B}\,\boldsymbol{d}+\boldsymbol{G_1}^{2}[|\varepsilon|]+\bar{\boldsymbol{G}}_{\boldsymbol{2}}[|\boldsymbol{u}|])}{\partial \boldsymbol{d}}\Big|_{n+1}^{(k)}\boldsymbol{A}\,\boldsymbol{\Delta d}_{n+1}^{(k+1)}\\
&- \boldsymbol{E_1}\frac{\partial(\boldsymbol{B}\,\boldsymbol{d}+\boldsymbol{G_1}^{1}[|\varepsilon|]+\bar{\boldsymbol{G}}_{\boldsymbol{2}}[|\boldsymbol{u}|])}{\partial [|\varepsilon|]}\Big|_{n+1}^{(k)}\boldsymbol{A}\,\boldsymbol{\Delta}[|\varepsilon|]_{n+1}^{(k+1)}\\
&+ \boldsymbol{E_2}\frac{\partial(\boldsymbol{B}\,\boldsymbol{d}+\boldsymbol{G_1}^{2}[|\varepsilon|]+\bar{\boldsymbol{G}}_{\boldsymbol{2}}[|\boldsymbol{u}|])}{\partial [|\varepsilon|]}\Big|_{n+1}^{(k)}\boldsymbol{A}\,\boldsymbol{\Delta}[|\varepsilon|]_{n+1}^{(k+1)}\\
&- \boldsymbol{E_1}\frac{\partial(\boldsymbol{B}\,\boldsymbol{d}+\boldsymbol{G_1}^{1}[|\varepsilon|]+\bar{\boldsymbol{G}}_{\boldsymbol{2}}[|\boldsymbol{u}|])}{\partial [|\boldsymbol{u}|]}\Big|_{n+1}^{(k)}\boldsymbol{A}\,\boldsymbol{\Delta}[|\boldsymbol{u}|]_{n+1}^{(k+1)}\\
&+ \boldsymbol{E_2}\frac{\partial(\boldsymbol{B}\,\boldsymbol{d}+\boldsymbol{G_1}^{2}[|\varepsilon|]+\bar{\boldsymbol{G}}_{\boldsymbol{2}}[|\boldsymbol{u}|])}{\partial [|\boldsymbol{u}|]}\Big|_{n+1}^{(k)}\boldsymbol{A}\,\boldsymbol{\Delta}[|\boldsymbol{u}|]_{n+1}^{(k+1)} = -\boldsymbol{A}\,\boldsymbol{h}_{[|\varepsilon|]}\Big|_{n+1}^{(k)}
\end{aligned}
\tag{A.110}
$$

By deriving the equation (A.110) according to the relation to $\boldsymbol{d}, \boldsymbol{d}, [|\varepsilon|]$ and $[|\boldsymbol{u}|]$ with dividing on $\boldsymbol{A}$ we obtain:

$$
\begin{aligned}
&- \boldsymbol{E_1}\boldsymbol{B}\,\boldsymbol{\Delta d}_{n+1}^{(k+1)} + \boldsymbol{E_2}\boldsymbol{B}\,\boldsymbol{\Delta d}_{n+1}^{(k+1)} - \boldsymbol{E_1}\boldsymbol{G_1}^{1}\,\boldsymbol{\Delta}[|\varepsilon|]_{n+1}^{(k+1)}\\
&+ \boldsymbol{E_2}\boldsymbol{G_1}^{2}\,\boldsymbol{\Delta}[|\varepsilon|]_{n+1}^{(k+1)} - \boldsymbol{E_1}\bar{\boldsymbol{G}}_{\boldsymbol{2}}\,\boldsymbol{\Delta}[|\boldsymbol{u}|]_{n+1}^{(k+1)}\\
&+ \boldsymbol{E_2}\bar{\boldsymbol{G}}_{\boldsymbol{2}}\,\boldsymbol{\Delta}[|\boldsymbol{u}|]_{n+1}^{(k+1)} = -\,\boldsymbol{h}_{[|\varepsilon|]}\Big|_{n+1}^{(k)}
\end{aligned}
\tag{A.111}
$$

Linearization of equation (A.106) is:

$$
\frac{\partial \boldsymbol{\Phi}}{\partial \boldsymbol{t}_{\boldsymbol{\Gamma}}}\Big|_{n+1}^{(k)}\boldsymbol{\Delta t}_{\boldsymbol{\Gamma}\,n+1}^{(k+1)} + \frac{\partial \boldsymbol{\Phi}}{\partial \boldsymbol{q}}\Big|_{n+1}^{(k)}\boldsymbol{\Delta q}_{n+1}^{(k+1)} = -\boldsymbol{\Phi}\Big|_{n+1}^{(k)}
\tag{A.112}
$$

Finally, the equation (A.103) can be linearized with $\boldsymbol{\Delta q} = \acute{\boldsymbol{k}}([|\boldsymbol{u}|])\boldsymbol{\Delta}[|\boldsymbol{u}|]$ as follows:

$$(\theta \boldsymbol{E_1} \boldsymbol{B} + (1-\theta)\boldsymbol{E_2}\boldsymbol{B})\ \boldsymbol{\Delta d}_{n+1}^{(k+1)} + (\theta \boldsymbol{E_1}\boldsymbol{G_1}^{1} + (1-\theta)\boldsymbol{E_2}\boldsymbol{G_1}^{2}\ \boldsymbol{\Delta}[|\boldsymbol{\varepsilon}|]_{n+1}^{(k+1)}$$
$$+ (\theta \boldsymbol{E_1}\bar{\boldsymbol{G}}_{\boldsymbol{2}} + (1-\theta)\boldsymbol{E_2}\bar{\boldsymbol{G}}_{\boldsymbol{2}} - \acute{\boldsymbol{k}}([|\boldsymbol{u}|]))\ \boldsymbol{\Delta}[|\boldsymbol{u}|]_{n+1}^{(k+1)} = -\boldsymbol{\Phi}\Big|_{n+1}^{(k)} \tag{A.113}$$

Finally the equations (A.109),(A.110) and (A.113) can be written in the following matrix format:

$$\begin{pmatrix} \boldsymbol{K} & \boldsymbol{F} & \boldsymbol{H} \\ \boldsymbol{F^T} & \boldsymbol{b} & \boldsymbol{c} \\ -\boldsymbol{H^T} & -\boldsymbol{c} & \boldsymbol{e} \end{pmatrix}_{n+1}^{(k)} \begin{pmatrix} \boldsymbol{\Delta d} \\ \boldsymbol{\Delta}[|\boldsymbol{\varepsilon}|] \\ \boldsymbol{\Delta}[|\boldsymbol{u}|] \end{pmatrix}_{n+1}^{(k+1)} = \begin{pmatrix} -\boldsymbol{A}_{e=1}^{n_{elm}}[\boldsymbol{f}_{int}^{e} & -\boldsymbol{f}_{ext}^{e}] \\ -\boldsymbol{h}_{[|\boldsymbol{\varepsilon}|]} \\ -\boldsymbol{\Phi} \end{pmatrix}_{n+1}^{(k)} \tag{A.114}$$

where

$$\boldsymbol{K} = \boldsymbol{A}_{e=1}^{n_{elm}}[\boldsymbol{B^T}\boldsymbol{E_1}\boldsymbol{B}\ \boldsymbol{A}\theta\ell + \boldsymbol{B^T}\boldsymbol{E_2}\boldsymbol{B}\ \boldsymbol{A}(1-\theta)\ell]$$
$$\boldsymbol{F} = \boldsymbol{B^T}[-\boldsymbol{E_1} + \boldsymbol{E_2}]\boldsymbol{A}$$
$$\boldsymbol{H} = -\boldsymbol{B^T}(\theta \boldsymbol{E_1} + (1-\theta)\boldsymbol{E_2})\boldsymbol{A}$$
$$\boldsymbol{b} = -\boldsymbol{E_1}\boldsymbol{G_1}^{1} + \boldsymbol{E_2}\boldsymbol{G_1}^{2} = \frac{\boldsymbol{E_1}}{\theta\ell} + \frac{\boldsymbol{E_2}}{(1-\theta)\ell}$$
$$\boldsymbol{c} = -\boldsymbol{E_1}\boldsymbol{G_2} + \boldsymbol{E_2}\boldsymbol{G_2} = \frac{\boldsymbol{E_1}}{\ell} + \frac{\boldsymbol{E_2}}{(\ell}$$
$$\boldsymbol{e} = (\theta \boldsymbol{E_1}\bar{\boldsymbol{G}}_{\boldsymbol{2}} + (1-\theta)\boldsymbol{E_2}\bar{\boldsymbol{G}}_{\boldsymbol{2}} - \acute{\boldsymbol{k}}([|\boldsymbol{u}|])) = -\frac{\theta \boldsymbol{E_1}}{\ell} - \frac{(1-\theta)\boldsymbol{E_2}}{(\ell} - \acute{\boldsymbol{k}}([|\boldsymbol{u}|])) \tag{A.115}$$

A.5 Meso-scale mechanical model

In this section, a brief description of the mechanical model has been given. For readers who are interested in more details, a complete description of the model,

its numerical implementation and a number of illustrative examples of the model predictive capabilities can be found by Benkemoun et al. [Benkemoun et al., 2010]. In this study work, there is a focus on using the meso-scale model due to several reasons as shown below:

1. **Representing 3D heterogeneous materials such as concrete (aggregate melts into mortar).**

2. **Discretization of crack opening in quasi-brittle material such as concrete and the crack dimensions with its position and its pathway can be investigated.**

The numerical model for the mechanical simulations is based upon a two-phase (stiff aggregates embedded into a mortar matrix) quasi-brittle model that is capable of representing the behavior of concrete-like materials under complex loading paths. In order to take into account the influence of the shape, the size, the distribution and the mechanical properties of the aggregates on the mechanical behavior of concrete, the mesoscale by (Wriggers and Moftah [Wriggers and Moftah, 2006], Borja and Andrade [Borja and Andrade, 2006]) is chosen to be the scale of computation. The numerical approach that I am working with, at the mesoscale, is based upon a 3D lattice finite element model by (Schlangen and van Mier [Schlangen and van Mier, 1992], Schlangen and Garboczi [Schlangen and Garboczi, 1997], Yip et al. [Yip et al., 2005] and Lachihab and Sab [Lachihab and Sab, 2005]) whose truss elements kinematics is enhanced by two discontinuities embedded in the elements.

The first discontinuity is a weak discontinuity – continuous displacement field and discontinuous strain field by Ortiz et al. [Ortiz et al., 1987] – introduced because of the non-adaptated meshing process by Moës et al. [Moës et al., 2003]. This process consists of a unique homogeneous mesh whose nodes are placed independently from the morphology of the aggregates. A significant amount of com-

putation time is saved at this stage. However, some truss elements are cut into two parts, each having different elastic properties (see Figure A.1 for a two-phase material). That's why in order to take into account this special kinematics in the truss elements, this weak discontinuity is introduced. Equation (A.116) refers to first enhancement of the bar elements at the interfacial zone between two materials (two modulus of elasticity), also the computations are done by this equation in the deformation field (finite strain jump), where $\boldsymbol{\ell}$ is the length of the bar element, and $\boldsymbol{\theta}$ is the scalar dimensionless.

$$\boldsymbol{G_1}^{1/2} = \begin{cases} \boldsymbol{G_1}^{1} = -\frac{1}{\theta\ell} \ , \ \ \boldsymbol{x} \in [0, \theta\ell] \\ \boldsymbol{G_1}^{2} = \frac{1}{(1-\theta)\ell} \ , \ \ \boldsymbol{x} \in [\theta\ell, \ell] \end{cases} \tag{A.116}$$

The second discontinuity is a strong discontinuity – discontinuous displacement field and unbounded strain field by Simo et al. [Simo et al., 1993] – introduced in order to represent micro-cracks that may occur in any of different phases (aggregates or mortar matrix for two-phase materials) and to capture the interface failure (debonding). Moreover, the key point pertains to strong discontinuities capability to model softening behavior without any mesh dependency which is the major issue dealing with the failure of quasi-brittle materials. . The strong discontinuity is introduced by means of a yield function $\boldsymbol{\Phi}$ which is triggered only in traction. Thus two constitutive models appear for a truss element: a continuum one (outside the discontinuity) which is elastic (see Figure A.4(a)), and a discrete one (over the discontinuity) which is quasi-brittle, see Figure (A.4(b)). We denote by $\boldsymbol{t_\Gamma}$ the traction vector over the discontinuity and $[|\boldsymbol{u}|]$ the crack width which belongs to the set of unknowns. The yield function as shown:

$$\boldsymbol{\Phi} = \boldsymbol{t_\Gamma} - (\boldsymbol{\sigma_u} - \boldsymbol{q}) \tag{A.117}$$

where $\boldsymbol{q}$ is the stress as shown:

$$\boldsymbol{q} = \boldsymbol{\sigma_u}\left(\mathbf{1} - \boldsymbol{exp}(-\frac{\boldsymbol{\sigma_u}}{\boldsymbol{G_u}}[|\boldsymbol{u}|])\right) \tag{A.118}$$

In summary, there are altogether eight model parameters: the Young modulus $\boldsymbol{E_1}$ for the mortar matrix and $\boldsymbol{E_2}$ for aggregates, for the continuum model and the ultimate tensile strength before softening, $\boldsymbol{\sigma_{u_i}}$ and the fracture energy, $\boldsymbol{G_{u_i}}$ ($\boldsymbol{i} = 1$, 2, 3 for respectively the mortar matrix, aggregates and interfaces) for the discrete model. We note $\boldsymbol{G_{u_i}}$ the area under the curve $\boldsymbol{t_\Gamma} - [|\boldsymbol{u}|]$ into Figure (A.4(b)).

Appendix B

HYDRO-MECHANICAL MODEL

B.1 Modeling of fluid transfer in cracked concrete

Remark: this section presents the method used in the study of Xavier Jourdain et al. [Jourdain et al., 2013].

This section focuses on the finite element formulation of the permeability of fluids (compressible fluids) such as gases. To model this problem in a heterogeneous material, specimens from the meso-scale model (mechanical model) were used. Darcy's law for porous media was used when applying a pressure gradient of gas on cylinder specimens without cracks (uncracked section) to compute the gas permeability. Then, Poiseuille's law was used when applying a pressure gradient to compute the gas permeability with a crack (cracked section).

From the above mentioned, it can be noted that gas permeability in a heterogeneous material is classified through two phenomena:

1. Modeling fluid transfer in pores for uncracked section using Darcy's law.

2. Modeling fluid transfer in cracked section using Poiseuille's law.

According to Poiseuille's law, the mass flow in the crack opening for an incompressible fluid (water) and a compressible fluid (gas) can be represented in equations (B.1) and (B.2), respectively:

$$\boldsymbol{q_x = -\rho \frac{b[|u|]^3}{12\mu} grad(p) \Longrightarrow v_x = -\frac{[|u|]^3}{12\mu L} grad(p)} \tag{B.1}$$

$$\boldsymbol{q_x = -\rho \frac{M\ b[|u|]^3}{24RT\ \mu} grad(p^2) \Longrightarrow v_x = -\frac{M[|u|]^3}{24RT\ \mu L} grad(p^2)} \tag{B.2}$$

where $\boldsymbol{q_x}$ is the mass flow in the direction $\boldsymbol{x}$ in (kg/s), $\boldsymbol{v}$ is the velocity of flow in the direction $\boldsymbol{x}$ in (m/s), $\boldsymbol{\rho}$ is the bulk density of the fluid in (kg/m^3), $\boldsymbol{\mu}$ is the dynamic viscosity of the fluid in (Pa.s), $\boldsymbol{p}$ is the pressure of the fluid in (Pa), $\boldsymbol{M}$ is the molar mass of the gas in (g/mol), $\boldsymbol{R}$ is the universal gas constant in (J/mol.K), which is equal to 8.314472 J/mol.K, $\boldsymbol{L, b}$ and $[|u|]$ are the geometrical properties of the problem as pointed out in this chapter, as shown in Figure (B.1):

B.1.1 Finite element formulation of the problem

Herein, we present the finite element formulation for the **compressible fluid** (gas) with a weak form problem, after we have obtained the crack opening in a meso-scale model. This problem will be formulated, therefore will be resulted the permeability at the macro-scale, which depends on the meso-scale with a different: crack opening and pathway of broken bar elements.

According to the Navier-Stock and the equation of the conservation of the mass for the domain $\boldsymbol{\Omega}$ can be written:

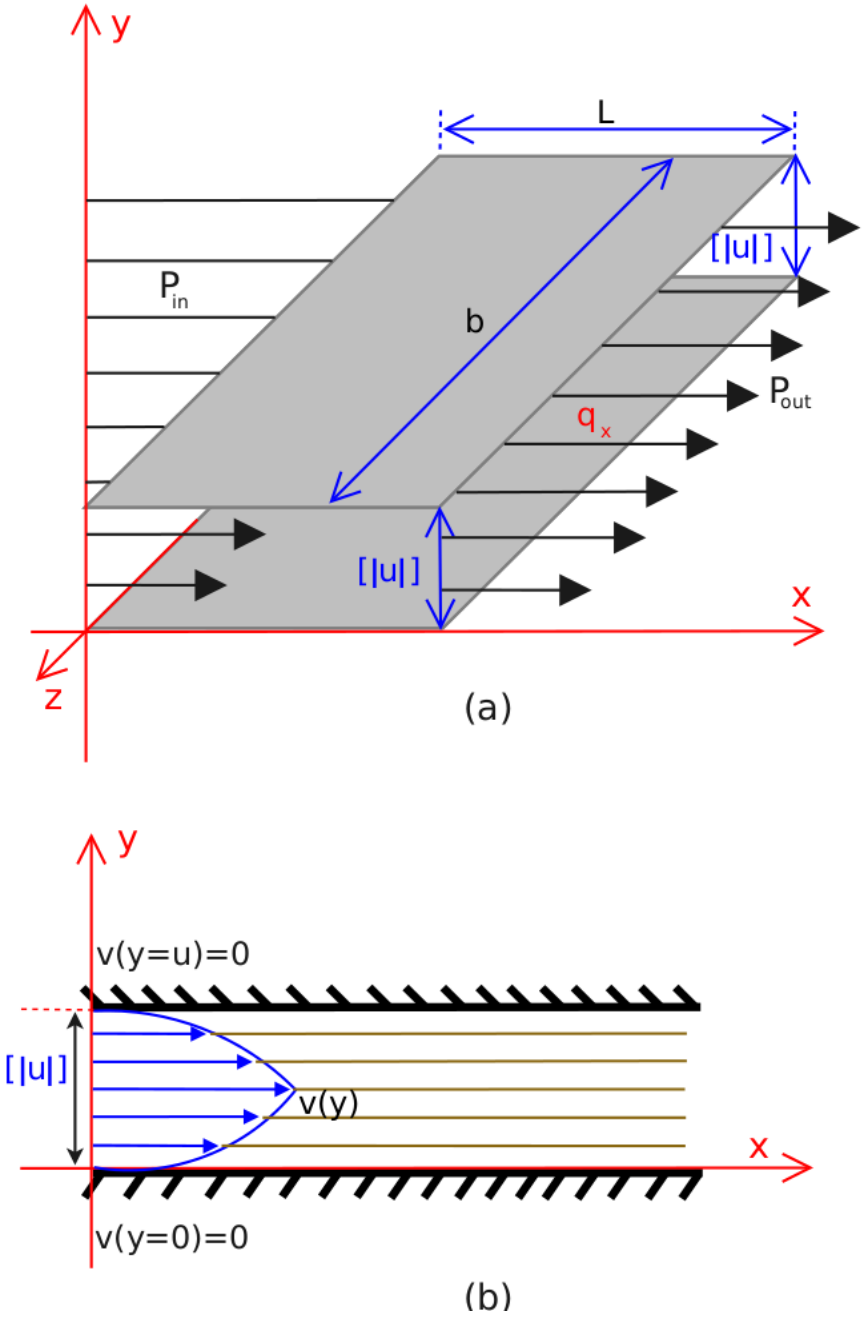

Figure B.1: Geometrical shape of the crack opening with flow of fluid in three dimensions (a) and cross-section in two dimensions (b).

$$\boldsymbol{div(\rho v) = div(v) = 0} \tag{B.3}$$

By using Darcy's law, the intrinsic permeability ($\boldsymbol{k}$) for an uncracked section of concrete can be obtained as below:

$$\boldsymbol{v = -\frac{\rho k}{\mu} grad(p)} \tag{B.4}$$

When we considered the compressible fluid is a gas, its density according to the ideal gas law can be written as:

$$\boldsymbol{\rho = p\frac{M}{RT}} \tag{B.5}$$

where:

- $\boldsymbol{M_{air} = 28.95}$ g/mol;
- $\boldsymbol{\mu_{air} = 1.82 * 10^5}$ Pa.s;
- $\boldsymbol{\rho_{air} = 1.2}$ kg/m$^{\mathbf{3}}$;
- $\boldsymbol{R = 8.314472}$ J/mol.K;
- $\boldsymbol{T = 293.15}$ Kelvin.

Finally, by injecting equation (B.5) into equation (B.4), we obtain:

$$\boldsymbol{v = -\frac{k}{2\mu}\frac{M}{RT} grad(p^2)} \tag{B.6}$$

The last formulation is considered a strong form for the mass flow of a compressible fluid, therefore this problem can be written as:

Find $\boldsymbol{p^2 \in S}$ so that $\forall \boldsymbol{p^{*2} \in S_0}$,

$$\boldsymbol{\int_\Omega p^{*2} div(v(p^2)) d\Omega = 0} \tag{B.7}$$

where

$\boldsymbol{S = \{p^2 \mid p^2 \in H^1(\Omega),\ p^2 = p_0^2}$ on $\boldsymbol{S_p\}}$

$\boldsymbol{S_0 = \{p^{*2} \mid \in\ H^1(\Omega),\ p^{*2}\ =\ 0}$ on $\boldsymbol{S_p\}}$

$\boldsymbol{p^2}$ is the pressure-squared value of gas on the field space $\boldsymbol{S_p}$, $\boldsymbol{H^1(\Omega) = \{p^2\ \in L^2(\Omega); \forall = 1\ .\ .\ .\ n,\ \frac{\partial p^2}{\partial x_i} \in L^2(\Omega)\}}$ is a Hilbert space.

By applying the Green-Ostrogradski theorem and using an integration by parts we obtain:

$$\forall \boldsymbol{p^{*2}}\ \in \boldsymbol{S_0},\ \int_{\partial\Omega_v} \boldsymbol{p^{*2}\ v_0\ .\ n\ dS} - \int_{\Omega} \boldsymbol{grad(p^{*2}).\ v\ d\Omega} = 0 \tag{B.8}$$

Equation (B.8) can be solved according to the finite element method, which considers the pressure-squared value $\boldsymbol{p^{2,h}}$ is a vector as a function of $\boldsymbol{N}$ at each node, $\boldsymbol{n}$ is the number of nodes, and can be written:

$$\boldsymbol{p^{2,h} = \sum_{a} N_a\ p_a^2 = N^T.\ p^2} \tag{B.9}$$

Herein the element refers to the tetrahedral element that consists of four nodes (vertices), therefore the pressure-squared value in the tetrahedral element can be written as:

$$\boldsymbol{p^{2,h}}\Big|_{\boldsymbol{\Omega_e}} = \sum_{a=1}^{4} \boldsymbol{N_a^e\ p_a^{2,e} = N^{e,T}.\ p^{2,e}} \tag{B.10}$$

By using the derivatives of the shape functions, the pressure gradient can be computed as a function:

$$\boldsymbol{grad(p^{2,h})}\Big|_{\boldsymbol{\Omega_e}} = \boldsymbol{B^{e,T}.\ p^{2,e}} \tag{B.11}$$

where $\boldsymbol{B}$ is the elementary matrices whose components come from the derivatives of shape functions.

The discretization of finite element for the velocity of flow ($\boldsymbol{v}$) as a weak form depending on equations (B.10) and (B.11), can be written for each element $\boldsymbol{v^h}\big|_{\boldsymbol{\Omega_e}}$:

$$\boldsymbol{A}_{e=1}^{n_{elm}} \int_{\partial\Omega_{v,e}} \boldsymbol{N}^{e,T} . \boldsymbol{p}^{*2,e} . \boldsymbol{v}_0^e \, d\boldsymbol{S} - \boldsymbol{A}_{e=1}^{n_{elm}} \int_{\Omega_e} \boldsymbol{B}^{e,T} . \boldsymbol{p}^{*2,e} . \boldsymbol{v}^h \, \big|_{\Omega_e} \, d\boldsymbol{\Omega} = \boldsymbol{0} \quad \text{(B.12)}$$

Now by simplifying the above equation and varying the pressure from $\boldsymbol{p}^{*2,e}$ to $\boldsymbol{p}^{2e*}$, we can obtain:

$$\boldsymbol{A}_{e=1}^{n_{elm}} \int_{\partial\Omega_{v,e}} \boldsymbol{N}^{e,T} \, . \, \boldsymbol{v}_0^e \, d\boldsymbol{S} - \boldsymbol{A}_{e=1}^{n_{elm}} \int_{\Omega_e} \boldsymbol{A}_{e=1}^{n_{elm}} = \boldsymbol{0} \quad \text{(B.13)}$$

However, we can define the vector of internal forces as:

$$\boldsymbol{f}_{int}^e = - \int_{\Omega_e} \boldsymbol{B}^{e,T} \, . \, \boldsymbol{v}^h \, \big|_{\Omega_e} \, d\boldsymbol{\Omega} \quad \text{(B.14)}$$

and the external forces as:

$$\boldsymbol{f}_{ext}^e = \int_{\partial\Omega_{v,e}} \boldsymbol{N}^{e,T} \, . \, \boldsymbol{v}_0^e \, d\boldsymbol{S} \quad \text{(B.15)}$$

Finally, the problem as the finite elements is as shown:

$$\boldsymbol{f}_{int} = \boldsymbol{A}_{e=1}^{n_{elm}} [\boldsymbol{f}_{int}^e], \;\; \boldsymbol{f}_{ext} = \boldsymbol{A}_{e=1}^{n_{elm}} [\boldsymbol{f}_{ext}^e] \quad \text{(B.16)}$$

B.1.2 Linearization of the problem

To solve the problem in equation (B.16), which refers to a weak form at the minimum residual ($\boldsymbol{r_n}$) in each time step $\boldsymbol{n}$, can be written:

$$\boldsymbol{r_n} = \boldsymbol{f}_{ext,n} - \boldsymbol{f}_{int,n}(\boldsymbol{p_n^2}) \quad \text{(B.17)}$$

To obtain the convergence of the problem, we provide the iteration $\boldsymbol{(k)}$ at each time step, therefore the linearization in equation (A.63) gives:

$$\boldsymbol{\Psi}\big(\boldsymbol{r}_{n+1}^{(k+1)}\big) = \boldsymbol{r}_{n+1}^{(k)} + \frac{\boldsymbol{\partial r}}{\boldsymbol{\partial p^2}} \Big|_{n+1}^{(k)} . \, \boldsymbol{\Delta p^2}_{n+1}^{(k+1)} = \boldsymbol{0} \quad \text{(B.18)}$$

where $\boldsymbol{\Delta p^2}_{n+1}^{(k+1)}$ is the increment for the pressure-squared value.

The formulation of the residual (B.18) for each iteration $\boldsymbol{(k)}$ can be written:

$$\frac{\partial \boldsymbol{r}}{\partial \boldsymbol{p^2}}\Big|_{n+1}^{(k)} . \boldsymbol{\Delta p^2}_{n+1}^{(k+1)} = -\boldsymbol{r}_{n+1}^{(k)} \tag{B.19}$$

To explain the term $\frac{\partial \boldsymbol{r}}{\partial \boldsymbol{p^2}} \big|_{n+1}^{(k)}$ by deriving equation (B.17) from the relation of the pressure-squared value, we obtain:

$$\frac{\partial \boldsymbol{r}}{\partial \boldsymbol{p^2}}\Big|_{n+1}^{(k)} = \frac{\partial \boldsymbol{f_{int}}}{\partial \boldsymbol{p^2}}\Big|_{n+1}^{(k)} = \boldsymbol{K}_{n+1}^{(k)} = -\boldsymbol{A}_{e=1}^{n_{elm}} \int_{\Omega_e} \boldsymbol{B}^{e,T} . \frac{\partial \boldsymbol{v}^h \big|_{\Omega_e}}{\partial \boldsymbol{p}^{2,e}} \, d\boldsymbol{\Omega} \tag{B.20}$$

By applying Darcy's law (B.4), the relationship between the mass velocity ($\boldsymbol{v}$) in (kg/s.m^2) and the pressure ($\boldsymbol{p^2}$) in (Pa^2) can be obtained as:

$$\boldsymbol{v} = -\frac{1}{\boldsymbol{\mu}} \boldsymbol{\rho}\, \boldsymbol{k}\ \ \boldsymbol{grad}(\boldsymbol{p}) = -\frac{1}{\boldsymbol{\mu}} \boldsymbol{\rho}\, \boldsymbol{k}\ \ \boldsymbol{grad}(\sqrt{\boldsymbol{p^2}}) \tag{B.21}$$

By substituting equation (B.5) in equation (B.21) and simplifying we obtain:

$$\boldsymbol{v} = -\frac{1}{\boldsymbol{\mu}} \frac{\boldsymbol{M}}{\boldsymbol{RT}}\, \boldsymbol{k}\ \ \frac{\mathbf{1}}{\mathbf{2}}\, \boldsymbol{grad}(\boldsymbol{p^2}) \tag{B.22}$$

The problem for each finite element can be represented as:

$$\boldsymbol{v}^h\Big|_{\Omega_e} = -\frac{1}{\boldsymbol{\mu}} \frac{\boldsymbol{M}}{\boldsymbol{RT}}\, \boldsymbol{k}^e\ \ \frac{\mathbf{1}}{\mathbf{2}}\, \boldsymbol{grad}(\boldsymbol{p}^{2,h}) \big|_{\Omega_e} \tag{B.23}$$

From the pressure gradient in equation (B.11) and the equation (B.23) can be written:

$$\frac{\partial \boldsymbol{v}^h \big|_{\Omega_e}}{\partial \boldsymbol{p}^{2,h} \big|_{\Omega_e}} = \frac{\partial \boldsymbol{v}^h \big|_{\Omega_e}}{\partial \boldsymbol{grad}(\boldsymbol{p}^{2,h}) \big|_{\Omega_e}} \frac{\partial \boldsymbol{grad}(\boldsymbol{p}^{2,h}) \big|_{\Omega_e}}{\partial \boldsymbol{p}^{2,e}} = -\frac{\mathbf{1}}{\mathbf{2}\boldsymbol{\mu}} \frac{\boldsymbol{M}}{\boldsymbol{RT}}\, \boldsymbol{k}^e\, \boldsymbol{B}^e \tag{B.24}$$

By using equation (B.20) and equation (B.24), we obtain:

$$\left.\frac{\partial \boldsymbol{r}}{\partial \boldsymbol{p^2}}\right|_{n+1}^{(k)} = \boldsymbol{K}_{n+1}^{(k)} = \frac{\mathbf{1}}{\mathbf{2}\boldsymbol{\mu}}\frac{\boldsymbol{M}}{\boldsymbol{RT}} \boldsymbol{A}_{e=1}^{n_{elm}} \int_{\Omega_e} \boldsymbol{B}^{e,T}\, \boldsymbol{k}^e\, \boldsymbol{B}^e\, \boldsymbol{d\Omega} \tag{B.25}$$

where $\boldsymbol{k}^e$ is the elementary permeability matrix that components of 3 x 3.

Each iteration $(\boldsymbol{k})$ will result in a new increment of pressure $\boldsymbol{\Delta p^2}_{n+1}^{(k+1)}$ according to equation (B.19), then this iteration will update the pressure at the iteration $(\boldsymbol{k+1})$ as:

$$\boldsymbol{p^2}_{n+1}^{(k+1)} = \boldsymbol{p^2}_{n+1}^{(k)} + \boldsymbol{\Delta p^2}_{n+1}^{(k+1)} \tag{B.26}$$

Due to the updating of the pressure (new pressure), we can compute the relative energy which is compared with the tolerance ($\boldsymbol{tol}$) defined in the relationship below:

$$\frac{\boldsymbol{r}_{n+1}^{(k)^T} \cdot \boldsymbol{\Delta p^2}_{n+1}^{(k+1)}}{\boldsymbol{r}_{n+1}^{(0)^T} \cdot \boldsymbol{\Delta p^2}_{n+1}^{(1)}} < \boldsymbol{tol} \tag{B.27}$$

According to equation (B.27) which defined the energy, there is a new iteration $(\boldsymbol{k})$. Therefore, a new matrix tangent $\left.\frac{\partial \boldsymbol{r}}{\partial \boldsymbol{p^2}}\right|_{n+1}^{(k+1)}$ and residual $\boldsymbol{r}_{n+1}^{(k+1)}$ will be formed. Then, equation (B.19) is solved for the new iteration $(\boldsymbol{k+1})$ and this procedure is repeated until convergence is obtained.

B.1.3 Elementary permeability matrix

This section presents the procedure for computing the elementary permeability matrix ($\boldsymbol{k}^e$) in a heterogeneous material for each tetrahedral element. Figure (B.2(a)) shows a typical tetrahedral element with four nodes and six broken bar elements (edges). As previously mentioned, there are two kinds of permeability in concrete: the first is the permeability of uncracked material corresponding to the porosity of the material and noted the isotropic permeability ($\boldsymbol{k}_{\boldsymbol{iso}}^{\boldsymbol{e}}$) and the second is the permeability of cracked material, i.e. the movement of fluid through

the crack opening, noted the anisotropic permeability ($\boldsymbol{k^e_{ani}}$). Figure (B.2(b)) shows a broken bar element with the mass flow profile through the crack opening $[|\boldsymbol{u}|]$.

Therefore, we can represent the total elementary permeability as:

$$\boldsymbol{k^e = k^e_{iso} + k^e_{ani}} \tag{B.28}$$

where $\boldsymbol{e}$ is the tetrahedral element, in addition will be used the notations $\boldsymbol{n}$ and $\boldsymbol{m}$ for defining the nodes.

From equation (B.29), the elementary permeability matrix in the porosity of the material can be represented for each tetrahedral element based on the intrinsic permeability of concrete:

$$\boldsymbol{k^e_{iso} = \frac{k_{int}}{2.\mu.r.T}\,1} \tag{B.29}$$

where:

- $\boldsymbol{r = \frac{R}{M}}$;
- $\boldsymbol{M_{air} = 28.95}$ g/mol;
- $\boldsymbol{\mu_{air} = 1.82 * 10^5}$ Pa.s;
- $\boldsymbol{\rho_{air} = 1.2}$ kg/m^3;
- $\boldsymbol{R = 8.314472}$ J/mol.K;
- $\boldsymbol{T = 293.15}$ Kelvin.

To represent the permeability matrix through the crack opening $\boldsymbol{k^e_{ani}}$, the meso-scale mechanical model was taken into account. In other words, the crack openings $[|\boldsymbol{u}|]$ obtained from the mechanical model are used here and noted $[|\boldsymbol{u}|]_{\boldsymbol{nm}}$ as shown in Figure (B.2).

The value of the jump displacement $[|\boldsymbol{u}|]_{\boldsymbol{nm}}$ represents the crack opening of the bar element for nodes $\boldsymbol{n, m}$ in the tetrahedral element. To study the matrix

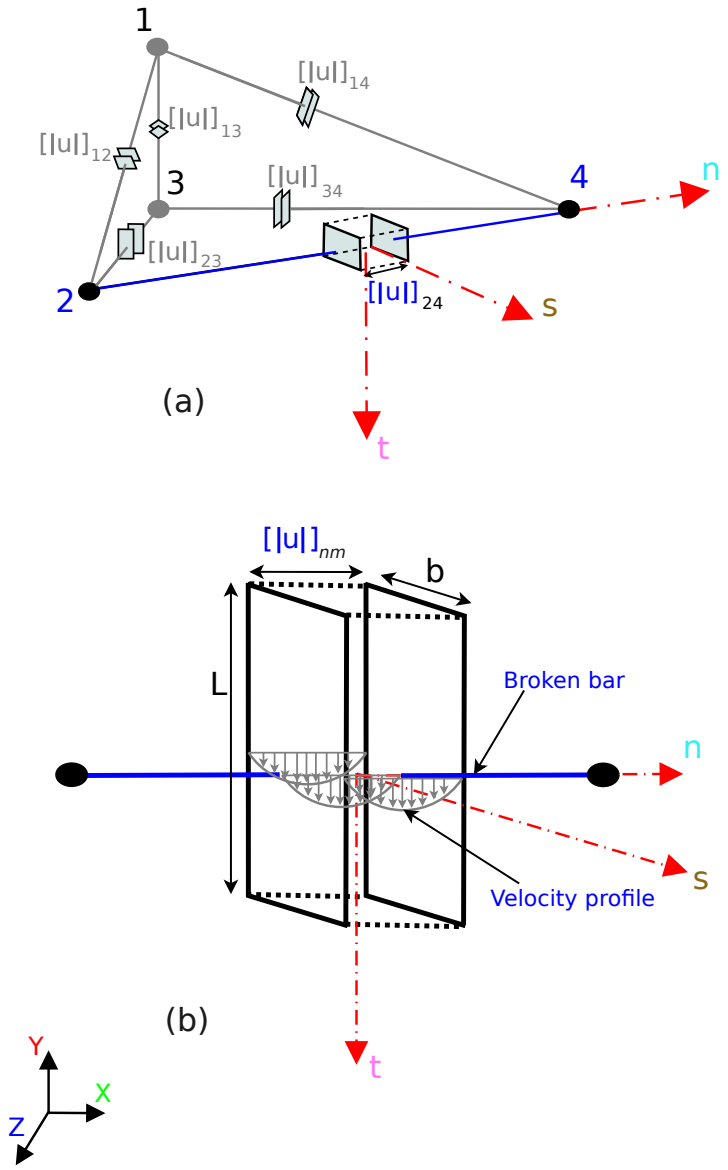

Figure B.2: Typical tetrahedral element with six broken bar elements (a) and a broken bar element with a mass flow profile (b) [Benkemoun, 2010].

$\boldsymbol{k}^{e}_{\boldsymbol{ani}}$ in the tetrahedral element, we carried out the global description $(\boldsymbol{X}, \boldsymbol{Y}, \boldsymbol{Z})$ and the local description $(\boldsymbol{n_{nm}}, \boldsymbol{s_{nm}}, \boldsymbol{t_{nm}})$.

Equation (B.30) is the matrix $\boldsymbol{k}^{e,nm}_{\boldsymbol{loc}}$ in the local description in the tetrahedral element:

$$\boldsymbol{k}^{e,nm}_{\boldsymbol{loc}} = \begin{bmatrix} \boldsymbol{k_n} & \mathbf{0} & \mathbf{0} \\ \mathbf{0} & \boldsymbol{k_s} & \mathbf{0} \\ \mathbf{0} & \mathbf{0} & \boldsymbol{k_t} \end{bmatrix}_{(n_{nm}, s_{nm}, t_{nm})} \tag{B.30}$$

where $\boldsymbol{k_s} = \boldsymbol{k_t} = \boldsymbol{k_{nm}}$ is the permeability of the bar element for nodes $\boldsymbol{n}$ and $\boldsymbol{m}$, i.e. the permeability through the crack opening $[|\boldsymbol{u}|]_{\boldsymbol{nm}}$ in the broken bar element is perpendicular to the crack opening while it is equal to zero in the direction $\boldsymbol{n}$ which is parallel to the crack opening as shown in Figure (B.2), $\boldsymbol{k_n} = \mathbf{0}$.

According to equation (B.2), the permeability through the crack opening $[|\boldsymbol{u}|]_{\boldsymbol{nm}}$ can be computed as:

$$\boldsymbol{k_{nm}} = \frac{[|\boldsymbol{u}|]^{\boldsymbol{3}}{}_{\boldsymbol{nm}}}{\mathbf{24}.\boldsymbol{\mu}.\boldsymbol{r}.\boldsymbol{T}.\boldsymbol{L_{nm}}} \tag{B.31}$$

where the parameter $\boldsymbol{r}$ refers to the relationship $\frac{\boldsymbol{R}}{\boldsymbol{M}}$ and $\boldsymbol{L_{nm}}$ is the length of the broken bar element.

However, by using the passage matrices $(\boldsymbol{P^{nm}_{G-L}}$ and $\boldsymbol{P^{nm}_{L-G}})$ the global matrices for all bar elements can be computed from local matrices in equation (B.30), and written as:

$$\boldsymbol{k}^{e,nm}_{\boldsymbol{glob}} = \boldsymbol{P^{nm}_{G-L}}.\boldsymbol{k}^{e,nm}_{\boldsymbol{loc}}.\boldsymbol{P^{nm}_{L-G}} \tag{B.32}$$

where $\boldsymbol{k}^{e,nm}_{\boldsymbol{glob}}$ is the matrix expressed by the matrix $\boldsymbol{k}^{e,nm}_{\boldsymbol{loc}}$ in the global description $(\boldsymbol{X}, \boldsymbol{Y}, \boldsymbol{Z})$.

Computing the elementary anisotropic permeability for the tetrahedral element ($\boldsymbol{e}$) depends on the summation of the matrices $\boldsymbol{k}_{\boldsymbol{glob}}^{\boldsymbol{e,nm}}$ for six edges of one tetrahedral element ($\boldsymbol{e}$) written as:

$$\boldsymbol{k}_{\boldsymbol{ani}}^{\boldsymbol{e}} = \boldsymbol{k}_{\boldsymbol{glob}}^{\boldsymbol{e,12}} + \boldsymbol{k}_{\boldsymbol{glob}}^{\boldsymbol{e,13}} + \boldsymbol{k}_{\boldsymbol{glob}}^{\boldsymbol{e,14}} + \boldsymbol{k}_{\boldsymbol{glob}}^{\boldsymbol{e,23}} + \boldsymbol{k}_{\boldsymbol{glob}}^{\boldsymbol{e,24}} + \boldsymbol{k}_{\boldsymbol{glob}}^{\boldsymbol{e,34}} \tag{B.33}$$

Finally, according to equations (B.25) and (B.28) the matrix of elementary permeability can be obtained including two scales: the first is the permeability in the porosity of the material and the second is the permeability in the cracked material. These two scales are written in the global description ($\boldsymbol{X}$, $\boldsymbol{Y}$, $\boldsymbol{Z}$) as:

$$\begin{aligned} \boldsymbol{K}^{\boldsymbol{e}} &= \frac{\boldsymbol{1}}{\boldsymbol{2\mu}} \frac{\boldsymbol{M}}{\boldsymbol{RT}} \int_{\boldsymbol{\Omega_e}} \boldsymbol{B}^{\boldsymbol{e,T}}\, \boldsymbol{k}^{\boldsymbol{e}}\, \boldsymbol{B}^{\boldsymbol{e}}\, \boldsymbol{d\Omega} \\ &= \frac{\boldsymbol{1}}{\boldsymbol{2\mu}} \frac{\boldsymbol{M}}{\boldsymbol{RT}} \int_{\boldsymbol{\Omega_e}} \boldsymbol{B}^{\boldsymbol{e,T}}\, (\boldsymbol{k}_{\boldsymbol{iso}}^{\boldsymbol{e}} + \boldsymbol{k}_{\boldsymbol{ani}}^{\boldsymbol{e}})\, \boldsymbol{B}^{\boldsymbol{e}}\, \boldsymbol{d\Omega} \end{aligned} \tag{B.34}$$

B.2 Permeability upscaling method: meso-macro approach

Pouya and Courtois in [Pouya and Courtois, 2002b] investigated the hydraulic behavior at macro-scale in cracked rock by using the homogeneous method; they considered the pressure gradient to be linear. The macroscopic flow can be represented by equation (B.35):

$$\boldsymbol{Q}^{\boldsymbol{M}} = -\boldsymbol{K}^{\boldsymbol{M}}.\boldsymbol{G}^{\boldsymbol{M}} \tag{B.35}$$

where $\boldsymbol{K}^{\boldsymbol{M}}$ is the macroscopic permeability obtained corresponding to the computation from the meso-scale and $\boldsymbol{G}^{\boldsymbol{M}}$ is the macroscopic pressure gradient like to micro-scale written as:

$$\boldsymbol{G^M} = \frac{\mathbf{1}}{\boldsymbol{\Omega}} \int_{\boldsymbol{\Omega}} \boldsymbol{grad(p^2) d\Omega} \tag{B.36}$$

and macroscopic flow can be written as:

$$\boldsymbol{Q^M} = \frac{\mathbf{1}}{\boldsymbol{\Omega}} \int_{\boldsymbol{\Omega}} \boldsymbol{q(x) d\Omega} \tag{B.37}$$

In addition, depending on the boundary condition according to the Dirichlet-type which defines the pressure gradient is linear as:

$$\boldsymbol{p(x) = G^M x + p_0} \quad \boldsymbol{\forall x \ \in \partial\Omega} \tag{B.38}$$

Figure (B.3) shows a homogeneous cube under three types of pressure gradient in three dimensions $(\boldsymbol{X}, \boldsymbol{Y}, \boldsymbol{Z})$. To compute the macroscopic flow $\boldsymbol{Q^M}$, after identifying the nine components of tensor $\boldsymbol{K^M}$ and choosing the vector $\boldsymbol{G^M}$ of the problem for each direction will be solved, i.e. the calculation of the macroscopic flow is unidirectional for three problems [Pouya and Courtois, 2002b] as:

$$\boldsymbol{Q^M} = \frac{\mathbf{1}}{\boldsymbol{\Omega}} \int_{\boldsymbol{\partial\Omega}} \boldsymbol{x \ (q(x) \ . \ n) d\Omega} \tag{B.39}$$

where $\boldsymbol{n}$ is the unit normal vector, which is perpendicular to the contour and whose direction is outside, and $\boldsymbol{q(x)}$ is the local flow for three columns of tensor $\boldsymbol{K^M}$.

In the previous section, the process for obtaining the macroscopic permeability tensor was presented, while in the next section, numerical examples and validation of the hydro-mechanical model will be provided.

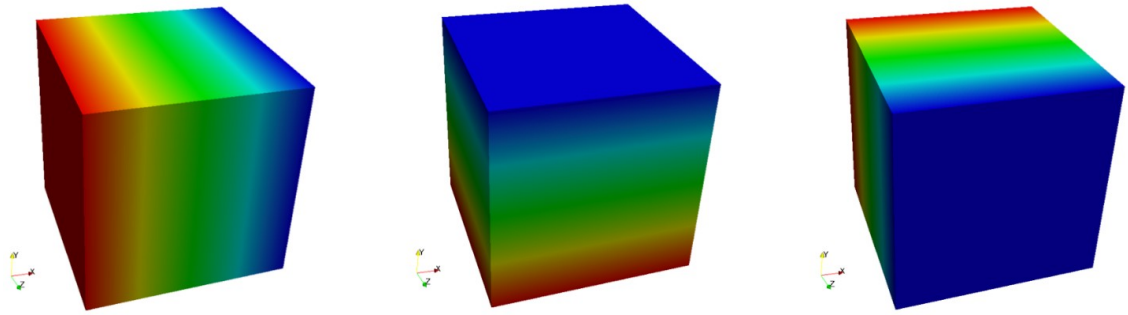

Figure B.3: Identification of the permeability tensor and Dirichlet boundary conditions: pressure gradient is constant in direction ***X*** (a) pressure gradient is constant in direction ***Y*** (b) pressure gradient is constant in direction ***Z*** [Jourdain, 2014].

Bibliography

[Abbas et al., 2000] Abbas, A., Carcasses, M., and Ollivier, J. (2000). The importance of gas permeability in addition to the compressive strength of concrete. *Magazine of concrete research*, 52(1):1–6.

[Abbas et al., 1999] Abbas, A., Carcasses, M., and Ollivier, J.-P. (1999). Gas permeability of concrete in relation to its degree of saturation. *Materials and structures*, 32(1):3–8.

[Akcay et al., 2012] Akcay, B., Agar-Ozbek, A. S., Bayramov, F., Atahan, H. N., Sengul, C., and Tasdemir, M. A. (2012). Interpretation of aggregate volume fraction effects on fracture behavior of concrete. *Construction and Building Materials*, 28(1):437–443.

[Akhavan et al., 2012] Akhavan, A., Rajabipour, F., et al. (2012). Quantifying the effects of crack width, tortuosity, and roughness on water permeability of cracked mortars. *Cement and Concrete Research*, 42(2):313–320.

[Aldea et al., 2000] Aldea, C. M., Ghandehari, M., Shah, S. P., and Karr, A. (2000). Estimation of water flow through cracked concrete under load. *ACI Structural Journal*, 97(5):567–575.

[Aldea et al., 1999] Aldea, C.-M., Shah, S., and Karr, A. (1999). Permeability of cracked concrete. *Materials and structures*, 32(5):370–376.

[Amparano et al., 2000] Amparano, F. E., Xi, Y., and Roh, Y.-S. (2000). Experimental study on the effect of aggregate content on fracture behavior of concrete. *Engineering Fracture Mechanics*, 67(1):65–84.

[ASTM C496, 1996] ASTM C496, C. (1996). *Test Method for Splitting Tensile Strength of Cylindrical Concrete Specimens.* Taylor and Francis, New York (USA).

[Bao-Chan, 2014] Bao-Chan, D. (2014). *Extending the Novel A-FEM to Model Arbitrary Cracking in Thermo-elastic Solids.* . PhD thesis, University of Miami Scholarly Repository.

[Barani et al., 2011] Barani, O., Khoei, A., and Mofid, M. (2011). Modeling of cohesive crack growth in partially saturated porous media; a study on the permeability of cohesive fracture. *International Journal of Fracture*, 167(1):15–31.

[Baroghel-Bouny, 1994] Baroghel-Bouny, V. (1994). Caractérisation des pâtes de ciment et des bétons-méthodes, analyse, interprétations.

[Basheer et al., 2005] Basheer, L., Basheer, P., and Long, A. (2005). Influence of coarse aggregate on the permeation, durability and the microstructure characteristics of ordinary portland cement concrete. *Construction and Building Materials*, 19(9):682–690.

[Bayramov et al., 2004] Bayramov, F., Akçay, B., Ağar, A., Atahan, H., Şengül, C., and Taşdemir, M. (2004). Determination of the true specific fracture energy of concrete. In *6th International Congress on Advances in Civil Engineering, Boğaziçi University, Istanbul, Turkey*, pages 6–8.

[Bažant, 2004] Bažant, Z. P. (2004). Probability distribution of energetic-statistical size effect in quasibrittle fracture. *Probabilistic Engineering Mechanics*, 19:307–319.

[Bazant and Jirásek, 2002] Bazant, Z. P. and Jirásek, M. (2002). Nonlocal integral formulations of plasticity and damage: survey of progress. *Journal of Engineering Mechanics*, 128(11):1119–1149.

[Bažant and Raftshol, 1982] Bažant, Z. P. and Raftshol, W. J. (1982). Effect of cracking in drying and shrinkage specimens. *Cement and Concrete Research*, 12(2):209–226.

[Bažnt and Raftshol, 1982] Bažnt, Z. P. and Raftshol, W. J. (1982). Effect of cracking in drying and shrinkage specimens. *Cement and Concrete Research*, 12(2):209–226.

[Benkemoun, 2010] Benkemoun, N. (2010). *Sequential multi-scale approch : application to heterogeneous quasi-brittle material*. Theses, École normale supérieure de Cachan - ENS Cachan.

[Benkemoun et al., 2010] Benkemoun, N., Hautefeuille, M., Colliat, J.-B., and Ibrahimbegovic, A. (2010). Modeling heterogeneous materials failure: 3D meso-scale models with embedded discontinuities. *International Journal of Numerical Methods in Engineering*, 82:1671–1688.

[Benkemoun et al., 2013] Benkemoun, N., Jourdain, X., Choinska, M., and Khelidj, A. (2013). Numerical modelling of the tensile splitting test and its coupling with gas permeability. VIII International Conference on Fracture Mechanics of Concrete and Concrete Structures, FraMCoS-8, Toledo, Spain.

[Biot, 1955] Biot, M. A. (1955). Theory of elasticity and consolidation for a porous anisotropic solid. *Journal of Applied Physics*, 26(2):182–185.

[Biot, 1962] Biot, M. A. (1962). Mechanics of deformation and acoustic propagation in porous media. *Journal of applied physics*, 33(4):1482–1498.

[Bisschop and Van Mier, 2002] Bisschop, J. and Van Mier, J. (2002). Effect of aggregates on drying shrinkage microcracking in cement-based composites. *Materials and Structures*, 35(8):453–461.

[Bolander and Saito, 1998] Bolander, J. E. and Saito, S. (1998). Fracture analyses using spring networks with random geometry. *Engineering Fracture Mechanics*, 61(5):569–591.

[Borja and Andrade, 2006] Borja, R. I. and Andrade, J. E. (2006). Critical state plasticity, part VI: Meso-scale finite element simulation of strain localization in discrete granular materials. *Computer Methods in Applied Mechanics and Engineering*, 195:5115–5140.

[Boulay et al., 2009] Boulay, C., Dal Pont, S., and Belin, P. (2009). Real-time evolution of electrical resistance in cracking concrete. *Cement and Concrete Research*, 39(9):825–831.

[Breysse and Gérard, 1997] Breysse, D. and Gérard, B. (1997). Transport of fluids in cracked media. *Rilem report*, pages 123–154.

[Bruggi et al., 2008] Bruggi, M., Casciati, S., and Faravelli, L. (2008). Cohesive crack propagation in a random elastic medium. *Probabilistic Engineering Mechanics*, 23(1):23–35.

[Brush and Thomson, 2003] Brush, D. J. and Thomson, N. R. (2003). Fluid flow in synthetic rough-walled fractures: Navier-stokes, stokes, and local cubic law simulations. *Water Resources Research*, 39(4).

[Cairns, 1961] Cairns, S. (1961). *Introductory Topology*. Ronald Press, New York.

[Camacho and Ortiz, 1996] Camacho, G. T. and Ortiz, M. (1996). Computational modelling of impact damage in brittle materials. *International Journal of solids and structures*, 33(20):2899–2938.

[Care and Derkx, 2011] Care, S. and Derkx, F. (2011). Determination of relevant parameters influencing gas permeability of mortars. *Construction and Building Materials*, 25(3):1248–1256.

[Carman, 1956] Carman, P. C. (1956). *Flow of gases through porous media*. Academic press.

[Chatzigeorgiou, 2004] Chatzigeorgiou, G. (2004). Coupling between damage, temperature and permeability of concrete: Experimental and numerical study. *Rapport technique, Ecole Centrale Nantes*.

[Chen and Liu, 2004] Chen, B. and Liu, J. (2004). Effect of aggregate on the fracture behavior of high strength concrete. *Construction and Building Materials*, 18(8):585–590.

[Choinska, 2006] Choinska, M. (2006). *Effets de la température, du chargement mécanique et de leurs interactions sur la perméabilité du béton de structure*. Theses, Ecole Centrale de Nantes (ECN) (ECN) (ECN) (ECN) ; Université de Nantes.

[Choinska et al., 2008a] Choinska, M., Dufour, F., Pijaudier-Cabot, G., Huerta, A., and Khelidj, A. (2008a). How can a crack opening be extracted from a continuous damage finite element computation? application for the estimation of permeability. In *Thermo-Hydromechanical and Chemical Coupling in Geomaterials and Applications: Proceedings of the 3 International Symposium GeoProc'2008*, pages 605–612. Wiley Online Library.

[Choinska et al., 2008b] Choinska, M., Dufour, F., Pijaudier-Cabot, G., Huerta, A., and Khelidj, A. (2008b). How to extract a crack opening from a continuous damage finite element computation ? application for the estimation of permeability. GeoProc2008: Proceedings of the 3rd International Symposium GeoProc'2008 (ISTE).

[Choinska et al., 2007] Choinska, M., Khelidj, A., Chatzigeorgiou, G., and Pijaudier-Cabot, G. (2007). Effects and interactions of temperature and stress-level related damage on permeability of concrete. *Cement and Concrete Research*, 37(1):79–88.

[Code,] Code, C.-F. M. 90. 1993. model code for concrete structures. comité euro-international du béton (ceb)–fédération internationale de la précontrainte (fip).

[Colliat et al., 2007] Colliat, J.-B., Hautefeuille, M., Ibrahimbegovic, A., and Matthies, H. G. (2007). Stochastic approach to size effect in quasi-brittle materials. *Comptes Rendus Mécanique*, 335(8):430–435.

[Committee et al., 2014] Committee, A., Institute, A. C., and for Standardization, I. O. (2014). Building code requirements for structural concrete (aci 318-08) and commentary. American Concrete Institute.

[Crandall et al., 2010] Crandall, D., Bromhal, G., and Karpyn, Z. T. (2010). Numerical simulations examining the relationship between wall-roughness and fluid flow in rock fractures. *International Journal of Rock Mechanics and Mining Sciences*, 47(5):784–796.

[Cunha et al., 2011] Cunha, V. M., Barros, J. A., and Sena-Cruz, J. (2011). An integrated approach for modelling the tensile behaviour of steel fibre reinforced self-compacting concrete. *Cement and Concrete Research*, 41(1):64–76.

[Dal Pont et al., 2005] Dal Pont, S., Schrefler, B., and Ehrlacher, A. (2005). Experimental and finite element analysis of a hollow cylinder submitted to high temperatures. *Materials and structures*, 38(7):681–690.

[Damgaard Jensen and Chatterji, 1996] Damgaard Jensen, A. and Chatterji, S. (1996). State of the art report on micro-cracking and lifetime of concretepart 1. *Materials and Structures*, 29(1):3–8.

[Darcy, 1856] Darcy, H. (1856). *Les fontaines publiques de la ville de Dijon: exposition et application...* Victor Dalmont.

[Djerbi et al., 2008] Djerbi, A., Bonnet, S., and Khelidj, A. (2008). Influence of traversing crack on chloride diffusion into concrete. *Cement and Concrete Research*, 38 (6):877–883.

[Dormieux and Kondo, 2004] Dormieux, L. and Kondo, D. (2004). Approche micromécanique du couplage perméabilité–endommagement. *Comptes Rendus Mécanique*, 332(2):135–140.

[Dullien, 2012] Dullien, F. A. (2012). *Porous media: fluid transport and pore structure*. Academic press.

[Dvorkin et al., 1990] Dvorkin, E. N., Cuitiño, A. M., and Gioia, G. (1990). Finite elements with displacement interpolated embedded localization lines insensitive to mesh size and distortions. *International journal for numerical methods in engineering*, 30(3):541–564.

[El Dandachy et al., 2016] El Dandachy, E., Briffaut, M., Dufour, F., and Dal Pont, S. (2016). An original semi-discrete approach to assess gas conductivity of concrete structures. *International Journal for Numerical and Analytical Methods in Geomechanics*.

[Elices and Rocco, 2008] Elices, M. and Rocco, C. (2008). Effect of aggregate size on the fracture and mechanical properties of a simple concrete. *Engineering Fracture Mechanics*, 75(13):3839–3851.

[Elsharief et al., 2003] Elsharief, A., Cohen, M. D., and Olek, J. (2003). Influence of aggregate size, water cement ratio and age on the microstructure of the interfacial transition zone. *Cement and Concrete Research*, 33(11):1837–1849.

[Escadeillas and Maso, 1990] Escadeillas, G. and Maso, J. (1990). Approach of the initial state in cement paste, mortar, and concrete. *Ceram. Trans.*, 16:169–184.

[Fabien, 2012] Fabien, A. J. (2012). *Etude du couplage comportement hydromécanique–durabilité dans le béton de la structure: application à la maquette MAREVA*. PhD thesis, Nantes.

[Fairbairn and Ulm, 2002] Fairbairn, E. M. and Ulm, F. J. (2002). A tribute to fernando llb carneiro (1913–2001) engineer and scientist who invented the brazilian test. *Materials and Structures*, 35(3):195–196.

[FaL, 1992] FaL, D. (1992). Porous media: fluid transport and pore structure. *AcademicPress, SanDiego,*, 1:992.

[Feyel and Chaboche, 2001] Feyel, F. and Chaboche, J.-L. (2001). Multi-scale non-linear FE^2 analysis of composite structures: damage and fiber size effects. *Revue européenne des Éléments Finis: NUMDAM'00 issue*, 10:449–472.

[Fischmeister, 1974] Fischmeister, H. (1974). *Pore Structure and Properties of Materials*. Academia, Prague.

[Gerard, 1996] Gerard, B. (1996). *Contribution of the mechanical, chemical, and transport couplings in the long-term behavior of radioactive waste repository structures*. PhD thesis, Univ. Laval and Ecole Normale Supérieure de Cachan.

[Gérard et al., 1996] Gérard, B., Breysse, D., Ammouche, A., Houdusse, O., and Didry, O. (1996). Cracking and permeability of concrete under tension. *Materials and Structures*, 29(3):141–151.

[Gerard et al., 1997] Gerard, B., Reinhardt, H., and Breysse, D. (1997). Measured transport in cracked concrete. *Rilem report*, pages 265–324.

[Gettu et al., 1996] Gettu, R., Mobasher, B., Carmona, S., and Jansen, D. C. (1996). Testing of concrete under closed-loop control. *Advanced Cement Based Materials*, 3(2):54–71.

[Grabiec et al., 2015] Grabiec, A. M., Zawal, D., and Szulc, J. (2015). Influence of type and maximum aggregate size on some properties of high-strength concrete made of pozzolana cement in respect of binder and carbon dioxide intensity indexes. *Construction and Building Materials*, 98:17–24.

[Grassl et al., 2012] Grassl, P., Grégoire, D., Rojas-Solano, L., and Pijaudier-Cabot, G. (2012). Meso-scale modelling of the size effect on the fracture process zone of concrete. *International Journal of Solids and Structures*, 49(13):1818–1827.

[Grassl et al., 2010] Grassl, P., Wong, H. S., and Buenfeld, N. R. (2010). Influence of aggregate size and volume fraction on shrinkage induced micro-cracking of concrete and mortar. *Cement and concrete research*, 40(1):85–93.

[Guinea et al., 2002] Guinea, G., El-Sayed, K., Rocco, C., Elices, M., and Planas, J. (2002). The effect of the bond between the matrix and the aggregates on the cracking mechanism and fracture parameters of concrete. *Cement and concrete research*, 32(12):1961–1970.

[Hearn, 1999] Hearn, N. (1999). Effect of shrinkage and load-induced cracking on water permeability of concrete. *Materials Journal*, 96(2):234–241.

[Hearn and Lok, 1998] Hearn, N. and Lok, G. (1998). Measurement of permeability under uniaxial compression–a test method. *ACI Materials Journal*, 95(6).

[Herrmann et al., 1989] Herrmann, H. J., Hansen, A., and Roux, S. (1989). Fracture of disordered, elastic lattices in two dimensions. *Physical Review B*, 39(1):637.

[Hillerborg, 1983] Hillerborg, A. (1983). Concrete fracture energy tests performed by 9 laboratories according to a draft rilem recommendation: Report to rilem tc50-fmc. *Report TVBM*.

[Hillerborg, 1984] Hillerborg, A. (1984). Additional concrete fracture energy tests performed by 6 laboratories according to a draft rilem recommendation. *Report TVBM*.

[Hillerborg, 1985] Hillerborg, A. (1985). Results of three comparative test series for determining the fracture energyg f of concrete. *Materials and Structures*, 18(5):407–413.

[Hobbs, 1974] Hobbs, D. (1974). Influence of aggregate restraint on the shrinkage of concrete. In *Journal Proceedings*, volume 71, pages 445–450.

[Hoseini et al., 2009] Hoseini, M., Bindiganavile, V., and Banthia, N. (2009). The effect of mechanical stress on permeability of concrete: a review. *Cement and Concrete Composites*, 31(4):213–220.

[Hudson et al., 1972] Hudson, J. A., Crouch, S. L., and Fairhurst, C. (1972). Soft, stiff and servo-controlled testing machines: a review with reference to rock failure. *Engineering Geology*, 6(3):155–189.

[Hwang and Young, 1984] Hwang, C.-L. and Young, J. (1984). Drying shrinkage of portland cement pastes i. microcracking during drying. *Cement and Concrete Research*, 14(4):585–594.

[Ibrahimbegovic, 2006] Ibrahimbegovic, A. (2006). Mécanique non linéaire des solides déformables: formulation théorique et résolution par éléments finis. *Lavoisier*.

[Ibrahimbegovic et al., 2011] Ibrahimbegovic, A., Colliat, J.-B., Hautefeuille, M., Brancherie, D., and Melnyk, S. (2011). Probability based size effect representation for failure in civil engineering structures built of heterogeneous materials. In *Computational Methods in Stochastic Dynamics*, pages 291–313. Springer.

[Ibrahimbegovic and Wilson, 1991] Ibrahimbegovic, A. and Wilson, E. (1991). A modified method of incompatible modes. *Communications in Applied Numerical Methods*, 7(3):187–194.

[Jacobs, 1998] Jacobs, F. (1998). Permeability to gas of partially saturated concrete. *Magazine of concrete research*, 50(2).

[Jirásek, 2000] Jirásek, M. (2000). Comparative study of finite elements with embedded discontinuities. *Computer Methods in Applied Mechanics and Engineering*, 188:307–330.

[Johnston, 1970] Johnston, C. (1970). Strength and deformation of concrete in uniaxial tension and compression. *Magazine of concrete research*, 22(70):5–16.

[Jourdain, 2014] Jourdain, X. (2014). *Étude numérique méso-macro des propriétés de transfert des bétons fissurés*. PhD thesis, École normale supérieure de Cachan-ENS Cachan.

[Jourdain et al., 2013] Jourdain, X., Colliat, J., De Sa, C., Benboudjema, F., and Gatuingt, F. (2013). Upscaling permeability for fractured concrete: mesomacro numerical approach coupled to strong discontinuities. *International Journal for Numerical and Analytical Methods in Geomechanics*, 38(5):536–550.

[Khoei et al., 2011] Khoei, A., Barani, O., and Mofid, M. (2011). Modeling of dynamic cohesive fracture propagation in porous saturated media. *International Journal for Numerical and Analytical Methods in Geomechanics*, 35(10):1160–1184.

[Kleinschrodt and Winkler, 1986] Kleinschrodt, H. and Winkler, H. (1986). The influence of the maximum aggregate size and the size of the specimen on fracture mechanics parameters. *Fracture toughness and fracture energy of concrete*, 18(8):391–402.

[Klinkenberg et al., 1941] Klinkenberg, L. et al. (1941). The permeability of porous media to liquids and gases. In *Drilling and production practice*. American Petroleum Institute.

[Kollek, 1989] Kollek, J. (1989). The determination of the permeability of concrete to oxygen by the cembureau methoda recommendation. *Materials and structures*, 22(3):225–230.

[Lachihab and Sab, 2005] Lachihab, A. and Sab, K. (2005). Aggregate composites: a contact based modeling. *Computational Material Science*, 33:467–490.

[Lawler et al., 2002] Lawler, J. S., Zampini, D., and Shah, S. P. (2002). Permeability of cracked hybrid fiber-reinforced mortar under load. *Materials Journal*, 99(4):379–385.

[Li et al., 2011] Li, K., Ma, M., and Wang, X. (2011). Experimental study of water flow behaviour in narrow fractures of cementitious materials. *Cement and Concrete Composites*, 33(10):1009–1013.

[Li et al., 2004a] Li, Q., Deng, Z., and Fu, H. (2004a). Effect of aggregate type on mechanical behavior of dam concrete. *ACI materials journal 101*, 6:483–492.

[Li et al., 2004b] Li, Q., Deng, Z., and Fu, H. (2004b). Effect of aggregate type on mechanical behavior of dam concrete. *ACI materials journal*, 101(6):483–492.

[Lomize, 1951] Lomize, G. (1951). Flow in fractured rocks. *Gosenergoizdat, Moscow*, 127:197.

[Louis, 1974] Louis, C. (1974). Introduction à l'hydraulique des roches. *BULL BRGM, III*, (4).

[Maleki and Pouya, 2010] Maleki, K. and Pouya, A. (2010). Numerical simulation of damage – Permeability relationship in brittle geomaterials. *Computers and Geotechnics*, 37(5):619 – 628.

[Maso, 1982] Maso, J. (1982). La liaison entre les granulats et la pâte de ciment hydratée, 7ième congrès international de la chimie des ciments.

[Matallah and La Borderie, 2016] Matallah, M. and La Borderie, C. (2016). 3D numerical modeling of the crack-permeability interaction in fractured concrete. 9th International Conference on Fracture Mechanics of Concrete and Concrete Structures, FraMCoS-9, Berkeley, USA.

[Matallah et al., 2010] Matallah, M., La Borderie, C., and Maurel, O. (2010). A practical method to estimate crack openings in concrete structures. *International Journal for Numerical and Analytical Methods in Geomechanics*, 34(15):1615–1633.

[Mazars, 1984] Mazars, J. (1984). *Application de la mécanique de l'endommagement au comportement non linéaire et à la rupture du béton de structure*. PhD thesis.

[Mechtcherine and Müller, 1998] Mechtcherine, V. and Müller, H. (1998). Effect of the test set-up on fracture mechanical parameters of concrete. *Fracture mechanics of concrete structures, Proceedings FraMCoS-3, Gifu (Japan), Aedificatio*, pages 377–386.

[Mehta and Monteiro, 2006] Mehta, P. and Monteiro, P. J. M. (2006). *Concrete: Microstructure, Properties and Materials*. McGraw-Hill Companies, New York, USA.

[Mehta, 1986] Mehta, P. K. (1986). Concrete. structure, properties and materials.

[Meschke et al., 2011] Meschke, G., Grasberger, S., Becker, C., and Jox, S. (2011). Smeared crack and x-fem models in the context of poromechanics. In *Numerical Modeling of Concrete Cracking*, pages 265–327. Springer.

[Meziani and Skoczylas, 1999] Meziani, H. and Skoczylas, F. (1999). An experimental study of the mechanical behaviour of a mortar and of its permeability under deviatoric loading. *Materials and structures*, 32(6):403–409.

[Mihashi et al., 1989a] Mihashi, H., Nomura, N., and Izumi, M. (1989a). Fracture of concrete and rock. In Shah, S., Swartz, S., and Barr, B., editors, *Influence of matrix strength and gravel size on fracture properties of concrete*, pages 503–512. Elsevier.

[Mihashi et al., 1989b] Mihashi, H., Nomura, N., and Izumi, M. (1989b). Influence of matrix strength and gravel grain size on fracture properties of concrete. fracture of concrete and rock: Recent developments. papers presented at the inter-

national conference, university of wales, college of cardiff, school of engineering, september 20-22, 1989. *Publication of: Society of Automotive Engineers*.

[Mihashi et al., 1991] Mihashi, H., Nomura, N., and Niiseki, S. (1991). Influence of aggregate size on fracture process zone of concrete detected with three dimensional acoustic emission technique. *Cement and Concrete Research*, 21(5):737–744.

[Moës and Belytschko, 2002] Moës, N. and Belytschko, T. (2002). Extended finite element method for cohesive crack growth. *Engineering fracture mechanics*, 69(7):813–833.

[Moës et al., 2003] Moës, N., Cloirec, M., Cartraud, P., and Remacle, J.-F. (2003). A computational approach to handle complex microstructure geometries. *Computer Methods in Applied Mechanics and Engineering*, 192:3163–3177.

[Muskat and Meres, 1936] Muskat, M. and Meres, M. W. (1936). The flow of heterogeneous fluids through porous media. *Journal of Applied Physics*, 7(9):346–363.

[Neithalath et al., 2006] Neithalath, N., Weiss, J., and Olek, J. (2006). Characterizing enhanced porosity concrete using electrical impedance to predict acoustic and hydraulic performance. *Cement and Concrete Research*, 36(11):2074–2085.

[Neville, 1997] Neville, A. M. (1997). Aggregate bond and modulus of elasticity of concrete. *ACI Materials Journal*, 94(1):71–74.

[Neville, 2011] Neville, A. M. (2011). *Properties of concrete*.

[Nilenius et al., 2015] Nilenius, F., Larsson, F., Lundgren, K., and Runesson, K. (2015). Mesoscale modelling of crack-induced diffusivity in concrete. *Computational Mechanics*, 55(2):359–370.

[Ortiz et al., 1987] Ortiz, M., Leroy, Y., and Needleman, A. (1987). A finite element method for localized failure analysis. *Computer Methods in Applied Mechanics and Enginnering*, 61:189–214.

[Park et al., 2001] Park, S., Song, H., and Byun, K. (2001). Model for chloride diffusivity and water permeability in cracked concrete. *J. KSCE*, 21(6-A):915–924.

[Park et al., 2012] Park, S.-S., Kwon, S.-J., Jung, S. H., and Lee, S.-W. (2012). Modeling of water permeability in early aged concrete with cracks based on micro pore structure. *Construction and building materials*, 27(1):597–604.

[Peng, 2009] Peng, C. (2009). *Apports de lanalyse microtomographique dans la modélisation des effets du séchage des matériaux à matrice cimentaire.* PhD thesis, Lille 1.

[Pereira et al., 2009] Pereira, C. G., Castro-Gomes, J., and de Oliveira, L. P. (2009). Influence of natural coarse aggregate size, mineralogy and water content on the permeability of structural concrete. *Construction and Building Materials*, 23(2):602–608.

[Petersson, 1980] Petersson, P. (1980). Fracture energy of concrete: practical performance and experimental results. *Cement and Concrete research*, 10(1):91–101.

[Picandet, 2001] Picandet, V. (2001). *Influence dun endommagement mécanique sur la perméabilité et sur la diffusivité hydrique des bétons.* PhD thesis, Ecole Centrale de Nantes.

[Picandet et al., 2001] Picandet, V., Khelidj, A., and Bastian, G. (2001). Effect of axial compressive damage on gas permeability of ordinary and high-performance concrete. *Cement and Concrete Research*, 31(11):1525–1532.

[Picandet et al., 2009] Picandet, V., Khelidj, A., and Bellegou, H. (2009). Crack effects on gas and water permeability of concretes. *Cement and Concrete Research*, 39(6):537–547.

[Pijaudier-Cabot et al., 2009] Pijaudier-Cabot, G., Dufour, F., and Choinska, M. (2009). Permeability due to the increase of damage in concrete : From diffuse to localized damage distributions. *Journal of Engineering Mechanics*, 135:1022–1028.

[Poiseuille, 1844] Poiseuille, J. L. (1844). *Recherches expérimentales sur le mouvement des liquides dans les tubes de très-petits diamètres*. Imprimerie Royale.

[Pouya and Courtois, 2002a] Pouya, A. and Courtois, A. (2002a). Définition de la perméabilité équivalente des massifs fracturés par des méthodes d'homogénéisation. *Surface Geosciences (Hydrology-Hydrogeology)*, 334:975–979.

[Pouya and Courtois, 2002b] Pouya, A. and Courtois, A. (2002b). Définition de la perméabilité équivalente des massifs fracturés par des méthodes d'homogénéisation. *Comptes Rendus Geoscience*, 334(13):975 – 979.

[Quenard and Sallee, 1991] Quenard, D. and Sallee, H. (1991). *Le transfert isotherme de la vapeur d'eau condensable dans les matériaux microporeux du bâtiment*. CSTB.

[Ramtani, 1990] Ramtani, S. (1990). *Contribution à la modélisation du comportement multiaxial du béton endommagé avec description du caractère unilatéral*. PhD thesis, Paris 6.

[Ramtani et al., 1992] Ramtani, S., Berthaud, Y., and Mazars, J. (1992). Orthotropic behavior of concrete with directional aspects: modelling and experiments. *Nuclear Engineering and Design*, 133(1):97–111.

[Rao and Prasad, 2002] Rao, G. A. and Prasad, B. R. (2002). Fracture energy and softening behavior of high-strength concrete. *Cement and Concrete Research*, 32(2):247–252.

[Rapoport et al., 2002] Rapoport, J., Aldea, C.-M., Shah, S. P., Ankenman, B., and Karr, A. (2002). Permeability of cracked steel fiber-reinforced concrete. *Journal of materials in civil engineering*, 14(4):355–358.

[Rastiello et al., 2014] Rastiello, G., Boulay, C., Dal Pont, S., Tailhan, J.-L., and Rossi, P. (2014). Real-time water permeability evolution of a localized crack in concrete under loading. *Cement and Concrete Research*, 56:20–28.

[Rastiello et al., 2015] Rastiello, G., Tailhan, J.-L., Rossi, P., and Dal Pont, S. (2015). Macroscopic probabilistic cracking approach for the numerical modelling of fluid leakage in concrete. *Annals of Solid and Structural Mechanics*, 7(1-2):1–16.

[Réthoré et al., 2007] Réthoré, J., Borst, R. d., and Abellan, M.-A. (2007). A two-scale approach for fluid flow in fractured porous media. *International Journal for Numerical Methods in Engineering*, 71(7):780–800.

[Reynouard et al., 2009] Reynouard, J.-M., Pijaudier-Cabot, G., and Torrenti, J.-M. (2009). *Mechanical behavior of concrete*. Wiley, New-York.

[Rocco et al., 1999] Rocco, C., Guinea, G. V., Planas, J., and Elices, M. (1999). Mechanism of rupture in splitting test. *Materials Journal*, 96(1):52–60.

[Romm, 1966] Romm, E. (1966). Flow characteristics of fractured rocks. *Nedra, Moscow*, 283.

[Rossi and Boulay, 1990] Rossi, P. and Boulay, C. (1990). Influence of free water in concrete on the cracking process. *Magazine of concrete research*, 42(152):143–146.

[Rossi et al., 1992] Rossi, P., Van Mier, J., Boulay, C., and Le Maou, F. (1992). The dynamic behaviour of concrete: influence of free water. *Materials and Structures*, 25(9):509–514.

[Roubin, 2013] Roubin, E. (2013). *Meso-scale FE and morphological modeling of heterogeneous media : applications to cementitious materials*. PhD thesis, École Normal Supérieure de Cachan.

[Roubin et al., 2015] Roubin, E., Vallade, A., Benkemoun, N., and Colliat, J.-B. (2015). Multi-scale failure of heterogeneous materials: A double kinematics enhancement for embedded finite element method. *International Journal of Solids and Structures*, 52:180–196.

[Samaha and Hover, 1992] Samaha, H. R. and Hover, K. C. (1992). Influence of microcracking on the mass transport properties of concrete. *Materials Journal*, 89(4):416–424.

[Saouma et al., 1991] Saouma, V. E., Broz, J. J., Brühwiler, E., and Boggs, H. L. (1991). Effect of aggregate and specimen size on fracture properties of dam concrete. *Journal of Materials in Civil Engineering*, 3(3):204–218.

[Schlangen and Garboczi, 1997] Schlangen, E. and Garboczi, E. J. (1997). Fracture simulations of concrete using lattice models: computational aspects. *Engineering Fracture Mechanics*, 57:319–332.

[Schlangen and van Mier, 1992] Schlangen, E. and van Mier, J. G. M. (1992). Simple lattice model for numerical simulation of fracture of concrete materials and structures. *Materials and Structures*, 25:534–542.

[Scrivener, 2001] Scrivener, K. (2001). *Cours on-line*. EPFL.

[Scrivener et al., 2004] Scrivener, K. L., Crumbie, A. K., and Laugesen, P. (2004). The interfacial transition zone (itz) between cement paste and aggregate in concrete. *Interface Science*, 12(4):411–421.

[Setzer, 1975] Setzer, M. (1975). Zum mikrogefüge des zementsteins und dessen einfluss auf das mechanische verhalten des betons. *ZEMENT U BETON*, (85/86).

[Shah and Sankar, 1987] Shah, S. and Sankar, R. (1987). Internal cracking and strain softening response of concrete under uniaxial compression. *Materials Journal*, 84(3):200–212.

[Simo and Hughes, 1997] Simo, J. and Hughes, T. (1997). *Computational Inelasticity*. Interdisciplinary Applied Mathematics. Springer Verlag, New York, Berlin, Heidelberg.

[Simo et al., 1993] Simo, J., Oliver, J., and Armero, F. (1993). An analysis of strong discontinuities induced by strain-softening in rate independent inelastic solids. *Computational Mechanics*, 12:277–296.

[Simo and Oliver, 1994] Simo, J. C. and Oliver, J. (1994). A new approach to the analysis an simulation of strain softening in solids. In *Fracture and Damage in Quasibrittle Structures*, E & FN Spon, pages 25–39. London, z. p. bazant, z. bittar, m. jirásek and j. mazars edition.

[Slattery, 1967] Slattery, J. C. (1967). Flow of viscoelastic fluids through porous media. *AIChE Journal*, 13(6):1066–1071.

[Snow, 1969] Snow, D. (1969). *A Parallel Plate Model of Permeable Fractured Media.* . PhD thesis, University of California at Berkley.

[Stock et al., 1979] Stock, A., Hannantt, D., and Williams, R. (1979). The effect of aggregate concentration upon the strength and modulus of elasticity of concrete. *Magazine of concrete research*, 31(109):225–234.

[Struble, 1987] Struble, L. (1987). Microstructure and fracture at the cement paste-aggregate interface. In *MRS Proceedings*, volume 114, page 11. Cambridge Univ Press.

[Syroka-Korol et al., 2013] Syroka-Korol, E., Tejchman, J., and Mróz, Z. (2013). Fe calculations of a deterministic and statistical size effect in concrete under bending within stochastic elasto-plasticity and non-local softening. *Engineering Structures*, 48:205–219.

[Tasdemir et al., 1996] Tasdemir, C., Tasdemir, M. A., Lydon, F. D., and Barr, B. I. (1996). Effects of silica fume and aggregate size on the brittleness of concrete. *Cement and Concrete Research*, 26(1):63–68.

[TCS, 1985] TCS, R. (1985). Determination of the fracture energy of mortar and concrete by means of three-point bend tests on notched beams. *EnMaterials and Structures*, 18(6):287–290.

[Terrien, 1980] Terrien, M. (1980). Emission acoustique et" comportement mecanique post-critique" d'un beton sollicite en traction. *BULL LIAISON LAB PONTS CHAUSS*, (105).

[Van Mier and Van Vliet, 2002] Van Mier, J. and Van Vliet, M. (2002). Uniaxial tension test for the determination of fracture parameters of concrete: state of the art. *Engineering Fracture Mechanics*, 69(2):235–247.

[Villain et al., 2001] Villain, G., Baroghel-Bouny, V., Kounkou, C., and Hua, C. (2001). Measuring the gas permeability as a function of saturation rate of concrete. *Fr J Civ Eng*, 5:251–268.

[Wang, 1994] Wang, J. (1994). Development and application of a micromechanics-based numerical approach for the study of crack propagation in concrete.

[Wang et al., 1997] Wang, K., Jansen, D. C., Shah, S. P., and Karr, A. F. (1997). Permeability study of cracked concrete. *Cement and Concrete Research*, 27(3):381–393.

[Ward, 1969] Ward, M. (March 1969). *The testing of concrete materials by precisely controlled uniaxial tension.* PhD thesis, University of London for the degree of PhD.

[Washizu, 1982] Washizu, K. (1982). *Variational methods in elasticity and plasticity.* Technical Report 25-18, MIT, Pergamon Press, New York, 3 edition edition.

[Whitaker, 1986a] Whitaker, S. (1986a). Flow in porous media i: A theoretical derivation of darcy's law. *Transport in porous media*, 1(1):3–25.

[Whitaker, 1986b] Whitaker, S. (1986b). Flow in porous media ii: The governing equations for immiscible, two-phase flow. *Transport in porous media*, 1(2):105–125.

[Wilson et al., 1973] Wilson, E., Taylor, R., Doherty, W., and Ghaboussi, J. (1973). Incompatible displacement models. *Numerical and computer methods in structural mechanics*, 43.

[Witherspoon et al., 1980] Witherspoon, P. A., Wang, J. S., Iwai, K., and Gale, J. E. (1980). Validity of cubic law for fluid flow in a deformable rock fracture. *Water resources research*, 16(6):1016–1024.

[Wong et al., 2009] Wong, H., Zobel, M., Buenfeld, N., and Zimmerman, R. (2009). Influence of the interfacial transition zone and microcracking on the

diffusivity, permeability and sorptivity of cement-based materials after drying. *Mag. Concr. Res*, 61(8):571–589.

[Wriggers and Moftah, 2006] Wriggers, P. and Moftah, S. O. (2006). Mesoscale models for concrete: Homogenisation and damage behaviour. *Finite Elements in Analysis and Design*, 42:623–636.

[Wu et al., 2015] Wu, Z., Wong, H., and Buenfeld, N. (2015). Influence of drying-induced microcracking and related size effects on mass transport properties of concrete. *Cement and Concrete Research*, 68:35–48.

[Yaman et al., 2002] Yaman, I. Ö., Hearn, N., and Aktan, H. M. (2002). Active and non-active porosity in concrete. part I: experimental evidence. *Materials and Structures*, 35:102–109.

[Yang and Xu, 2008] Yang, Z. and Xu, X. F. (2008). A heterogeneous cohesive model for quasi-brittle materials considering spatially varying random fracture properties. *Computer methods in applied mechanics and engineering*, 197(45):4027–4039.

[Yi et al., 2011] Yi, S.-T., Hyun, T.-Y., and Kim, J.-K. (2011). The effects of hydraulic pressure and crack width on water permeability of penetration crack-induced concrete. *Construction and Building Materials*, 25(5):2576–2583.

[Yip et al., 2005] Yip, M., Mohle, J., and Bolander, J. E. (2005). Automated modeling of three-dimensional structural components using irregular lattices. *Computer-Aided Civil anf Infrastructure Engineering*, 120:393–407.

[Yssorche-Cubaynes and Ollivier, 1999] Yssorche-Cubaynes, M.-P. and Ollivier, J. (1999). La microfissuration d'autodessiccation et la durabilité des bhp et bthp. *Materials and Structures*, 32(1):14–21.

[Zhang et al., 2005] Zhang, J., Liu, Q.-q., and Wang, L.-s. (2005). Effect of coarse aggregate size on relationship between stress and crack opening in normal and high strength concretes. *JOURNAL OF MATERIALS SCIENCE AND TECHNOLOGY-SHENYANG-*, 21(5):691.

[Zhou et al., 2006] Zhou, J., Shao, J.-F., and Xu, W. (2006). Coupled modeling of damage growth and permeability variation in brittle rocks. *Mechanics Research Communications*, 33(4):450–459.

UNIVERSITE BRETAGNE LOIRE

UNIVERSITÉ DE NANTES

Thèse de Doctorat

Hayder AL-KHAZRAJI

Influence of crack opening, aggregates size and volume fraction on hydro-mechanical properties of concrete in a Brazilian splitting test: 3D meso-macro scale modeling and experimental work

Résumé

La perméabilité influe indirectement sur la durabilité des structures en béton. Elle gouverne le taux de pénétration des agents agressifs, responsables de dégradations, sous un gradient de pression. Ce travail a pour but l'étude des interactions entre l'ouverture des fissures et le transport des fluides dans le béton, soumis à un essai Brésilien de traction indirect par fendage. Cette étude est composée de deux parties : une numérique et une expérimentale. La première concerne la modélisation des matériaux hétérogènes, tels que le béton, et met en évidence ses deux particularités : l'aspect multiphasique du matériau et la propagation 3D de fissures. Ainsi, nous proposons un couplage entre l'ouverture de fissure et la perméabilité au gaz selon un modèle hydro-mécanique à l'échelle mésoscopique. L'objectif de la deuxième partie expérimentale est de fournir des données pour des modèles numériques et de les valider ainsi. Ce travail est réalisé sur des éprouvettes de mortier avec 3 différents tailles de granulat, soumises au transfert de gaz au cours du chargement par l'essai Brésilien. Le modèle numérique mésoscopique, employé dans cette étude, est basé sur une approche tridimensionnelle pour représenter l'hétérogénéité du matériau et les mécanismes de rupture du béton. Ce modèle considère le béton comme un matériau bi-phasique où les granulats sont fondus dans la pâte du ciment. Afin de pallier aux hétérogénéités du matériau et l'emploi du maillage non-adaptatif, une faible discontinuité a été introduite dans le premier enrichissement de la cinématique. Le deuxième enrichissement de la cinématique introduite ici est la discontinuité du déplacement (forte) afin de représenter l'ouverture de la fissure (champ du déplacement discontinu). Le modèle hydromécanique représente le transport du fluide (gaz) dans le béton par l'intermédiaire de la loi de Darcy pour la section non fissurée (porosité) et par la loi de Poiseuille pour la section fissurée (flux laminaire). Dans ce modèle, une interaction entre l'ouverture de fissure, obtenue par le modèle mécanique (mésoscopique), et la perméabilité du gaz est considérée. Le travail expérimental effectué est présenté pour la validation du modèle hydro-mécanique numérique proposé. Les résultats de simulations numériques sont en accord avec des travaux expérimentaux et théoriques précédents.

Mots clés

Essai Brésilien de traction indirecte par fendage, Modélisation méso-échelle, Faible discontinuité, Forte discontinuité, Méthode des éléments finis, Perméabilité aux gaz

Abstract

Permeability is a parameter that may indirectly influence the durability of concrete structures by governing the rate of penetration of aggressive substances responsible for degradation under a pressure gradient. The aim of this thesis is to study the interaction between the crack opening and the transfer of fluids in concrete of the Brazilian splitting tensile test (BSTT). Herein, the influence of aggregates size and volume fraction on hydro-mechanical properties of concrete is investigated. This study consists of two parts: the numerical and the experimental one. The first one focuses on the meso-scale modeling of a heterogeneous material like a concrete, which may be characterized by two features: multi-phase behavior and 3D crack propagation. The numerical study deals therefore with the coupling between crack opening and gas permeability according to a developed hydro-mechanical model at a meso-scale. The objective of the second, experimental part, is to provide data for numerical models and to validate the latter. This work is carried out on mortar specimens with 3 different aggregate sizes, submitted to gas transfer during a BSTT. The numerical meso-scale model is based upon a 3D lattice approach to represent the heterogeneity of the material and the failure mechanism of concrete. This model considers concrete as a two-phases material in which aggregates melt within a cement paste. Because a non-adapted meshing process was used to mesh the microstructure, a weak discontinuity was introduced in the first enhancement of the kinematics. The second enhancement of kinematics introduced here is the displacement discontinuity (strong) to represent crack opening (discontinuous displacement-field). The hydro-mechanical model represents the transport of fluids (gases) through the concrete, depending on Darcy's law for a uncracked section (porosity) and Poiseuille's law for a cracked section (laminar flow). In this model, the interaction between the crack opening, obtained from the mechanical model (meso-scale), and the gas permeability is investigated. The experimental work is presented for the validation of the hydro-mechanical model. The numerical results show good agreement with some previous experimental and theoretical studies.

Key Words

Brazilian splitting tensile test, Meso-scale modeling, Weak discontinuity, Strong discontinuity, Finite Element Method, Gas permeability

L'Université Bretagne Loire